CIVIL ENGINEERING STUDIES
STRUCTURAL RESEARCH SERIES NO. 260

MOMENT-ROTATION CHARACTERISTICS OF REINFORCED CONCRETE MEMBERS SUBJECTED TO BENDING, SHEAR, AND AXIAL LOAD

By
R. YAMASHIRO
C. P. SIESS

A REPORT ON A RESEARCH PROJECT
Sponsored by
THE PORTLAND CEMENT ASSOCIATION

UNIVERSITY OF ILLINOIS
URBANA, ILLINOIS
DECEMBER, 1962

MOMENT-ROTATION CHARACTERISTICS OF REINFORCED CONCRETE MEMBERS SUBJECTED TO BENDING, SHEAR, AND AXIAL LOAD

by

R. Yamashiro
C. P. Siess

University of Illinois
Urbana, Illinois
December 1962

TABLE OF CONTENTS

TABLE OF CONTENTS (Cont'd)

LIST OF TABLES

LIST OF FIGURES

LIST OF FIGURES (Cont'd)

LIST OF FIGURES (Cont'd)

LIST OF FIGURES (Cont'd)

LIST OF FIGURES (Cont'd)

1. INTRODUCTION

1.1 Object and Scope

The work reported herein was carried out as part of an investigation to obtain fundamental information on the strength and deformation characteristics of beam-column connections. An earlier phase, involving specimens subjected to transverse load only, was reported by Burns (1)* in January 1962. The current phase is concerned with beam-column connections subjected to combined transverse and axial loading. The experimental work was oriented so as to obtain maximum information about deformations.

Extensive investigations on the strength of reinforced concrete members subjected to the most usual cases of loading have been conducted and reported in the technical literature, and it is now possible to predict their strength with satisfactory accuracy. However, little is known and a relatively small amount of research has been done regarding their capacity for deformation.

A knowledge of the deformation capacity of a reinforced concrete member is important in many aspects of reinforced concrete design. The ability of a structure to withstand safely earthquake motions or blast loadings depends on both the strength and the deformation capacity of its members. This knowledge is also needed if limit design procedures are to be applied to reinforced concrete structures.

The deformation capacity of reinforced concrete frames subjected primarily to lateral loading or deformation depends mainly on the deformation capacity of the connections, because it is at the connections where most of the deformations occur. In rectangular frames, there are basically three

---

* Numbers in parentheses refer to entries in the List of References.

geometrically different types of connections, as shown in the upper sketch of Fig. 1.1. However, the variety of loading conditions they may be subjected to is very great, and a given type of connection may behave differently under different loading conditions.

The types of connections and loading conditions that have been the subject of earlier investigations are shown in the lower part of Fig. 1.1. Type A was studied by McCollister (2), Type B_1 by Ernst (3) and Burns (1), and Type C by Glanville and Thomas (4).

In this investigation, which consisted of both experimental and analytical phases, eleven connections of Type B_2 were tested. Since the tests were concerned mainly with column members, the amount of reinforcement at both faces were equal. The primary variables were the magnitude of the axial load and the amount of longitudinal reinforcement; four values of the axial load, including zero, and three percentages of longitudinal reinforcement were used. On the basis of studies of the results of these tests as well as those by McCollister (2) and Burns (1), analytical procedures for estimating moments and deformations at three stages of the behavior of the specimens were developed; the three stages considered were: yield of the tension reinforcement, first visible signs of crushing in the concrete, and collapse of the member. These procedures then were used to compute moments and deflections at all three stages for all specimens in the three test programs, except that values were not computed at collapse for the specimens tested by McCollister. Finally, the computed quantities were compared with the measured values.

Chapter 2 of this report describes briefly the test program and procedures* and Chapter 3 presents and discusses the results of the tests. Analytical procedures for estimating moments and deflections at yield, crushing,

---

* A more complete description is given in Appendices A and B.

and ultimate, are developed in Chapter 4. In Chapter 5, these procedures are used to compute moments and deflections for the specimens in this program and for those tested by McCollister and Burns, and the computed values are compared with those measured in the tests.

1.2 Acknowledgment

These studies were carried out at the Structural Research Laboratory of the Department of Civil Engineering of the University of Illinois, and were sponsored by the Portland Cement Association.

The experimental program was planned by Dr. C. P. Siess, Professor of Civil Engineering, and Dr. M. A. Sozen, Associate Professor of Civil Engineering, of the University of Illinois, in cooperation with Mr. A. L. Parme, Principal Engineer, Advanced Engineering Group, and Mr. L. H. Corning, Chief Consulting Structural Engineer, of the Portland Cement Association.

Dr. Siess was director and supervisor of the project, and this report was written as a doctoral thesis under his direction.

Appreciation is due to Dr. Sozen for his helpful suggestions during the course of these studies. The valuable assistance in conducting the tests and analyzing the data of Peter Gergely and Joseph Colaco, research assistants, and of Dr. Hiroyuki Aoyama, visiting research scientist from the University of Tokyo, is gratefully acknowledged.

1.3 Notation

A_s = area of tensile reinforcement.

A'_s = area of compressive reinforcement.

A''_s = cross-sectional area of transverse reinforcement.

C_c = total compressive force in concrete.

C'_c = compressive force in concrete not enclosed by lateral reinforcement.

C''_c = compressive force in concrete enclosed by lateral reinforcement.

C_s = force in compressive reinforcement.

D' = diameter of compression bars.

D_s = diameter of concrete cored confined by lateral reinforcement.

E_c = Young's modulus of elasticity of concrete.

E_s = Young's modulus of elasticity of steel.

E_t = tangent modulus of steel.

M^* = bending moment about mid-depth of section.

M_{cr} = bending moment at cracking.

M_r = resisting moment.

P = axial load.

T = force in tensile reinforcement.

V = total shear force at a section.

V_c = shear force carried by concrete.

V_s = shear force carried by transverse reinforcement.

a = length of tensile reinforcement between the face of the stub and the first theoretical inclined crack.

b = width of rectangular beam or beam-column.

b'' = width of concrete core enclosed by lateral reinforcement.

c = depth from compression face to neutral axis.

d = depth from compression face to centroid of tensile reinforcement.

d' = depth from compression face to centroid of compressive reinforcement.

---

* See end of this list for definition of subscripts.

d'' = depth from inside face of the ties to centroid of tensile reinforcement.

fcn = function notation.

f'_c = compressive strength of 6 by 12-in. cylinders.

f''_c = compressive strength of unconfined concrete.

f_{cr} = (critical) stress in compression bars at which buckling occurs.

f_s = stress in tensile reinforcement.

f'_s = stress in compressive reinforcement.

f''_s = stress in lateral reinforcement.

f_y = yield stress of tensile reinforcement.

f'_y = yield stress of compressive reinforcement.

f''_y = yield stress of lateral reinforcement.

f_1 = compressive strength of confined concrete.

$f_2 = \frac{1}{2}(f_{21} + f_{22})$ = measure of lateral confinement

f_{21}, f_{22} = lateral normal stresses in perpendicular directions.

h = height of concrete section enclosed by lateral reinforcement.

$j = 1 - \frac{1}{3}\frac{c}{d}$ = ratio of distance between centroids of compressive stresses in concrete and tensile stresses to effective depth $\underline{d}$.

k_2 = ratio of depth of centroid of compressive stresses in concrete to depth of neutral axis at crushing.

$\bar{k}_2$ = same definition as for k_2 except that it refers to any stage of behavior.

$k_1 k_3$ = ratio of average compressive stresses in concrete at crushing to the cylinder strength f'_c.

$\bar{k}_1 \bar{k}_3$ = ratio of average compressive stresses in concrete at any stage of behavior to the confined strength f_1.

ℓ = distance from support to face of the stub (shear span).

$n = E_s/E_c$ = modular ratio.

$p = A_s/bd$ = tension steel ratio.

$\bar{p}$ = $(A_s + \frac{P}{f_y})/bd$ = equivalent tension steel ratio at yield.

p' = A'_s/bd = compression steel ratio.

p'' = ratio of volume of lateral reinforcement to volume of concrete enclosed by the lateral reinforcement.

p_g = ratio of total area of longitudinal reinforcement to gross area of cross-section.

r = radius of bar.

s = longitudinal spacing of the lateral reinforcement.

w = length of stub.

x^* = elongation of tensile reinforcement in wedge. See Fig. 4.15.

Δ^* = equivalent midspan deflection. See Figs. 3.1 and 4.16c.

Δ_b^* = deflection due to deformations in beam. See Fig. 4.16c.

Δ_i^* = deflection due to deformations in wedge. See Fig. 4.16c.

Δ_s^* = deflection due to deformations in stub. See Fig. 4.16c.

Δf_c = increase of concrete strength over the unconfined value due to confinement.

$\sum o$ = sum of perimeters of bars of tensile reinforcement.

ϵ_c = compressive strain in concrete at extreme fiber.

ϵ_s = strain in tensile reinforcement.

ϵ'_s = strain in compressive reinforcement.

ϵ_y = yield strain of tensile reinforcement.

ϵ'_y = yield strain of compressive reinforcement.

ϵ_u = compressive strain in concrete at extreme fiber at crushing.

φ^* = curvature.

θ^* = rotation. See Fig. 4.16c.

---

* See end of this list for definition of additional subscripts.

θ_s^* = rotation of beam due to deformations in stub. See Fig. 4.16c.

θ_b^* = rotation of chord between face of stub and support due to deformations in beam. See Fig. 4.16c.

θ_i^* = rotation of beam due to deformations in wedge. See Fig. 4.16c.

Subscripts not defined in preceding notation:

c = crushing stage.

f = due to flexural deformations.

p = due to plastic strain, $\epsilon_s - \epsilon_y$, in the tensile reinforcement.

u = ultimate stage.

y = yield stage.

---

* See end of this list for definition of additional subscripts.

2. TEST PROGRAM

2.1 Preliminary Remarks

In this chapter, the test program is described. In order to understand better the reasoning behind the planning of the current series of tests, interaction curves and load-deformation characteristics for sections under combined bending and axial load are discussed briefly in Section 2.2. The outline of the test program is given and the test specimens are described in Section 2.3. Section 2.4 deals with those details of the test procedure and measurements which are essential to follow the presentation of the test results in Chapter 3. More detailed information on the test specimens and procedures are given in Appendices A and B.

Since results from the tests by McCollister (2) and Burns (1) are also used in this study, the properties of their specimens are listed in Tables 2 and 3, respectively.

2.2 Interaction Curves

The theoretical considerations that guided the planning of the current test program were supplied by a study of interaction curves and the associated curves relating the deformations to axial load or moment for sections under combined bending and axial load. The curves used are shown in Fig. 2.1. The two sets of curves on the left represent the combinations of axial load, P, and moment*, M, corresponding to certain specified stages in the loading history of

---

* For convenience, the bending moment is taken about the plastic centroid of the section, which is defined as the point of application of the resultant of the internal forces when a uniform strain, equal to the one corresponding to the peak concrete stress, is assumed for the entire cross-section. At this strain, about 0.002, the longitudinal reinforcement for most usual cases, is in the plastic range; that is, the stress is equal to the yield value. Since the specimens had equal tensile and compressive reinforcement, the plastic centroid was at mid-depth of the section.

the two cross-sections considered. The two sets of curves on the right show the curvatures, φ, corresponding to the same stages, and are plotted as functions of the axial load P. For the purposes of this study, the stages considered are those corresponding to first yielding of the tensile reinforcement (Curves 1) and first crushing of the concrete (Curves 2), assumed to occur at some limiting strain.

For example, Curve 1 on the P-M plot represents all combinations of moment and axial load on the section which will just produce yielding of the tension reinforcement. In the same manner, Curve 1 on the plot of P versus φ represents the curvature at first yielding for the combination of M and P from the other plot corresponding to the value of P chosen. The sets of curves labelled "2" have similar significance in relation to the stage corresponding to first crushing of the concrete at some limiting strain.

In discussing the effect of the variables on the deformation characteristics, the curvatures at crushing will be used as a measure of ductility. At this stage in the planning of the tests, first crushing of the concrete was the most advanced stage of behavior for which rational procedures to compute M, P, and φ were available. Although the corresponding values at ultimate may be many times larger than those at crushing, especially when properly tied compressive reinforcement is provided, the ratios of curvature at crushing to that at first yielding supply acceptable means for visualizing the effect of the variables on the ductility.

Curves 2, for crushing, in Fig. 2.1 were obtained for the following assumptions:

a) strains are distributed linearly,

b) stress-strain relationships for the concrete and the reinforcement are known,

c) concrete crushes at a limiting strain.

As will be discussed in Section 4.6, the stress-strain relationship for steel from tests of coupons and the properties of the stress-strain curve for concrete given by Eqs. 4.16-18 were used in the computations. Three points on Curves 2 of the P-M plot deserve special attention. The P-axis intercept is the axial load capacity of the section. The M-axis intercept is the crushing moment value for bending alone. The break in the curve represents the combinations of P and M corresponding to simultaneous yielding of the tensile reinforcement and crushing of the concrete and is called the "balance point" since it represents a condition just balanced between crushing and yielding. Above this point, concrete crushes before the tensile reinforcement yields; below it, yield of the tensile reinforcement occurs before the concrete crushes.

The Curves 2 in the P-φ plot show that the curvature at crushing decreases with an increase in axial load. The major part of the reduction takes place between P = 0 and the balance point.

Curves 1 in the P-M and P-φ plots, which correspond to yield of the tensile reinforcement, stop at the balance point because above this point the tensile reinforcement does not yield before the concrete crushes. Curves 1 in reference to Curves 2 give a good picture of the effect of the axial force on the load-deformation characteristics of a section under combined bending and axial load. The curves in the P-M plot indicate that there is little increase in the bending moment beyond yield; the curves in the P-φ plot show that the deformation beyond yield, an index of the ductility of a member, becomes smaller and smaller as the axial load increases. This deformation is zero at the balance point.

The load-deformation characteristics are also affected by the amount of longitudinal reinforcement. For a section subjected to moment only, it is well known that the ductility increases with the amount of compressive

reinforcement, and decreases with the amount of tensile reinforcement. However, in the usual column, the amounts of tensile and compressive reinforcement are equal. When this is the case, it is difficult to visualize, without computations, the effect of increasing the amount of longitudinal reinforcement since increases in the amount of both tension and compression reinforcement have compensating effects on the ductility as measured by the plastic deformation at crushing. The effect of the longitudinal reinforcement can be studied better by means of interaction curves. Figure 2.1 shows interaction curves for two sections that differ only in the amounts of longitudinal reinforcement. The effects of the longitudinal reinforcement on the strength and the ductility can readily be visualized from these curves. For a given axial load, the crushing moment increases with the amount of longitudinal reinforcement. For the same M/P ratio (equal to the eccentricity of the resultant of the internal forces about the plastic centroid of the section), both P and M increases with the amount of longitudinal reinforcement. Note that the axial load at the balance point is the same for both sections because both the compression and tension steel are at the yield stress.* For the same value of P, the curvature beyond yield is larger for the section with the smaller amount of reinforcement.

In addition to the axial load and the longitudinal reinforcement, there are many other variables which influence the load-deformation characteristics of a reinforced concrete section. They include the concrete strength, the dimensions of the cross-section, the quality of the reinforcement, and the amount and spacing of the transverse reinforcement. There is an additional variable that affects not the ductility of a section but the ductility of the

---

* This condition will exist at the balance point for most common sections and materials. When it does, the forces in the equal tensile and compressive reinforcement balance each other and do not contribute to the axial load.

member as a whole, the shear force, which is a function of the loading on the member. There are many variables, their ranges are quite large, and much research will be needed to clarify the complex interrelationships among them. This investigation was limited to a study of only two of these variables as described in the next section.

2.3 Outline of Tests

The study of interaction curves indicated that the axial force and the longitudinal reinforcement were two of the major variables influencing the ductility of reinforced concrete members. For this reason, they were made the two principal variables in this test series. The values of these variables for the 11 specimens tested are given in Table 1, and points representing the specimens are shown on the interaction curves for crushing in Fig. 2.1. The axial load, which was kept constant during the test of each specimen, was varied from zero to 75 kips. The maximum ratio of the applied axial load to the axial load at the balance point was 0.58; that is, all the specimens were subjected to conditions below the balance point. The amount of longitudinal reinforcement was varied from $p_g = 0.0111$ to 0.0555. This range covers most practical cases.

The specimens had the same shape as those tested by Burns. Figure 2.2 shows elevations and cross sections of the specimens, and other properties are given in Table 1. They were simply supported members with a stub at midspan to simulate a connection between beams and columns. They were 13 ft long over-all and had a 12-ft span between supports. Except for specimens J-15 and J-16, which were tested during the exploratory stage of this investigation, all specimens had a cross-section of 6 by 12 in.; J-15 and J-16 had a cross-section of 8 by 12 in.; the sections were kept smaller than those tested by Burns, so

that a larger ratio of the applied axial load to the axial load capacity of the section could be attained with the equipment available.

Except for J-34, all specimens contained #3 ties at 6-in. centers; J-34 contained #3 ties at 3-in. centers for a length of 12 in. out from the stub face; the remainder of the ties were spaced at 6 in. In all cases, there was a tie at 3 in. out from the stub face. The closer tie spacing for J-34 was used in order to explore the effect of lateral reinforcement on the ductility; the companion specimen, J-27, had shown a very small amount of ductility; both J-34 and J-27 were subjected to 75 kips axial loads, the highest in this series.

All other quantities were kept constant, except for minor variations in the quality of the materials. The shear span was 66 inches; the effective depth, 10 inches; and the top and bottom cover (measured to the center of the bars), 2 inches. Intermediate grade reinforcement with yield points from 44.7 to 50.3 ksi, and concrete with cylinder strengths from 4280 to 5060 psi were used (Table 1).

2.4 Test Procedure

The specimens were tested under combined bending, axial load, and shear to simulate the more usual conditions in column members of a reinforced concrete frame. Figures B.2 and B.3 show photographs of the test frame and loading apparatus. The test set-up is described in Appendix B.

The axial load was applied at the ends of the specimens at mid-depth; it was applied at the beginning of the test and kept constant thereafter. The transverse load was applied through the stub in increments up to collapse of the member; these increments were from two to five kips up to yield of the member; then, until the first visible signs of crushing were detected, the

mid-span deflection was increased by increments of 0.1 in.; after crushing, the deflection increments were from 0.5 to 1.0 in. until the specimen failed. The test was discontinued when the axial load could not be kept constant because of loss of strength of the member. The transverse load was removed and reapplied at various levels of deflection in order to obtain information on the change in stiffness of the member with the extent of damage.

Extensive measurements were taken during the tests. Transverse and axial loads, and deflections at various locations were measured for each load or deflection increment. Deflections were measured at the stub face and at the mid-point between the stub face and the support, on either side of the stub. Steel and concrete strains were measured at several locations. Table B.1 in the appendix lists these strain measurements.

In addition to the loads and deflections measured at each load increment, a continuous plot of the transverse load versus the mid-span deflection was recorded with an automatic plotter. This record was very useful both during the tests, and later, in the reduction of test data.

The total testing time was four to six hours. Except in two instances, control cylinders and beams were tested on the same day as the beam-column specimens.

3. RESULTS OF TESTS

3.1 Preliminary Remarks

Before any reliable analytical procedure for estimating the load-deformation characteristics of a member framing into a connection can be developed, a sufficient understanding of the behavior and modes of failure of this type of members, and of the effects of the variables on the behavior and modes of failure is necessary. The results of tests at the University of Illinois carried out in 1961-1962, which were designed for this purpose, are presented and discussed in this chapter. The measured moments and deflections at yield, crushing and ultimate and the observed modes of failure are listed in Table 4.

Section 3.2 presents and discusses the behavior of the test specimens. Section 3.3 describes, and examines the causes for, the various modes of failure observed in the tests. The effects of the variables are presented and discussed in Section 3.4. Because the stub had important effects on the strength and the deformation capacity of the connections, its effects are discussed in Section 3.5. Some aspects of the behavior, which can be explained better after a rational theory is developed because of the complicated interrelationship of the variables, will be considered in Chapters 4 and 5.

3.2 Behavior of Test Specimens

Moment-Rotation Relationships

The most important index of the response to load of a member is given by its load-deformation characteristics, which provide information on both the strength and the ductility of the member. In this study, the moment-rotation (M-θ) curves for the eleven specimens tested, shown in Figs. 3.2

through 3.12 have been chosen as a basis for studying these characteristics for two reasons; first, by using moment rather than load, the action of both the transverse and the axial load can be considered simultaneously; and second, it is the rotation (θ) as defined in Fig. 3.1 that is the quantity of interest as a measure of the capacity for deformation of a connection. The total bending moment is equal to the sum of the moments due to the transverse load and the longitudinal load, all about mid-depth of the section at the face of the stub. Curves for the moment due to transverse load and that due to longitudinal load are also shown in the figures. Since the specimens deflected asymmetrically, and failure occurred on the side of the stub that rotated the most, θ is the largest measured rotation and it was determined using the deflections with respect to the supports measured at both faces of the stub as shown in Fig. 3.1. For convenience, a scale for equivalent deflection $\Delta(= \theta \ell)$ has also been provided. The deflection Δ is larger than the midspan deflection, and is equivalent to the midspan deflection in the ideal case that the specimen deflects symmetrically, both measured at the same stage of behavior. For example, if a specimen deflecting asymmetrically fails when the midspan deflection is 10 in. and the equivalent deflection is 15., the same specimen deflecting symmetrically would fail when the midspan deflection is 15 in.

The characteristics of the M-θ curves will be described with reference to the curve for specimen J-25 (p_g = 0.0111, P = 25 kips) shown in Fig. 3.3. Since the characteristics of the M-θ curve vary with the axial load, the longitudinal reinforcement, and other variables, the variations observed in these tests will be discussed later in Section 3.4.

Four breaks can be distinguished in the M-θ curve. They are marked with the numerals 1, 2, 4 and 5 in Fig. 3.3. Except for the first break,

point 1, all of them can be readily noticed in Fig. 3.3; the first break can be clearly seen in Fig. 3.13, which shows the M-θ curve for J-25 with an enlarged rotation scale. With a liberal definition of failure, observations and measurements taken during the tests indicated that these four points could be related to various kinds of local failures in the member. Thus, Point 1 corresponds to the appearance of the first flexural crack, a concrete tension failure; the midspan deflection at this stage was about 0.03 in. for J-25. Point 2 represents the stage at which the tensile reinforcement yielded, a steel "tension failure"; the midspan deflection at this stage was 0.42 in. Point 4 corresponds to spalling of the concrete, a localized concrete compression failure and is accompanied by a decrease in moment capacity; the deflection at this stage was about 2.6 in., more than six times the yield deflection. Finally, Point 5 represents the stage at which failure of any of the elements at the critical section, which by this time were resisting the action of the external loads as a statically determinate system, brought about the actual collapse of the member in one of the modes described in Section 3.3; the equivalent midspan deflection at this stage was 13.0 in. for J-25, about 31 times the yield deflection.

Of these four points on the curve, those corresponding to yield and collapse of the member are perhaps the most important. The coordinates of Point 2 (yield) give a measure of the stiffness in the working load range; the coordinates of Point 5 (collapse) give a measure of the energy-absorption capacity of the connection.

Appearance of the Member at Various Stages of Behavior

At the beginning of the test, the specimen was uncracked. The tensile strength of the concrete, being much lower than both its compressive strength and the yield strength of the reinforcement, was the first one to be

reached. The first tension crack, at or near the stub face (where the moment is the largest) appeared at the stage represented by Point 1 on the M-θ curve. Additional vertical cracks (flexural cracks), more or less evenly spaced, appeared as the load was increased. Their location coincided usually with that of the transverse reinforcement. These cracks extended in length at a rather fast rate once they appeared; but they were so narrow before yield, that a close look was needed to see them; some of the cracks could be detected only with the use of a magnifying glass.

After yield, the width of the cracks increased at a rather fast rate. They could easily be seen with the naked eye. The order in which the increase of width of the cracks occurred corresponded with the manner in which yield spread in the tensile reinforcement; that is, as yield started at the stub face and propagated gradually toward the support, correspondingly the crack nearest the stub face was the first to grow wider, then the adjacent crack followed, and so on. Their length also increased somewhat. Few new vertical cracks, if any, appeared at the early stages after yield.

All the cracks were not vertical, however; there were also inclined cracks. As a matter of fact, in some specimens, the inclined cracks were the predominant ones, as shown in Figs. 3.16b and 3.17b. Inclined cracks formed because all the specimens were subjected to shear forces in addition to bending and axial forces; the shear forces produced diagonal tensile stresses in the concrete and inclined cracks formed when the tensile strength of the concrete was reached on inclined planes. Figure 3.17 shows photographs of the crack pattern shortly after yield for specimens J-25 and J-29, with low and high steel ratios, respectively. The cracks were marked so that they would clearly show in the pictures; the numbers next to the short lines crossing the cracks represent the load increments at which the end of the crack reached the

point indicated. Load increment 6 for J-25, and 7 for J-29, correspond approximately to yield. In the specimens with high steel ratios, J-28 to J-31 (p_g = 0.0555), inclined cracks were observed before yield. In the other specimens, with lower steel ratios (and consequently smaller shear forces), the inclined cracks were observed only after yield. At very advanced stages of behavior, all specimens had inclined cracks, as shown in the photographs of Figs. 3.19b and 3.20.

At some stage between yield and the point at which the maximum moment was reached, the first signs of crushing were noticed, Point 3 in Fig. 3.3. The photographs of Fig. 3.18 illustrate the appearance of the members at this stage. The trend of the M-θ curve did not change at this stage.* However, as deflections were increased, crushing spread downward and outward from the stub, and the concrete on the compression side became less and less effective in carrying its share of the internal forces. Eventually, the stage corresponding to Point 4 was reached, and the resisting moment started to decrease. Not all the crushed concrete became ineffective, however. Observations upon removal of the loose concrete after the tests indicated that, although crushing spread below the level of the compression reinforcement, the ties and the compression reinforcement held the bound concrete together and prevented it from becoming completely ineffective. Strain measurements in the ties at the spalled region also supported these observations; they will be discussed in Section 3.4 when the effects of transverse reinforcement are considered.

---

* It should be pointed out that the stage at which the first signs of crushing are noticed is not necessarily the same as that corresponding to the maximum capacity of the section. Apparently, first crushing occurs when the concrete reaches a limiting strain which depends on the concrete strength only, while the concrete strain at which the maximum moment is reached varies with many factors, such as concrete strength, amount and quality of reinforcement, etc.

When concrete started to spall, the specimens which had been deflecting symmetrically up to this stage, started to deflect asymmetrically. In the specimens with the low steel ratio (J-25, J-26, J-27, and J-34), the asymmetry became more and more pronounced as deflections were increased, and damage of the member progressed only on one side of the face of the stub; on the other side, little further damage, if any, occurred after first crushing. However, in the specimens with the high steel ratio (J-28 - J-31), the deflected shape, after being asymmetric for a range of the deflections, tended to become symmetric again; and at ultimate, both sides of the stub were almost equally damaged. The manner in which the specimens deflected was determined by their respective M-θ characteristics (Figs. 3.2-3.12). Up to spalling of the concrete both sides of a member were equally stiff, and since the loading was symmetrical, the specimens deflected symmetrically. Because concrete is non-homogeneous, one side of the member was weaker than the other, and therefore started to spall first; this side then became less stiff than the other and consequently the specimen started to deflect asymmetrically. As deflections increased, the resisting moment, which had been decreasing after the concrete began to spall, leveled off. Up to this point, the M-θ curves for all specimens varied in the same way and they thus deflected in the same manner. Beyond this point, however, the significant characteristics of the M-θ curves for specimens with low steel ratio were different from those for specimens with high steel ratio and accordingly their responses to load were different. According to Figs. 3.2-3.6, for small amounts of steel, the resisting moment after spalling never became greater than at spalling; therefore, the stronger side, whose capacity was not exceeded when the moment was the maximum, did not suffer further damage while the weaker side did; consequently, the asymmetry of deflections increased. For large amounts of steel, however, the

weaker side started to regain strength shortly after the tension steel entered strain hardening, and by the time failure occurred, the resisting moment was substantially larger than at first spalling (Figs. 3.7 - 3.12). At a certain stage before ultimate, the moment became large enough to cause spalling of the concrete on the less damaged side of the specimen, which then became the weaker side and started to deform faster than the other until the resisting moments on both sides became equal, when the deflections were symmetrical, or nearly so. From this point on, the deflections on both sides increased at practically the same rate, because their corresponding strengths did.

Horizontal cracks in the stub approximately at the level of the compression reinforcement formed at advanced stages of behavior as shown in the photograph of Fig. 3.20b. In the specimens with $p_g = 0.0111$, which contained #4 bars as longitudinal reinforcement, horizontal "bond cracks" along the tension reinforcement were noticed only at the very advanced stages. However, in the specimens with $p_g = 0.0555$, which contained #9 bars (and thus had larger bond stresses), such cracks were noticed at about crushing; at advanced stages they were quite numerous, indicating a considerable loss of bond. The top cover was lost long before the collapse stage was reached; the side shells, however, seemed to be at least partially effective until failure occurred. After failure, large deformations at the critical region caused the side shells to spall off in some of the specimens. The location at which crushing and spalling occurred is significant in relation to the location of the critical section and, for convenience, will be discussed in Section 3.5.

Variation of Internal Forces with Deformations

The magnitude of the forces in the concrete and the reinforcement and the location of the resultant of the forces in the concrete changed as deformations increased. The changes that occurred at the section at the stub

face for seven of the specimens tested are presented and discussed here in order to develop an understanding of the manner in which the various elements of a cross-section contribute to its strength throughout its loading history.

The variation of the internal forces as deformation increased for these specimens are shown in the lower part of Figs. 3.22 to 3.28. These figures show curves for the force in the compression steel, C_s, the compression force in the concrete, C_c, the total compression force, $C_c + C_s$, and the distance from the location of C_c to the center of the tension bars, jd, all plotted versus the rotation, θ.

The force C_s was determined using strains measured with electrical gages and stress-strain relationships from coupon tests. The other quantities were obtained using measured quantities and equilibrium conditions. Figure 3.21 shows a free-body diagram of a transverse slice of one of the specimens tested. The moment M and the force P, which represent the action of the external loads, and the internal forces are shown acting on the free-body. For convenience, P is considered to be applied at mid-depth, therefore M is the moment of the external loads about mid-depth, it includes the moment due to both the transverse load and the eccentricity of the longitudinal load due to deflection of the member. The total compression force, $C_c + C_s$, was obtained from the equilibrium of the longitudinal forces

$$C_c + C_s = P + T \qquad (3.1)$$

where P was the measured axial load and T was determined using measured strains and stress-strain relationships from coupon tests. Having the total compression force, $C_c + C_s$, and the force C_s, the force C_c was computed by subtracting the second force from the first. The quantity jd was determined by taking moments of all the forces about the center of the tension bars

$$M + P\left(\frac{d - d'}{2}\right) - C_s(d - d') - C_c\, jd = 0 \qquad (3.2)$$

From this equation

$$jd = \frac{M + P\left(\frac{d - d'}{2}\right) - C_s\,(d - d')}{C_c} \qquad (3.3)$$

where the forces P, C_s and C_c were determined as mentioned above, the quantity $\underline{d - d'}$ was the distance from the center of the compression bars to the center of the tension bars, and the moment M was determined using the measured transverse and longitudinal loads, and measured deflections at the section considered. The portions of the curves shown in broken lines were obtained using strains determined by extrapolation of strain-rotation curves.

The variations of the internal forces as deformations increased will be presented and discussed first; and afterwards, the effects of the axial load and the longitudinal reinforcement will be presented and discussed.

For any one test, the applied axial load, P, was kept as constant as possible. Therefore, the total internal compression force, $C_c + C_s$ $(= P + T)$, varied primarily with variations of the force in the tension reinforcement, T. Thus, as shown in Figs. 3.22 - 3.28, after the test was started, $C_c + C_s$ increased until the tension reinforcement yielded; it then remained fairly constant between the beginning of yield and the beginning of strain hardening; and finally, it increased again because of work hardening of the tension reinforcement. Because specimens J-28 to J-31 had a large amount of tension reinforcement, the effect of strain hardening is more noticeable for these specimens than for those with smaller amounts of tension steel (J-25, J-26 and J-27). It should be noted that although $C_c + C_s$ must have been constant while the tension steel yielded, this is not easily seen on the curves because

it took only a little additional deformation for the steel to enter strain hardening once it yielded (Fig. 3.33).

Part of the compression force, C_c, was carried by the concrete, and the remaining, C_s, by the compression steel. Up to the yield stage, both C_c and C_s increased with an increase in the deformations, as shown by the curves in Figs. 3.22-3.28. After yield, several redistributions of the total internal compression force occurred, as follows:

1) At yield, the trend of C_c and C_s was the same as before yield in all specimens except J-25; that is, they increased. In J-25, C_s, which was increasing before yield, started to decrease after yield.

2) When the concrete cover over the compression bars began to flake off, C_c, which was increasing, started to decrease. C_s increased; this represented a continuation of the same trend for all specimens except J-25, for which it was a reversal.

3) Starting from the stage at which the compression steel yielded, C_s remained constant and C_c became almost constant in all specimens.

4) When the compression reinforcement entered the strain hardening range, C_s increased except in J-25, in which the compression steel did not strain harden. C_c followed an erratic trend after this stage--increasing in some cases and decreasing in others.

The first redistribution was the result of the combined action of two processes: the upward shift of the neutral axis associated with yield, and the increase of the curvature. These processes had opposite effects on the magnitude of C_s; the decrease of the depth of the neutral axis tended to

cause C_s to decrease, while the increase of the curvature tended to cause it to increase. The final result depended upon the relative magnitudes of the two effects. In specimen J-25, the effect of the shifting of the neutral axis was dominant and therefore C_s decreased. In all the other specimens the opposite was true.

The second redistribution resulted primarily from the downward shifting of the neutral axis as the concrete cover spalled. Due to this movement and to the additional effect of the increase of the curvature, C_s increased, regardless of its previous trend. The value of C_s increased rather sharply, and since the total compression force increased slowly as deformations increased, the force in the concrete, C_c, decreased.

The third redistribution occurred, obviously, as a result of the plastic behavior of the compression steel. The value of C_s became constant, and since the total internal compression force varied slowly as deformations increased, C_c became almost constant.

The fourth redistribution can be explained in a manner similar to the third, except that C_s increased as a result of strain hardening. The erratic variation of the "measured" values of C_c were due mainly to inaccuracies in the test measurements. However, it can be said that any variation in C_c after yield of the compression steel was small.

The variation of jd during the tests was typical for all specimens. The quantity jd increased until the concrete on the compression face started to flake off; it then decreased, but tended to level off as deformations increased. The variation of jd reflects clearly the movement of the neutral axis. The increase in the initial part of the loading process occurred as the result of the upward movement of the neutral axis, due first to flexural cracking, and later to yield of the tensile reinforcement and subsequent

plastic behavior of the concrete on the compression side. The neutral axis moved downward as the concrete on the compression face spalled, and jd decreased accordingly. Finally, because both the transverse and the compression reinforcement prevented the bound concrete from becoming ineffective, the neutral axis tended to become stationary and consequently jd tended to level off.

By means of Eq. 3.2, and the curves for the internal forces and jd shown in Figs. 3.22 - 3.28, it is easy to explain the ups and downs in the moment values. As an aid in discussion, M-θ curves have been plotted above the curves for the internal forces. It can be seen that the first drop in the moment value was due mainly to a decrease in the value of jd because of spalling of the concrete on the compression side. The subsequent increase was due to strain hardening of the tension reinforcement, which more than compensated for the effect of the decrease of jd. It should be noted, however, that since the tensile reinforcement did not enter strain hardening in specimen J-27, and since jd decreased at a fast rate with deformations, the resisting moment dropped sharply after spalling of the concrete in this specimen (Fig. 3.24).

Effects of Variables on Internal Forces

The effects of the axial load and the amount of longitudinal reinforcement on the magnitude of the internal forces also can be studied by means of Figs. 3.22 - 3.28. As the axial load, P, was increased, for a given deformation: 1) the total compression force, $C_c + C_s$, increased; 2) the concrete took the greatest share of this increase; and 3) jd decreased slightly. The first effect resulted from the fact that since T for a given deformation beyond yield did not change significantly for the various specimens with the same reinforcement, $C_c + C_s$ (= P + T) increased as P was increased. The concrete took the greatest share in the increase of $C_c + C_s$ because the

compression reinforcement could take little additional load once it yielded, whereas the concrete could take a larger force through an increase of its area in compression. The lever arm jd decreased because the centroid of the concrete compression stress block shifted downward as P increased; since jd is equal to the effective depth minus the distance from the compression face to the point of application of C_c, the decrease of jd was only slight because the movement of the point of application of C_c was small compared to the effective depth.

A comparison of the curves for specimens with the same P indicates the following changes as the amount of longitudinal reinforcement, p_g, increased:

1) $C_c + C_s$ increased;
2) both C_c and C_s increased, but the increase of C_s was proportionately greater than that of C_c; as a result, for the specimens tested, the ratio C_s/C_c reversed from a value smaller than unity for $p_g = 0.0111$ to a value larger than unity for $p_g = 0.0555$;
3) jd decreased slightly.

The increase of $C_c + C_s$ again resulted from the fact that since P was the same for the two specimens being compared, $C_c + C_s$ increased with the increase in T (caused by the larger p_g). The increase of both C_c and C_s was due to the increase of the depth of the neutral axis, as indicated by the decrease of jd. Since both the tension and the compression reinforcement were beyond the yield point when the deformations were large, and their amounts were the same, the compression steel took the largest part of the increase of $C_c + C_s$ due to the increase of T. Finally, the decrease of jd was due to the increase of the depth to the neutral axis; and again, this decrease was small because the amount of shift of the neutral axis was small compared to the effective depth.

Measured Strains in the Concrete and the Reinforcement

(1) Measured Concrete Strains

Figures 3.29 and 3.30 illustrate relationships between the compressive strain in the concrete at the extreme fiber near the face of the stub and the midspan deflection. In J-25 and J-26, the electrical strain gages were located at 1-in. from the face of the stub and in all the other specimens at 1-1/2 in. It can be noted that these strains increase almost linearly with the midspan deflection. In some cases these strains start to decrease when the first visual signs of crushing appear. However, in other cases this decrease occurs only at a deflection significantly larger than that corresponding to the appearance of the first signs of crushing. It can be seen in Figs. 3.29 and 3.30 that in most cases this strain is smaller than 0.004, which has been assumed as the constant limiting strain corresponding to this stage by other investigators.

Distributions of concrete strains on the compression face at various stages of behavior for specimens J-25 and J-30 are illustrated in Figs. 3.31 and 3.32, respectively. Specimen J-25 had $p_g = 0.0111$ and P = 25 kips; J-30 had $p_g = 0.0555$ and P = 50 kips. Both figures show that, beyond the stage corresponding to yield, there is a large concentration of strain near the face of the stub, as would be expected.

(2) Measured Steel Strains

The increase of strains at several points on the tensile reinforcement of J-30 as the equivalent midspan deflection increased is illustrated in the upper part of Fig. 3.33. The shape of the curves shown in this figure was typical for all specimens of this program. The strain at a certain point after reaching the yield value, increased very rapidly with very little increase of deflection until it entered work-hardening. This indicates that the increase

of strain was very much localized at the point that yielded. When the strain at that point entered strain hardening, the rate of increase of strain decreased.

The lower part of Fig. 3.33 illustrates the distribution of strains along the tensile reinforcement at various stages of behavior for specimen J-30. The curves shown are also typical for the specimens tested. Comparing the curves for various stages, the gradual spread of the yielding from the stub toward the supports as the deflections increased can be noted. It is interesting to note that even at the center of the stub the tension reinforcement yielded, the strain reaching a value as large as four percent. However, it must be pointed out that this was true only for the specimens with a large amount of steel; for the specimens with a small amount of steel (J-24 through J-27, and J-34), the steel strains in the stub were small.

Figures 3.34 - 3.36 illustrates distributions of strains at ultimate along the longitudinal reinforcement for specimens of this program. These strains were obtained by measuring distances between punch marks along the reinforcement both before casting the specimen and after the test was finished. The punch marks were made at 2-in. centers nominal and extended about two feet either side of midspan.

The first thing to be noted is the high level of strains at this stage. The strains in both the tensile and compressive reinforcements are well in the work hardening range. Strains as large as 18 percent were measured in a tension bar of J-24 in the region where the companion bar fractured. In the specimens with the low tension steel ratio (Fig. 3.34) the largest tensile strain usually was measured at a point 5 in. out from the face of the stub; the strains decreased from this point on both sides. In the specimens with the large tension steel ratio (Figs. 3.35 and 3.36), the largest tensile strains

were measured between the face of the stub and a section at about 6 in. out. Strains in the compressive reinforcement were measured only in the specimens with large amounts of reinforcement (Figs. 3.35 and 3.36). Large concentrations of strain may be noted in the region where the bars buckled. The level of compressive strains at buckling was over three percent, as indicated by the largest measured strains in the compression steel on the side of the specimen that did not fail.

3.3 Modes of Failure

Preliminary Remarks

A rational procedure for estimating moments and deformations at a specified stage of the loading history of a member must satisfy certain necessary conditions corresponding to that stage. For example, for the yield stage it must be assumed that the tension reinforcement is at the yield strain; and for the stage corresponding to crushing, it must be assumed that the maximum compressive strain in the concrete is equal to the limiting strain that causes the appearance of the first visible signs of crushing. Thus, each of these stages is linked to a single property of one of the materials constituting a reinforced concrete member. However, since the member can fail in various ways, the ultimate capacity is governed by a different material property for each mode of failure. Consequently, the various modes of failure have to be considered in an analysis for this stage, and a knowledge of the possible modes of failure is needed. They will be described in this section and the conditions leading to them will be discussed.

The way the various elements of the specimens tested contributed to their resistance is well described by the expression

$$M_r = C_c y_c + C_s y'_s + T y_s \qquad (3.4)$$

where M_r = resisting moment about mid-height of the section

C_c, C_s, and T = force in the concrete, compression reinforcement, and tension reinforcement, respectively

y_c, y'_s, and y_s = lever arm about mid-height of the section of the forces in the concrete, in the compression reinforcement, and in the tension reinforcement, respectively

Since the members were subjected to a transverse load, they had to be capable also of carrying the shear force necessary to develop the moment capacity of the critical section. The shear capacity V of the members can be expressed as

$$V = V_c + V_s \tag{3.5}$$

where V_c = shear carried by concrete

V_s = shear carried by web reinforcement

Part of the total shear was carried by dowelling action of the longitudinal reinforcement, but this action can be ignored because of its small magnitude as compared to the amounts of shear taken by the concrete and the web reinforcement.

Equations 3.4 and 3.5 show that the strength of the specimens in this investigation depended upon the capacity of the concrete to take compression and shear forces, and on the strength of the compression, tension, and web reinforcement. Failure of any of these elements to carry its share of the internal forces brought about the failure of the specimen. The various possible modes of failure can be classified into three groups:

1) tension failure

2) compression failure

3) shear failure

These classifications, as used herein, refer to the conditions governing final collapse of the member, as will be discussed in the following paragraphs.

Tension Failure

In this mode of failure, the tension steel fractures before the resisting moment of the critical section begins to decrease significantly. Only one specimen, J-24 (p_g = 0.0111, P = 0), failed in this manner. Obviously, the probability of this mode of failure should increase as the rupture strain for the steel decreases. Some of the specimens tested by Carneiro (5) and Diaz de Cossio (6), which were reinforced with steel that had rupture strains of only about 3.5 percent, failed in tension. However, even if the tension steel is very ductile, tension failures may occur under certain conditions that lead to high tensile strains. If the ratio of the depth of the neutral axis, c, to the effective depth of the section, d, is small; the ratio of tensile strain to compression strain is large. Thus, if this ratio is small enough, the rupture strain of the tension steel may be reached before a failure occurs in compression. However, it should be pointed out here that if this ratio is small a shear failure may also occur; this possibility will be discussed under the heading of shear failures. Large tensile strains may also occur if the ratio of the area of the tension steel to that of the concrete below the neutral axis, $A_s/b(d-c)$, is small, because in this case the number of cracks is small and the concentration of strains at the cracks is large. These two conditions, small c/d and small $A_s/b(d-c)$, existed in J-24, the only specimen of this series that failed in tension.

Compression Failure

The total compression force is carried by the compression reinforcement and the concrete above the neutral axis; consequently, there are two possible types of compression failures:

1) steel compression failure

2) concrete compression failure

In the first type, the decrease in the resisting moment of the section is due primarily to buckling of the compression bars; in the second type, it is due to the decrease of the compressive force in the concrete and/or its lever arm.

Although the compression bars in all the specimens that failed in compression were found to be buckled, as shown in Fig. 3.19a, when the loose concrete was removed at the end of the test, it was difficult to determine whether failure was of the first or second type. The tests were discontinued only after the resisting moment had decreased significantly, and buckling could have occurred after the specimen had already begun to lose strength, in which case failure would have been of the second type, or it could have occurred before the resisting moment began to decrease, in which case failure would have been of the first type.

Theoretical considerations, which will be explained in Section 4.9 when the determination of the moment and curvature at ultimate is discussed, seem to indicate that specimens J-25, J-26, J-27 and J-34, with small amounts of compression steel (2 #4 bars), had concrete compression failures, whereas specimens J-29, J-30 and J-31, with large amounts of compression steel (2 #9 bars), had steel compression failures. This is in agreement with the relative contribution of the steel and the concrete to the strength of the compression side of the member. As shown in Figs. 3.22 - 3.24, the concrete in the specimens with small amounts of compression steel took the greater share of the compression force. The opposite was true in the specimens with large amounts of compression steel; as shown in Figs. 3.26 - 3.28, the compression bars took the greater share of the compression force. Thus, it seems reasonable that for small amounts of compression steel the mode of failure was determined by the strength of the concrete, while for large amounts of compression steel it was determined by the strength of the compression bars.

It is noteworthy that buckling occurred only long after the compressive reinforcement yielded. Strains as large as three percent in the #9 bars (Figs. 3.35 - 3.36) and larger than one percent in the #4 bars were measured before they became unstable. There is a very logical explanation to these observed facts. On the one hand, the concrete enclosed within the ties exerted lateral pressure on the bars, thus increasing their tendency toward an unstable condition. On the other hand, the concrete surrounding the bars (especially the shell) provided some restraint and therefore decreased the probability of buckling. Apparently, this restraint was sufficient to prevent instability of the compression bars while they were strained in the plastic range (when they had little or no flexural stiffness) until they entered the work hardening range and regained some flexural stiffness. In the meantime, the restraining forces decreased due to increase in damage of the compressed concrete, whereas the lateral pressure on the bars did not. Eventually, the effect of the lateral pressure became the larger of the two and the difference of the two effects had to be carried by the compressed bars through their flexural stiffness. The amount of additional deformation beyond this stage depended on the stiffness of the compression steel which was larger for the #9 bars than for the #4 bars. This explains why the #9 bars had strains at ultimate much larger than the #4 bars.

Buckling of the compression bars, whether it was the primary cause of failure or not, always occurred between two adjacent ties. The buckled shape resembled that of a member restrained at both ends against rotation and displacement (Fig. 3.19a). It is interesting to note that the bars always buckled outwards on a horizontal plane. They could not buckle inwards or downwards because of the restraint offered the bars by the concrete, and they could not buckle upwards because they were curved in the same direction as the member.

Shear Failure

Although the elements at the critical section may be strong enough to carry the compression and tension forces, the member will fail if any section along the beam cannot carry the shear force necessary to develop the moment capacity at the critical section. This mode of failure is characterized by a faulting type of movement in the plane of an inclined crack, as shown in Fig. 3.19b for specimen J-28 (p_g = 0.0555, P = 0), and is thus referred to as a "shear failure." However, since this mode of failure may occur after crushing, it should be noted that the term "shear failure" is not used in its usual sense, in which case it refers to a mode of failure that always occurs before the moment at crushing, which is taken as the full moment capacity, is reached.

The occurrence of this mode of failure depends primarily on the amount of shear the concrete can carry. As indicated by Eq. 3.5, the shear force is carried by the concrete above the neutral axis and the transverse reinforcement. In most cases this reinforcement has yielded and therefore carries a constant force long before failure occurs. Consequently, failure in shear will take place when the shear strength of the concrete becomes insufficient to transfer its share of the total shear force necessary to develop the moment capacity at the critical section.

The amount of shear the concrete can carry decreases with a decrease of the area of concrete in compression. Therefore, the probability of a shear failure increases with a decrease of the area of concrete in compression. It also increases with an increase in the shear force the concrete has to carry.

3.4 Effects of Variables

Two major variables, the axial load and the longitudinal reinforcement, and a minor one, the transverse reinforcement, were studied in this

investigation. Their effects on the strength, ductility, appearance, and modes of failure of the specimens are presented and discussed herein.

Effects of Axial Load

Figures 3.37, 3.38, and 3.39 show complete moment versus rotation curves for the eleven specimens of this program with the axial force as parameter for p_g = 0.0111, 0.0329, and 0.0555, respectively. Figures 3.13, 3.14, and 3.15 show the initial part of the same curves with an enlarged rotation scale; the points at which first yield and initial crushing were detected are indicated. The moments and deflections at yield, crushing, and ultimate and also the modes of failure observed in the tests are listed in Table 4. In each group with the same amount of steel, the following changes occurred as the axial load was increased:

1) the resisting moment at yield, crushing, and ultimate increased in all cases except for J-31 (P = 75 kips), in which case the moment at ultimate represented a decrease with respect to that for J-30, with smaller axial load (P = 50 kips),
2) the deflection at yield increased,
3) the deflection at crushing and ultimate decreased.

A study of the observed modes of failure indicated that with an increase in axial load the specimens tended to fail in compression. Specimen J-24, without axial load , failed in tension, and specimens J-8 and J-28, also without axial load, failed in shear; whereas all the others, which were subjected to axial loading, failed in compression.

All these effects were due to the increase of the depth of the neutral axis, c, caused by the increase in axial load. The effects on the resisting moment can be discussed with reference to Eq. 3.4. At yield, the force in the tension reinforcement, T, was the same regardless of the magnitude

of the axial load; the increase of $\underline{c}$ (due to the increase in P) made both the compression force in the concrete, C_c, and the force in the compression reinforcement, C_s, larger; and the lever arm of these forces did not change significantly; consequently, the resisting moment increased. Similar reasoning can be used to explain the increase of the moment at crushing with an increase in the axial load. At ultimate, an increase in $\underline{c}$ had two mutually compensating effects on the resisting moment of a section: on the one hand, it increased the forces on the compression side of the section; and on the other hand, it decreased the force in the tension reinforcement, which was in the work hardening range as indicated by strain measurements. In all cases, except J-31, the effect on the resisting moment due to the increase of the compression forces as P increased was dominant; therefore the resisting moment increased. In J-31 the opposite was true.

Since a direct discussion of the effects of an increase of P on the deflection is very difficult, an indirect approach will be followed. The effects of an increase of P on the curvature at yield, crushing and ultimate will be considered. Since deflections and curvatures at a section for a given member and a given type of loading vary in the same direction (i.e., one increases if the other increases, and vice versa), the effect of P on the deflection for the same type of member and loading will be in the same direction as its effect on the curvature.

At yield, the tension reinforcement was at the yield strain, ϵ_y, and $\underline{c}$ increased as P increased; therefore, the curvature at this stage, $\varphi_y = \epsilon_y/(d-c)$ (where the effective depth, d, was a constant), increased. At crushing, the concrete at the extreme compression fiber was at the limiting crushing strain, ϵ_c, regardless of the magnitude of P, consequently, an increase of $\underline{c}$ caused the curvature at this stage, $\varphi_c = \epsilon_c/c$, to decrease. At ultimate, reasoning

similar to that at crushing could be used, except that the strain at the extreme compression fiber was not a constant but varied somewhat; this variation, however, was not large enough to change the trend of the curvature values with an increase in the axial load.

Finally, the increase of c increased the area of concrete in compression and consequently the amount of shear the concrete could resist, and the force in the tension reinforcement also decreased as c increased. Therefore, when the axial force was sufficiently large, the possibilities of shear and tension failures were eliminated, and the specimens failed in compression.

Effects of Longitudinal Reinforcement

A comparison of the moments and deflections in Table 4, for the same axial load but for varying amounts of longitudinal reinforcement, indicates the following changes as p_g was increased.

1) the resisting moments at all stages increased,
2) the deflection at yield increased,
3) the deflections at crushing and at ultimate decreased for small axial loads and increased for large axial loads,

Observations during the tests also indicated that with an increase of p_g,

4) the number of inclined cracks increased, (Fig. 3.17)
5) horizontal (bond) cracks along the tension reinforcement became more noticeable,
6) The mode of failure for specimens without axial load changed; J-24 (p_g = 0.0111) failed in tension, and J-8 (P_g = 0.0329) and J-28 (p_g = 0.0555) failed in shear.

The increase of strength at all stages with an increase in the amount of longitudinal reinforcement was the obvious result of increasing the percentage of the stronger material in the member.

At any specified stage of behavior, part of the deflection, Δ_f, was due to the curvature distributed along the framing members and in the stub, and another part, Δ_i, was due to the concentrated rotation at the face of the stub, which in turn was due to loss of bond between the tensile reinforcement and the concrete near the stub as will be explained in Chapter 4. A rational discussion of the changes listed above in items 2 and 3 cannot be made without a consideration of the changes in Δ_i, which is a function of several variables as will be shown in Chapter 4. Therefore, no attempt to explain items 2 and 3 will be made at this point. However, it must be pointed out that such changes can be explained using the equations for computing Δ_i developed in Chapter 4.

The number of inclined cracks increased as p_g was increased, because the shear force increased. The fact that horizontal (bond) cracks along the tension reinforcement were more noticeable as the size of the bars were increased indicates that the splitting forces became larger.

The modes of failure for the specimens with zero axial load changed from tension to compression as p_g increased, mainly because the shear force increased. The depth to the neutral axis was small in these specimens and they could have failed either in tension or in shear as discussed in Section 3.3. Since both the bar size and the shear force were small in the case of J-24, it failed in tension. However, in J-8 and J-28, the shear force was larger than in J-24, and the tendency toward a shear failure increased. Evidently, the increase of p_g was large enough to cause specimens J-8 and J-28 to fail in shear, rather than in tension, as they did in the tests.

Effects of Transverse Reinforcement

Figure 3.40 shows the M-θ curves for J-27 and J-34, with 75 kips axial, which differed basically only in the spacing of the web reinforcement

near the stub. As shown in Fig. 2.2, J-27 contained #3 closed ties at 6-in. spacing throughout, and J-34 contained #3 closed ties at 3-in. spacing for a length of twelve inches out from the stub face and the remaining were #3 closed ties at 6-in. spacing; both specimens contained at #3 tie at 3 inches out from the stub face. A comparison of these curves shows that there was basically no change in the load-deformation characteristics until the top cover started to spall, but at ultimate the specimen with more ties, J-34, had a considerably larger deflection.

The better load-deformation characteristics for J-34 resulted primarily from the increase in ductility near the stub (where the deformations are the largest) due to the larger amount and closer spacing of the transverse reinforcement. It is well known that lateral compressive stresses in the concrete have beneficial effects on both the compressive strength and the capacity for deformation in the longitudinal direction. Such stresses existed in the concrete on the compression side of the specimen bound by the ties. They were induced by the ties as they reacted against the bound concrete, which tended to expand laterally. This lateral deformation was in turn due to the increase of the longitudinal compression strains as deflections were increased. Strains measured on ties near the stub indicated that the lateral stresses were small before crushing, but that they increased rapidly after crushing. At advanced stages of behavior, the vertical and horizontal legs on the compression side of the ties yielded, and strains in the work hardening range were measured near ultimate. Accordingly, the transverse reinforcement had little effect on the load-deformation characteristics of the connection before crushing, but its effect increased rapidly after crushing. Since the lateral stresses in the bound concrete were larger for the specimen with more closely spaced ties, its beneficial effects on this specimen were also greater.

The ductility of members failing in shear also may be increased with an increase in the amount of transverse reinforcement, because the shear force that the concrete has no carry decreases. Burns (1) made some tests on specimens failing in shear which differed basically only in the amount of transverse reinforcement. The specimens with larger amounts of web reinforcement had deflections at ultimate 1.4 to 2 times larger than the companion specimens which had about half as much web reinforcement.

Finally, the ductility of members failing because of buckling of the compression bars may be increased by decreasing the spacing of the ties. Such a decrease in tie spacing reduces the buckling length of the compression bars, and therefore their strength and ductility increase, which in turn causes the ductility of the member to increase. It should be noted that the main function of the ties in this mode of failure is to prevent the sections of the bars where the ties are located from displacing with respect to each other; therefore, in order to obtain a larger ductility of the connection, the amount of ties does not need to be increased as long as the individual ties are stiff enough to prevent relative displacements. That is, the ductility of the member can be increased by using the same amount of ties at a closer spacing.

3.5 Effects of Stub

The stub, which simulated other members framing into the connection, had beneficial effects on the capacity for both deformation and strength of the connection. It contributed to the deformation capacity directly through deformations within its mass which were caused by the forces being transferred through it from one side of the connection to the other. It contributed indirectly to the capacity for both deformation and strength of the connection by influencing the location of the failure section. The photographs in

Fig. 3.20 show the failure zones for two of the specimens tested. It can be seen that the weaker section was not at the stub face, where the moment was the largest, but was somewhat removed from it. The concrete cover in the vicinity of the stub was restrained against spalling by the stub. Therefore, the section at the stub face (and consequently the member) was stronger than it would have been without the stub, in which case the concrete cover would have been lost. Finally, because the critical section was removed from the stub face, large deformations could also occur in the length between the stub face and the critical section, which increased the ductility of the connection.

The critical (weaker) section was located at 3 to 6 in. out from the face of the stub for the specimens tested by Burns and in this investigation, in most cases at the greater distance (see photographs of Fig. 3.20). Since the location of the critical section was almost constant in these tests, it appears that it is not a function of either the effective depth or the depth to the neutral axis, both of which varied widely. It is possible that the distance from the face of the stub to the critical section is a function of the thickness of the top cover; if so, on the basis of the results of these tests, this distance is of the order of three times the thickness of the cover.

4. ANALYSIS OF STRENGTH AND DEFORMATIONS

4.1 Preliminary Remarks

The object of this chapter is to present a method for estimating the moment and the rotation of a member framing into a connection of the type B_2 shown in Fig. 1.1 for the stages corresponding to yield, crushing and ultimate. A rational rather than a simple method was sought. Therefore, the same basic assumptions were made for all stages of behavior.

In order to show the necessity for a new procedure, the inadequacies of those available are discussed first. In Section 4.3, one of the commonly accepted procedures for estimating moments up to the stage corresponding to crushing is used to determine rotations for the stages corresponding to yield and crushing, and the lack of agreement between the values computed in this manner and those measured in tests is shown. In Section 4.4, procedures developed in earlier investigations are presented and their range of applicability is discussed.

The new method is presented in Sections 4.5 through 4.9. In Section 4.5, the assumptions are listed and discussed. Since the stress-strain relationships of the materials that make up a reinforced concrete member are needed, they are presented in Section 4.6. Finally, the procedures for estimating the strength and the rotation for the stages corresponding to yield, crushing and ultimate are presented in Sections 4.7, 4.8 and 4.9, respectively.

In section 4.3 a procedure for estimating the contribution of the deformations in the stub to the rotation of the member is needed. Therefore, in Section 4.2, a procedure for making such an estimate is suggested. This procedure is also used in Sections 4.7 through 4.9.

4.2 Contribution of Deformations in the Stub to Rotation of Members Framing into It

In Section 3.5, it was stated that the deformations in the stub contributed directly to the rotation of members framing into it. These deformations result from the forces being transferred through the stub from one side to the other. Since the contribution of these deformations, however, is relatively small, a rigorous determination of it, which is highly difficult, can hardly be justified. Therefore, a simple approximate procedure was sought.

Two approaches were considered. One consisted of assuming that the stub behaved like an extension of the member framing into it. The effective depth of the extension could then be assumed to increase in some fashion from the stub face toward the center. Knowing the effective cross-section for each point in the stub, the curvatures at such sections could be determined using any of the procedures adopted for determining the curvatures in the framing member. However, it can be seen that this would be a long and tedious process and the amount of computation would be far out of proportion to the importance of the problem. Therefore, this approach was rejected.

The second approach, which was finally adopted, was based entirely on the strains measured at ultimate in the tension and compression bars of specimens J-28 through J-31. Such strains were measured mechanically at two-inch intervals continuously over a length of about two feet either side of midspan of the beam. With these strains, "curvatures" in the stub could be determined at two-inch intervals as follows:

$$\varphi_s = \frac{\epsilon_s + \epsilon'_s}{d - d'} \tag{4.1}$$

where φ_s = "curvature" in the stub at the distance s from the face

ϵ_s and ϵ'_s = measured strains at the distance s from the stub face in the tension and compression bars, respectively

$d - d'$ = center to center distance between compression and tension bars.

Plots of the "measured curvatures" versus several of the variables were tried. The plot of φ_s/φ_o versus s/c, shown in Fig. 4.1, was the best one. The curvature φ_o was the "measured curvature" at the face of the stub. The depth of the neutral axis at the face of the stub, c, measured from the top of the compression bars because the top cover had been lost at this stage, was determined as follows:

$$c = \frac{\epsilon'_s}{\epsilon_s + \epsilon'_s} (d - d') + \frac{D'}{2} \tag{4.2}$$

where D' = diameter of compression bars. The trend of the points in Fig. 4.1 is well described by the following expression:

$$\frac{\varphi_s}{\varphi_o} = \frac{1}{1 + \frac{s}{2c}} \tag{4.3}$$

which has been also plotted in Fig. 4.1.

The rotation of the member, θ_s, due to deformations in the stub can now be obtained by integrating φ_s from Eq. 4.3 from the center of the stub to the face, as follows:

$$\theta_s = \int_o^{w/2} \frac{\varphi_o \, ds}{1 + \frac{s}{2c}} = 2c \, \varphi_o \log_e \left(1 + \frac{w}{4c}\right) \tag{4.4}$$

where w = length of stub. This expression cannot be used easily because of the logarithmic term. A more usable expression can be obtained if the logarithmic function is expanded in series as follows:

$$\log_e \left(1 + \frac{w}{4c}\right) = 2 \left[\frac{w/4c}{2 + \frac{w}{4c}} + \frac{1}{3} \left(\frac{w/4c}{2 + \frac{w}{4c}}\right)^3 + \ldots \right] \tag{4.5}$$

and the first term of the series is taken as an approximation of the function. If this is done, Eq. 4.4 becomes

$$\theta_s = \frac{4_c \varphi_o}{\frac{\delta c}{w} + 1} \tag{4.6}$$

This equation yields values for θ_s which are slightly lower than those given by Eq. 4.4 because of the terms neglected in the series. Moreover, θ_s is located at the centroid of the area below the curvature diagram in the stub; therefore, to compute deflections this centroid must be located first. This equation was slightly modified in order to minimize the error due to the terms neglected in the series expansion and so that the rotation θ_s could be considered concentrated at the stub face. The modified form was:

$$\theta_s = \frac{4_c \varphi_o}{\frac{\delta c}{w} + 0.6} \tag{4.7}$$

The error in the rotation due to deformations in the stub computed using Eq. 4.7 rather than the curvatures given by Eq. 4.3 is less than two percent. The error due to this approximation in the total rotation is much smaller.

Although Eq. 4.7 was derived using strains measured for the stage corresponding to ultimate, it was also used for the stages corresponding to yield and crushing. This decision was justified by two facts: the variation of curvatures in the stub given by Eq. 4.3 was qualitatively correct, and pertinent information for stages other than ultimate were not available.

4.3 Determination of Deflections Using the Curvature Distribution Given by a Commonly Accepted Procedure for Computing Moments

Many procedures for computing M-φ curves for reinforced concrete sections are available in the technical literature. The typical assumptions made in those procedures are the following:

1) Strains in the compressed concrete vary linearly.

2) The relation between strains in the tension steel and in the outer fiber of the concrete at a cross-section is

$$\epsilon_s/\epsilon_c = (1-k)/k$$

where ϵ_s = tension steel strain

ϵ_c = concrete strain at extreme fiber

k = ratio of depth of neutral axis to effective depth

3) Stresses in the concrete and in the reinforcement are uniquely related to the strains in accordance with known stress-strain relationships.

4) Concrete does not carry tension.

Figure 4.2 shows M-φ curves for a given section and various constant axial loads computed by Pfrang (7) using the above assumptions. For the concrete he assumed a stress-strain curve which was a very close approximation of that for cylinder tests. For the reinforcement he assumed an elasto-plastic stress-strain curve. The curves on Fig. 4.2 can be represented ideally by the elasto-plastic M-φ curve shown on Fig. 4.3. On the basis of this curve and Eq. 4.3, the curvature diagram corresponding to the moment diagram for the stages corresponding to yield and crushing (Fig. 4.4c) can be obtained. The methods for computing M_y, φ_y, M_c and φ_c, which are needed for the evaluation of the deflections are explained in the following paragraphs.

Moment and Curvature at Yield

To compute the moment and curvature at yield, the straight-line equations were used. Thus, the depth of the neutral axis, c, was determined first using the following equation:

$$\frac{c}{d} = \sqrt{2\left[\bar{p}n + p'(n-1)\frac{d'}{d}\right] + \left[p'(n-1) + \bar{p}n\right]^2} - \left[p'(n-1) + \bar{p}n\right] \qquad (4.8)$$

and

$$M_y = (P + A_s f_y - A'_s f'_s)\, jd + A'_s f'_s\, (d - d') - P\, (\frac{d-d'}{2}) \qquad (4.9)$$

$$\varphi_y = \frac{\epsilon_y}{d - c} \qquad (4.10)$$

where $\bar{p} = (A_s + \frac{P}{f_y})/bd$ = equivalent tensile reinforcement ratio

$n = E_s/E_c$ = modular ratio

$p' = A'_s/bd$ = compressive reinforcement ratio

d' = distance from compression face to center of compressive reinforcement

d = effective depth

M_y = moment about mid-depth of section corresponding to yielding of the tensile reinforcement

P = compressive axial load

A_s, A'_s = cross-sectional areas of tensile and compressive reinforcement, respectively

f_y = yield stress of tensile reinforcement

f'_s = stress in the compressive reinforcement

$j = 1 - \frac{1}{3}\frac{c}{d}$

φ_y = curvature corresponding to yield of the tensile reinforcement

$\epsilon_y = f_y/E_s$ = yield strain of the tensile reinforcement

The modulus of elasticity of the reinforcement was taken as 29,000,000 psi and that for the concrete was computed using Eq. 4.15.

Moment and Curvature at Crushing

To determine the moment and the curvature for the stage corresponding to crushing, the quantities ϵ_u, $k_1 k_3$, and k_2, describing the properties of the distribution of compressive stresses in the concrete, were computed using Eqs. 4.16, 4.17, and 4.18, respectively.

For the tensile reinforcement the stress-strain curve from coupon tests were used.

With these assumptions, the depth of the neutral axis at crushing, c, was obtained by a trial and error procedure. For each case, various values for c were tried until the internal and external longitudinal forces were in equilibrium. With c known, the moment and the curvature were determined as follows:

$$M_c = (P + A_s f_s - A'_s f'_s)(d - c) + A'_s f'_s (d - d') - P\left(\frac{d - d'}{2}\right) \qquad (4.11)$$

$$\varphi_c = \epsilon_u / c \qquad (4.12)$$

where M_c = moment corresponding to crushing of the concrete

φ_c = curvature corresponding to crushing of the concrete

To compute the stresses in the reinforcement, the corresponding strains were first obtained from the strain distribution at the cross-section. With these strains, the stresses were then obtained from the corresponding stress-strain curves.

Using Eq. 4.7 to compute the deflection due to deformations in the stub, the curvature diagrams shown in Fig. 4.4c, and the values of moments and curvatures obtained as explained above, the deflections for the stages corresponding to yield and crushing were computed for all the specimens tested in this investigation and by McCollister and Burns. The computed values are listed as Δ_f in column 7 of Tables 8, 9, and 10 for yield and in Tables 14, 15 and 16 for crushing. The values measured in the tests are listed in column 9 of these tables. It can be seen that the agreement between the measured and computed deflections is very poor as shown by the ratio $\frac{\text{meas. } \Delta}{\Delta_f}$ given in column 11 of the tables, and as discussed in Sections 5.2 and 5.3.

4.4 Analyses by Other Investigators

Other investigators have been aware of the disagreement between the actual deflections and those computed using the procedure outlined in

Section 4.3, and therefore attempted to develop procedures for predicting deflections with greater accuracy.

Analyses for Yield Stage

McCollister (2) suggested the curvature distribution shown in Fig. 4.5b for computing the deflection at yield. His procedure for computing φ_y was essentially the same as that described in Section 4.3. Although the deflections computed in this manner were somewhat larger than those computed in Section 4.3, they were still considerably smaller than the measured values.

Burns (1) suggested a procedure which involved the same distribution of curvature as that used by McCollister but a different procedure was used to compute the curvature corresponding to yield. To compute this curvature, he suggested that the strain ϵ_y to be used in Eq. 4.10 be computed as follows:

$$\epsilon_y = \frac{f_y(\text{psi})}{30{,}000{,}000} + 0.0003 \qquad (4.13)$$

The quantity 0.0003 represents an increase of about 20 percent over the theoretical yield strain. Therefore, both the curvature at yield determined using Eq. 4.10 and the area under the curvature diagram are also increased by this amount, and the deflection computed in this manner represents a considerable increase over the deflection computed using the procedure outlined in Section 4.3. The comparison between measured and computed deflections for this stage presented in Reference 4 indicates a good agreement, which would be expected since the expression for ϵ_y in Eq. 4.13 was derived empirically from the results of the tests. However, when the procedure was used for the specimens tested in this program, it yielded computed deflections which were too large in the case of the specimens with small amounts of steel and too small in the case of the specimens with a large amount of steel. Moreover,

Burns defined the measured "yield" deflection in a different manner from that used in this study, described in Section 5.2. Except in some of the specimens tested by McCollister, there was little difference between the measured deflections determined by the two procedures. The exceptions were the specimens with large amounts of tension reinforcement, for which the "measured deflections" determined according to the procedure described in Section 5.2 were up to 20 percent larger than those reported in Reference 4. Accordingly, the deflections computed using the procedure suggested by Burns were too small for these specimens.

Analyses for Crushing Stage

To compute the deflection for this stage, McCollister proposed an empirically derived procedure which can be represented by the curvature distribution shown in Fig. 4.5c. The curvature φ_c was determined using a procedure similar to that described in Section 4.3 for this stage. The strain ϵ_u was taken as 0.004 instead of the smaller values given by Eq. 4.16. The values for $k_1 k_3$ and k_2 were only slightly different from those given by Eqs. 4.17 and 4.18, respectively. As shown in Fig. 4.5c, McCollister recommended a spread length for the curvature φ_c equal to the effective depth of the beam. A good correlation between measured and computed deflection was found for his tests.

However, McCollister's recommendation for the spread length was based on tests of beams all having approximately the same effective depth, equal to about ten inches. Burns made calculations involving a spread length equal to the effective depth for his specimens, which had effective depths equal to 10, 14 and 18 in. Good correlation was obtained for the beams with d = 10 in.; however, for beams with d larger than 10 in. the computed deflections were considerably larger than the measured ones. Burns found a better

correlation between measured and computed deflections when a constant spread length equal to 10 inches was used, regardless of the depth of the member. However, when this procedure was used for the specimens of this program the agreement was not good for the specimens with large axial loads. Burns also proposed two other procedures for computing deflections at crushing, but again they failed to give good results for the specimens in this program with axial load.

Analyses for Ultimate Stage

The procedures for computing deflections for this stage of behavior are less rational than those available for yield and crushing. McCollister (2) developed a procedure empirically, after all attempts toward a rational solution failed. Burns (1) developed a procedure very similar to those he developed for crushing, on a basis which was partly rational but which was primarily empirical. Although both procedures yielded values which were in good agreement with those measured in their respective programs, the agreement was not satisfactory when they were used in these tests, especially when axial load was present.

4.5 General Assumptions in Proposed Theory

In this study, the procedures for computing moments and curvatures for the stages corresponding to yield, crushing, and ultimate have been derived according to the following general assumptions:

1) Strains in the compressed concrete vary linearly. There is little reason to believe that this assumption is not reasonably valid. Besides, any more complicated assumption can hardly be justified.

2) Cracks are inclined with respect to the axis of the member. It has always been assumed either implicitly or explicitly that cracks are

vertical. However, as discussed in Section 3.2 under the subheading for appearance of the member at various stages of behavior, most of the specimens considered in this analysis had inclined cracks before the tension steel yielded. This assumption makes it possible to explain the large concentration of deformations at the face of the stub, as will be done in Section 4.7, and thus to explain why the measured rotations are larger than those estimated using the procedures outlined in Section 4.3. Because of this assumption, this theory will be referred to hereafter as the "inclined-crack" theory in contrast to those based on vertical cracks which will be referred to as "vertical-crack" theories.

The inclined-crack theory requires a new definition for "cross-section." As shown in Fig. 4.13 a cross-section in this theory will be defined as a broken surface formed by two planes whose intersection is the neutral axis, the plane on the compression side being normal to the axis of the member and the other coinciding with the plane of the inclined crack. Therefore, the point on the tension steel which must be considered in relation to the plane AB in the compression zone (Fig. 4.13a) is point C on the inclined plane and not point D on the vertical extension of AB as would be considered in the vertical-crack theories.

3) <u>The relation between strains in the tension steel and in the outer fiber of the concrete at a cross-section is</u>

$$\frac{\epsilon_s}{\epsilon_c} = F\left(\frac{1-k}{k}\right) \tag{4.14}$$

where ϵ_s = strain in tension reinforcement

ϵ_c = compressive strain in concrete at extreme fiber

F = compatibility factor (equal to unity in this study)

k = ratio of depth of neutral axis to the effective depth of the section

It must be noted that the strain ϵ_s in Eq. 4.14 is at the point on the reinforcement where it is intersected by the "cross-section" as defined in the second assumption (Point C in Fig. 4.13d).

The compatibility factor F varies along the member. It may be larger than unity at the sections where cracks exist, or smaller than unity for sections between cracks. It may also be smaller than unity at sections disturbed by the presence of vertical and inclined cracks near each other, such as the sections near concentrated loads. This possibility is discussed in detail in References 8 and 9.

In this study, which is mainly concerned with deformations, the compatibility factor F is taken as unity. This is justified by the fact that of necessity this factor approaches unity if average strains over a sufficiently long gage length are considered. In a more rigorous analysis, the variation of F along the beam would have to be considered. Evidently, this is impracticable.

4) Stresses in the concrete and the reinforcement are uniquely related to the strains. For direct tension and compression tests under short time loading this is strictly correct. For members in flexure the correctness of the assumption cannot be proved directly. It is used here because this assumption in connection with assumptions 5 and 6 permits one to calculate the stresses in the concrete and in the reinforcement once the strains are known. Its use is further justified by the good results obtained in many other flexural theories.

5) The stress-strain relationship for all points in the compressed concrete is the same and is known. It is commonly assumed that the stress-strain curve for the compressed zone of a beam is identical with that for concrete in direct compression. The same assumption will be made herein. Recent tests (10) have proved conclusively that this is nearly true up to the

stage corresponding to crushing. For stages at which the confining effect of the stirrups is significant, this assumption is obviously incorrect for the reasons discussed in Section C.3 of Appendix C. Its use in this study is justified by expediency rather than by logic. The stress-strain relationships for concrete are presented and discussed in Section 4.6.

6) The stress-strain relationship for the reinforcement is known. The entire stress-strain relationship for the reinforcement determined from tension tests of coupons, which is presented and discussed in Section 4.6, is used here for both the tensile and the compressive reinforcements. The use of stress strain relationships from tension tests for the bars in compression is justified by the results of direct tension and compression tests conducted by Burns (1). He found that the stress-strain relationship for a coupon tested in compression up to the stage at which it buckled was very similar to that for another coupon from the same bar tested in tension.

7) Concrete does not carry tension. The results would not change significantly even if the tensile stresses in the concrete were considered.

The following two assumptions refer to two forces which have to be considered in addition to those considered in vertical-crack theories. As shown in Fig. 4.13d, the two new forces are the force in the web reinforcement and the vertical component of the force in the tension reinforcement, due to dowelling action. These assumptions are not completely general. They are made for the specimens considered in this study as expedient ways of avoiding the complications introduced by these forces, and are justified by the fact that their influence on the results sought is probably small. Such influence may not be small for cases in which heavy transverse reinforcement at small spacing is provided, and therefore these assumptions should not be applied for such cases.

8) The tension reinforcement does not carry any force by dowelling action. At present there are no means for estimating such force. However, it is probably small as compared to the component of the force in the tension reinforcement along its axis, especially when horizontal (bond) cracks in the concrete at the level of this reinforcement exist, and therefore can be neglected in the flexural computations.

9) The force in the web reinforcement is zero for flexural computations. That is, the web reinforcement can be considered to be non-existent insofar as computation of moments and curvatures is concerned. (However, the force in the web reinforcement should be considered when evaluating the shear strength of the member.) This assumption has the same justification as assumption 7.

4.6 Stress-Strain Relationships

Stress-Strain Relationship for Reinforcing Steel

Representative stress-strain curves for the three sizes of intermediate grade reinforcing bars used in these tests are shown in Fig. 4.6. The curves have an initial elastic portion, then a plastic range in which strains increase with little or no increase in stress, and finally a "work hardening" range in which stresses again increase as strains are increased.

The properties of the reinforcing bars used in these tests are listed in Table A.2. The average Young's modulus was 29,100,000 psi. The yield stress varied from 44.7 to 50.3 ksi. The maximum stress varied from 71.4 to 81.9 ksi, about 1.6 times the yield stress. The plastic range was roughly eight times the yield strain. The maximum stress occurred at strains equal to 14 to 18 percent (about 100 times the yield strain) and rupture occurred at strains equal to 17 to 25 percent. All these strains were measured over an 8-in. gage length.

The stress-strain relationships for the intermediate grade steel shown in Fig. 4.6 can be expressed mathematically as shown in Fig. 4.7.

Stress-Strain Relationship for Concrete

If concrete is compressed in one direction, it tends to expand laterally. If this expansion occurs freely, concrete is said to be "unconfined" and principal compressive stresses exist in one direction only. On the other hand, if such lateral expansion is restricted, concrete is said to be "confined" and, as a result of such restriction, compressive stresses develop in all directions. The stress-strain relationships for both confined and unconfined concrete, which are different, will be considered in this section because both will be needed in the analyses. Up to the stage corresponding to crushing, the concrete was essentially unconfined; beyond this stage, and especially at the stage corresponding to ultimate, the concrete core bound by the transverse reinforcement was confined. In this section, only those properties of confined concrete to be used in the analysis presented in Section 4.9 will be considered. A more detailed discussion of the properties of confined concrete is presented in Appendix C.

a) Stress-Strain Relationships for Unconfined Concrete

Typical stress-strain curves for unconfined concrete in compression are shown in Fig. 4.8. They were obtained from tests on 3 x 6-in. cylinders (11). All the curves have certain common characteristics. They have an initial portion which is almost linear. The slope of the curves decreases until the maximum stress is reached at a strain of approximately 0.002. Stress-strain curves obtained from eccentric compression tests (10) on members with unreinforced rectangular cross-sections are very similar to those obtained from concentric compression tests on cylinders.

For flexural computations, it is usually not necessary to know the complete stress-strain curve for the concrete in the member. Such computations can be carried out if the following properties of the stress block (as the distribution of the compressive strains in the concrete is often referred to) are known or can be determined:

1) the compressive strain at the extreme fiber on the concrete,

2) the total compressive force in the concrete,

3) the location of the resultant of the compressive forces in the concrete.

The two most important conditions for unconfined concrete (and the only ones considered in this section) are those corresponding to "elastic" behavior of the concrete and to the first visual signs of crushing.

When concrete behaves elastically (when the maximum concrete stress is less than about 0.7 f'_c), the only quantity needed for the determination of the properties of the stress block, as it will be illustrated in Section 4.7, is the value of the Young's modulus of the concrete, E_c, corresponding to the initial portion of the stress-strain curve. The following expression from Reference 9 will be used in this study:

$$E_c = \frac{30,000,000}{6 + \frac{10,000}{f'_c}} \qquad (4.15)$$

where both E_c and f'_c are in psi.

For the stage corresponding to first crushing of the concrete, the properties of the stress block needed for flexural computations are ϵ_u, k_1k_3, and k_2 as illustrated in Fig. 4.18, where

ϵ_u = compressive strain in concrete at extreme fiber corresponding to first crushing

k_1k_3 = ratio of the average compressive stress in concrete at crushing to the cylinder strength

k_2 = ratio of the depth of the centroid of the stress block to the depth of the neutral axis

The following expressions from Reference 10 will be used to determine these quantities in the analysis for crushing presented in Section 4.8:

$$\epsilon_u = 0.004 - \frac{f'_c}{6.5 \times 10^6} \tag{4.16}$$

$$k_1 k_3 = \frac{3900 + 0.35 f'_c}{3200 + f'_c} \tag{4.17}$$

$$k_2 = 0.50 - \frac{f'_c}{80{,}000} \tag{4.18}$$

where f'_c is the cylinder strength in psi. They were obtained using the results of eccentric compression tests on specimens with unreinforced rectangular cross sections. In those tests, the uncertainties due to the presence of longitudinal reinforcement and tensile stresses in the concrete were avoided through an ingenious testing procedure.

b) Stress-Strain Relationships for Concrete Confined by Rectilinear Ties

The three stress-strain curves for confined concrete to be used in the analysis for the stage corresponding to ultimate are shown in Fig. 4.9. These curves were assumed on the basis of those reported in Reference 12 for conditions comparable to those prevailing at ultimate in the specimens considered herein.

In addition to the shape of the stress-strain curves, given in Fig. 4.9, the peak ordinate of these curves is needed. As discussed in Section C.3 of Appendix C, this ordinate, f_1, can be estimated as follows:

$$f_1 = f'_c + \Delta f_c \tag{4.19}$$

where Δf_c, the increase of concrete compressive strength over the unconfined

value, is given by the following expression, derived in Section C.2 of Appendix C:

$$\Delta f_c = \frac{6000}{1 + \frac{2300}{f_2}} \tag{4.20}$$

and f_2, a measure of the effect of the transverse reinforcement, is taken as the average of the confining stresses in the directions parallel to the sides of the section computed according to the assumptions shown in Fig. C.3. Thus,

$$f_2 = \frac{1}{2}(f_{21} + f_{22}) = \frac{A''_s f''_y}{s}\left(\frac{1}{2c} + \frac{1}{b''}\right) \tag{4.21}$$

where $f_{21} = \frac{A''_s f''_y}{sc}$ = average normal stress on a plane perpendicular to the neutral axis,

$f_{22} = \frac{2A''_s f''_y}{sb''}$ = average normal stress on a plane parallel to the neutral surface,

A''_s = cross-sectional area of transverse reinforcement,

f''_y = yield stress of transverse reinforcement,

s = center to center spacing of transverse reinforcement,

c = depth of the neutral axis from the inside face of the transverse reinforcement,

b'' = width of core enclosed in the transverse reinforcement.

To facilitate the computation of the strength of confined concrete, f_1, the curves for Δf_c shown in Fig. 4.10 were prepared using Eqs. 4.20 and 4.21 for the various properties of the transverse reinforcement listed in the table shown in the figure. The computation of Δf_c for the specimens with U-stirrups deserve special interest. Since the stirrups were open in the upper part, it was assumed that the concrete was not confined in the direction parallel to the neutral axis and, therefore, $f_{21} = 0$ in Eq. 4.21. The remainder of the computations was carried out in the same manner as the specimens with closed ties.

The properties of the stress block for confined concrete that are needed for flexural computations are ϵ_c, $\bar{k}_1\bar{k}_3$, and $\bar{k}_2$, which are defined in Fig. 4.11. At the stage corresponding to the strain ϵ_c in the concrete, these quantities have a significance similar to that of the quantities ϵ_u, k_1k_3, and k_2, respectively, at the stage corresponding to crushing of the concrete. Since the properties of the stress block $\bar{k}_1\bar{k}_3$ and $\bar{k}_2$ (which are needed for the calculations for ultimate in Section 4.9) vary with ϵ_c and the properties of the transverse reinforcement, to facilitate their determination, the curves shown in Fig. 4.12 were computed using the assumed stress-strain curves given in Fig. 4.9. The computations involved in the determination of a point on these curves can readily be derived from the sketch shown in Fig. 4.11.

4.7 Analysis for Yield Stage

Moment and Curvature at Yield

Distributions of strain and stress for this stage are shown in the lower part of Fig. 4.13. In addition to the general assumptions listed in Section 4.5, the two specific assumptions made here are that both steel and concrete are in the elastic range. It can be observed that the strain and stress conditions shown in Fig. 4.13 are identical to those in the conventional straight-line theory (vertical cracks) as far as computations of moment and curvature are concerned. Therefore, Eqs. 4.8 - 10 can be used here to compute such quantities.

Curvature Diagram

The probable curvature diagram for the specimens considered in this analysis is illustrated in Fig. 4.14c. For the purpose of this discussion, the area under the curvature diagram can be divided in three parts. Part 1

represents the "curvatures" in the stub. Part 2 can be thought of as representing the curvatures distributed along the span of the member if the triangular wedge, marked 3 in Fig. 4.14a, does not deform. (The points of this wedge do not correspond to any of the cross-sections along the span of the member if the member behaves according to this - inclined crack - theory.) This part, however, deforms and, consequently, it causes the curvatures near the stub face to increase. This increase is Part 3, shown shaded in Fig. 4.14c.

For the purpose of computing deflections or rotations, the idealized curvature diagram shown in Fig. 4.14d was used. The effect of the stub, θ_{sy}, (concentrated at the face of the stub) was computed using Eq. 4.7. Part 2 of the curvature diagram was assumed to vary linearly from zero at the support to φ_y (Eq. 4.10) at the face of the stub. In the probable curvature diagram, since the uncracked sections are stiffer than those cracked, there is a break at the point corresponding to the cracking moment (Fig. 4.14c); however, the effect of neglecting this break on the value of computed deformations is small in most cases. The rotation θ_{iy} caused by the deformation in the wedge, represented by the shaded area in Fig. 4.14c was assumed to be concentrated at the face of the stub. This concentrated rotation was estimated using the procedure developed in the following paragraphs.

Determination of Concentrated Rotation at the Face of the Stub Due to Deformations in the Wedge

Figure 4.15 illustrates the interrelationship between the deformations in the wedge (Part 3) of the member and the accompanying concentrated rotation θ_i at the face of the stub. Due to the elongation $\underline{x}$ of the tension reinforcement in Part 3, the face of the inclined crack OB farthest from the stub rotates around point $\underline{O}$ to a position OB'. At yield, the relationship between the elongation $\underline{x}$ and the rotation at yield θ_{iy} is

$$\theta_{iy} = \frac{x}{\overline{OA}} \tag{4.22}$$

where $\overline{OA}$ is the distance from the center of the tension bars to the center of rotation O. In order to evaluate θ_{iy} the following assumptions were made:

1) The rotation takes place around the neutral axis at the section at the face of the stub. In other words,

$$\overline{OA} = d-c \tag{4.23}$$

This assumption is probably nearly correct, because in the actual member, the rotation is spread over a small length and the location of the neutral axis in this length should not vary significantly.

2) The elongation x is

$$x = \left[f_{cn}(f_y A_s / \Sigma o) \right] a \epsilon_y \tag{4.24}$$

If the tension reinforcement were completely unbonded over the length AB', the elongation would be $x_{unbonded} = a \epsilon_y$. However, bond is only partially lost and the actual elongation is a function of the amount of bond lost, which in turn is a function of the bond stresses in the length AB'. Therefore, the elongation x can be represented by Eq. 4.24, in which the coefficient $f_{cn}(f_y A_s/\Sigma o)$ is a function of the nominal bond stress, $f_y A_s/\Sigma o$, where

$f_y A_s$ = total force in the tension reinforcement;

Σo = sum of perimeters of tension bars.

Combining Eqs. 4.22-24, the rotation θ_{iy} was expressed as follows:

$$\theta_{iy} = \frac{[f_{cn}(f_y A_s/\Sigma o] a \epsilon_y}{d - c} \tag{4.25}$$

in which the quantities $[f_{cn}(f_y A_s/\Sigma o)]$ and a were evaluated with the aid of the theoretical procedures available to this point and the measured deflection at yield (Δ_y), as discussed in the following paragraphs.

Figure 4.16c illustrates the interrelationship between rotations and deflections. With reference to this figure, the deflection at yield can be expressed as follows:

$$\Delta_y = \Delta_{fy} + \Delta_{iy} \tag{4.26}$$

and

$$\theta_{iy} = \frac{\Delta_{iy}}{\ell} = \frac{\Delta_y - \Delta_{fy}}{\ell} \tag{4.27}$$

The rotation θ_{iy} was evaluated using Δ_y measured in the tests and $\Delta_{fy}(=\Delta_{sy}+\Delta_{by})$ determined according to the curvature diagram shown in Fig. 4.14d. The calculations involved in the determination of the ratio θ_{iy}/ϵ_y can be followed easily in Tables 5, 6, and 7 for the specimens tested by McCollister, Burns, and in this program, respectively.

In order to investigate the variation of the ratio θ_{iy}/ϵ_y with the quantities $f_y A_s/\sum o$ and a, Eq. 4.25 was rewritten as follows:

$$\theta_{iy}/\epsilon_y = [fcn(f_y A_s/\sum o)]\ \frac{a}{d-c} \tag{4.28}$$

The variation of θ_{iy}/ϵ_y with a was investigated first. This was done indirectly through a plot of θ_{iy}/ϵ_y versus the distance (d-c) for the specimens tested by Burns, all of which had nearly the same value for $f_y A_s/\sum o$. This plot showed that θ_{iy}/ϵ_y increased very little as (d-c) decreased; and, furthermore, this increase was relatively small as compared to the scatter of the values for θ_{iy}/ϵ_y. The implication was that the ratio a/(d-c) remained nearly constant as (d-c) varied, which was in reasonable agreement with the observed fact that the slope of the cracks, which can be measured by the ratio a/(d-c), varied very little in these tests. As a result of this study the ratio a/(d-c) was dropped as a variable. Therefore, Eq. 4.28 was written as follows:

$$\theta_{iy}/\epsilon_y = \text{fcn}(f_y A_s/\Sigma o) \qquad (4.29)$$

in which the function includes the effect of the inclination of the cracks as a constant.

Next, the plot of θ_{iy}/ϵ_y versus $f_y A_s/\Sigma o$ shown in Fig. 4.17 was made. The individual values of these quantities are listed in the last two columns of Tables 5 - 7. It can be observed in Fig. 4.17 that the points representing the test results form two separate groups, which can be represented by two parallel lines with a slope equal to 0.22. The points for the specimens tested by McCollister (Group 1) fall above the points tested by Burns and in this program (Group 2).

There was strong evidence indicating that the existence of two groups of points, instead of only one, was due to the difference in the shear span, $\underline{\ell}$; that is, the ratio θ_{iy}/ϵ_y appeared to be a function of $\underline{\ell}$ also, and, furthermore, such ratio appeared to increase as $\underline{\ell}$ decreased. For example, the shear span of all the specimens of Group 1 (48 in.) was shorter than that of the specimens of Group 2 (66 in.); and, as can be seen in Fig. 4.17, for the same $f_y A_s/\Sigma o$, the concentrated rotation θ_{iy} for the specimens of Group 1 was the larger of the two groups. More evidence is furnished by the tests conducted by Ernst (3) on specimens of the same type as those tested by Burns and in this program. The span between supports was nine feet, and the length of the stub was varied from 6 to 36 in.; or, for the purpose of this discussion, it can be said that the shear span was varied from 51 to 36 in. Because the sections in the stub were stiffer than the sections in the framing member, for beams with the same cross-sectional properties one would expect the deflection at yield to decrease as the length of the stub increased. However, this was not the case. All specimens having the same cross-section had about the same deflection at yield, regardless of the length of the stub. Since the

deflections due to curvatures in the stub and in the framing member (Δ_{fy} in Eq. 4.26) decreased as the length of the stub increased, the only possible way the deflection at yield could have remained constant was through an increase of the concentrated rotation θ_{iy}. To summarize, the tests conducted by Ernst also indicated that θ_{iy} increased as $\underline{\ell}$ decreased.

There were two other possible explanations why the specimens of Group 1 exhibited a larger θ_{iy} than those of Group 2 with the same $f_y A_s / \Sigma o$. First, the thickness of the cover over the reinforcement was larger for Group 2 than for Group 1; and second, except for T-15, all specimens of Group 1 did not have a stub at the bottom, whereas all specimens of Group 2 did. Because of lack of data, it can not be proved conclusively that the two variables mentioned above are not the major ones in the problem being discussed. But there is evidence which suggests this conclusion. For example, a comparison of the values of θ_{iy} for the specimens of Group 1 having approximately the same values for $f_y A_s / \Sigma o$ did not reveal any systematic variation of θ_{iy} as the thickness of the cover varied. Also, the point representing specimen T-15 (identified in Fig. 4.17) with a stub at the bottom of the beam still falls among the others of Group 1.

It was therefore concluded that the rotation θ_{iy} was also a function of $\underline{\ell}$, and a rational explanation for this interrelationship was sought.

It was thought that θ_{iy} increased as $\underline{\ell}$ decreased because the shear force increased. It should be kept in mind that the concentrated rotation θ_{iy} results from the formation of inclined cracks. It is well known that if the shear force is small enough, inclined cracks do not form. In such case, θ_{iy} does not exist. If the shear force is large enough, inclined cracks form, and a concentrated rotation θ_{iy} results. However, the transition from a "vertical-crack" type of behavior to an "inclined-crack" type of behavior is

not an abrupt but rather a continuous process. As the shear force increases, the behavior approaches more and more that of an ideal specimen with only inclined cracks, and θ_{iy} increases accordingly.

With the above explanation in mind, it was possible to express the interrelationship between θ_{iy} and ℓ. Since the shear force increases as the inverse of ℓ, it follows that θ_{iy} should also increase as the inverse of ℓ. It was assumed that θ_{iy} depends linearly on the inverse of ℓ. With this assumption and the relation between θ_{iy} and $f_y A_s/\sum o$ derived from the plot on Fig. 4.17, the general equation for θ_{iy} is

$$\theta_{iy}/\epsilon_y = A + B\left(\frac{1}{\ell}\right) + 0.22\,\frac{f_y A_s}{\sum o} \qquad (4.30)$$

The coefficients A and B were evaluated using the values for the ordinates at the origin corresponding to the straight lines shown in Fig. 4.17, which are fair representations of the trends of the points representing the test results. Thus, for $f_y A_s/\sum o = 0$

$$A + B\left(\frac{1}{48}\right) = -1.08 \qquad \text{Group 1 } (\ell = 48 \text{ in.})$$

$$A + B\left(\frac{1}{66}\right) = -1.82 \qquad \text{Group 2 } (\ell = 66 \text{ in.})$$

The solution of this system of simultaneous equations yields A = -3.83 and B = 132. Therefore, Eq. 4.30 becomes

$$\theta_{iy}/\epsilon_y = 0.22\,\frac{f_y A_s}{\sum o} + \frac{132}{\ell} - 3.83 \qquad (4.31)$$

which is the equation that was used to determine θ_{iy}.

4.8 Analysis for Crushing Stage

Moment and Curvature at Crushing

Distributions of strain and stress for this stage are shown in the lower part of Fig. 4.18. The complete stress-strain curve for the reinforcement

obtained from tests of coupons and the properties of the stress block given by Eqs. 4.16-18 are used here. As in the case for yield, the strain and stress conditions at crushing according to this theory, shown in Fig. 4.18, are identical to those for the vertical-crack theory presented in Section 4.3 as far as computations of moment and curvature are concerned. Therefore, the procedure outlined in that section can be used here to determine such quantities.

Curvature Diagram

The probable curvature diagram at crushing for the specimens considered in this analysis is illustrated in Fig. 4.19c. As was done for the stage corresponding to yield, the area under the curvature diagram can be divided in three parts, each of which has the same significance at crushing as its counterpart in Fig. 4.14 had at yield. Thus, Part 1 represents the "curvatures" in the stub, Part 2 represents the curvature diagram for the framing member if the triangular wedge marked 3 in Fig. 4.19a, did not deform, and the shaded area (Part 3) represents the increase of curvatures near the stub resulting from deformations in the wedge.

To simplify the calculations for deflections or rotations, the idealized curvature diagram shown in Fig. 4.19d was used. The rotation θ_{sc} due to "curvatures" in the stub, was assumed to be concentrated at the face of the stub and it was computed using Eq. 4.7. In accordance with the idealized M-φ curve from Fig. 4.3, Part 2 of the curvature diagram was assumed to vary linearly from zero at the support to $(M_c/M_y)\varphi_y$ at the face of the stub. The rotation due to deformations in the wedge, θ_{ic}, was also assumed to be concentrated at the face of the stub and it was determined using the procedure developed in the following paragraphs.

Determination of the Concentrated Rotation at the Face of the Stub Due to Deformations in the Wedge

The mechanism for the concentrated rotation illustrated in Fig. 4.15a is also applicable for the stage corresponding to crushing. With reference to this figure, the rotation at crushing θ_{ic} can be expressed as follows:

$$\theta_{ic} = \frac{x}{\overline{OA}} \tag{4.32}$$

In order to evaluate θ_{ic} the following assumptions were made:

1) The rotation θ_{ic} occurs around the neutral axis at the section at the face of the stub. That is,

$$\overline{OA} = d-c \tag{4.33}$$

This assumption is equivalent to the one at yield on the basis of which Eq. 4.23 was written.

2) The elongation x can be expressed as follows:

$$x = x_y + x_p \tag{4.34}$$

where x_y = elongation due to loss of bond in the elastic range,

x_p = elongation due to loss of bond in the plastic range.

3) The rotation due to the elongation x_y is obtained from Eq. 4.31. This equation gives θ_{iy} which is equal to $x_y/(d-c)$, for the stage corresponding to yield. Since the location of the neutral axis (given by c) is different at crushing than at yield, this assumption is not strictly correct. However, the effect of this difference in the result is small and was therefore neglected.

4) The elongation x_p is expressed as

$$x_p = [f_{cn}(\epsilon_s - \epsilon_y)]\, a\, (\epsilon_s - \epsilon_y) \tag{4.35}$$

which is very similar in form to Eq. 4.24 for yield. The coefficient $f_{cn}(\epsilon_s - \epsilon_y)$, which represents the effect of loss of bond in the plastic range was assumed to be a function of the plastic strain $(\epsilon_s - \epsilon_y)$ only, because this strain was the only new variable at this stage.

On the basis of these assumptions, an expression for θ_{ic} was derived. Equations 4.32-34 were combined as follows:

$$\theta_{ic} = \frac{x_y}{d-c} + \frac{x_p}{d-c} \tag{4.36}$$

But

$$\theta_{iy} = \frac{x_y}{d-c} \tag{4.37}$$

and making

$$\theta_{ip} = \frac{x_p}{d-c} \tag{4.38}$$

Eq. 4.36 could be written as follows:

$$\theta_{ic} = \theta_{iy} + \theta_{ip} \tag{4.39}$$

The substitution of the value for x_p given by Eq. 4.35 into Eq. 4.38 gave the following expression:

$$\theta_{ip} = \frac{[f_{cn}(\epsilon_s-\epsilon_y)]\ a(\epsilon_s-\epsilon_y)}{d-c} \tag{4.40}$$

which was written as follows in order to investigate the interrelationship between x_p and $\epsilon_s - \epsilon_y$:

$$x_p = \theta_{ip}(d-c) = [f_{cn}(\epsilon_s-\epsilon_y)]\ a(\epsilon_s-\epsilon_y) \tag{4.41}$$

The plot which yielded the best results was the one of x_p versus $(\epsilon_s-\epsilon_y)$ shown in Fig. 4.20. The rotation θ_{ip}, needed for the determination of x_p, was obtained in a similar manner as θ_{iy} in Section 4.7. According to Eq. 4.39 and the sketch at the lower part of Fig. 4.16, which illustrates the

interrelationship between rotations and deflections, θ_{ip} was expressed as follows:

$$\theta_{ip} = \theta_{ic} - \theta_{iy} = \frac{\Delta_c - \Delta_{fc}}{\ell} - \theta_{iy} \qquad (4.42)$$

The rotation θ_{ip} was evaluated with this equation using Δ_c measured in the tests, $\Delta_{fc} = \Delta_{sc} + \Delta_{bc}$ determined according to the curvature diagram shown in Fig. 4.19d, and θ_{iy} from Eq. 4.31. The depth of the neutral axis, c, and the plastic strain, $\epsilon_s - \epsilon_y$, were the values computed according to the proposed theory. The values of x_p and $\epsilon_s - \epsilon_y$ determined in this way are listed in the last two columns of Tables 11-13 and plotted in Fig. 4.20. The trend of the points in Fig. 4.20 can be represented by the following equation:

$$x_p = \theta_{ip}(d-c) = 265(\epsilon_s - \epsilon_y)^2 + 1.95(\epsilon_s - \epsilon_y) \qquad (4.43)$$

which was the equation used to determine θ_{ip}. It can be noted that x_p does not depend on a. Although a varied widely for the specimens tested by Burns, the points representing the results of the tests plotted better when the length a was not considered. It appears that because the plastic strains are mostly concentrated at the cracks, the length a has no significance, as far as the magnitude of θ_{ip} is concerned.

For the purpose of calculating θ_{ic}, only Eqs. 4.39 and 4.43 are needed from this section; θ_{iy} can be determined using Eq. 4.31. To facilitate the calculations the plot of θ_{ip} versus $\epsilon_s - \epsilon_y$ shown in Fig. 4.21 was prepared on the basis of Eq. 4.43.

4.9 Analysis for Ultimate Stage

The procedure for estimating moments and curvature at ultimate presented here involves lengthy calculations. First, interaction curves (Figs. 4.22-23) for certain arbitrarily assumed compressive strains in the

concrete at the extreme fiber have to be determined. Second, M-φ curves, such as those shown in Figs. 4.24-25, must be determined using the interaction curves previously computed. Finally, moments and curvatures for ultimate must be taken from these M-φ curves according to a certain criterion. These three steps will be developed in detail in the following subsections with reference to the analysis made here for the specimens tested by Burns and the author.

Interaction Curves at Advanced Stages of Behavior

The interaction curves shown in Figs. 4.22-23 were computed according to the following assumptions, which complement those of Section 4.5:

1) The effective cross-section was as shown in Fig. 4.27b. As discussed in Section 3.2, the cover over the compression bars was lost at advanced stages of behavior. Although the amount of cover lost may be larger or smaller than assumed here, this assumption is as good as any other that could be made for these stages.

2) The stress-strain relationships for the compressed concrete enclosed within the ties and for the concrete on the side shells for the various specimens were those shown in Fig. 4.9. The effect of confinement was considered in the assumption of the stress-strain relationships for the concrete enclosed by the ties. The concrete outside of the ties was considered unconfined. Up to a strain of about 0.008, the stress-strain curve for unconfined concrete was based on the curves of Fig. 4.8; beyond this strain, the curve was assumed.

For the reinforcement, complete stress-strain curves for coupon tests were used.

Each of the P-M and P-φ curves shown on Figs. 4.22-23 were computed assuming a constant compressive strain ϵ_c at the extreme fiber of the concrete and certain arbitrary depths of the neutral axis, c. For each value of c assumed, the moment, the curvature and other quantities were computed.

Figures 4.27c and d illustrate typical distributions of strain and stresses, respectively, over the depth of a cross-section for certain assumed values of ϵ_c and $\underline{c}$. Typical calculations will now be illustrated. With reference to Figs. 4.27c and d,

$$\varphi = \frac{\epsilon_c}{c} \tag{4.44}$$

$$\epsilon'_s = \varphi(c - \frac{D'}{2}) \tag{4.45}$$

$$\epsilon_s = \varphi(d''-c) \tag{4.46}$$

where φ = curvature

ϵ'_s = strain in the compression steel

D' = diameter of compression bars

ϵ_s = strain in the tension steel

d'' = depth from the inside face of the ties to the center of the tension bars.

The stresses corresponding to the computed steel strains were taken from the stress-strain curves obtained from coupon tests. Next, the axial force P was computed from the equilibrium of the longitudinal forces as follows:

$$P = C'_c + C''_c + C_s - T \tag{4.47}$$

where

$$C'_c = \bar{k}'_1 \bar{k}'_3 f'_c (b-b'') c$$

$$C''_c = \bar{k}''_1 \bar{k}''_3 f_1 (b''c-A'_s)$$

$$C_s = A'_s f'_s$$

$$T = A_s f_s$$

The quantities not defined in Fig. 4.27 have their usual meaning. The values for $\bar{k}_1 \bar{k}_3$ were obtained for the assumed ϵ_c using the corresponding curves of Fig. 4.12a. The strength of confined concrete, f_1, was determined using

Eq. 4.19, and Δf_c was determined for the assumed $\underline{c}$ using the corresponding curve of Fig. 4.10.

The moment M about mid-depth of the original section was determined by taking moments of the forces about the center of the tension bars (Fig. 4.27d). The resulting equation for M was

$$M = C'_c(d''-\bar{k}'_2 c) + C''_c(d''- \bar{k}''_2 c) + C_s(d'' - \frac{D'}{2}) - P\,(\frac{d-d'}{2}) \qquad (4.48)$$

The values for $\bar{k}_2$ were obtained for the assumed ϵ_c from the corresponding curves of Fig. 4.12b.

As mentioned earlier, the curves for P-M and P-φ shown in Figs. 4.22-23 were determined making calculations as those just described for numerous arbitrarily assumed sets of values of ϵ_c and $\underline{c}$. It is interesting to note a break in some of the P-M curves at the values of P and M corresponding to the beginning of strain hardening in the tension steel. Below this point the tension steel is in the work-hardening range; above it, the tension steel is not in the work-hardening range.

Moment-Curvature (M-φ) Relationships

Figures 4.24-25 show M-φ curves for certain values of constant axial loads for the sections with p_g = 0.0111 and 0.0555, respectively, corresponding to specimens tested in this investigation. Each of these curves were obtained by taking from either Fig. 4.22 or 4.23 a number of sets of corresponding values of M and φ along the horizontal line representing the constant axial load P for which the M-φ curve was being constructed.

Moment and Curvature at Ultimate

Once the M-φ curve was obtained, the next step consisted of selecting the point on this curve representing ultimate. Good agreement between measured

and computed rotations for ultimate were obtained in this investigation when the following criterion for determining the curvature for this stage was used together with the curvature diagram suggested later in this section:

> Ultimate is represented by that point on the M-φ curve corresponding to either the absolute maximum moment or buckling of the compression bars as explained below, whichever occurs first.

It should be noted that the absolute maximum must be considered when the curve has more than one maximum, such as the M-φ curve for J-31 in Fig. 4.25. The application of this criterion will be illustrated with reference to the idealized M-φ curve shown in Fig. 4.26, for the two possible cases.

Case 1: Buckling of the compression bars, point 1 in Fig. 4.26, occurs before the absolute maximum of the M-φ curve is reached at point m. According to the criterion stated above, ultimate is represented by point 1.

Case 2: The absolute maximum of the M-φ curve, at point m, is reached before the point corresponding to buckling of the compression steel is reached at point 2. According to the criterion stated above, point m represents ultimate.

To determine the stress (or strain) at which the bars buckled, the following assumptions were made:

1) the bars buckled between two adjacent ties and the sections at the ties were perfectly restrained against relative displacements and rotations,

2) buckling occurred in the work hardening range,

3) when buckling occurred the concrete did not offer any restraint.

These assumptions are based on observations and measurements made in the tests, which are discussed in Section 3.3 under the subheading for compression failure. Thus, as shown in the photograph of Fig. 3.19a, the bars buckled as assumed, and strain measurements indicated that the bars were in the work-hardening range when they buckled. Apparently, the restraint offered by the concrete surrounding the bars was sufficient to prevent them from buckling

before strain hardening started. However, because of the limited amount of data, it is not possible to say whether this will be true for all cases.

With the assumptions listed above, the stress f_{cr} at which the bars buckle, according to the tangent modulus theory, is

$$f_{cr} = \frac{\pi^2 E_t}{(s/r)^2} \tag{4.49}$$

where E_t = tangent modulus of steel

s = center to center spacing of ties

r = radius of compression bars

The moment and curvature corresponding to buckling of the compression bars were determined as follows: first, the strain corresponding to f_{cr} (Eq. 4.49) was determined from the stress-strain curve for the compression steel; the moment and curvature corresponding to this strain were then obtained through interpolation of the corresponding values obtained for other values of the strain in the compression steel.

In this analysis, it was found that the point representing ultimate was that corresponding to the absolute maximum of the M-φ curve for the specimens with small amounts of reinforcement (Fig. 4.24), and that corresponding to buckling of the compression bars for the specimens with large amount of reinforcement (Fig. 4.25).

Curvature Diagram

The probable curvature diagram for the ultimate stage is illustrated in Fig. 4.28c. For the purpose of this discussion, the area under this diagram will be divided in four parts. Part 1 represents the "curvatures" in the stub. Part 2 is the curvature diagram corresponding to that part of the framing member between the support and the critical section, marked 2 in Fig. 4.28a.

Part 3 represents the curvatures corresponding to sections in that part of the framing member between the critical section and the face of the stub, marked 3 in Fig. 4.28a, if the triangular wedge, marked 4 in Fig. 4.28a, did not deform. Part 4 of the curvature diagram represents the increase of curvature at points near the stub resulting from deformation in the wedge.

In the calculations, the simpler, idealized curvature diagram shown in Fig. 4.28d was used. The rotation θ_{su} was determined using Eq. 4.7. Part 2 of the curvature diagram was assumed to vary linearly from zero at a certain Point A to φ_u at the critical section. The critical section was assumed to be located at six inches from the face of the stub,* and Point A was determined using the idealized M-φ curve shown in Fig. 4.29. Part 3 of the curvature diagram was assumed to be constant. The rotation θ_{iu}, due to the deformations in the wedge, was also assumed to be concentrated at the face of the stub, and it was determined using the procedure developed in the following paragraphs.

Determination of the Concentrated Rotation at the Face of the Stub Due to Deformations in the Wedge

Since Parts 2 and 3 of the curvature diagram were grossly approximated, as explained in the preceding paragraph, a very refined procedure for computing the inclined-cracking rotation was not justified. Therefore, the procedure for computing θ_{iu}, the concentrated rotation due to deformations in the wedge, was derived with simplicity as an important criterion.

The mechanism for the concentrated rotation illustrated in Fig. 4.15 is also applicable for this stage. The rotation θ_{iu} is

$$\theta_{iu} = \frac{x}{\overline{OA}} \tag{4.50}$$

---

* See Section 3.5.

The following assumptions were made to compute θ_{iu}:

1) The rotation θ_{iu} occurs around the neutral axis at the section at the face of the stub. That is,

$$\overline{OA} = d-c \tag{4.51}$$

2) The elongation x is

$$x = (d-c)\ \epsilon_s \tag{4.52}$$

This may be interpreted as containing implicitly the assumptions that the inclined crack OB in Fig. 4.15 is inclined at 45° and that the length $\overline{AB}$ is completely unbonded.

Combining Eqs. 4.50-52, the following expression for θ_{iu} was obtained:

$$\theta_{iu} = \epsilon_s \tag{4.53}$$

which was the equation used in this study to determine θ_{iu}.

5. COMPARISON OF MEASURED AND COMPUTED QUANTITIES

5.1 Preliminary Remarks

The object of this chapter is to present a comparison of measured moments and deflections with the corresponding values computed using the procedures presented in Chapter 4 for the stages corresponding to yield, crushing and ultimate. These procedures were used to compute moments and deflections at all three stages for all specimens in the three test programs considered in this study, except that values were not computed at ultimate for the specimens tested by McCollister.* Since each of the three stages can be and have been defined differently by various investigators, the way in which the measured values used herein were determined is described in the appropriate sections below.

5.2 Measured and Computed Quantities at Yield

Yield is the stage at which the tensile reinforcement yields, and corresponds to a sharp break in the load-deflection curve. In these tests, the yield stage was that at which strains on the tension bars measured at points one inch out from the face of the stub increased rapidly with little increase in deflection. The values of the transverse and axial loads corresponding to this stage were used to determine the measured moment. For the beams tested by McCollister, the measured yield moments reported in Reference 2 correspond very closely to the breaks in the load-deflection curves, and were therefore taken as the measured values in this study; however, the measured deflections

---

* They were omitted because of the very lengthy calculations involved. It was felt that the most important variables were already included in the tests made by Burns and in this investigation.

reported in that reference do not correspond to these breaks and the measured values reported here were obtained from the original data. For the beams tested by Burns, the measured moments and deflections reported in Reference 1 both correspond very nearly to the breaks in the curves, and were therefore taken as measured values in this study. In all cases, the measured moments include the effect of dead weight.

Moments at Yield

Measured and computed yield moments for the specimens tested by McCollister, Burns, and the author are listed in Tables 8, 9, and 10, respectively. The measured values were determined as described above. The computed values for the beams tested by McCollister and Burns were obtained using Eqs. 4.8-4.9; but, for the specimens of this investigation, they were obtained from interaction curves for yield, such as Curves 1 of the P-M plot on Fig. 2.1. These curves were computed according to the assumptions listed in Section 4.5 using stress-strain relationships for concrete from tests of cylinders.

It can be seen in Tables 8 - 10 that there is good agreement between measured moments and the corresponding computed values for all specimens of the three programs. The mean and the range of the ratios of measured to computed yield moments (Tables 8 - 10, column 14) for each of the three programs are the following:

	Mean	Range
McCollister	1.05	0.95-1.10*
Burns	1.03	0.99-1.06
This investigation	1.00	0.97-1.04

* Specimen S-12, tested by McCollister, has been omitted in this comparison because it is evident that there is something wrong with the values corresponding to this specimen. As McCollister points out, even if the moment arm jd were equal to the effective depth, d, the computed moment would still be smaller than the measured value.

This good correlation between measured and computed moments at yield is also illustrated by the plot of Fig. 5.1.

Deflections at Yield

Measured and computed yield deflections for the specimens of the three programs are also listed in Tables 8 - 10. The measured values were determined as described at the beginning of this section. The computed values were determined using the procedure presented in Section 4.7. With reference to Fig. 4.16c, the deflection at yield can be expressed as follows:

$$\Delta_y = \Delta_{sy} + \Delta_{by} + \Delta_{iy} \tag{5.1}$$

where $\Delta_{sy} = \theta_{sy}\ell$; $\Delta_{by} = \varphi_y \ell^2/3$; and $\Delta_{iy} = \theta_{iy}\ell$

The quantities θ_{sy}, φ_y, and θ_{iy} were determined using Eqs. 4.7, 4.10 and 4.31, respectively. The values for the partial deflections Δ_{sy}, Δ_{by} and Δ_{iy} are also listed in Tables 8 - 10.

The agreement between measured and computed deflections at yield is very good for all specimens of the three test programs. The mean and the range of the ratios of measured to computed yield deflections (Tables 8 - 10, column 10) for each of the three programs are the following:

	Mean	Range
McCollister	1.01	0.91-1.12
Burns	0.99	0.89-105
This investigation	1.03	0.98-1.09

The plot of measured versus computed values for all specimens shown in Fig. 5.2 also illustrates this good correlation.

To illustrate the inadequacy of the procedure for computing deflections presented in Section 4.3, the measured deflections were compared to the deflections computed using that procedure (Δ_{fy} in Tables 8 - 10). The

ratio of the measured deflection to the deflection thus computed has a range of 0.90 - 1.71 (Tables 8 - 10, column 11). This correlation is evidently very poor as compared to that obtained using the procedure proposed in this study.

5.3 Measured and Computed Quantities at Crushing

Crushing is the stage at which the first visible signs of distress in the compressed concrete appear. This stage is very difficult to detect, because there is no corresponding change in the trend of the load-deflection response of the member, and also because it easily escapes visual detection. (The photographs on Fig. 3.18 show the appearance of the member at this stage.) For this reason, and also because the initiation of crushing may occur prematurely if local irregularities in the member exist, a large scatter of the values of measured deflections is not unlikely. To avoid the uncertainties inherent in the visual method of detecting crushing, other investigators (1) (2)(3) have proposed to define this stage as that corresponding to reversal of strain readings on a gage located in the distressed area. In this investigation, both the visual method and the reversal of strain criterion were used for detecting this stage. The plots of concrete strains at points on the compressed face 1 to 1-1/2 in. from the face of the stub versus the midspan deflection shown in Figs. 3.29 and 3.30 indicate that although reversal of concrete strains and the first visual signs of crushing coincide in several cases, in others they do not, the reversal of the strain readings occurring at deflections significantly larger than those corresponding to the first visual signs of crushing. Where such differences existed, the stage corresponding to the appearance of these first visual signs of crushing was taken as representing this stage. Since the measured moments and deflections for the beams tested by McCollister and Burns reported in Reference 1 were

obtained using a similar criterion, those values are also taken here as the measured values.

Moments at Crushing

Measured and computed crushing moments for specimens of the three test programs are listed in Tables 14 - 16. The measured values were obtained as indicated above. The computed values were obtained using the trial and error procedure described in Section 4.3 for the beams tested by McCollister and Burns; for the specimens of this program they were obtained from interaction curves for crushing, such as Curves 2 of the P-M plot on Fig. 2.1. All computations were carried out according to the assumptions listed in Section 4.5 using the stress-strain relationships for concrete and steel presented in Section 4.6.

There is very good agreement (almost as good as for yield) between the measured moments and those computed using the procedure proposed in this study for all specimens of the three test programs. The mean and the range of the ratios of measured to computed crushing moments (Tables 14 - 16, column 14) for each of the three programs were the following:

	Mean	Range
McCollister	1.00	0.87-1.07
Burns	1.03	0.98-1.09
This investigation	1.02	1.00-1.09

This excellent correlation is also illustrated in Fig. 5.3.

Deflections at Crushing

Measured and computed deflections at crushing are also listed in Tables 14 - 16 for specimens of the three test programs. The measured values were obtained as explained at the beginning of this section. The computed

values were obtained using the procedure developed in Section 4.8. With reference to Fig. 4.16c, the deflection at crushing may be expressed as follows:

$$\Delta_c = \Delta_{sc} + \Delta_{bc} + \Delta_{ic} \tag{5.2}$$

and $\Delta_{sc} = \theta_{sc}\ell$; $\Delta_{bc} = \frac{M_c}{M_y}\frac{\varphi_y \ell^2}{3}$; and $\Delta_{ic} = \theta_{ic}\ell$

The quantities θ_{sc} and φ_y were determined using Eqs. 4.7 and 4.10, respectively; θ_{ic} was computed using Eqs. 4.39 and 4.31, and the curves of Fig. 4.21. M_c and M_y are the moments at crushing and yield, respectively, computed as explained earlier.

The measured and computed crushing deflections are in very good agreement for all specimens of the three test programs. The mean and the range of the ratios of measured to computed crushing deflections (Tables 14 - 16, column 10) for each of the three programs were the following:

	Mean	Range
McCollister	0.97	0.83-1.11
Burns	1.05	0.88-1.21
This investigation	1.03	0.89-1.16

This good correlation is also shown in Fig. 5.4. However, the scatter of the points in this figure is larger than for yield deflections (Fig. 5.2) and even larger than for moments at either crushing or yield (Figs. 5.3 and 5.1, respectively). This results from the difficulties in detecting crushing, as discussed earlier, which are greater than for yield. Failure in detecting crushing at the instant it occurs may result in relatively large error in the deflection; however, since the moments do not change greatly in this range of behavior, the error in moments is not as large as in deflections.

It is noteworthy that all points in Fig. 5.4 except two fall in a small area. This small variation in the value of the crushing deflection can be partially explained by the fact that, although the curvatures near the face of the stub varied widely due to the large variation in the depth of the neutral axis, the spread of these large curvatures varied so as to compensate the effect of the variation of the curvature on the total deflection. For example, as the depth to the neutral axis increased, the curvature at the face of the stub decreased, but the spread of the large curvatures increased; and as the depth to the neutral axis decreased, the curvature at the face of the stub increased, but the spread of the large curvatures decreased.

To illustrate the lack of accuracy of the procedure for computing deflections at crushing described in Section 4.3, the deflections thus computed, Δ_{fc}, are compared to the measured deflections in column 11 of Tables 14 - 16. The ratio of the measured deflections to these computed deflections has a range of 1.14 - 2.64 which is indeed very unsatisfactory.

5.4 Measured and Computed Quantities at Ultimate

Ultimate is the stage at which the resisting moment of the critical section starts to decrease significantly. It should be noted that this stage does not necessarily coincide with that for maximum moment. For example, on Fig. 3.4, the point corresponding to ultimate is well beyond that corresponding to the maximum moment. In the determination of the measured deflection at ultimate, the rotation of the stub was considered, as shown in Fig. 3.1. The deflections for the beams tested by Burns were determined using original data because the values reported in Reference 1 were obtained using a different definition for ultimate and, furthermore, the rotation of the stub was not considered. The measured moments for ultimate were also determined in a manner which was different from that of Reference 1. As discussed in Section 3.5,

the specimens failed at a section somewhat removed from the face of the stub. In the analysis from this stage (Section 4.9), it was assumed that failure occurred at a section 6 in. out from the face of the stub; therefore, the computed moments are compared to the measured moments corresponding to this section.

Moments at Ultimate

Measured and computed ultimate moments for specimens tested by Burns and in this investigation are listed in Tables 17 and 18, respectively. The measured values were obtained as indicated above. The computed values were obtained using the procedure described in Section 4.9.

It can be seen in Tables 17 and 18 that the agreement between measured and computed moments is good for those specimens that failed in compression. The mean and the range of the ratios of measured to computed ultimate moments (Tables 17 and 18, column 15) for these specimens were:

	Mean	Range
Burns	0.96	0.88-1.01
This investigation	1.00	0.90-1.08

This good correlation is also shown in Fig. 5.5.

For the specimens of the two programs that failed either in shear or by fracture of the reinforcement, the agreement was not as good as for compression failures, but it can still be considered satisfactory. The ratio of measured to computed ultimate moments for these specimens ranged from 0.83 to 0.95, and thus remained always smaller than unity as would be expected because these specimens failed "prematurely" before reaching the stage corresponding to a compression failure, which was assumed in the analysis.

It is interesting to note in Table 18 that the ratios of measured to computed ultimate moments for each group of specimens having the same

cross-section tend to increase as the axial load increases. This tendency may also be noticed on the P-M plots for ultimate for the groups of specimens having p_g = 0.0111 and 0.0555, shown in Figs. 5.7 and 5.8, respectively, in which the points representing the results of the tests are also plotted. The best explanation for this tendency is the fact that the amount of cover lost at this stage was not necessarily the same for all values of the axial load, as assumed in the analysis. This can be explained with reference to the idealized M-φ curves shown in Fig. 5.9c and d. The M-φ curve computed according to the analysis presented in Chapter 4 shows a discontinuity at the point representing crushing; the moment at this point dropping from that corresponding to the full section to that for the section without the top cover. However, the actual M-φ curve does not have a discontinuity at crushing. Since spalling of the concrete is a gradual process, the actual M-φ curve approaches gradually that of the section without top cover. If the ultimate occurs shortly after crushing (Fig. 5.9d), the cover is not yet completely lost and the ratio of measured to computed moment is larger than unity; this is the case for specimens with large axial loads, as shown in Table 18 for the specimens with 50 and 75 kips axial load. On the other hand, if the ultimate occurs significantly beyond crushing (Fig. 5.9c), this ratio decreases, and may become smaller than unity if more than the assumed amount of cover is lost; this is the case for specimens with small axial loads as shown in Table 18 for the specimens with zero and 25 kips axial load and in Table 17, for specimens without axial load. On the basis of this discussion, the actual P-M curve should be as shown in Fig. 5.9a.

Deflections at Ultimate

Measured and computed ultimate deflections for specimens tested by Burns and in this investigation are also listed in Tables 17 and 18,

respectively. The measured values were obtained as explained at the beginning of this section. The computed values were determined using the procedure described in Section 4.9. With reference to Fig. 4.16c, the deflection at ultimate may be expressed as follows:

$$\Delta_u = \Delta_{su} + \Delta_{bu} + \Delta_{iu} \tag{5.3}$$

where $\Delta_{su} = \theta_{su}\ell$; $\Delta_{bu} = \varphi_u \left[6(\ell-3) + \frac{m}{2}\left(\ell - 6 - \frac{m}{3}\right)\right]$; and $\Delta_{iu} = \theta_{iu}\ell$

The quantities θ_{su} and θ_{iu} were computed using Eqs. 4.7 and 4.53, respectively; the curvature φ_u was determined as described in Section 4.9; and the distance $\underline{m}$, defined in Fig. 4.28, was determined using an idealized M-φ curve like that shown in Fig. 4.29.

The agreement between measured and computed ultimate deflections listed in Tables 17 and 18 may be considered satisfactory for those specimens that failed in compression. The mean and the range of the ratios of measured to computed ultimate deflections (Tables 17 and 18, column 12) for these specimens were:

	Mean	Range
Burns	1.05	0.78-1.33
This investigation	1.07	0.70-1.23

The rather low ratio 0.70 for J-29 indicates that this specimen may have failed in shear rather than in compression, although this could not be told from the observations made during the tests. The measured and computed values are also compared in Fig. 5.6. As would be expected, the scatter of the test results is larger than for other stages of behavior because, in addition to errors in the analysis, the properties of the specimens are to some extent modified at random by spalling of the concrete.

For the specimens of the two programs that failed prematurely either in shear or by fracture of the tensile reinforcement the agreement between measured and computed ultimate deflections was very poor, the ratio of the measured to the corresponding computed value ranging from as low as 0.43 to 0.79 as would be expected because the specimens failed before reaching the stage assumed in the analysis (compression failure). This indicates the necessity for procedures that will consider shear and tension (fracture of the steel) failures.

It is interesting to note the shape of the computed P-φ curves for ultimate shown in Figs. 5.7 and 5.8. For axial loads smaller than a certain value, the tension steel is in the work-hardening range and the curvatures are many times larger than those for larger axial loads, in which cases the tension steel is not in the work-hardening range. This explains the very small ductility of J-27, which had a large axial load (75 kips), the only specimen of these tests that failed while the tension steel was not in the work-hardening range.

6. SUMMARY

6.1 Outline of Investigation

The primary object of this investigation was to obtain fundamental information on the strength and deformation characteristics of reinforced concrete members subjected to combined transverse and axial loading. Tests of eleven specimens simulating a beam-column connection (Fig. 2.2) are described in this report. The two principal variables were the axial load and the amount of longitudinal reinforcement. The axial load, which was kept constant during the test of each specimen, was varied from zero to 75 kips. The amount of longitudinal reinforcement was varied from 1.11 to 5.55 percent, and was equally distributed between the tension and the compression reinforcement. All specimens were tested under conditions below the balance point of the interaction curve as shown in Fig. 2.1.

Each specimen was tested to failure in four to six hours. Records of load, deflection, and concrete and steel strains were obtained throughout all stages of loading.

On the basis of the results of these tests and those by McCollister (2) and Burns (1), procedures were developed for estimating moments and rotation of a member at a connection for the stages corresponding to yield, crushing and ultimate.

6.2 Results of Tests

The moment-rotation curve for specimen J-25 in Fig. 3.3 is a typical representation of the response to load of the eleven specimens of these tests. The most important points on the curve are those corresponding to yield (point 2) and ultimate (point 5), which give a measure of the stiffness in the

working load range and the energy-absorption capacity of the member, respectively. At a certain point shortly after yield, the first signs of crushing were observed (point 3). This point does not correspond to any significant change in the response to load of the member, and contrary to what is commonly assumed, it is not the ultimate stage in the loading history of the member. The deflection at ultimate is quite sensitive to variations in the amounts of transverse and compression reinforcement, whereas the deflection at crushing is not. Depending on the amounts of these two types of reinforcement, the deflection at ultimate was from 2 to 12 times the crushing deflections.

As shown in Figs. 3.37 - 3.39, the ductility of the members decreased as the axial load increased, as would be expected. However, as the equal amounts of tension and compression steel increased, the ductility of members with small axial loads (P=0 or 25 kips) did not vary significantly, but for specimens with large axial loads (P=50 or 75 kips) the ductility increased.

The observed modes of failure were classified into three categories: tension, compression, and shear. These terms refer to conditions at collapse and therefore should not be confused with their more common usage in reference to primary modes of failure. In a "tension" failure, the tension reinforcement fractured before the resisting moment at the critical section started to decrease. This mode of failure was observed in J-24, which did not have axial load and had a low tensile steel ratio. Two types of "compression" failures were observed: (a) buckling of the compression steel, and (b) distress of the compressed concrete. In the first type, the compression bars buckled before the resisting moment of the critical section started to decrease. This mode of failure was observed in the specimens with large amounts of steel subjected

to axial loads (J-15, J-16, J-29 through J-31). In the second type of compression failures, the resisting moment decreased because of a significant loss of strength of the concrete. This mode of failure was observed in the specimens having the low steel ratio and which were subjected to axial loads (J-25 through J-27, and J-34). The "shear" failure was characterized by a faulting type of movement along the plane of an inclined crack, which was accompanied by a decrease in the load carrying capacity of the member. This mode of failure was observed in specimen J-28, having the highest steel ratio and without axial load. To summarize further, the specimens without axial load failed in tension for low steel ratios and in shear for high steel ratios, and the specimens subjected to axial load failed in compression by buckling of the compression steel for high steel ratios or by significant loss of strength of the compressed concrete for low steel ratios.

6.3 Analysis of Results

Procedures for computing moments and deformations for yield, crushing, and ultimate were developed and were then used to compute the corresponding quantities for the specimens tested in the various investigations.

An important feature of these procedures is the assumption that cracks are inclined. This made it possible to explain the concentrated rotation in the vicinity of the face of the stub as observed in the tests and to develop rational procedures for computing it. The contribution of the deformations in the stub to the deformations of the member were considered in the analysis for all stages of behavior. For ultimate, some additional important considerations in the analysis included the geometry of the critical section, the properties of the confined concrete enclosed by the transverse reinforcement, the type of compression failure, and the actual location of the critical section.

These procedures were used to compute moments at the three stages for specimens tested by McCollister (2), by Burns (1) and in this investigation. A total of 47 specimens from the three investigations were analyzed for yield and crushing, but only those from the last two test programs (28 specimens) were analyzed for ultimate. Variables in all of these tests include: effective depth, shear span, amount of tension reinforcement, amount of compression reinforcement, amount of transverse reinforcement, concrete strength, and axial load.

As shown in Figs. 5.1 - 5.6, the agreement between measured and computed moments and deflections was good for all stages of behavior, except for the deflections at ultimate corresponding to specimens that failed either in shear or by fracture of a tension bar. This is as would be expected because these specimens failed "prematurely" before reaching the conditions for a compression failure which were assumed in the analysis. This indicates the need for procedures applicable to modes of failure other than compression if a more accurate estimate of the deflection corresponding to these modes of failure is desired.

The most important findings in this study can be summarized as follows: The ductility of reinforced concrete members decreases as the axial load increases as would be expected. Crushing is not a significant stage insofar as the ductility of the member is concerned. The ductility of members failing in compression increases with the amount of properly tied compression steel and with the amount of the transverse reinforcement. The procedures developed here for computing moments and rotations at yield and at crushing gave good results for a wide range of variables, and they can be used with great confidence. Although the analysis for ultimate developed here for members failing in compression also gave good results, stress-strain

relationships for the confined concrete were assumed for the particular cases studied; there is still need for a procedure for predicting such relationships in terms of the appropriate variables. Finally, to solve the problem thoroughly, additional procedures applicable to modes of failure other than compression are also needed.

7. REFERENCES

1. Burns, N. H., and C. P. Siess, "Load-Deformation Characteristics of Beam-Column Connections in Reinforced Concrete," Civil Engineering Studies, Structural Research Series No. 234, University of Illinois, Urbana, Illinois, January 1962.

2. McCollister, H. M., C. P. Siess, and N. M. Newmark, "Load-Deformation Characteristics of Simulated Beam-Column Connections in Reinforced Concrete," Civil Engineering Studies, Structural Research Series No. 76, University of Illinois, Urbana, Illinois, June 1954.

3. Ernst, G. C., "Plastic Hinging at the Intersection of Beams and Columns," ACI Journal, V. 28, No. 12, June 1957, (Proceedings V.53), pp. 1119-1144.

4. Glanville, W. H., and F. G. Thomas, "Studies in Reinforced Concrete - Section V," Technical Paper No. 22, Department of Scientific and Industrial Research, England, 1939.

5. Carneiro, F. L. L. B., "Compte Rendu des Essais de Flexion de Trois Séries de Poutres en Béton Armé," published by Instituto Nacional de Tecnologia, Rio de Janeiro, Brazil, 1962.

6. Diaz de Cossío, R., unpublished report of test results enclosed with memorandum of 7 April 1962 to members of Comission XI of the Comité Européan du Béton.

7. Pfrang, E. O., and C. P. Siess, "Analytical Study of the Behavior of Long Restrained Reinforced Concrete Columns Subjected to Eccentric Loads," Civil Engineering Studies, Structural Research Series No. 214, University of Illinois, Urbana, Illinois, June 1961.

8. Warwaruk, J., M. A. Sozen, and C. P. Siess, "Investigation of Prestressed Reinforced Concrete for Highway Bridges, Part III; Strength and Behavior in Flexure of Prestressed Concrete Beams," University of Illinois Engineering Experiment Station Bulletin No. 464, August 1962.

9. Sozen, M. A., E. M. Zwoyer, and C. P. Siess, "Investigation of Prestressed Concrete for Highway Bridges, Part 1; Strength in Shear of Beams Without Web Reinforcement," University of Illinois Engineering Experiment Station Bulletin No. 452, April 1959.

10. Hognestad, E., N. W. Hanson, and D. McHenry, "Concrete Stress Distribution in Ultimate Strength Design," ACI Journal, V. 27, No. 4, December 1955, Proceedings V. 52, pp. 455-479.

11. Blanks, R. F., and D. McHenry, "Plastic Flow of Concrete at High Loads Relieves Stress Concentrations," Civil Engineering, Vol. 19, No. 5, May 1949, pp. 320-322.

12. Szulczynski, T., and M. A. Sozen, "Load-Deformation Characteristics of Concrete Prisms with Rectilinear Transverse Reinforcement," Civil Engineering Studies, Structural Research Series No. 224, University of Illinois, Urbana, Illinois, September 1961.

13. Richart, F. E., A. Brandtzaeg, and R. L. Brown, "A Study of the Failure of Concrete Under Combined Compressive Stresses," University of Illinois Engineering Experiment Station Bulletin No. 185, Urbana, Illinois, November 1928.

14. Richart, F. E., A. Brandtzaeg, and R. L. Brown, "The Failure of Plain and Spirally Reinforced Concrete in Compression," University of Illinois Engineering Experiment Station Bulletin No. 190, Urbana, Illinois, April 1929.

15. Richart, F. E., and R. L. Brown, "An Investigation of Reinforced Concrete Columns," University of Illinois Engineering Experiment Station Bulletin No. 267, June 1934.

16. Chan, W. W. L., "The Ultimate Strength and Deformation of Plastic Hinges in Reinforced Concrete Frameworks," Magazine of Concrete Research (London), V. 7, No. 21, November 1955, pp. 121-132.

17. Soretz, S., Stumpf, A., "Beitrag zum Bruchverhalten von Stahlbetonsäulen," Beton-und Stahlbetonbau, Heft 5, Berlin, May 1959.

18. Blume, J. A., N. M. Newmark, and L. H. Corning, "Design of Multistory Reinforced Concrete Buildings for Earthquake Motions," Portland Cement Association, Chicago, 1961.

TABLE 1

PROPERTIES OF SPECIMENS TESTED
IN THIS PROGRAM

(Dimensions and details for test specimens are shown in Fig. 2.2)

Mark	Nom. Axial Load	Cylinder Strength	Reinforcement				
			Amt. and Size	Ratio Tens. and Comp.	Column Ratio	Yield Stress Tens.	Comp.
	P	f'_c	Each	$p = p'$	p_g	f_y	f'_y
	kips	psi	Face	%	%	ksi	ksi
J-24	0	5060	2-#4	0.67	1.11	48.5	47.8
J-25	25	5050	2-#4	0.67	1.11	49.2	49.2
J-26	50	4600	2-#4	0.67	1.11	49.9	49.0
J-27	75	4920	2-#4	0.67	1.11	50.0	50.1
J-34*	75	4520	2-#4	0.67	1.11	48.8	50.3
J-16**	25	4550	2-#8	1.98	3.29	45.9	44.7
J-15**	50	4400	2-#8	1.98	3.29	46.9	47.3
J-28	0	5020	2-#9	3.33	5.55	46.9	46.7
J-29	25	4410	2-#9	3.33	5.55	48.8	48.6
J-30	50	4500	2-#9	3.33	5.55	47.0	47.2
J-31	75	4280	2-#9	3.33	5.55	48.3	47.9

* Tie spacing 3 in.; all others 6 in.; see Fig. 2.2.

** b = 8 in.; all others 6 in.; see Fig. 2.2.

TABLE 2

PROPERTIES OF SPECIMENS TESTED BY McCOLLISTER (2)

(b = 6 in., shear span ℓ = 48 in., length of stub w = 12 in., for all specimens.)

Mark	Effect. Depth of Reinf.		Cylinder Strength	Reinforcement						Tie Size and Spacing
				Amt. and Size		Ratio		Yield Stress		
	Tens.	Comp.		Tens.	Comp.	Tens.	Comp.	Tens.	Comp.	
	d	d'	f'_c			p	p'	f_y	f'_y	
	in.	in.	psi			%	%	ksi	ksi	
S-6	10.72	-	4151	3-#4	-	0.93	0	44.8	-	- - -
S-7	10.72	-	4073	2-#4	-	0.62	0	45.0	-	- - -
S-8	10.72	-	2642	2-#4	-	0.62	0	45.0	-	- - -
S-12	10.79	-	2484	2-#3	-	0.34	0	43.6	-	- - -
T-1	10.58	1.28	3897	2-#4	2-#4	1.39	0.63	41.8	47.9	#3 at 6 in.
T-2	10.37	1.41	3858	2-#9	2-#7	3.21	1.93	45.4	50.0	#3 at 4 in.
T-3	10.20	1.56	4266	2-#11	2-#8	5.10	2.58	44.7	46.1	#3 at 3 in.
T-7	10.58	1.42	4540	2-#6	2-#6	1.39	1.39	40.9	42.5	#3 at 6 in.
T-10	10.58	1.33	4330	2-#6	2-#3	1.39	0.35	42.6	46.3	#3 at 6 in.
T-11	10.58	1.84	4470	2-#6	2-#10	1.39	4.00	42.5	46.1	#3 at 6 in.
T-12	10.28	1.84	4367	2-#10	2-#9	4.11	3.24	46.0	45.8	#3 at 4 in.
T-13	10.37	1.69	4847	2-#9	2-#10	3.21	4.08	56.9	46.0	#3 at 4 in.
T-14	10.58	1.52	4030	2-#6	2-#6	1.39	1.39	41.4	40.9	#3 at 6 in.
T-15	10.58	1.50	3700	2-#6	2-#6	1.39	1.39	47.0	40.5	#3 at 6 in.
T-4	10.65	1.28	2230	2-#5	2-#4	0.97	0.63	47.1	45.7	#3 at 6 in.
T-5	10.51	1.35	2021	2-#7	2-#5	1.90	0.98	48.4	46.6	#3 at 6 in.
T-6	10.37	1.49	1905	2-#9	2-#7	3.21	1.93	56.5	49.7	#3 at 4 in.
T-8	10.58	1.74	2440	2-#6	2-#7	1.39	1.89	45.0	49.2	#3 at 6 in.
T-9	10.72	1.54	2693	2-#4	2-#6	0.62	1.37	52.5	41.5	#3 at 6 in.

TABLE 3

PROPERTIES OF SPECIMENS TESTED BY BURNS

(b = 8 in., shear span ℓ = 66 in., for all specimens except as noted.)

Mark	Effect. Depth of Reinf.		Cylinder Strength	Reinforcement						Tie Size and Spacing
				Amt. and Size		Ratio		Yield Stress		
	Tens.	Comp.		Tens.	Comp.	Tens.	Comp.	Tens.	Comp.	
	d	d'	f'_c			p	p'	f_y	f'_y	
	in.	in.	psi			%	%	ksi	ksi	
J-1	10.0	2.0	4930	2-#8	-	1.98	0	47.6	-	#3 at 6 in.
J-11	10.0	2.0	4110	2-#8	-	1.98	0	46.9	-	#3 at 6 in.
J-2	10.0	2.0	4080	2-#8	2-#6	1.98	1.10	48.0	48.6	#3 at 6 in.
J-8	10.0	2.0	4680	2-#8	2-#8	1.98	1.98	45.4	45.5	#3 at 6 in.
J-17	10.0	2.0	3900	2-#8	2-#8	1.98	1.98	46.9	46.8	#3 at 6 in.
J-18*	10.0	2.0	4410	2-#8	2-#8	2.64	2.64	45.4	47.1	#3 at 6 in.
J-10	14.0	2.0	3590	2-#8	-	1.41	0	45.1	-	#3 at 6 in.
J-14	14.0	2.0	4500	2-#8	2-#6	1.41	0.79	47.1	50.0	#3 at 6 in.
J-13	14.0	2.0	4800	2-#8	2-#8	1.41	1.41	45.6	46.0	#3 at 6 in.
J-19	14.0	2.0	3900	2-#8	-	1.41	0	45.8	-	#2U at 6 in.
J-20	14.0	2.0	4380	2-#8	2-#8	1.41	1.41	45.8	46.5	#2 at 6 in.
J-4	18.0	2.0	4820	2-#8	-	1.10	0	44.9	-	#3 at 6 in.
J-9	18.0	2.0	4190	2-#8	-	1.10	0	47.0	-	#3 at 6 in.
J-5	18.0	2.0	5000	2-#8	2-#6	1.10	0.61	45.1	48.9	#3 at 6 in.
J-6	18.0	2.0	5160	2-#8	2-#8	1.10	1.10	46.2	46.4	#3 at 6 in.
J-21	18.0	2.0	4350	2-#8	-	1.10	0	47.6	-	#2U at 6 in.
J-22	18.0	2.0	4420	2-#8	2-#8	1.10	1.10	46.2	46.4	#2 at 6 in.

* b = 6 in.

TABLE 4

SUMMARY OF RESULTS OF TESTS MADE IN THIS INVESTIGATION

Mark	Nom. Axial Load	Steel Ratio	Column Steel Ratio	Moments			Deflections			Mode of Failure*
				Yield	Crush.	Ult.	Yield	Crush.	Ult.	
	P	$p = p'$	p_g	M_y	M_c	M_u	Δ_y	Δ_c	Δ_u	
	kips	%	%	in. - kips			inches			
J-24	0	0.67	1.11	181	223	233	0.37	1.70	17.0	T
J-25	25	0.67	1.11	284	318	287	0.42	1.18	13.0	C
J-26	50	0.67	1.11	379	410	379	0.50	0.95	7.5	C
J-27	75	0.67	1.11	474	491	___**	0.53	0.86	___**	C
J-34+	75	0.67	1.11	470	474	373	0.60	0.74	3.8	C
J-8++	0	1.98	3.29	629	652	799	0.53	1.26	17.0	S
J-16++	25	1.98	3.29	711	738	845	0.57	1.26	13.6	C
J-15++	50	1.98	3.29	843	855	909	0.64	1.10	10.9	C
J-28	0	3.33	5.55	766	797	1030	0.63	1.20	13.5	S
J-29	25	3.33	5.55	920	919	1095	0.71	1.02	11.2	C
J-30	50	3.33	5.55	970	987	1120	0.74	1.09	12.9	C
J-31	75	3.33	5.55	1072	1074	1030	0.79	1.06	7.3	C

* T = tension failure; C = compression failure; S = shear failure.
** Point of M-Δ curve representing ultimate could not be selected; see Fig. 3.5.
\+ #3 ties at 3-in. centers, all others #3 at 6-in. centers; see Fig. 2.2.
++ b = 8 in., all others b = 6 in; see Fig. 2.2.

TABLE 5

"MEASURED" θ_{iy} FOR SPECIMENS TESTED BY McCOLLISTER (2)

Mark	Eff. Depth	Tens. Steel Ratio	Depth Neut. Axis	Curvature	Strain Tens. Steel	Deflection					$\frac{\Delta_{iy}}{\epsilon_y \ell}$	Nom. Bond Stress
						Total Meas.	Due to deformations in					
							Stub	Beam	(8)+(9)	Wedge		
	d	p	c	$\varphi_y \times 10^3$	ϵ_y	Δ_y	Δ_{sy}	Δ_{by}	Δ_{fy}	Δ_{iy}	θ_{iy}/ϵ_y	$f_y A_s/\Sigma o$
	in.	%	in.	rad/in.	%	← inches →						kips/in.
(1)	(2)	(3)	(4)	(5)	(6)	(7)	(8)	(9)	(10)	(11)	(12)	(13)
S-6	10.72	0.93	3.44	0.213	0.155	0.250	0.048	0.163	0.211	0.039	0.52	5.70
S-7	10.72	0.62	2.91	0.198	0.155	0.205	0.042	0.152	0.194	0.011	0.14	5.72
S-8	10.72	0.62	3.08	0.203	0.155	0.225	0.045	0.155	0.200	0.025	0.34	5.72
S-12	10.79	0.34	2.42	0.179	0.150	0.170	0.038	0.137	0.175	-0.005	-0.07	4.08
T-1	10.58	1.39	3.78	0.212	0.144	0.260	0.048	0.163	0.211	0.049	0.71	7.80
T-2	10.37	3.21	4.68	0.274	0.156	0.400	0.065	0.211	0.276	0.124	1.65	12.80
T-3	10.20	5.10	5.26	0.312	0.154	0.500	0.078	0.239	0.317	0.183	2.48	15.74
T-7	10.58	1.39	3.50	0.203	0.144	0.245	0.045	0.156	0.201	0.044	0.64	7.63
T-10	10.58	1.39	3.83	0.218	0.147	0.260	0.051	0.167	0.218	0.042	0.59	7.95
T-11	10.58	1.39	3.14	0.197	0.147	0.250	0.045	0.151	0.196	0.054	0.77	7.93
T-12	10.28	4.11	4.81	0.291	0.159	0.470	0.072	0.223	0.295	0.175	2.30	14.62
T-13	10.37	3.21	4.19	0.317	0.196	0.530	0.074	0.243	0.317	0.213	2.26	16.06
T-14	10.58	1.39	3.56	0.204	0.143	0.245	0.045	0.156	0.201	0.044	0.63	7.73
T-15	10.58	1.39	3.59	0.232	0.162	0.290	0.054	0.178	0.232	0.058	0.74	8.77
T-4	10.65	0.97	3.49	0.226	0.162	0.245	0.051	0.173	0.224	0.021	0.26	7.44
T-5	10.51	1.90	4.42	0.274	0.167	0.390	0.065	0.210	0.275	0.115	1.43	10.58
T-6	10.37	3.21	5.01	0.364	0.195	0.630	0.090	0.279	0.369	0.261	2.78	15.94
T-8	10.58	1.39	3.64	0.224	0.155	0.260	0.051	0.172	0.223	0.037	0.50	8.40
T-9	10.72	0.62	2.69	0.225	0.181	0.265	0.048	0.173	0.221	0.044	0.50	6.68

TABLE 6

"MEASURED" θ_{iy} FOR SPECIMENS TESTED BY BURNS (1)

Mark	Eff. Depth	Tens. Steel Ratio	Depth Neut. Axis	Curvature	Strain Tens. Steel	Deflection					$\frac{\Delta_{iy}}{\epsilon_y \ell}$	Nom. Bond Stress
						Total Meas.	Due to deformations in					
							Stub	Beam	(8)+(9)	Wedge		
	d	p	c	$\varphi_y \times 10^3$	ϵ_y	Δ_y	Δ_{sy}	Δ_{by}	Δ_{fy}	Δ_{iy}	θ_{iy}/ϵ_y	$f_y A_s / \Sigma o$
	in.	%	in.	rad/in.	%	← inches →						kips/in.
(1)	(2)	(3)	(4)	(5)	(6)	(7)	(8)	(9)	(10)	(11)	(12)	(13)
J-1	10	1.98	4.21	0.283	0.164	0.600	0.091	0.411	0.502	0.098	0.91	11.97
J-11	10	1.98	4.29	0.284	0.162	0.610	0.091	0.413	0.504	0.106	0.99	11.79
J-2	10	1.98	4.03	0.278	0.166	0.590	0.087	0.404	0.491	0.099	0.91	12.07
J-8	10	1.98	3.80	0.245	0.152	0.530	0.076	0.355	0.431	0.099	0.92	11.41
J-17	10	1.98	3.86	0.264	0.162	0.535	0.082	0.383	0.465	0.070	0.66	11.79
J-18	10	2.64	4.12	0.267	0.157	0.575	0.085	0.388	0.473	0.102	0.99	11.41
J-10	14	1.41	5.38	0.181	0.156	0.396	0.061	0.263	0.324	0.072	0.70	11.34
J-14	14	1.41	4.92	0.178	0.162	0.400	0.059	0.259	0.318	0.082	0.77	11.84
J-13	14	1.41	4.66	0.168	0.157	0.380	0.055	0.244	0.299	0.081	0.78	11.46
J-19	14	1.41	5.34	0.182	0.158	0.380	0.061	0.264	0.325	0.055	0.53	11.51
J-20	14	1.41	4.69	0.170	0.158	0.370	0.056	0.247	0.303	0.067	0.64	11.51
J-4	18	1.10	6.07	0.130	0.155	0.295	0.045	0.189	0.234	0.061	0.60	11.29
J-9	18	1.10	6.15	0.137	0.162	0.310	0.047	0.199	0.246	0.064	0.60	11.82
J-5	18	1.10	5.71	0.127	0.156	0.300	0.043	0.184	0.227	0.073	0.71	11.34
J-6	18	1.10	5.40	0.126	0.159	0.290	0.042	0.183	0.225	0.064	0.61	11.61
J-21	18	1.10	6.14	0.138	0.164	0.300	0.048	0.201	0.249	0.051	0.47	11.97
J-22	18	1.10	5.49	0.127	0.159	0.290	0.043	0.184	0.227	0.063	0.60	11.61

TABLE 7

"MEASURED" θ_{iy} FOR SPECIMENS TESTED IN THIS INVESTIGATION

Mark	Nom. Axial Load P kips	Tens. Steel Ratio p %	Depth Neut. Axis c in.	Curvature $\varphi_y \times 10^3$ rad/in.	Strain Tens. Steel ϵ_y %	Deflection: Total Meas. Δ_y	Deflection due to deformations in: Stub Δ_{sy}	Beam Δ_{by}	(8)+(9) Δ_{fy}	Wedge Δ_{iy}	$\frac{\Delta_{iy}}{\epsilon_y \ell}$ θ_{iy}/ϵ_y	Nom. Bond Stress $f_y A_s/\Sigma o$ kips/in.
						←	inches			→		
(1)	(2)	(3)	(4)	(5)	(6)	(7)	(8)	(9)	(10)	(11)	(12)	(13)
J-24	0	0.67	2.50	0.227	0.172	0.37	0.06	0.33	0.39	-0.02	-0.18	6.18
J-25	25	0.67	3.50	0.263	0.172	0.42	0.08	0.38	0.46	-0.04	-0.36	6.25
J-26	50	0.67	4.25	0.296	0.172	0.50	0.09	0.43	0.52	-0.02	-0.18	6.35
J-27	75	0.67	4.80	0.332	0.172	0.53	0.11	0.48	0.59	-0.06	-0.54	6.37
J-34	75	0.67	5.24	0.353	0.168	0.60	0.11	0.52	0.63	-0.03	-0.27	6.10
J-15	50	1.98	4.62	0.301	0.162	0.64	0.10	0.43	0.53	0.11	1.03	11.46
J-16	25	1.98	4.24	0.275	0.158	0.57	0.09	0.40	0.49	0.08	0.77	11.72
J-28	0	3.33	4.15	0.292	0.164	0.63	0.09	0.42	0.51	0.12	1.11	13.23
J-29	25	3.33	4.60	0.314	0.164	0.71	0.10	0.46	0.56	0.15	1.39	13.76
J-30	50	3.33	5.00	0.338	0.164	0.74	0.11	0.49	0.60	0.14	1.30	13.26
J-31	75	3.33	5.30	0.364	0.164	0.79	0.12	0.53	0.65	0.14	1.30	13.63

TABLE 8

MOMENTS AND DEFLECTIONS AT YIELD FOR SPECIMENS TESTED BY McCOLLISTER (2)

Mark	Eff. Depth	Tens. Steel Ratio	Deflection: Due to deformations in Stub	Beam	Wedge	(4)+(5)	Total: Comp.	Meas.	Meas./Comp.	Meas. Δ_y / Δ_{fy}	Moment: Comp.	Meas.	Meas./Comp.
	d	p	Δ_{sy}	Δ_{by}	Δ_{iy}	Δ_{fy}*	Δ_y	Δ_y			M_y	M_y	
	in.	%	inches								in - kips		
(1)	(2)	(3)	(4)	(5)	(6)	(7)	(8)	(9)	(10)	(11)	(12)	(13)	(14)
S-6	10.72	0.93	0.048	0.163	0.013	0.211	0.224	0.250	1.12	1.19	258	280	1.09
S-7	10.72	0.62	0.042	0.152	0.013	0.194	0.207	0.205	0.99	1.06	175	192	1.10
S-8	10.72	0.62	0.045	0.155	0.013	0.200	0.213	0.225	1.06	1.13	174	189	1.09
S-12	10.79	0.34	0.038	0.137	-0.013	0.175	0.162	0.170	1.05	0.97	96	111	1.16
T-1	10.58	1.39	0.048	0.163	0.044	0.211	0.255	0.260	1.02	1.23	343	343	1.00
T-2	10.37	3.21	0.065	0.211	0.130	0.276	0.406	0.400	0.99	1.45	805	805	1.00
T-3	10.20	5.10	0.078	0.239	0.176	0.317	0.493	0.500	1.01	1.58	1188	1217	1.02
T-7	10.58	1.39	0.045	0.156	0.041	0.201	0.242	0.245	1.01	1.22	336	356	1.06
T-10	10.58	1.39	0.051	0.167	0.048	0.218	0.266	0.260	0.98	1.19	348	376	1.08
T-11	10.58	1.39	0.045	0.151	0.047	0.196	0.243	0.250	1.03	1.28	341	355	1.04
T-12	10.28	4.11	0.072	0.223	0.163	0.295	0.458	0.470	1.03	1.59	1003	1070	1.07
T-13	10.37	3.21	0.074	0.243	0.230	0.317	0.547	0.530	0.97	1.67	1004	1073	1.07
T-14	10.58	1.39	0.045	0.156	0.043	0.201	0.244	0.245	1.00	1.22	338	367	1.09
T-15	10.58	1.39	0.054	0.178	0.066	0.232	0.298	0.290	0.97	1.25	385	406	1.05
T-4	10.65	0.97	0.051	0.173	0.044	0.224	0.260	0.245	0.91	1.09	276	273	0.99
T-5	10.51	1.90	0.065	0.210	0.100	0.275	0.375	0.390	1.04	1.42	526	537	1.02
T-6	10.37	3.21	0.090	0.279	0.228	0.369	0.597	0.630	1.05	1.71	992	985	0.99
T-8	10.58	1.39	0.051	0.172	0.057	0.223	0.280	0.260	0.93	1.17	364	346	0.95
T-9	10.72	0.62	0.048	0.173	0.034	0.221	0.255	0.265	1.04	1.20	202	215	1.06
							Mean		1.01	1.30			1.05**
							Range		0.91-112	0.97-1.71			0.95-1.10**

* Δ_{fy} is equal to the deflection given by the procedure for yield presented in Section 4.3.

** Values for S-12 not included. See Section 5.2.

TABLE 9

MOMENTS AND DEFLECTIONS AT YIELD FOR SPECIMENS TESTED BY BURNS (1)

Mark	Eff. Depth	Tens. Steel Ratio	Deflection: Due to deformations in Stub	Beam	Wedge	(4)+(5)	Total: Comp.	Meas.	Meas./Comp.	Meas. Δ_y / Δ_{fy}	Moment: Comp.	Meas.	Meas./Comp.
	d	p	Δ_{sy}	Δ_{by}	Δ_{iy}	Δ_{fy}*	Δ_y	Δ_y			M_y	M_y	
	in.	%	inches								in - kips		
(1)	(2)	(3)	(4)	(5)	(6)	(7)	(8)	(9)	(10)	(11)	(12)	(13)	(14)
J-1	10	1.98	0.091	0.411	0.087	0.502	0.589	0.600	1.02	1.20	648	639	0.99
J-11	10	1.98	0.091	0.413	0.082	0.504	0.586	0.610	1.04	1.21	635	648	1.02
J-2	10	1.98	0.087	0.404	0.091	0.491	0.582	0.590	1.01	1.20	647	685	1.06
J-8	10	1.98	0.076	0.355	0.072	0.431	0.503	0.530	1.05	1.17	612	629	1.03
J-17	10	1.98	0.082	0.383	0.082	0.465	0.547	0.535	0.98	1.15	629	635	1.01
J-18+	10	2.64	0.085	0.388	0.072	0.473	0.545	0.575	1.05	1.22	603	619	1.03
J-10	14	1.41	0.061	0.263	0.069	0.324	0.393	0.396	1.00	1.22	870	892	1.02
J-14	14	1.41	0.059	0.259	0.084	0.318	0.402	0.400	1.00	1.26	916	956	1.04
J-13	14	1.41	0.055	0.255	0.073	0.299	0.372	0.380	1.02	1.27	889	940	1.06
J-19	14	1.41	0.061	0.264	0.074	0.325	0.399	0.380	0.95	1.17	885	910	1.03
J-20	14	1.41	0.056	0.247	0.074	0.303	0.377	0.370	0.98	1.22	893	940	1.05
J-4	18	1.10	0.045	0.189	0.067	0.234	0.301	0.295	0.98	1.26	1135	1194	1.05
J-9	18	1.10	0.047	0.199	0.083	0.246	0.329	0.310	0.94	1.26	1185	1214	1.02
J-5	18	1.10	0.043	0.184	0.069	0.227	0.296	0.300	1.01	1.32	1146	1184	1.03
J-6	18	1.10	0.042	0.183	0.078	0.225	0.303	0.290	0.96	1.29	1179	1194	1.01
J-21	18	1.10	0.048	0.201	0.089	0.249	0.338	0.300	0.89	1.21	1200	1219	1.01
J-22	18	1.10	0.043	0.184	0.078	0.227	0.305	0.290	0.95	1.28	1179	1204	1.02
							Mean		0.99	1.23			1.03
							Range		0.89-1.05	1.15-132			0.99-1.06

+ b = 6 in.; all others b = 8 in.

* Δ_{fy} is equal to the deflection given by the procedure for yield presented in Section 4.3.

TABLE 10

MOMENTS AND DEFLECTIONS AT YIELD FOR SPECIMENS TESTED IN THIS INVESTIGATION

Mark	Nom. Axial Load P kips	Tens. Steel Ratio p %	Deflection: Due to deformations in Stub Δ_{sy} inches	Beam Δ_{by} inches	Wedge Δ_{iy} inches	(4)+(5) Δ_{fy}* inches	Total: Comp. Δ_y inches	Meas. Δ_u inches	Meas./Comp.	Meas. Δ_y / Δ_{fy}	Moment: Comp. M_y in-kips	Meas. M_y in-kips	Meas./Comp.
(1)	(2)	(3)	(4)	(5)	(6)	(7)	(8)	(9)	(10)	(11)	(12)	(13)	(14)
J-24	0	0.67	0.06	0.33	-0.05	0.39	0.34	0.37	1.09	0.95	182	181	0.99
J-25	25	0.67	0.08	0.38	-0.05	0.46	0.41	0.42	1.02	0.91	290	284	0.98
J-26	50	0.67	0.09	0.43	-0.05	0.52	0.47	0.50	1.06	0.96	392	379	0.97
J-27	75	0.67	0.11	0.48	-0.05	0.59	0.54	0.53	0.98	0.90	482	474	0.98
J-34	75	0.67	0.11	0.52	-0.05	0.63	0.58	0.60	1.03	0.95	460	470	1.02
J-8	0	1.98	0.08	0.35	0.07	0.43	0.50	0.53	1.06	1.17	612	629	1.03
J-16	25	1.98	0.09	0.40	0.07	0.49	0.56	0.57	1.02	1.16	721	711	0.99
J-15	50	1.98	0.10	0.43	0.08	0.53	0.61	0.64	1.05	1.21	833	843	1.01
J-28	0	3.33	0.09	0.42	0.12	0.51	0.63	0.63	1.00	1.24	790	766	0.97
J-29	25	3.33	0.10	0.46	0.13	0.56	0.69	0.71	1.03	1.27	886	920	1.04
J-30	50	3.33	0.11	0.49	0.12	0.60	0.72	0.74	1.03	1.23	979	970	0.99
J-31	75	3.33	0.12	0.53	0.13	0.65	0.78	0.79	1.01	1.22	1064	1072	1.01
							Mean		1.03	1.09			1.00
							Range		0.98-1.09	0.90-1.27			0.97-1.04

* Δ_{fy} is equal to the deflection given by the procedure for yield presented in Section 4.3.

TABLE 11

"MEASURED" θ_{ip} FOR SPECIMENS TESTED BY McCOLLISTER (2)

Mark	Eff. Depth	Tens. Steel Ratio	Depth Neut. Axis	Curvature	Comp. Moment		Deflection						Plast. Elong.	Plast. Strain
					Crush.	Yield	Total Meas.	Due to deformations in						
								Stub	Beam	(9)+(10)	Wedge Crush.	Wedge Yield		
	d	p	c	$\varphi_c \times 10^3$	M_c	M_y	Δ_c	Δ_{sc}	Δ_{bc}	Δ_{fc}	Δ_{ic}	Δ_{iy}	$\theta_{ip}(d-c)$	$\epsilon_s - \epsilon_y$
	in.	%	in.	rad/in.	in-kips		inches						x_p in.	%
(1)	(2)	(3)	(4)	(5)	(6)	(7)	(8)	(9)	(10)	(11)	(12)	(13)	(14)	(15)
S-6	10.72	0.93	1.70	1.98	345	258	1.21	0.36	0.22	0.58	0.63	0.01	0.116	1.63
S-7	10.72	0.62	1.28	2.66	258	175	1.80	0.45	0.23	0.68	1.12	0.01	0.216	2.36
S-8	10.72	0.62	1.49	2.43	219	174	1.22	0.44	0.20	0.64	0.58	0.01	0.109	2.09
T-1	10.58	1.39	1.77	1.93	396	343	1.20	0.37	0.19	0.56	0.64	0.04	0.111	1.56
T-2	10.37	3.21	2.43	1.41	832	805	0.85	0.30	0.22	0.52	0.33	0.13	0.033	0.97
T-3	10.20	5.10	3.60	0.93	1204	1188	0.70	0.21	0.24	0.45	0.25	0.18	0.009	0.47
T-7	10.58	1.39	1.60	2.08	380	336	1.19	0.38	0.18	0.56	0.63	0.04	0.111	1.72
T-10	10.58	1.39	1.85	1.81	387	348	1.09	0.35	0.18	0.53	0.56	0.05	0.093	1.43
T-11	10.58	1.39	1.90	1.75	400	341	1.10	0.34	0.18	0.52	0.58	0.05	0.096	1.37
T-12	10.28	4.11	2.77	1.21	1020	1003	0.77	0.26	0.23	0.49	0.28	0.16	0.019	0.75
T-13	10.37	3.21	2.35	1.40	1032	1004	0.90	0.29	0.25	0.54	0.36	0.23	0.022	0.92
T-14	10.58	1.39	1.70	2.00	370	338	1.00	0.38	0.17	0.55	0.45	0.04	0.076	1.64
T-15	10.58	1.39	1.80	1.92	419	385	1.10	0.37	0.19	0.56	0.54	0.07	0.086	1.52
T-4	10.65	0.97	1.85	1.98	326	276	1.15	0.38	0.21	0.59	0.56	0.04	0.095	1.58
T-5	10.51	1.90	2.75	1.34	533	526	0.72	0.29	0.18	0.47	0.25	0.10	0.027	0.87
T-6	10.37	3.21	5.25	0.71	950	992	---*	0.18	0.28	0.46	---*	0.23	----*	---*
T-8	10.58	1.39	2.05	1.78	407	364	1.00	0.36	0.19	0.55	0.45	0.06	0.069	1.36
T-9	10.72	0.62	1.65	2.18	260	202	1.20	0.41	0.22	0.63	0.57	0.03	0.102	1.80

* Value for Δ_c not reported in Reference 1.

TABLE 12

"MEASURED" θ_{ip} FOR SPECIMENS TESTED BY BURNS (1)

Mark	Eff. Depth	Tens. Steel Ratio	Depth Neut. Axis	Curvature	Comp. Moment		Deflection						Plast. Elong.	Plast. Strain
					Crush.	Yield	Total Meas.	Due to deformations in Stub	Beam	(9)+(10)	Wedge Crush.	Wedge Yield	$\theta_{ip}(d-c)$	
	d	p	c	$\varphi_c \times 10^3$	M_c	M_y	Δ_c	Δ_{sc}	Δ_{bc}	Δ_{fc}	Δ_{ic}	Δ_{iy}	x_p	$\epsilon_s - \epsilon_y$
	in.	%	in.	rad/in.	in-kips		← inches →						in.	%
(1)	(2)	(3)	(4)	(5)	(6)	(7)	(8)	(9)	(10)	(11)	(12)	(13)	(14)	(15)
J-1	10	1.98	2.85	1.14	673	648	1.11	0.29	0.44	0.73	0.38	0.09	0.031	0.66
J-11	10	1.98	3.10	1.09	639	635	1.05	0.30	0.42	0.72	0.33	0.08	0.026	0.59
J-2	10	1.98	2.50	1.36	666	647	1.13	0.28	0.42	0.70	0.43	0.09	0.039	0.85
J-8	10	1.98	2.20	1.50	635	612	1.26	0.27	0.39	0.66	0.60	0.07	0.063	1.01
J-17	10	1.98	2.30	1.49	645	629	1.31	0.27	0.39	0.66	0.65	0.08	0.067	0.98
J-18	10	2.64	2.45	1.36	627	603	1.32	0.28	0.41	0.69	0.63	0.07	0.064	0.87
J-10	14	1.41	3.25	1.06	895	870	1.04	0.30	0.28	0.58	0.46	0.07	0.068	0.99
J-14	14	1.41	2.40	1.39	956	916	1.10	0.27	0.28	0.55	0.55	0.08	0.084	1.45
J-13	14	1.41	2.25	1.46	966	889	1.30	0.27	0.26	0.53	0.77	0.07	0.125	1.55
J-19	14	1.41	3.10	1.10	912	885	0.92	0.30	0.28	0.58	0.34	0.07	0.045	1.04
J-20	14	1.41	2.25	1.49	932	893	1.21	0.27	0.26	0.53	0.68	0.07	0.109	1.59
J-4	18	1.10	2.65	1.24	1204	1135	0.92	0.28	0.20	0.48	0.44	0.07	0.086	1.75
J-9	18	1.10	3.05	1.10	1238	1185	1.00	0.29	0.20	0.49	0.51	0.08	0.097	1.49
J-5	18	1.10	2.40	1.35	1317	1146	1.18	0.28	0.22	0.50	0.68	0.07	0.145	1.95
J-6	18	1.10	2.30	1.40	1364	1179	1.31	0.28	0.22	0.50	0.81	0.08	0.174	2.04
J-21	18	1.10	3.00	1.12	1252	1200	0.97	0.28	0.22	0.50	0.47	0.09	0.086	1.51
J-22	18	1.10	2.35	1.42	1368	1179	1.26	0.27	0.31	0.58	0.68	0.08	0.142	2.06

TABLE 13

"MEASURED" θ_{ip} FOR SPECIMENS TESTED IN THIS INVESTIGATION

Mark	Nom. Axial Load	Tens. Steel Ratio	Depth Neut. Axis	Curvature	Comp. Moment		Deflection						Plast. Elong.	Plast. Strain
					Crush.	Yield	Total Meas.	Due to deformations in						
								Stub	Beam	(9)+(10)	Wedge			
											Crush.	Yield		
	d	p	c	$\varphi_c \times 10^3$	M_c	M_y	Δ_c	Δ_{sc}	Δ_{bc}	Δ_{fc}	Δ_{ic}	Δ_{iy}	$\theta_{ip}(d-c)$	$\epsilon_s - \epsilon_y$
	in.	%	in.	rad/in.	in-kips		← inches →						x_p in.	%
(1)	(2)	(3)	(4)	(5)	(6)	(7)	(8)	(9)	(10)	(11)	(12)	(13)	(14)	(15)
J-24	0	0.67	1.55	2.08	204	182	1.70	0.51	0.36	0.87	0.83	-0.05	0.112	1.59
J-25	25	0.67	2.15	1.55	310	790	1.18	0.41	0.41	0.82	0.36	-0.05	0.049	1.05
J-26	50	0.67	2.85	1.14	406	392	0.95	0.33	0.45	0.78	0.17	-0.05	0.024	0.65
J-27	75	0.67	3.75	0.84	486	482	0.86	0.26	0.49	0.75	0.11	-0.05	0.015	0.36
J-34	75	0.67	3.95	0.84	474	460	0.74	0.26	0.52	0.78	-0.04	-0.05	0.009	0.34
J-15	50	1.98	3.17	1.05	832	833	1.10	0.31	0.44	0.75	0.35	0.08	0.028	0.56
J-16	25	1.98	2.65	1.25	728	721	1.26	0.32	0.45	0.77	0.49	0.07	0.047	0.76
J-28	0	3.33	2.65	1.21	800	791	1.20	0.34	0.44	0.78	0.42	0.12	0.033	0.73
J-29	25	3.33	3.00	1.06	896	886	1.02	0.31	0.46	0.77	0.25	0.13	0.014	0.58
J-30	50	3.33	3.50	0.92	990	979	1.09	0.28	0.49	0.77	0.32	0.12	0.020	0.44
J-31	75	3.33	4.00	0.80	1076	1064	1.06	0.25	0.54	0.79	0.27	0.13	0.013	0.32

TABLE 14

MOMENTS AND DEFLECTIONS AT CRUSHING FOR SPECIMENS TESTED BY McCOLLISTER (2)

Mark	Eff. Depth	Tens. Steel Ratio	Deflection: Due to deformations in Stub	Beam	Wedge	(4)+(5)	Deflection: Total Comp.	Meas.	Meas./Comp.	Meas. Δ_c / Δ_{fc}	Moment: Comp.	Meas.	Meas./Comp.
	d	p	Δ_{sc}	Δ_{bc}	Δ_{ic}	Δ_{fc}*	Δ_c	Δ_c			M_c	M_c	
	in.	%	inches								in - kips		
(1)	(2)	(3)	(4)	(5)	(6)	(7)	(8)	(9)	(10)	(11)	(12)	(13)	(14)
S-6	10.72	0.93	0.36	0.22	0.67	0.58	1.25	1.21	0.97	2.08	345	312	0.90
S-7	10.72	0.62	0.45	0.23	1.01	0.68	1.69	1.80	1.06	2.64	258	224	0.87
S-8	10.72	0.62	0.44	0.20	0.83	0.64	1.47	1.22	0.83	1.91	219	223	1.02
T-1	10.58	1.39	0.36	0.19	0.56	0.55	1.11	1.20	1.08	2.18	396	388	0.97
T-2	10.37	3.21	0.29	0.22	0.40	0.51	0.91	0.85	0.93	1.67	832	831	1.00
T-3	10.20	5.10	0.21	0.24	0.29	0.45	0.74	0.70	0.95	1.56	1204	1211	1.01
T-7	10.58	1.39	0.38	0.17	0.64	0.55	1.19	1.19	1.00	2.16	380	388	1.02
T-10	10.58	1.39	0.34	0.18	0.52	0.52	1.08	1.09	1.01	2.10	387	415	1.07
T-11	10.58	1.39	0.33	0.18	0.48	0.51	0.99	1.10	1.11	2.16	400	428	1.07
T-12	10.28	4.11	0.25	0.23	0.35	0.48	0.83	0.77	0.93	1.60	1020	1078	1.06
T-13	10.37	3.21	0.28	0.25	0.41	0.53	0.94	0.90	0.96	1.70	1032	1079	1.04
T-14	10.58	1.39	0.37	0.17	0.60	0.54	1.14	1.00	0.88	1.85	370	393	1.06
T-15	10.58	1.39	0.36	0.19	0.57	0.55	1.12	1.10	0.98	2.00	419	428	1.02
T-4	10.65	0.97	0.37	0.21	0.57	0.58	1.15	1.15	1.00	1.72	326	308	0.94
T-5	10.51	1.90	0.28	0.18	0.31	0.46	0.77	0.72	0.94	2.04	533	545	1.02
T-6	10.37	3.21	0.17	0.28	0.26	0.45	0.71	0.63**	0.89	1.40	950	881	0.93
T-8	10.58	1.39	0.35	0.19	0.50	0.54	1.04	1.00	0.96	1.78	407	388	0.95
T-9	10.72	0.62	0.40	0.22	0.68	0.62	1.30	1.20	0.92	1.48	260	259	1.00
							Mean		0.97	1.92			1.00
							Range		0.83-1.11	1.48-2.64			0.87-1.07

* Δ_{fc} is equal to the deflection given by the procedure presented in Section 4.3.

** No value reported in Reference 4. This value was taken equal to the deflection at yield.

TABLE 15

MOMENTS AND DEFLECTIONS AT CRUSHING FOR SPECIMENS TESTED BY BURNS (1)

Mark	Eff. Depth	Tens. Steel Ratio	Deflection: Due to deformations in Stub	Beam	Wedge	(4)+(5)	Deflection: Total Comp.	Meas.	Meas./Comp.	Meas. Δ_c / Δ_{fc}	Moment: Comp.	Meas.	Meas./Comp.
	d	p	Δ_{sc}	Δ_{bc}	Δ_{ic}	Δ_{fc}*	Δ_c	Δ_c			M_c	M_c	
	in.	%	inches								in - kips		
(1)	(2)	(3)	(4)	(5)	(6)	(7)	(8)	(9)	(10)	(11)	(12)	(13)	(14)
J-1	10	1.98	0.29	0.44	0.29	0.73	1.02	1.11	1.09	1.52	673	729	1.08
J-11	10	1.98	0.30	0.42	0.28	0.72	1.00	1.05	1.05	1.46	639	651	1.02
J-2	10	1.98	0.28	0.42	0.41	0.70	1.11	1.13	1.02	1.61	666	730	1.09
J-8	10	1.98	0.27	0.39	0.48	0.66	1.14	1.26	1.10	1.91	635	652	1.03
J-17	10	1.98	0.27	0.39	0.48	0.66	1.14	1.31	1.15	1.98	645	652	1.01
J-18+	10	2.64	0.28	0.41	0.40	0.69	1.09	1.32	1.21	1.91	627	630	1.00
J-10	14	1.41	0.30	0.28	0.35	0.58	0.93	1.04	1.12	1.79	895	958	1.07
J-14	14	1.41	0.27	0.28	0.56	0.55	1.11	1.10	0.99	2.00	956	1002	1.05
J-13	14	1.41	0.27	0.26	0.61	0.53	1.14	1.30	1.14	2.45	966	988	1.02
J-19	14	1.41	0.30	0.28	0.37	0.58	0.95	0.92	0.97	1.59	912	937	1.03
J-20	14	1.41	0.27	0.26	0.63	0.53	1.16	1.21	1.04	2.28	932	950	1.02
J-4	18	1.10	0.28	0.20	0.57	0.48	1.05	0.92	0.88	1.92	1204	1289	1.07
J-9	18	1.10	0.29	0.20	0.48	0.49	0.97	1.00	1.03	2.04	1238	1327	1.07
J-5	18	1.10	0.28	0.22	0.67	0.50	1.17	1.18	1.01	2.36	1317	1359	1.03
J-6	18	1.10	0.28	0.22	0.72	0.50	1.22	1.31	1.07	2.62	1364	1339	0.98
J-21	18	1.10	0.28	0.22	0.49	0.50	0.99	0.97	0.98	1.94	1252	1260	1.01
J-22	18	1.10	0.27	0.31	0.74	0.58	1.32	1.26	0.95	2.17	1368	1350	0.99
							Mean		1.05	1.97			1.03
							Range		0.88-1.21	1.46-2.62			0.98-1.09

+ b = 6 in.; all others b = 8 in.

* Δ_{fc} is the deflection given by the procedure for crushing presented in Section 4.3.

TABLE 16

MOMENTS AND DEFLECTIONS AT CRUSHING FOR SPECIMENS TESTED IN THIS INVESTIGATION

Mark	Nom. Axial Load	Tens. Steel Ratio	Deflections								Moment		
			Due to deformations in				Total						
			Stub	Beam	Wedge	(4)+(5)	Comp.	Meas.	Meas. / Comp.	Meas. Δ_c / Δ_{fc}	Comp.	Meas.	Meas. / Comp.
	P	p	Δ_{sc}	Δ_{bc}	Δ_{ic}	Δ_{fc}*	Δ_c	Δ_c			M_c	M_c	
	kips	%	inches								in - kips		
(1)	(2)	(3)	(4)	(5)	(6)	(7)	(8)	(9)	(10)	(11)	(12)	(13)	(14)
J-24	0	0.67	0.51	0.36	0.72	0.87	1.59	1.70	1.07	1.95	204	223	1.09
J-25	25	0.67	0.41	0.41	0.39	0.82	1.21	1.18	0.98	1.44	310	318	1.03
J-26	50	0.67	0.33	0.45	0.17	0.78	0.95	0.95	1.00	1.22	406	410	1.01
J-27	75	0.67	0.26	0.49	0.05	0.75	0.80	0.86	1.08	1.15	486	491	1.01
J-34	75	0.67	0.26	0.52	0.05	0.78	0.83	0.74	0.89	1.14	474	474	1.00
J-8	0	1.98	0.27	0.39	0.48	0.66	1.14	1.26	1.10	1.91	635	652	1.03
J-16	25	1.98	0.32	0.45	0.34	0.77	1.11	1.26	1.13	1.64	728	738	1.01
J-15	50	1.98	0.31	0.44	0.20	0.75	0.95	1.10	1.16	1.47	832	855	1.03
J-28	0	3.33	0.34	0.44	0.38	0.78	1.16	1.20	1.03	1.32	800	797	1.00
J-29	25	3.33	0.31	0.46	0.32	0.77	1.09	1.02	0.94	1.22	896	919	1.03
J-30	50	3.33	0.28	0.49	0.27	0.77	1.04	1.09	1.05	1.36	990	987	1.00
J-31	75	3.33	0.25	0.54	0.23	0.79	1.02	1.06	1.04	1.32	1076	1074	1.00
							Mean		1.03	1.38			1.02
							Range		0.89-1.16	1.14-1.95			1.00-1.09

* Δ_{fc} is equal to the deflection given by the procedure for crushing presented in Section 4.3.

TABLE 17

MOMENTS AND DEFLECTIONS AT ULTIMATE FOR BEAMS TESTESTED BY BURNS (1)

Mark	Eff. Depth	Steel Ratio	Depth Neut. Axis	Curvature	Strain Tens. Steel	Deflection: Due to deformations in Stub	Beam	Wedge	Total Comp.	Total Meas.	Meas./Comp.	Moment: Comp.	Meas.	Meas./Comp.	Mode of Failure**
	d	p	c	$\varphi_u \times 10^3$	ϵ_s	Δ_{su}	Δ_{bu}	Δ_{iu}	Δ_u	Δ_u		M_u	M_u		
	in.	%	in.	rad/in	%	← inches →						in - kips			
(1)	(2)	(3)	(4)	(5)	(6)	(7)	(8)	(9)	(10)	(11)	(12)	(13)	(14)	(15)	(16)
J-1	10	1.98	2.95	3.4	1.9	1.0	2.5	1.3	4.8	4.8	1.00	663	671	1.01	C
J-11	10	1.98	2.75	3.2	1.8	1.0	1.4	1.2	3.6	4.8	1.33	560	561	1.00	C
J-2	10	1.98	2.15	7.4	4.6	2.1	5.3	3.0	10.4	9.5	0.91	865	835	0.97	C
J-8	10	1.98	1.97	15.2	10.0	4.1	10.8	6.6	21.5	17.0	0.79	847	799	0.94	S+
J-17	10	1.98	2.10	14.3	9.2	4.0	9.2	6.1	19.3	18.2	0.94	871	811	0.93	SC+
J-18*	10	2.64	2.33	12.9	7.9	3.7	8.5	5.2	17.4	15.7	0.90	847	797	0.94	SC+
J-10	14	1.41	3.65	3.2	2.9	1.0	2.4	1.9	5.3	6.1	1.15	891	858	0.96	C
J-14	14	1.41	2.60	6.2	6.0	1.8	5.0	4.0	10.8	12.1	1.12	1195	1178	0.99	C
J-13	14	1.41	2.23	13.5	13.7	3.9	9.5	9.0	22.4	16.0	0.71	1333	1265	0.95	S+
J-19	14	1.41	3.60	2.7	2.4	0.8	1.8	1.6	4.2	5.3	1.26	868	852	0.98	C
J-21	14	1.41	2.09	14.4	14.9	4.0	10.5	9.8	24.3	10.9	0.45	1318	1125	0.85	S+
J-4	18	1.10	3.21	3.7	4.9	1.1	3.0	3.2	7.3	7.8	1.07	1425	1353	0.95	C
J-9	18	1.10	3.70	3.2	4.2	1.0	2.8	2.8	6.6	7.4	1.12	1410	1233	0.88	C
J-5	18	1.10	2.54	6.3	8.7	1.9	4.7	5.8	12.4	12.8	1.03	1700	1637	0.96	T
J-6	18	1.10	1.60	8.8	13.1	2.2	5.9	8.7	16.8	10.0	0.60	1813	1582	0.87	S
J-21	18	1.10	3.96	3.0	3.8	1.0	2.3	2.5	5.8	4.5	0.78	1315	1239	0.94	C
J-22	18	1.10	2.20	9.1	12.7	2.6	6.3	8.4	17.3	7.4	0.43	1800	1500	0.83	S
										Mean	1.05++			0.96++	
										Range	0.78-1.33++			0.88-1.01++	

* b = 6 in., all others b = 8 in.

** C = compression failure; S = shear failure; SC = difficult to tell whether failure was in compression or in shear; T = tension failure.

\+ Computed quantities correspond to buckling of compression bars. All others correspond to absolute maximum of M-φ curve.

++ C and SC only.

TABLE 18

MOMENTS AND DEFLECTIONS AT ULTIMATE FOR SPECIMENS TESTED IN THIS INVESTIGATION

Mark	Nom. Axial Load	Steel Ratio	Depth Neut. Axis	Curvature	Strain Tens. Steel	Deflection: Due to deformations in Stub	Beam	Wedge	Deflection: Total Comp.	Total Meas.	Meas./Comp.	Moment: Comp.	Moment: Meas.	Meas./Comp.	Mode of Failure**
	P	p=p'	c	$\varphi_u \times 10^3$	ϵ_s	Δ_{su}	Δ_{bu}	Δ_{iu}	Δ_u	Δ_u		M_u	M_u		
	kips	%	in.	rad/in	%	← inch →			← inch →			in - kips			
(1)	(2)	(3)	(4)	(5)	(6)	(7)	(8)	(9)	(10)	(11)	(12)	(13)	(14)	(15)	(16)
J-24	0	0.67	0.50	17.5	13.6	2.5	13.6	9.0	25.1	17.0	0.68	260	233	0.90	T
J-25	25	0.67	1.40	9.0	6.2	2.2	6.3	4.1	12.6	13.0	1.03	320	287	0.90	C
J-26	50	0.67	2.30	5.0	3.0	1.4	2.8	2.0	6.2	7.5	1.21	352	379	1.08	C
J-27	75	0.67	3.20	1.5	0.8	0.5	0.7	0.5	1.7	----	----	385	---	----	C
J-34*	75	0.67	2.78	2.9	1.6	0.9	1.2	1.0	3.1	3.8	1.23	385	373	0.97	C
J-8+	0	1.98	1.97	15.2	10.0	4.1	10.8	6.6	21.5	17.0	0.79	847	799	0.94	S++
J-16+	25	1.98	2.98	10.1	5.6	3.1	6.5	3.7	13.3	13.6	1.02	858	845	0.98	C++
J-15+	50	1.98	3.94	7.6	3.5	2.5	4.7	2.3	9.5	10.9	1.15	840	909	1.08	C++
J-28	0	3.33	2.80	14.0	8.2	4.2	12.5	5.4	22.1	13.5	0.61	1180	1030	0.87	S++
J-29	25	3.33	3.72	11.0	5.2	3.6	9.1	3.4	16.1	11.2	0.70	1150	1095	0.95	C++
J-30	50	3.33	4.60	8.8	3.4	2.9	6.3	2.2	11.4	12.9	1.13	1100	1120	1.02	C++
J-31	75	3.33	5.50	7.2	2.3	2.5	2.8	1.5	6.8	7.3	1.07	1030	1030	1.00	C++
									Mean		1.07+++			1.00+++	
									Range		0.70-1.23+++			0.90-1.08+++	

* #3 ties at 3-in. centers; all others #3 at 6 in.; see Fig. 2.2.

** T = tension failure, C = compression failure., S = shear failure.

\+ b = 8 in., all others b = 6 in.

++ Computed quantities correspond to buckling of compression bars; all other correspond to absolute maximum of M-φ curve.

+++ Compression failures only.

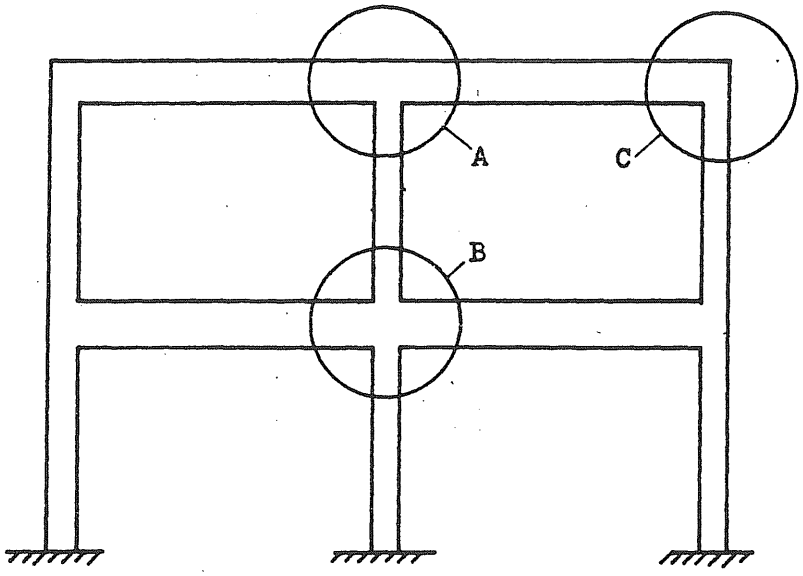

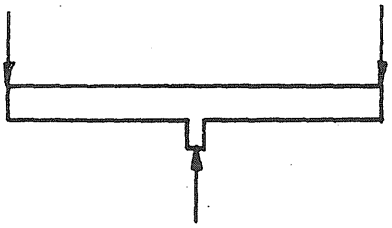

Type A

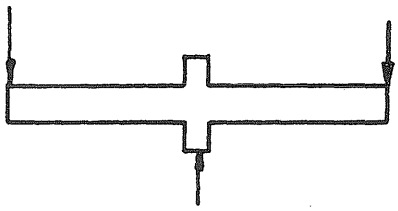

Type B_1

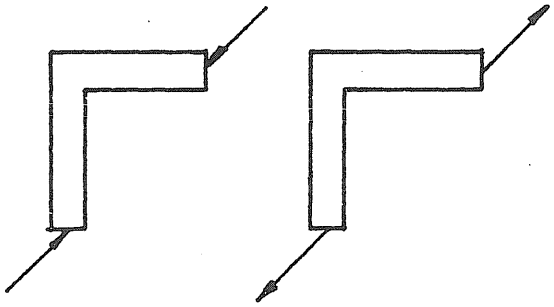

Type C

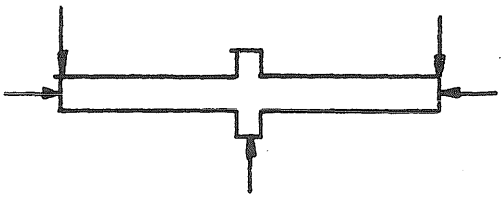

Type B_2

FIG. 1.1 BASIC TYPES OF CONNECTIONS IN RECTANGULAR FRAMES

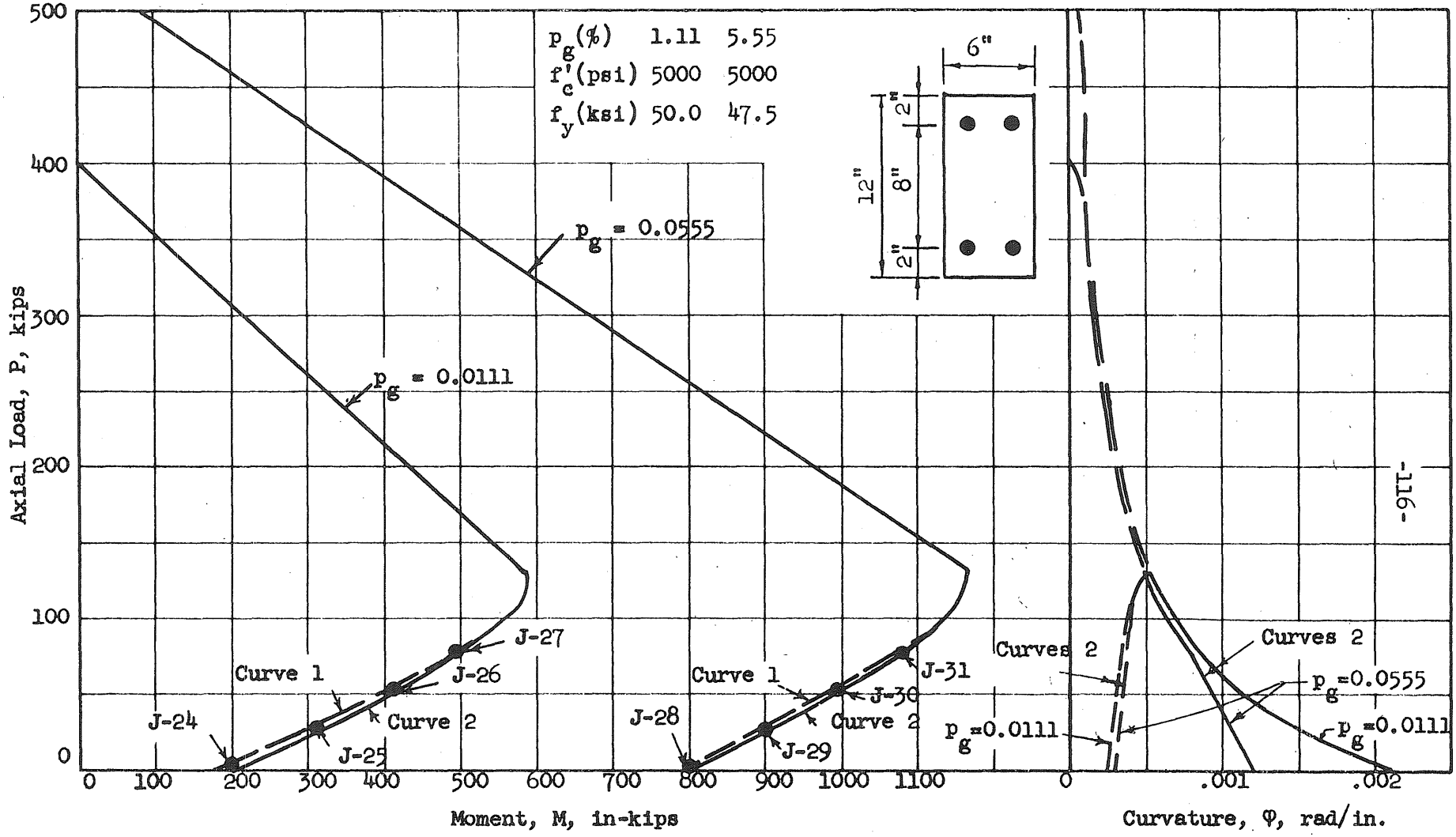

FIG. 2.1 INTERACTION CURVES

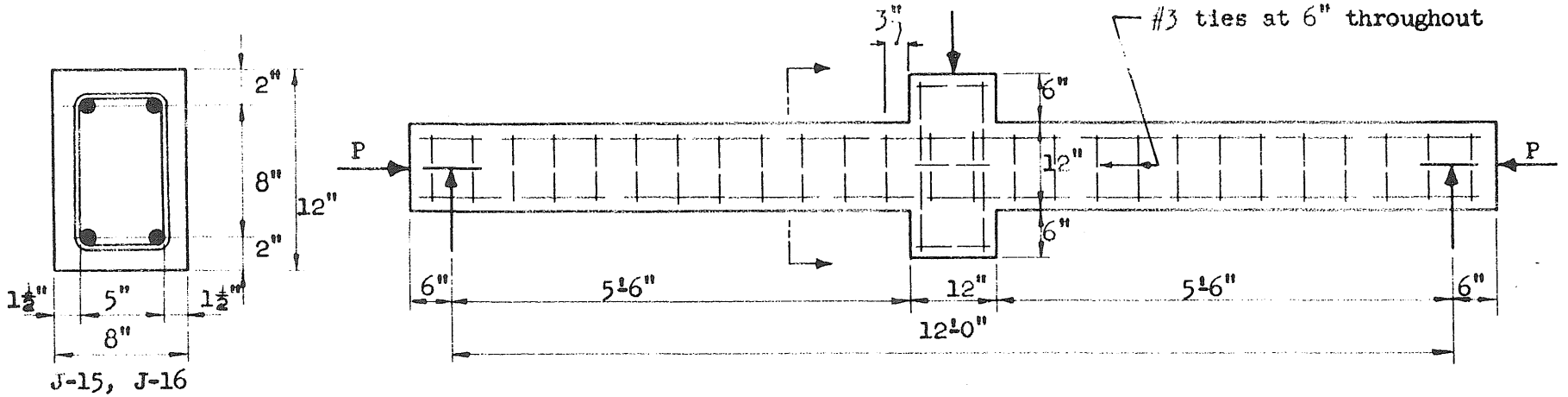

J-15, J-16

(a) Specimens J-15, J-16, J-24 through J-31

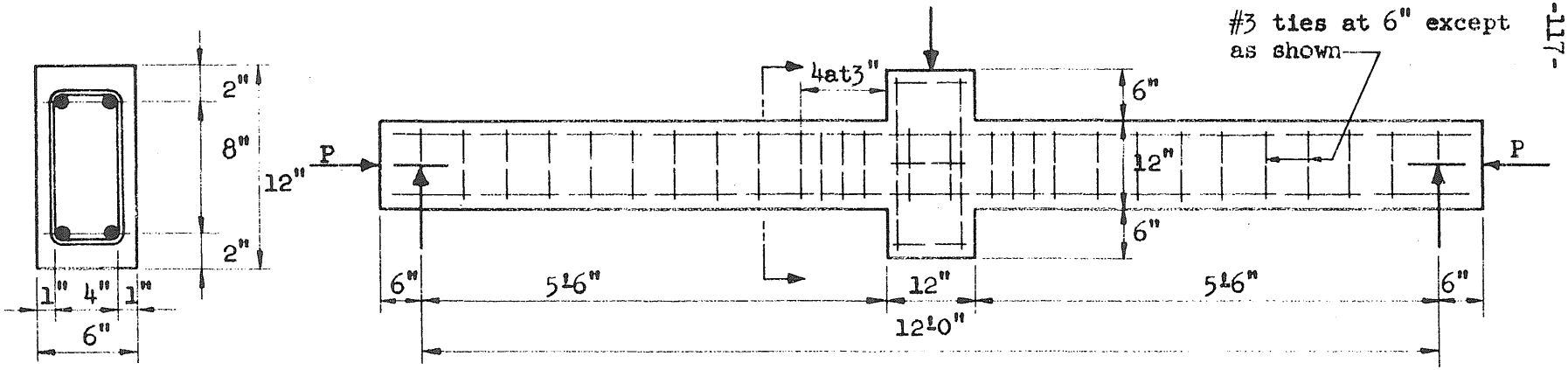

J-24 through J-31, and J-34

(b) Specimen J-34

Additional information on the properties of test specimens is given in Table 1.

FIG. 2.2 TEST SPECIMENS

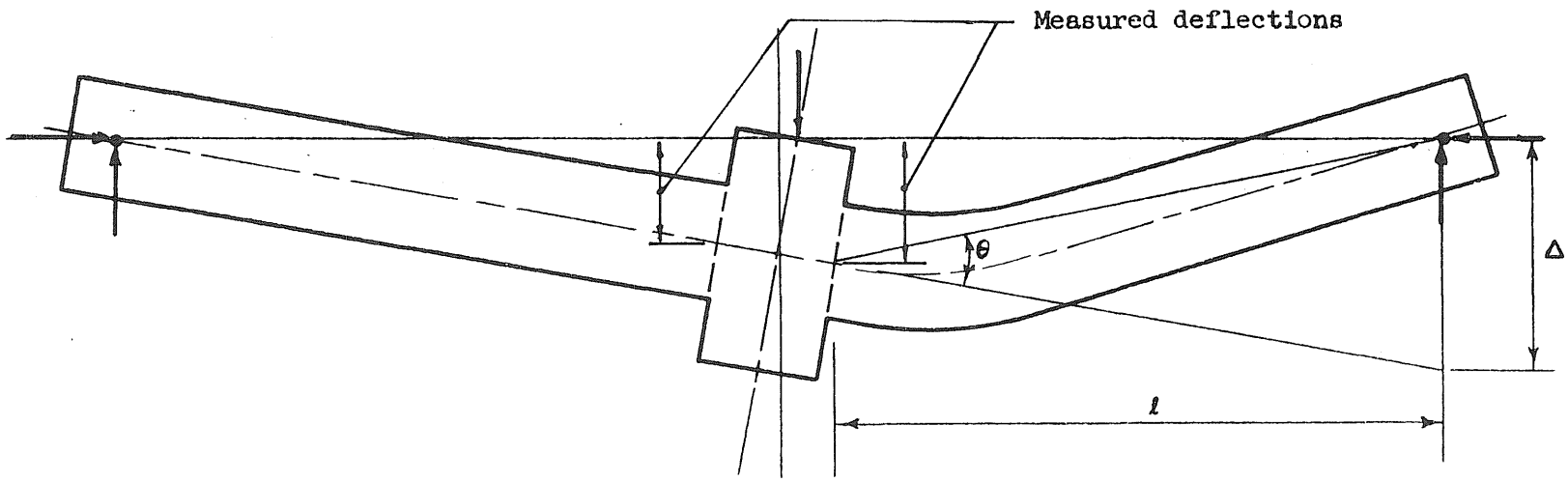

FIG. 3.1 EQUIVALENT MIDSPAN DEFLECTION

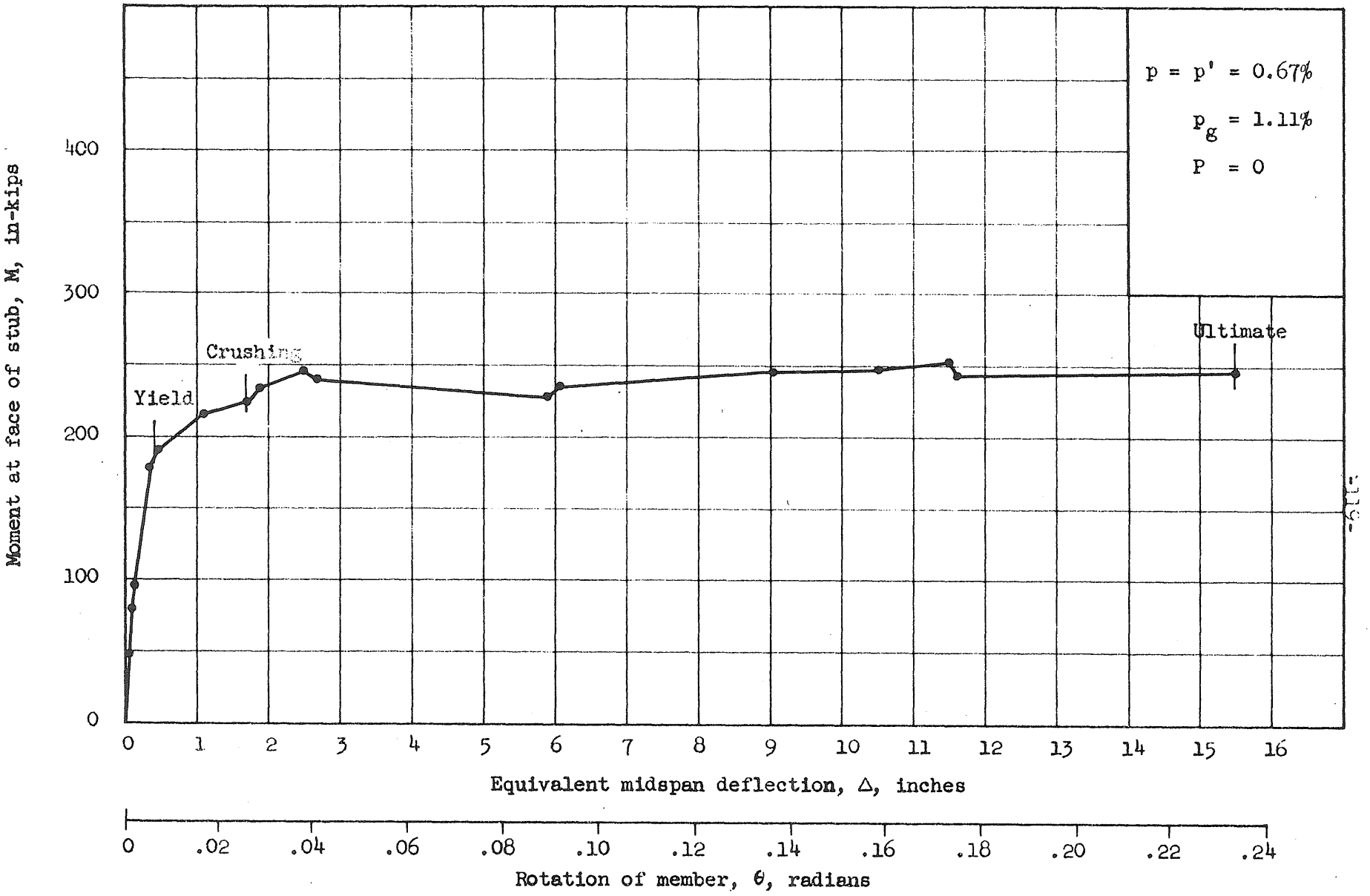

FIG. 3.2 MOMENT VERSUS ROTATION FOR SPECIMEN J-24

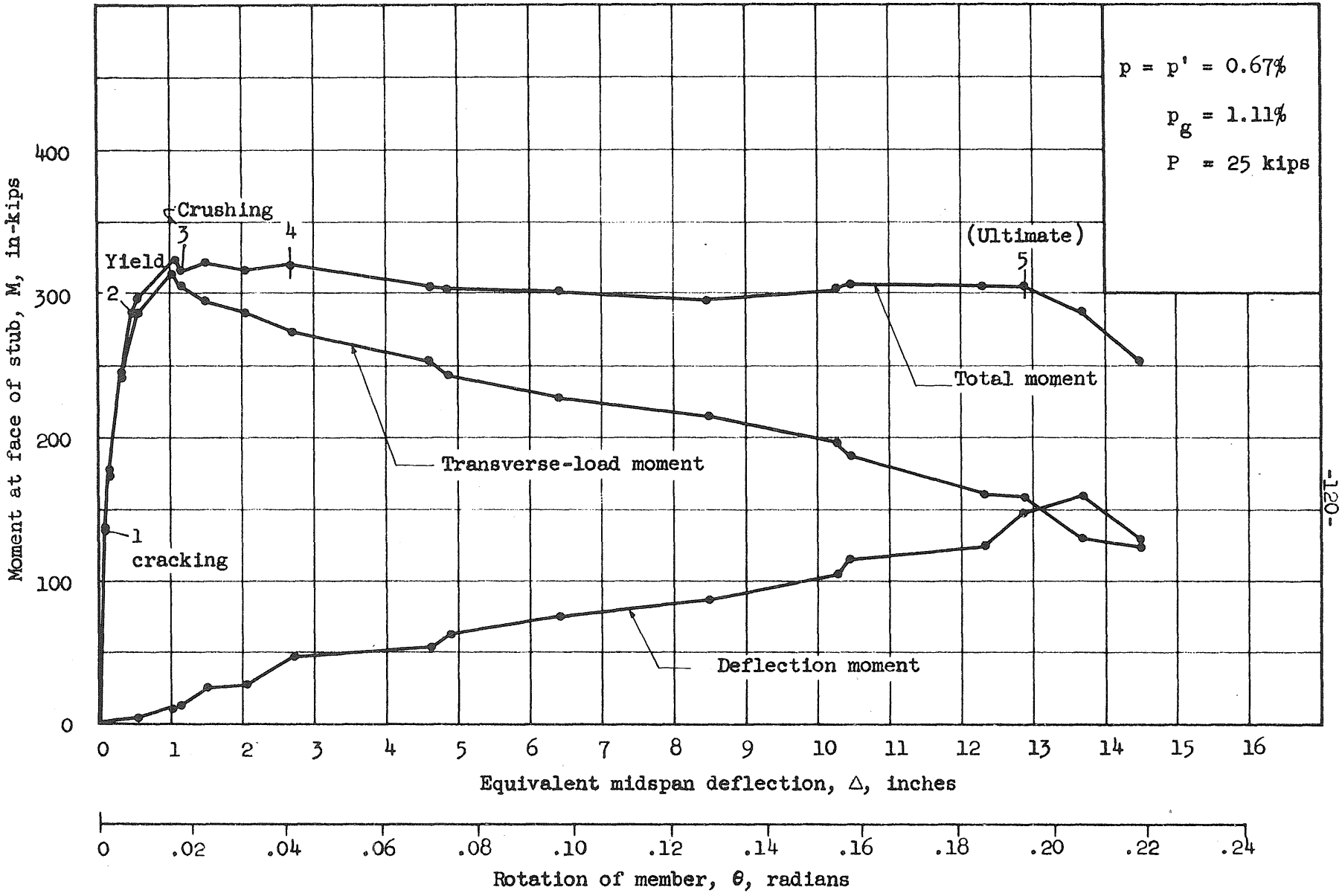

FIG. 3.3 MOMENT VERSUS ROTATION FOR SPECIMEN J-25

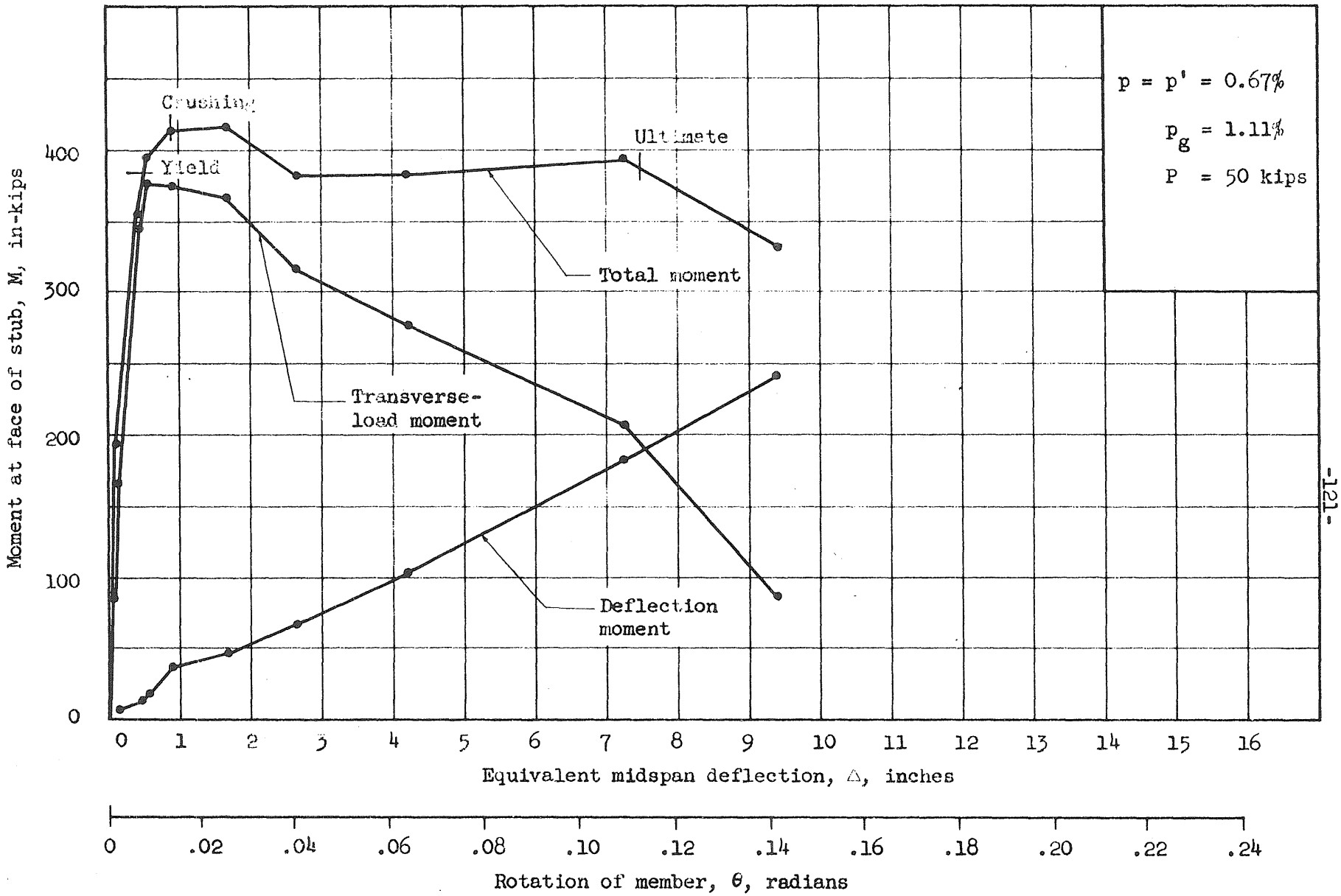

FIG. 3.4 MOMENT VERSUS ROTATION FOR SPECIMEN J-26

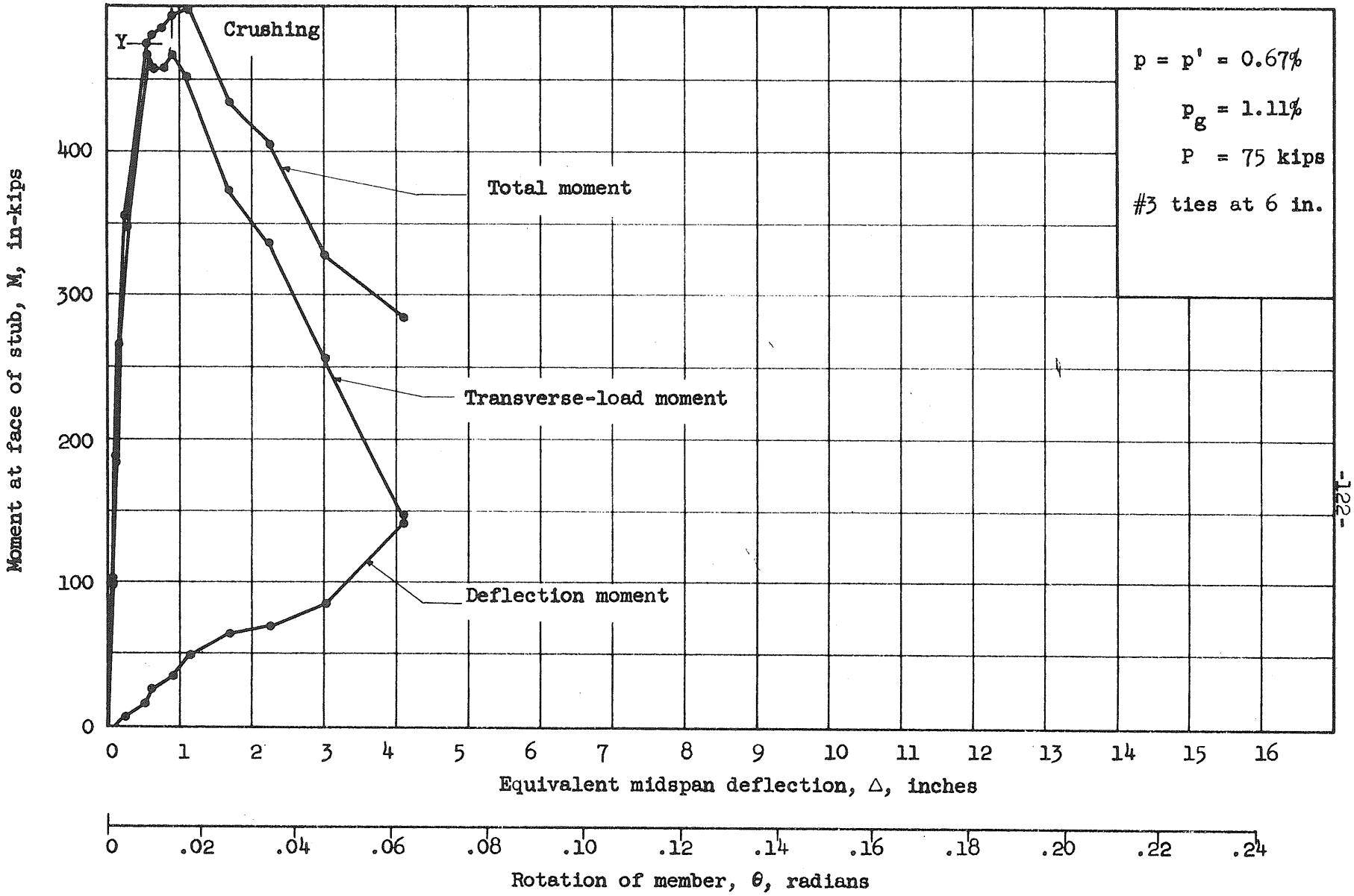

FIG. 3.5 MOMENT VERSUS ROTATION FOR SPECIMEN J-27

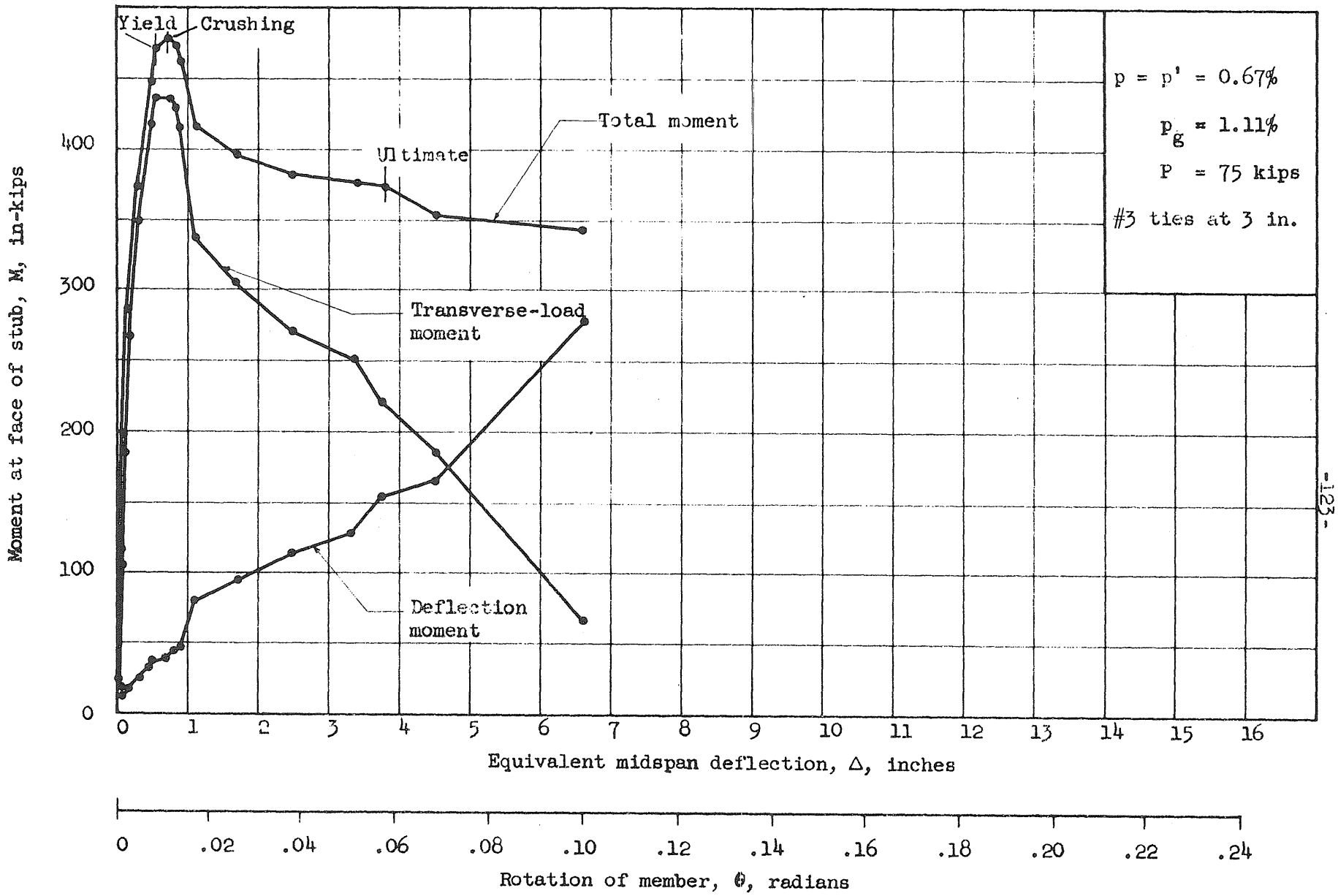

FIG. 3.6 MOMENT VERSUS ROTATION FOR SPECIMEN J-34

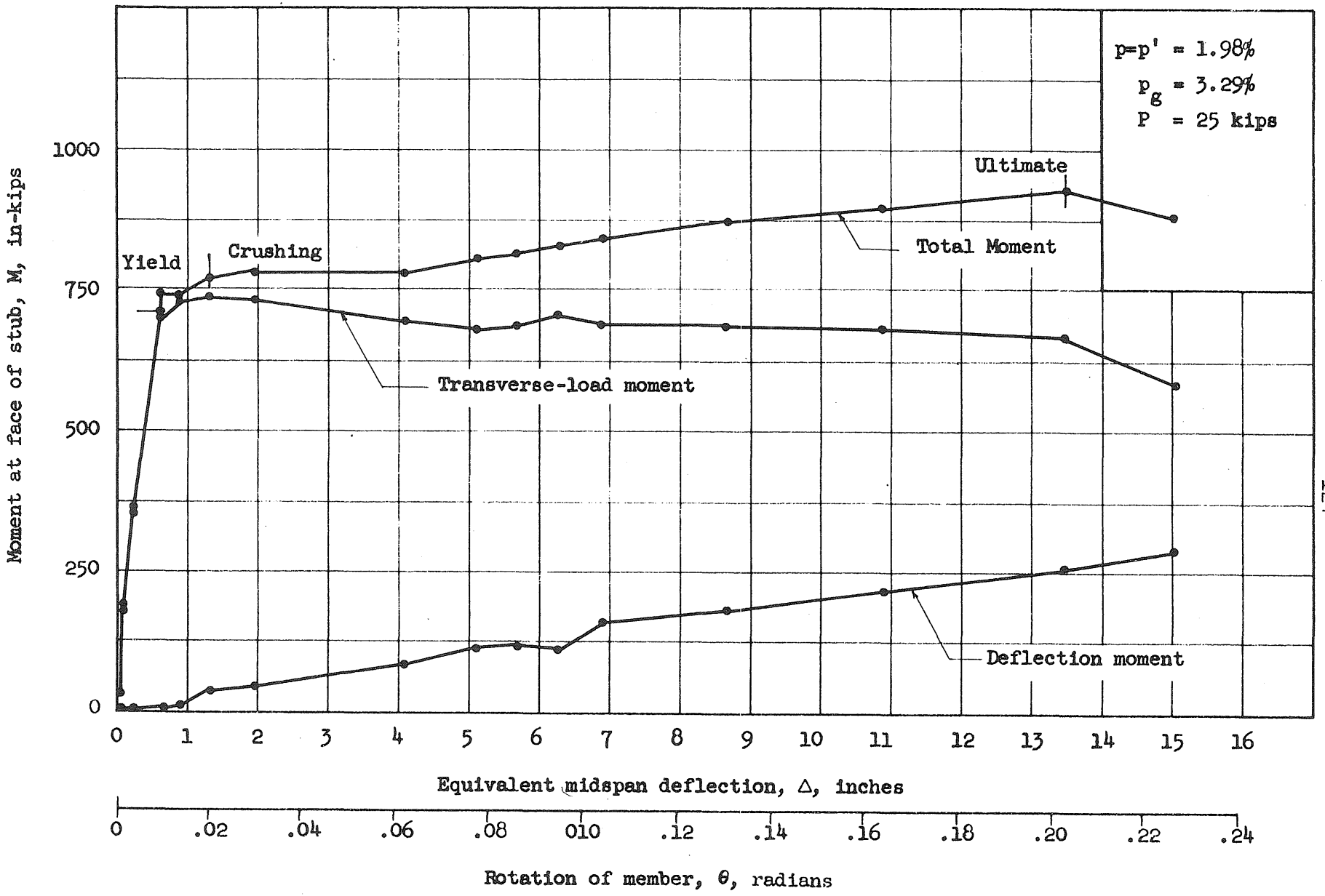

FIG. 3.7 MOMENT VERSUS ROTATION FOR SPECIMEN J-16

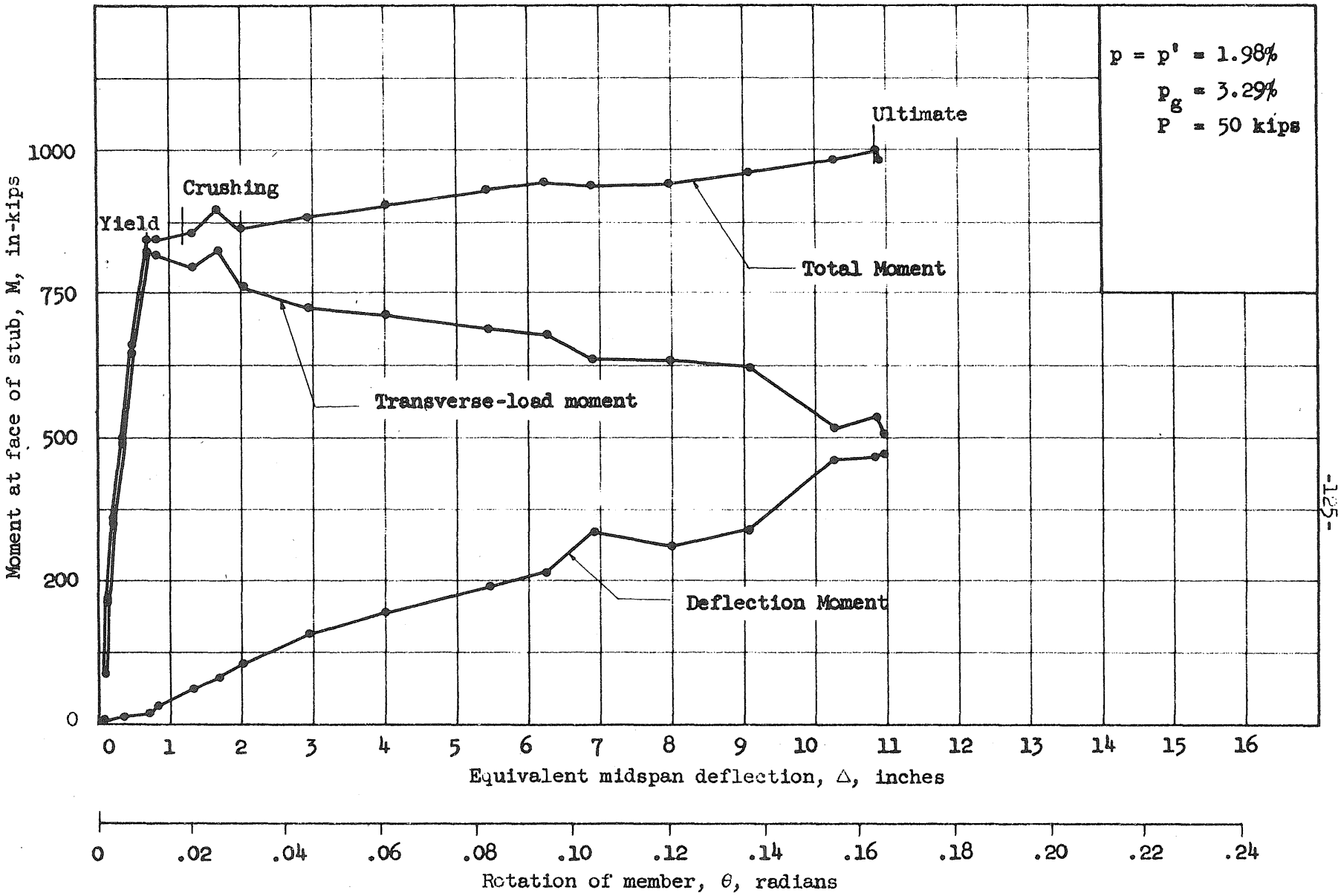

FIG. 3.8 MOMENT VERSUS ROTATION FOR SPECIMEN J-15

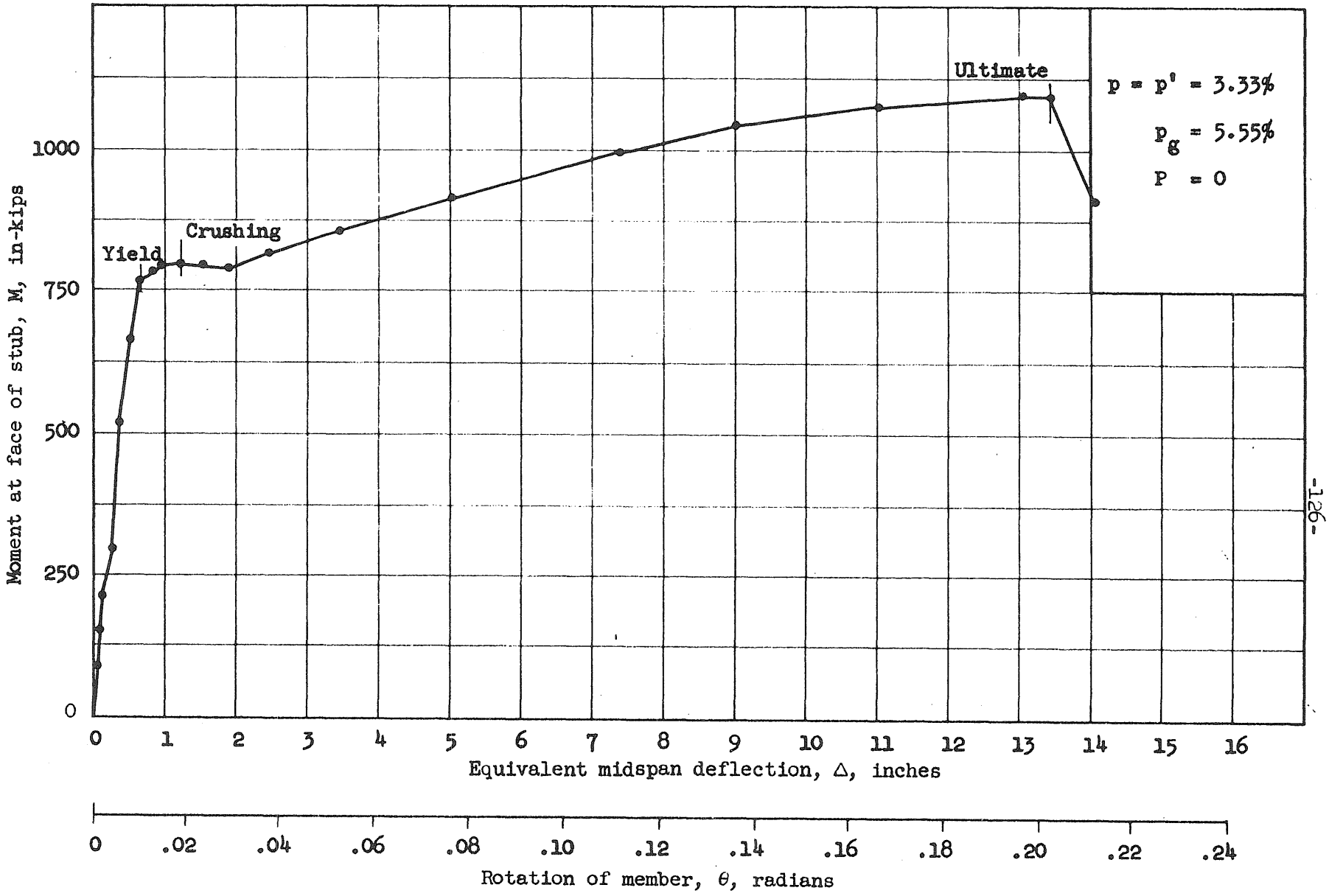

FIG. 3.9 MOMENT VERSUS ROTATION FOR SPECIMEN J-28

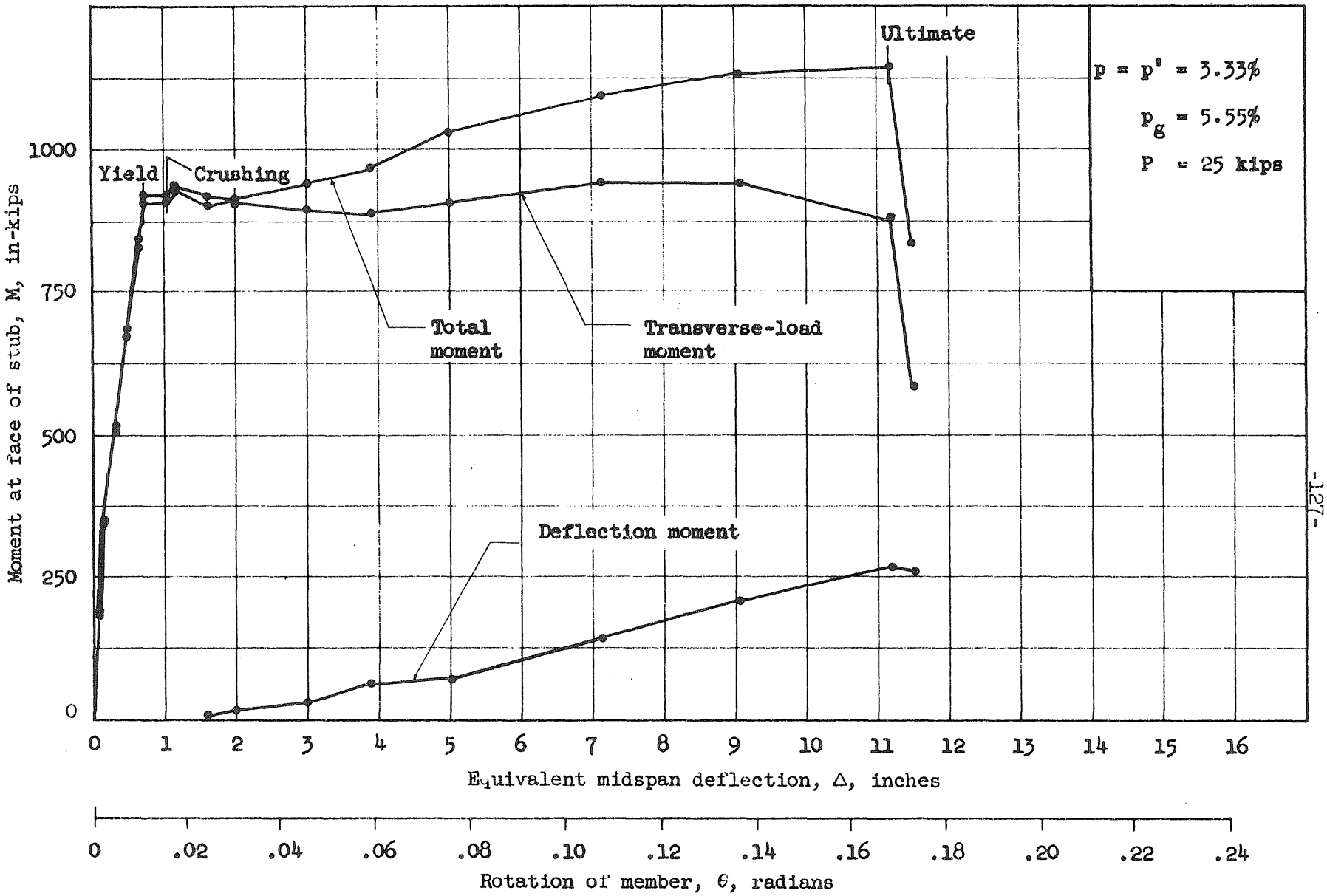

FIG. 3.10 MOMENT VERSUS ROTATION FOR SPECIMEN J-29

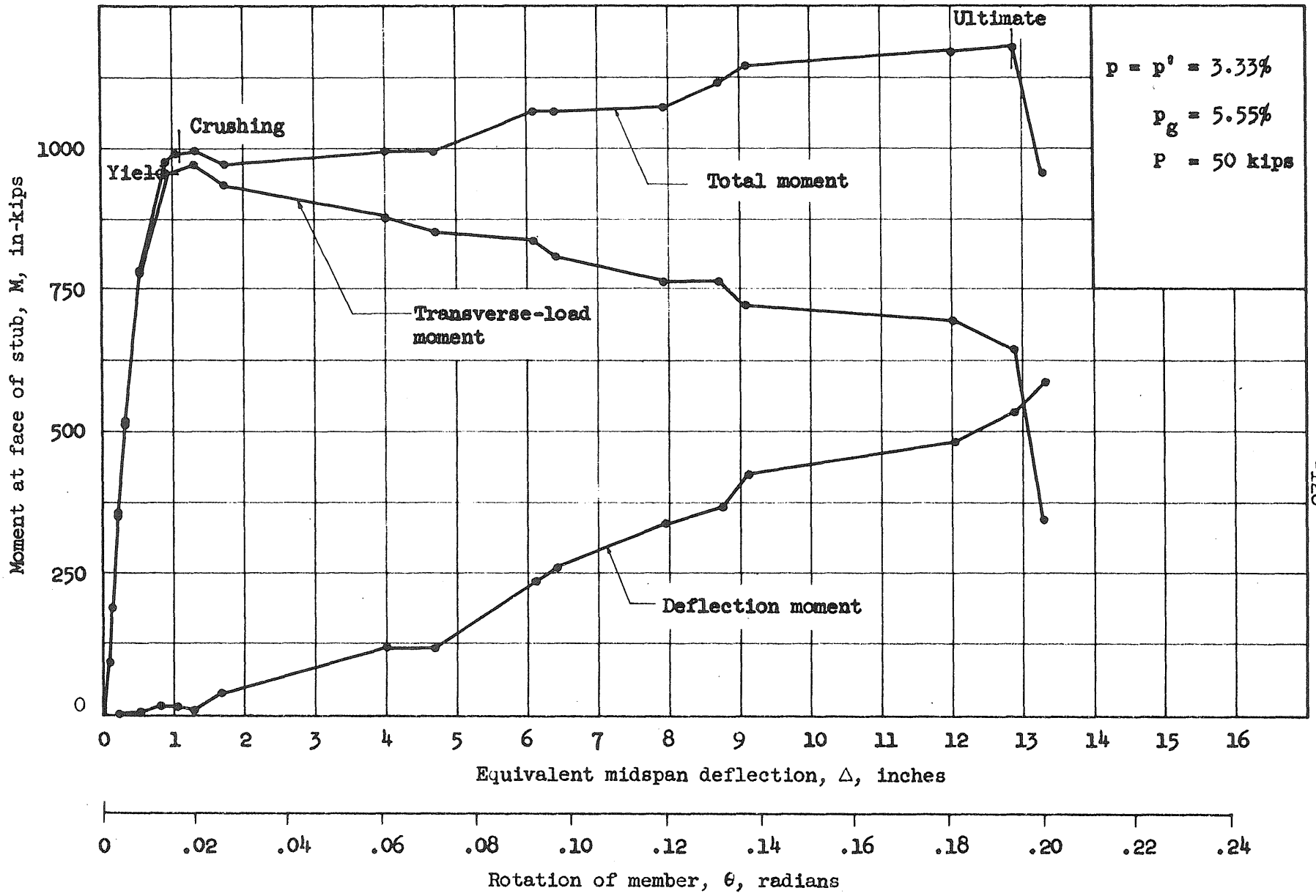

FIG. 3.11 MOMENT VERSUS ROTATION FOR SPECIMEN J-30

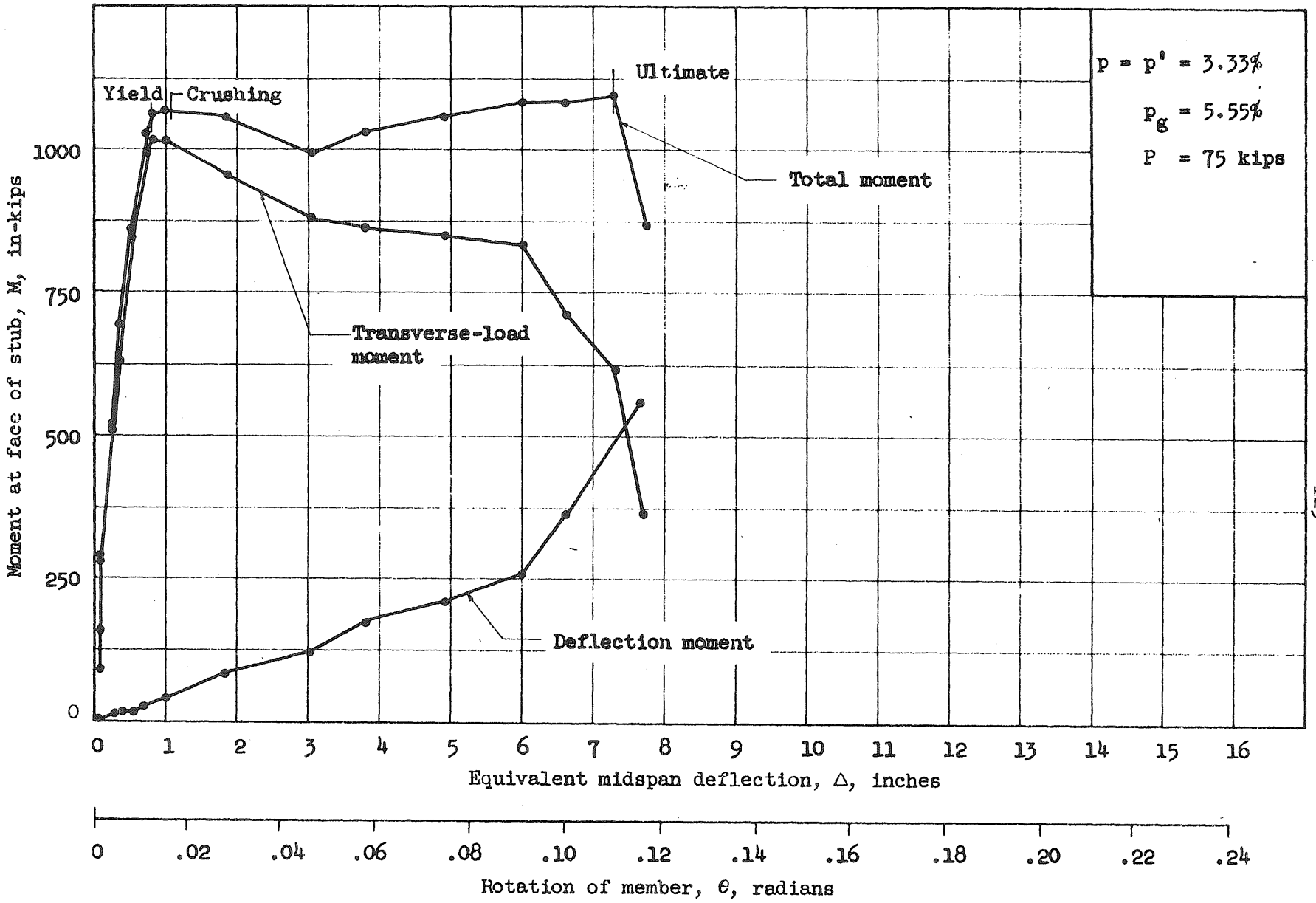

FIG. 3.12 MOMENT VERSUS ROTATION FOR SPECIMEN J-31

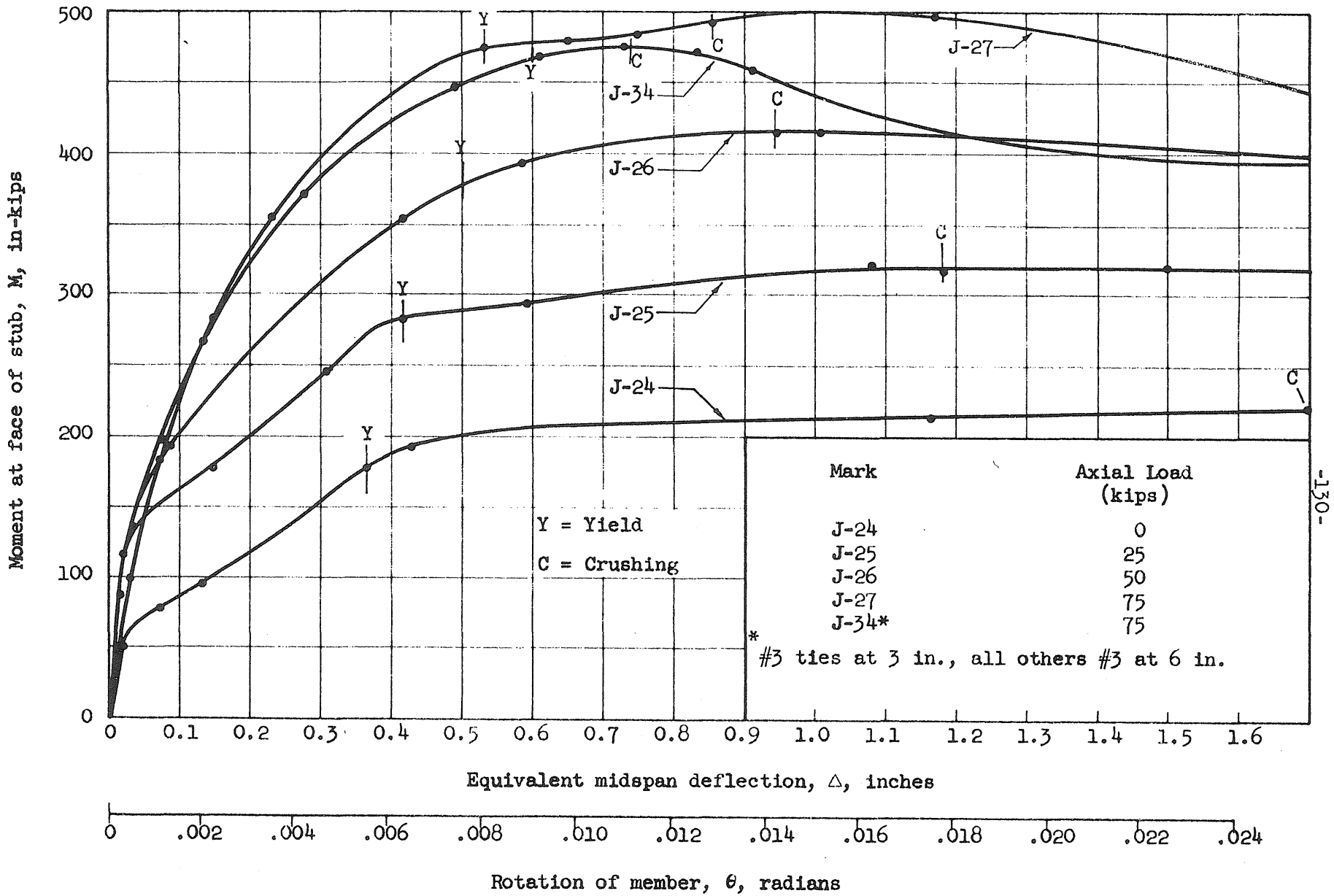

FIG. 3.13 MOMENT VERSUS ROTATION, p_g = 1.11% (enlarged rotation scale)

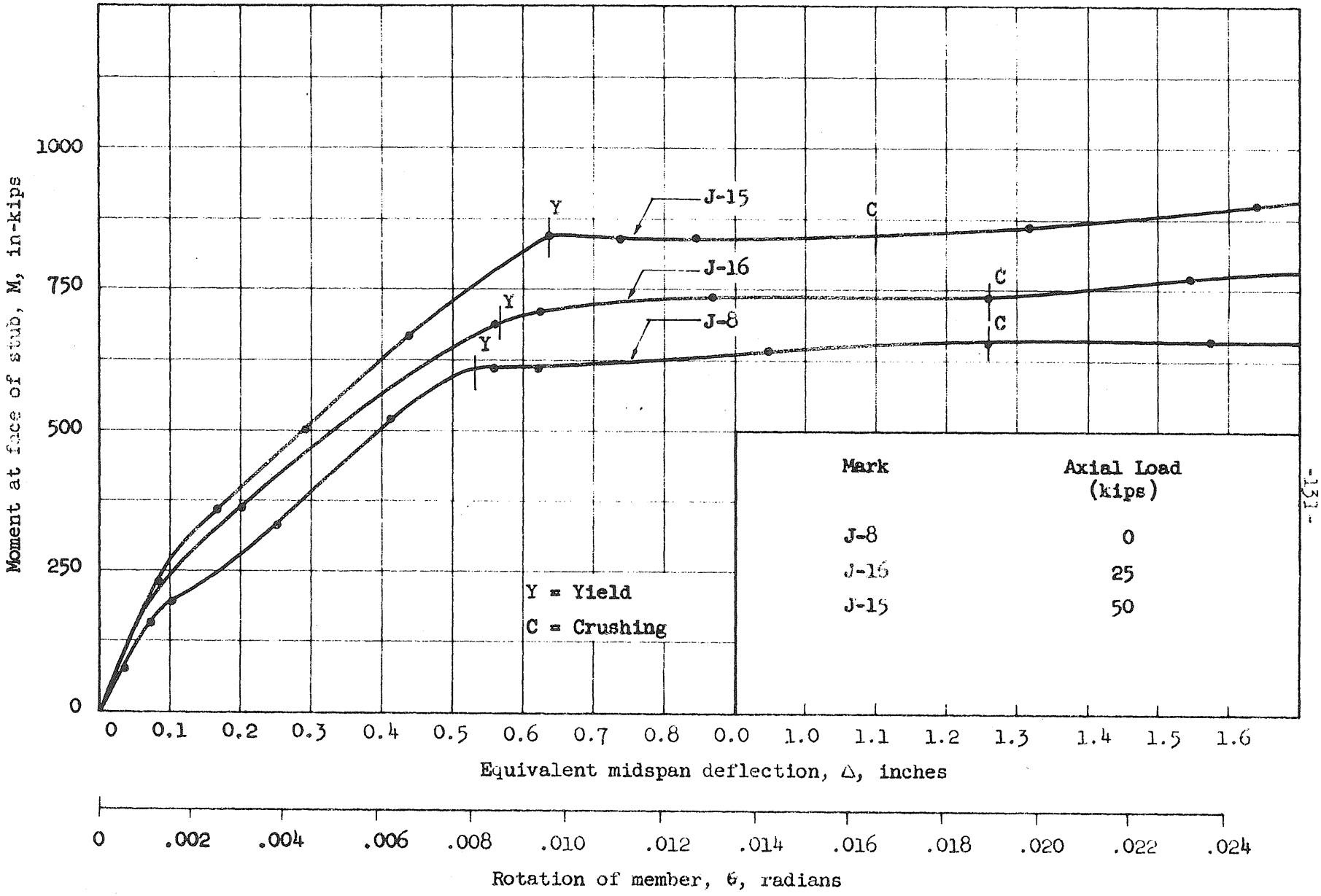

FIG. 3.14 MOMENT VERSUS ROTATION, p_g = 3.29% (enlarged rotation scale)

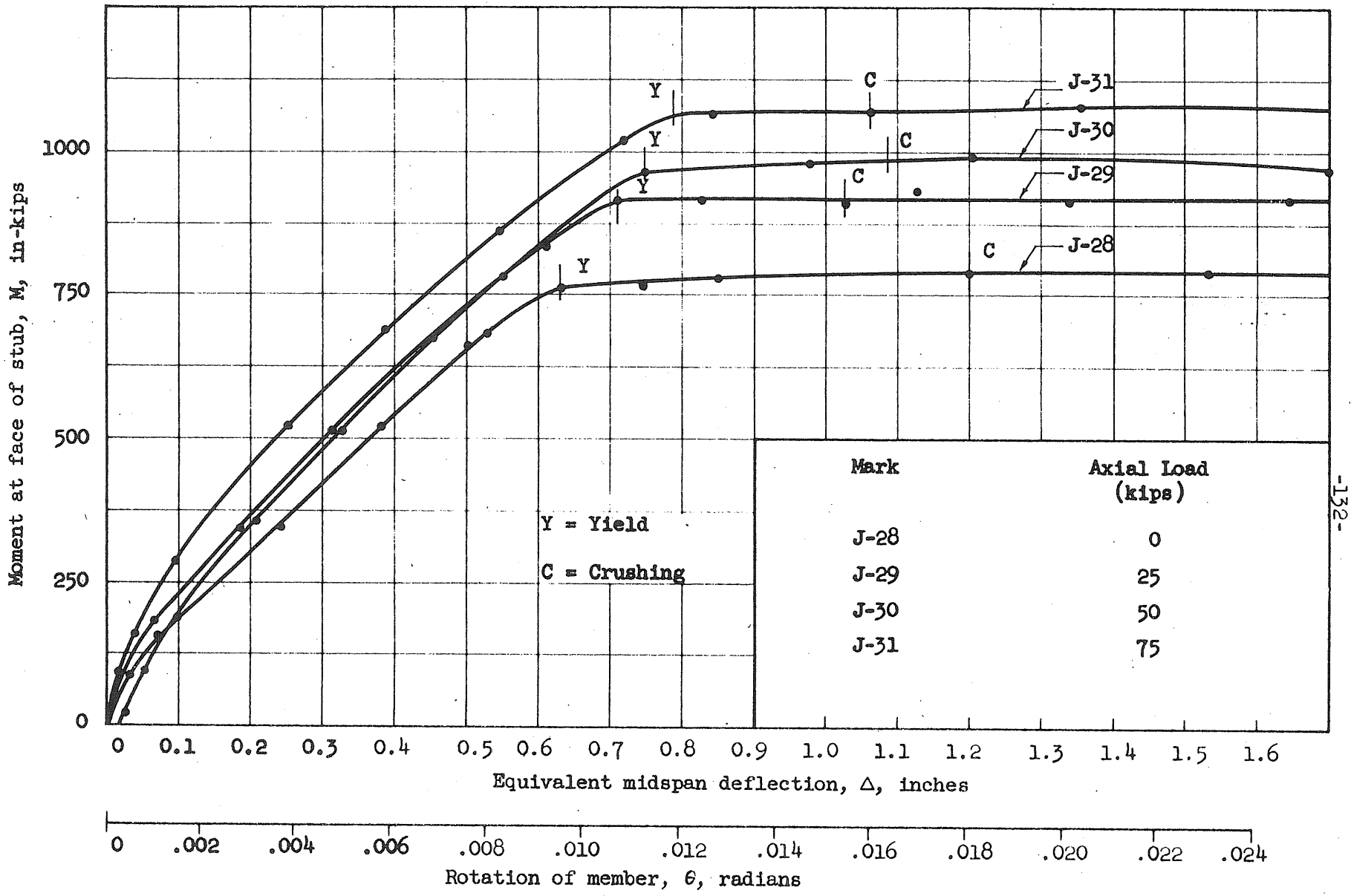

FIG. 3.15 MOMENT VERSUS ROTATION, p_g = 5.55% (enlarged rotation scale)

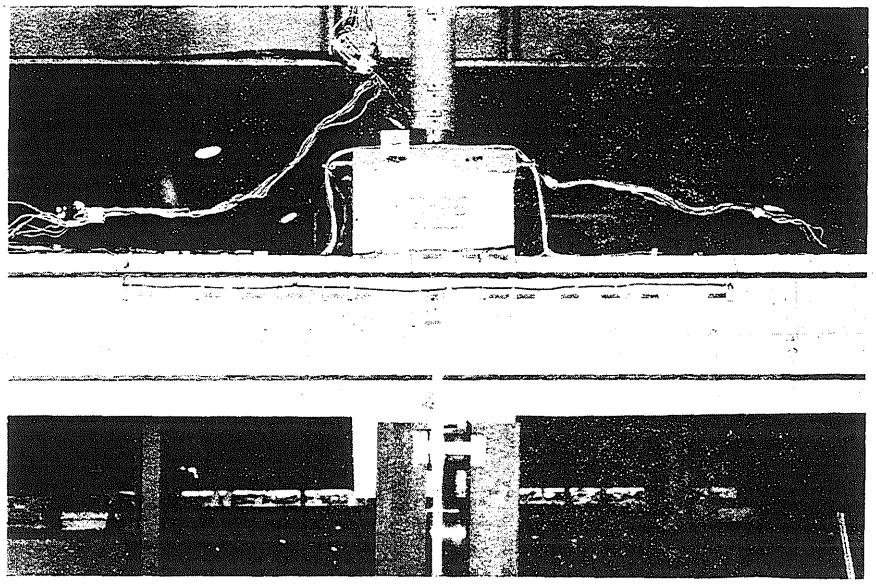

(a) Specimen J-26 at Yield (P = 50 kips, p_g = 1.11%)

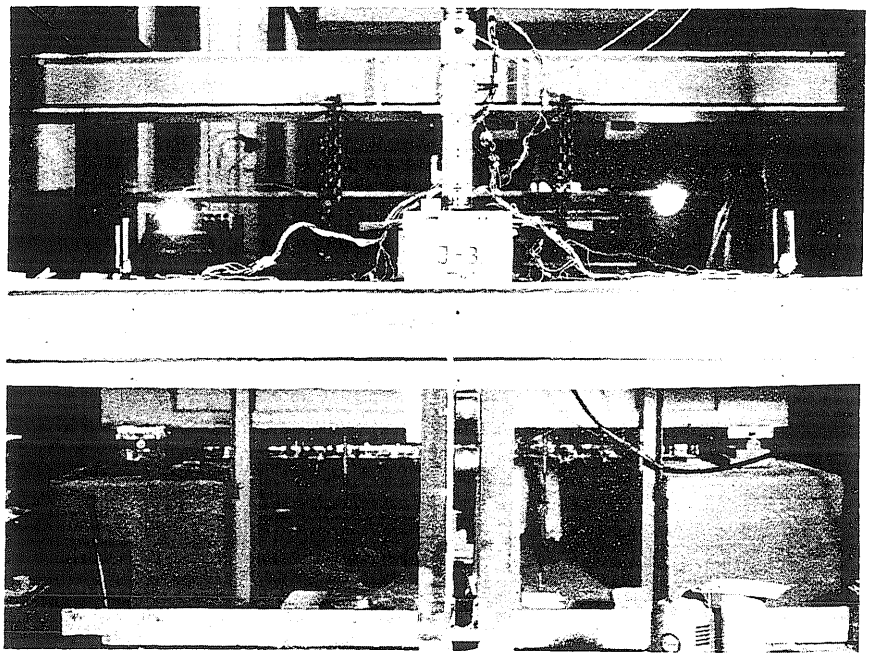

(b) Specimen J-31 at Crushing (P = 75 kips, p_g = 5.55%)

FIG. 3.16 PHOTOGRAPHS SHOWING CRACK PATTERN

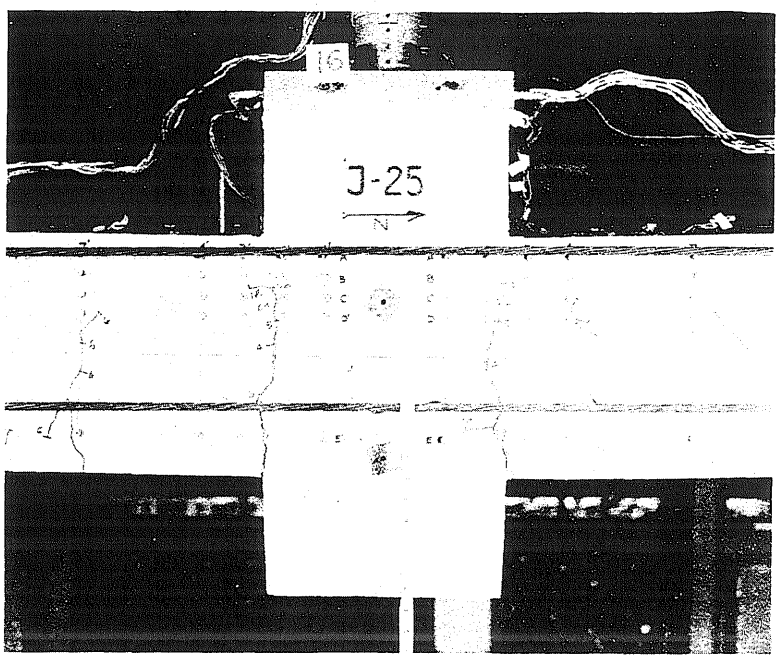

(a) Specimen J-25 at Crushing (P = 25 kips, p_g = 1.11%)

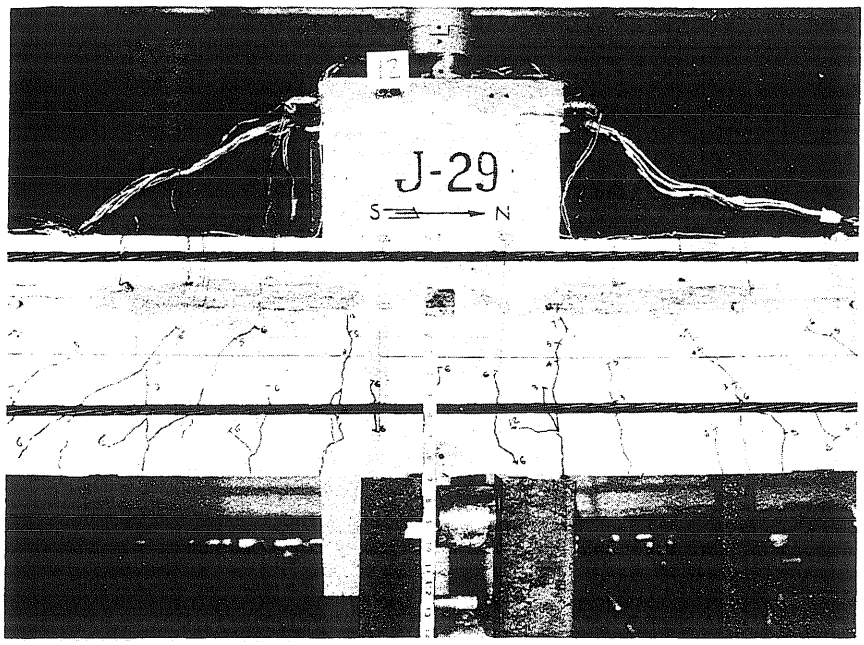

(t) Specimen J-29 at Crushing (P = 25 kips, p_g = 5.55%)

FIG. 3.17 PHOTOGRAPHS SHOWING CRACK PATTERN

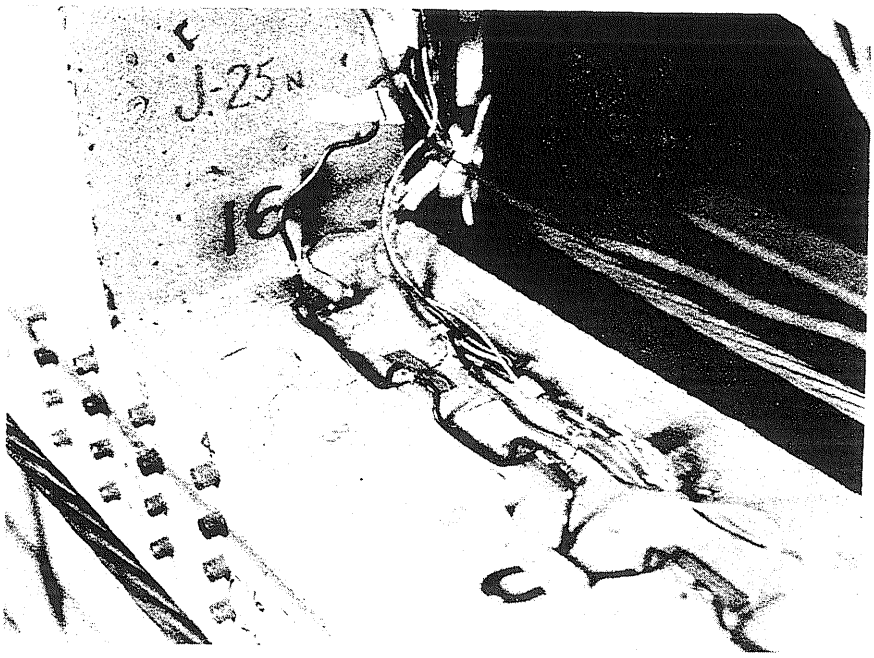

(a) Specimen J-25 (P = 25 kips, p_g = 1.11%)

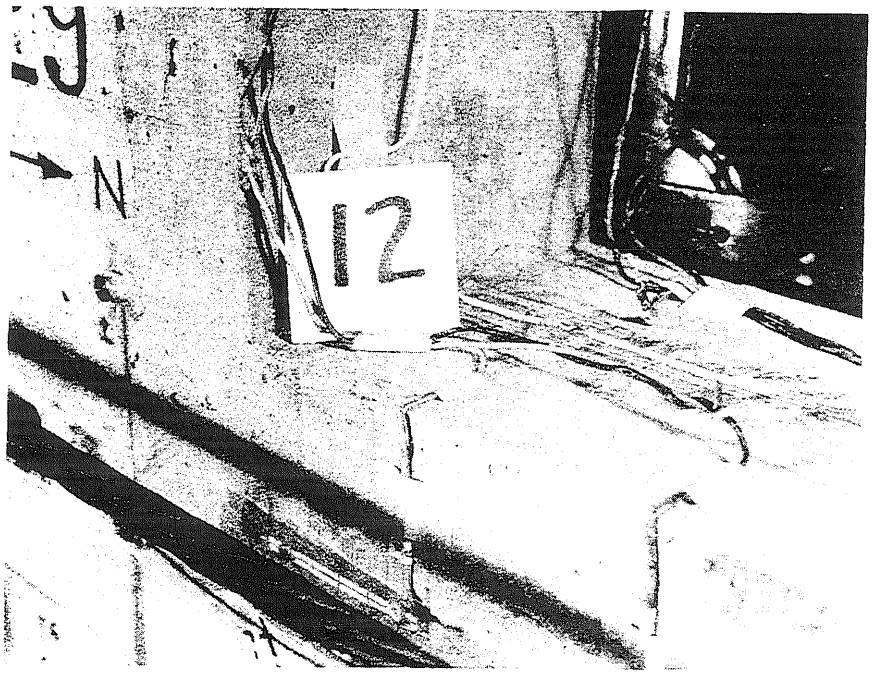

(b) Specimen J-29 (P = 25 kips, p_g = 5.55%)

FIG. 3.18 PHOTOGRAPHS SHOWING FIRST VISIBLE SIGNS OF CRUSHING

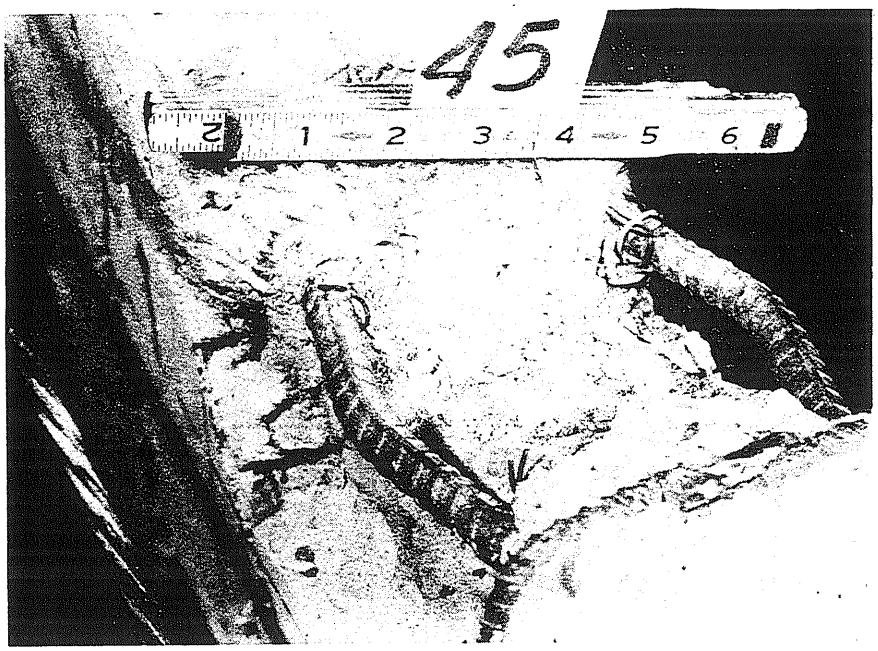

(a) Compression Failure (Specimen J-25 - P = 25 kips, p_g = 1.11%)

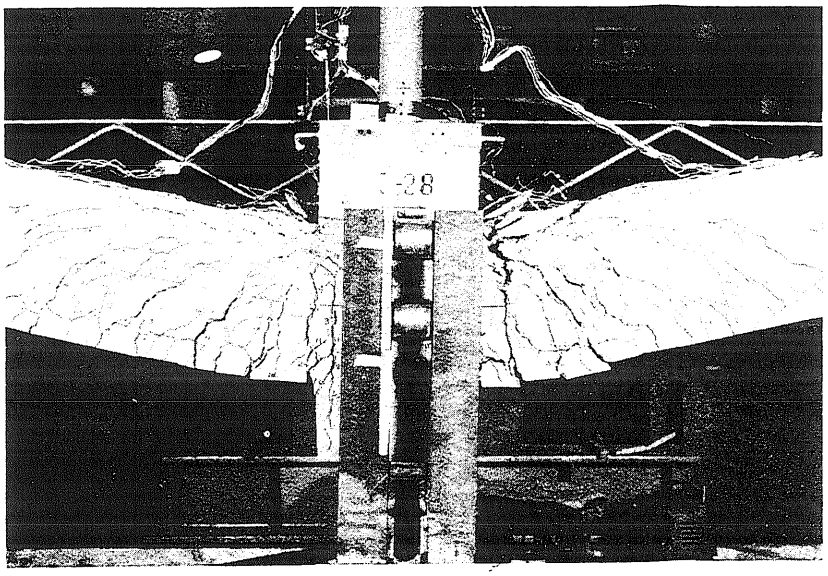

(b) Shear Failure (Specimen J-28 - P = 0, p_g = 5.53%)

FIG. 3.19 PHOTOGRAPHS SHOWING COMPRESSION AND SHEAR FAILURES

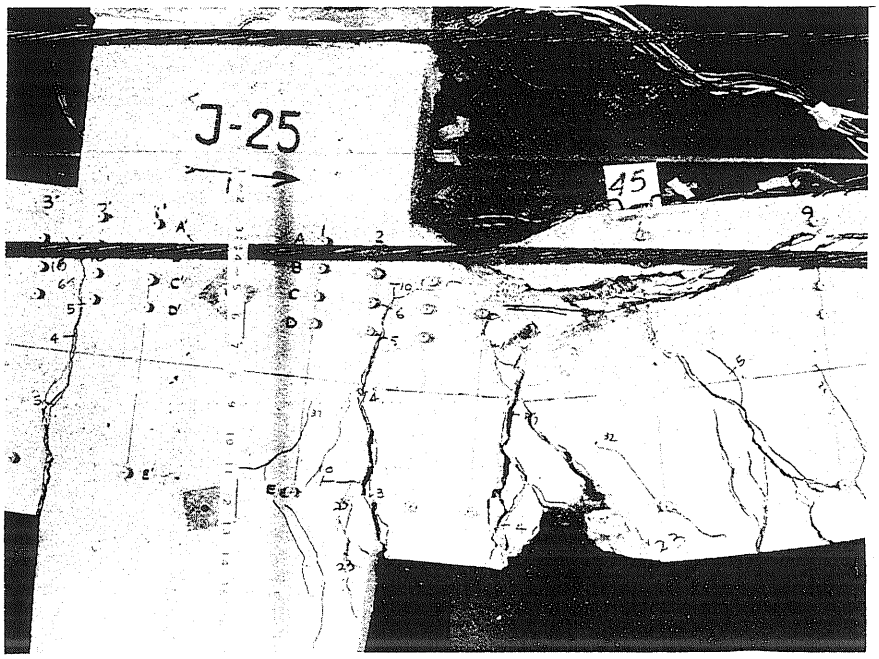

(a) Specimen J-25 (P = 25 kips, p_g = 1.11%)

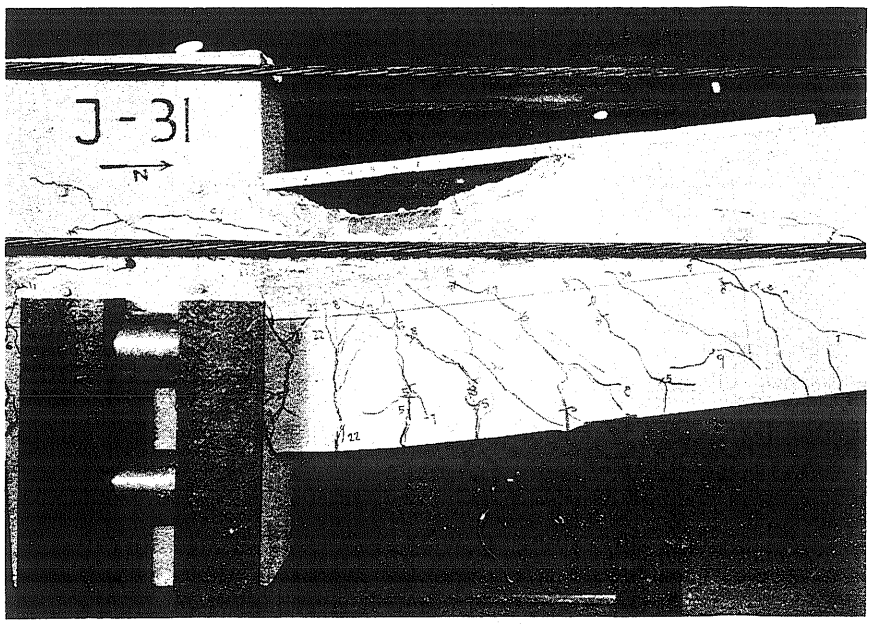

(b) Specimen J-31 (P = 75 kips, p_g = 5.55%)

FIG. 3.20 PHOTOGRAPHS SHOWING LOCATION OF CRITICAL SECTION

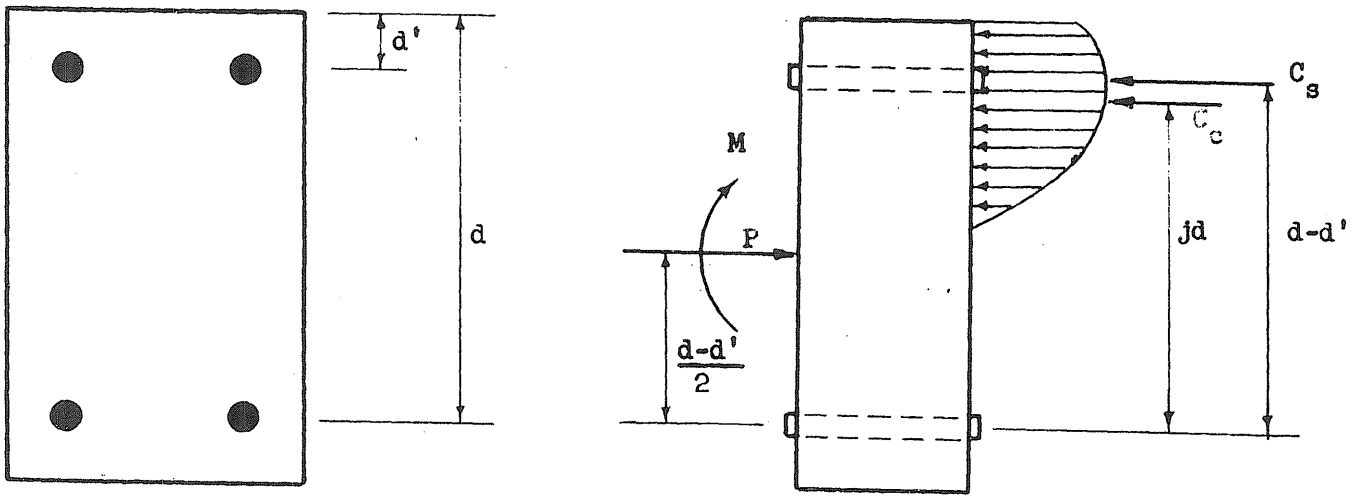

FIG. 3.21 FREE-BODY DIAGRAM OF A TRANSVERSE SLICE OF A SPECIMEN

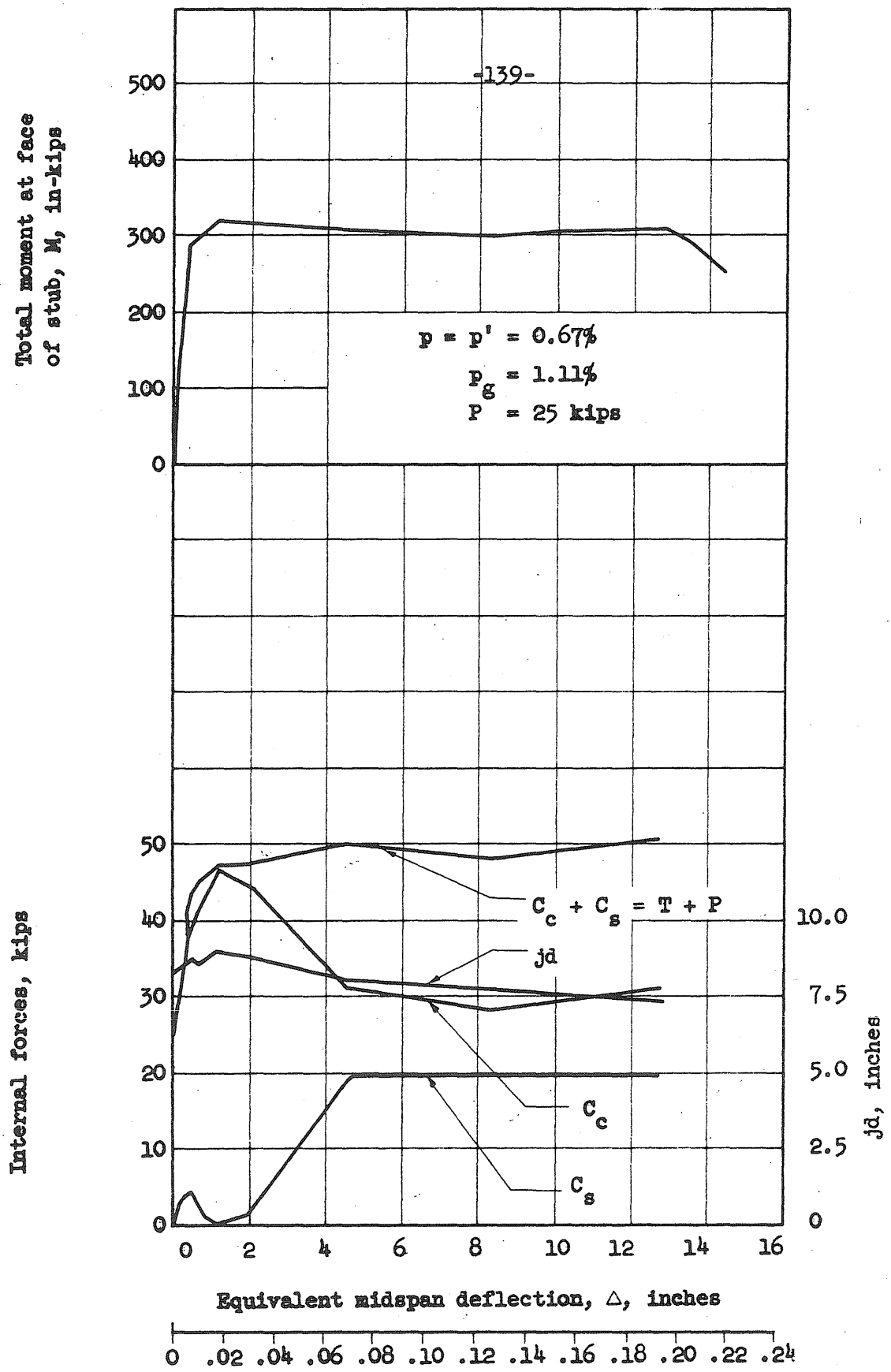

FIG. 3.22 INTERNAL FORCES VERSUS ROTATION FOR SPECIMEN J-25

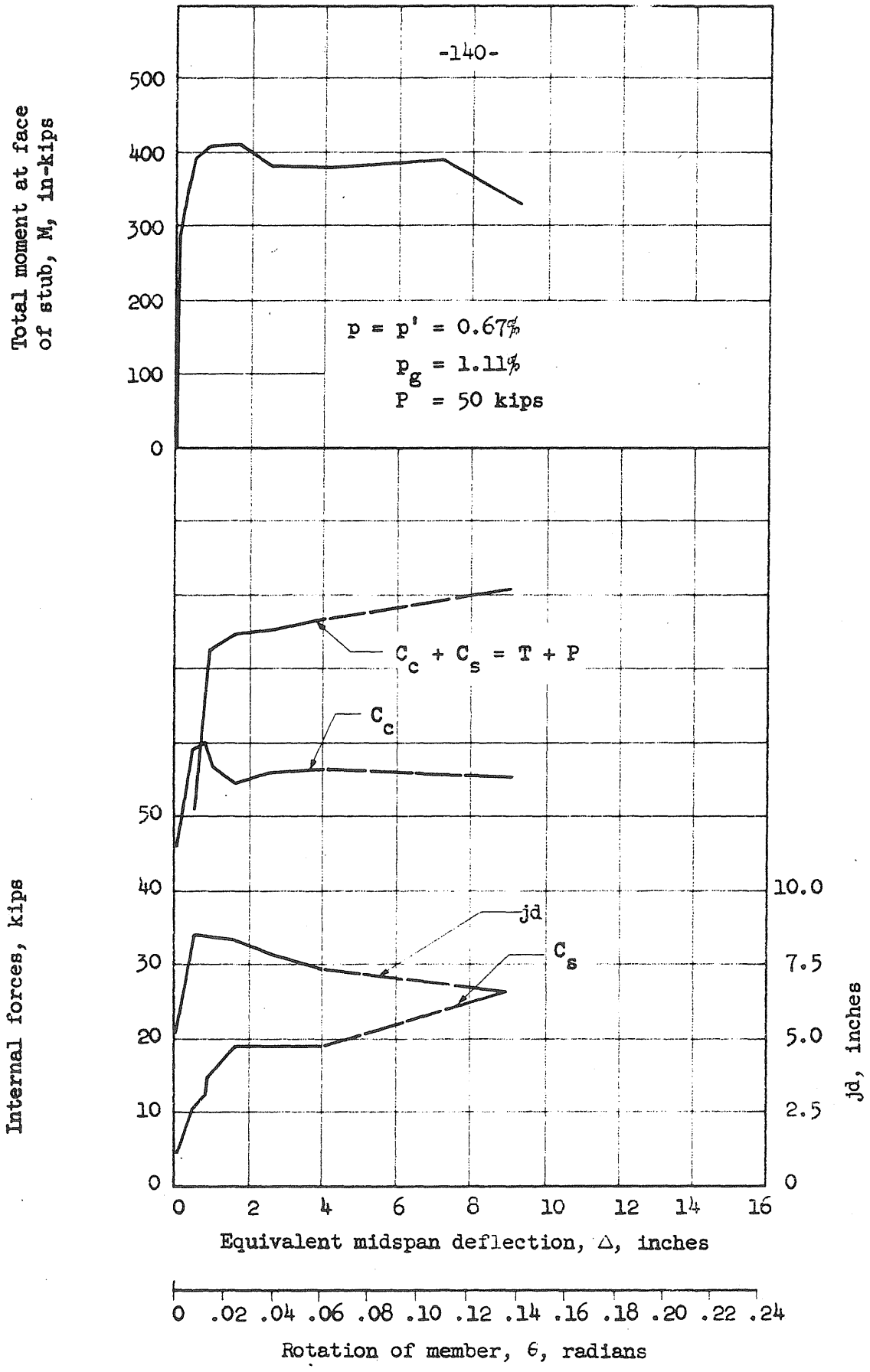

FIG. 3.23 INTERNAL FORCES VERSUS ROTATION FOR SPECIMEN J-26

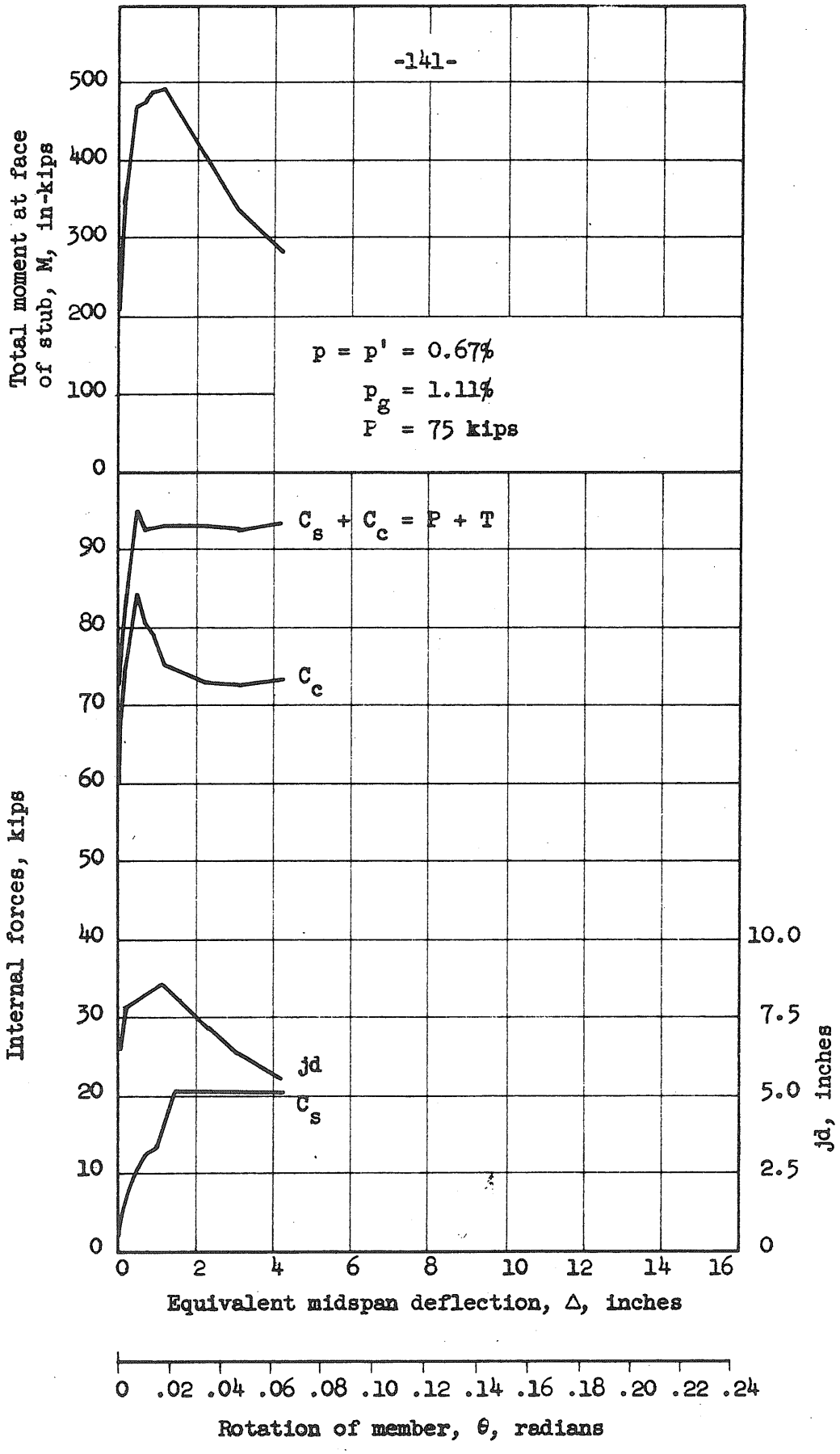

FIG. 3.24 INTERNAL FORCES VERSUS ROTATION FOR SPECIMEN J-27

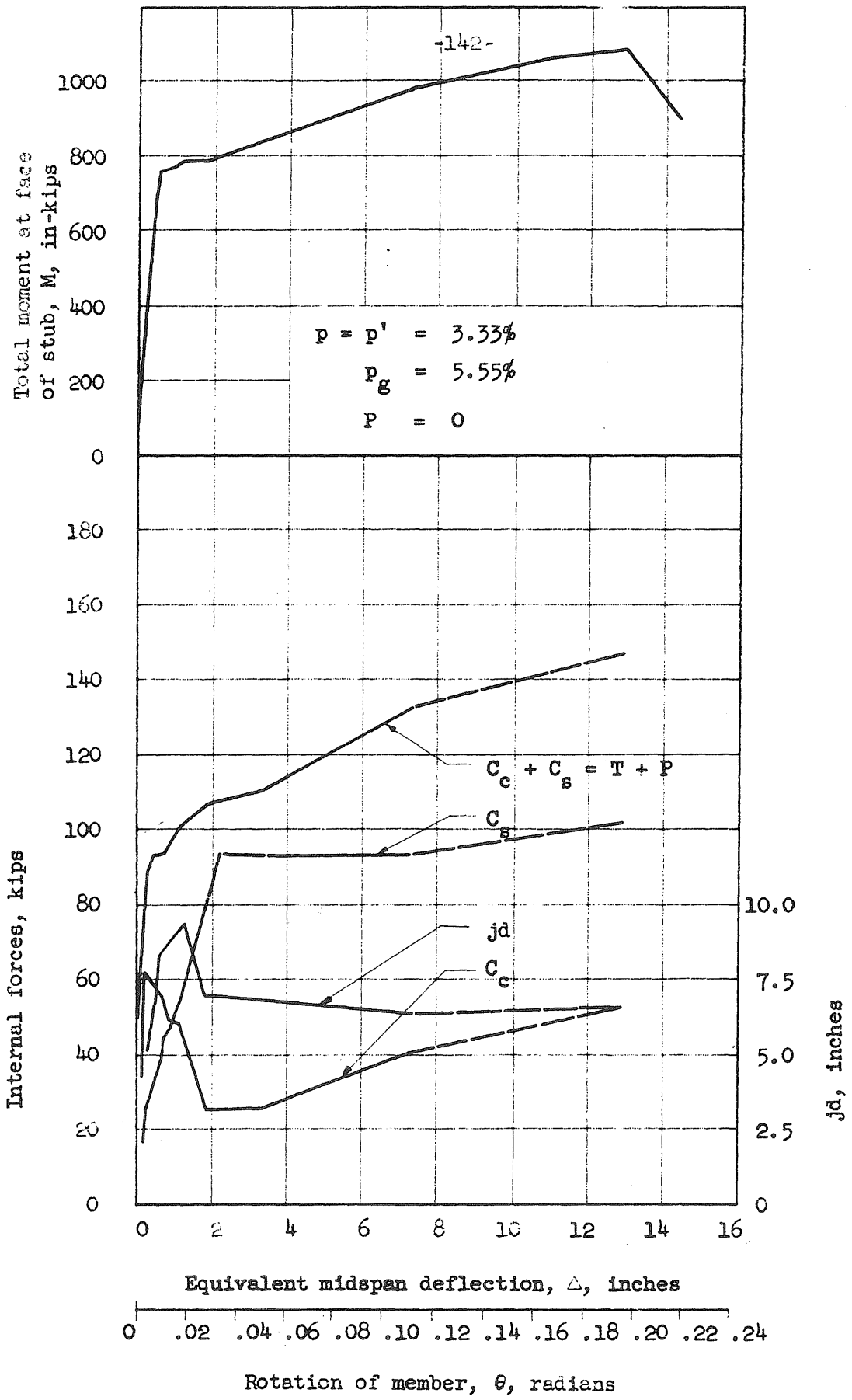

FIG. 3.25 INTERNAL FORCES VERSUS ROTATION FOR SPECIMEN J-28

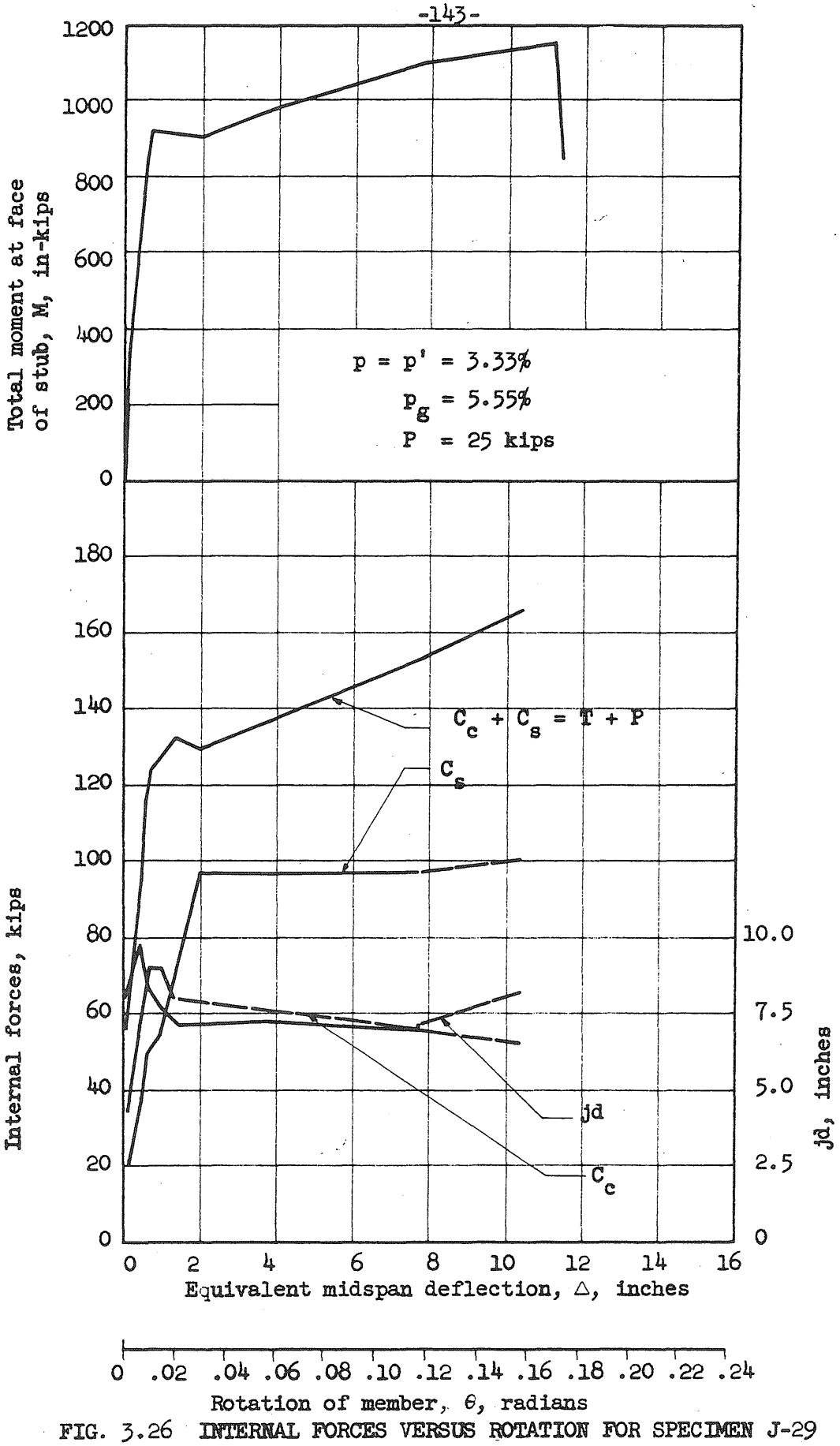

FIG. 3.26 INTERNAL FORCES VERSUS ROTATION FOR SPECIMEN J-29

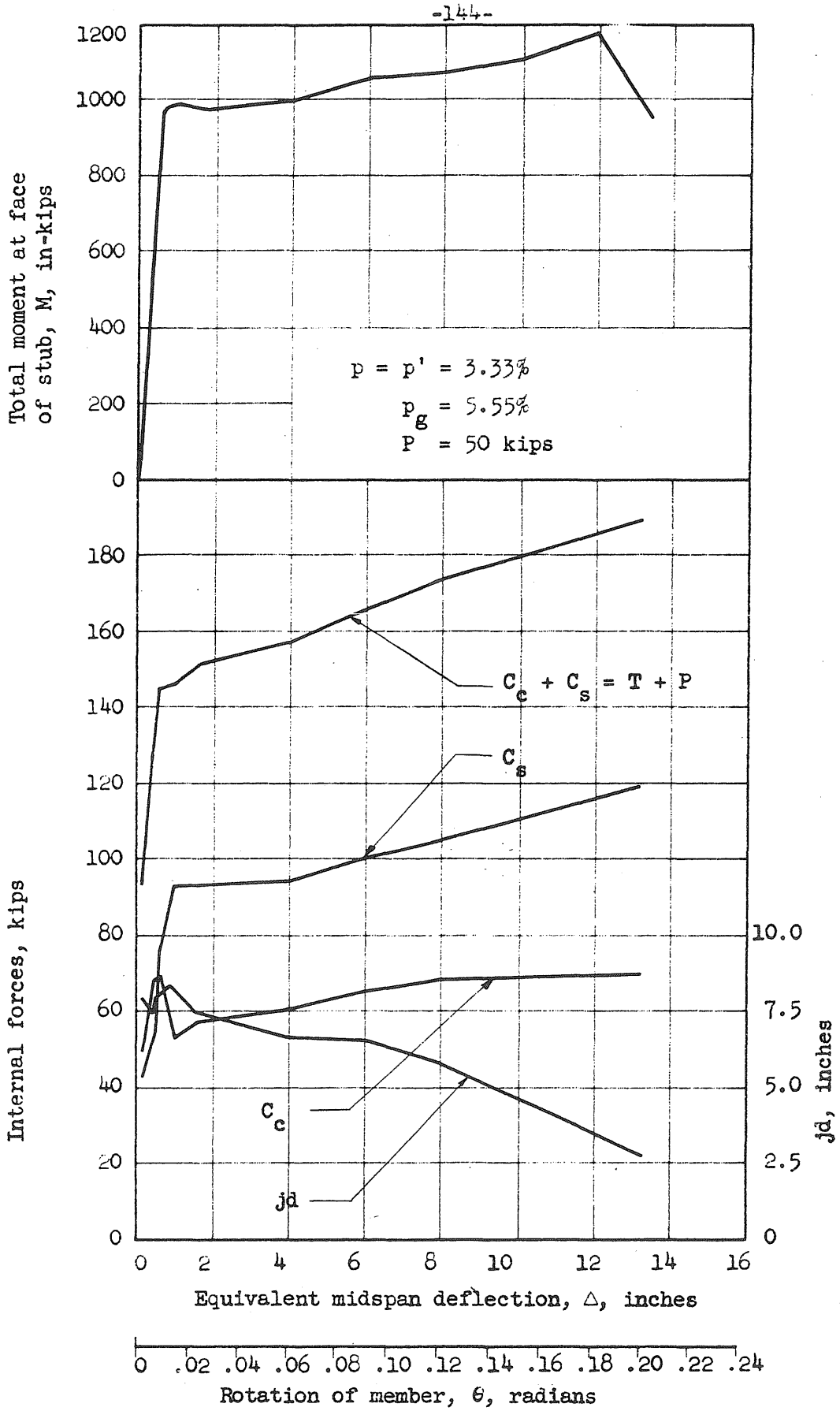

FIG. 3.27 INTERNAL FORCES VERSUS ROTATION FOR SPECIMEN J-30

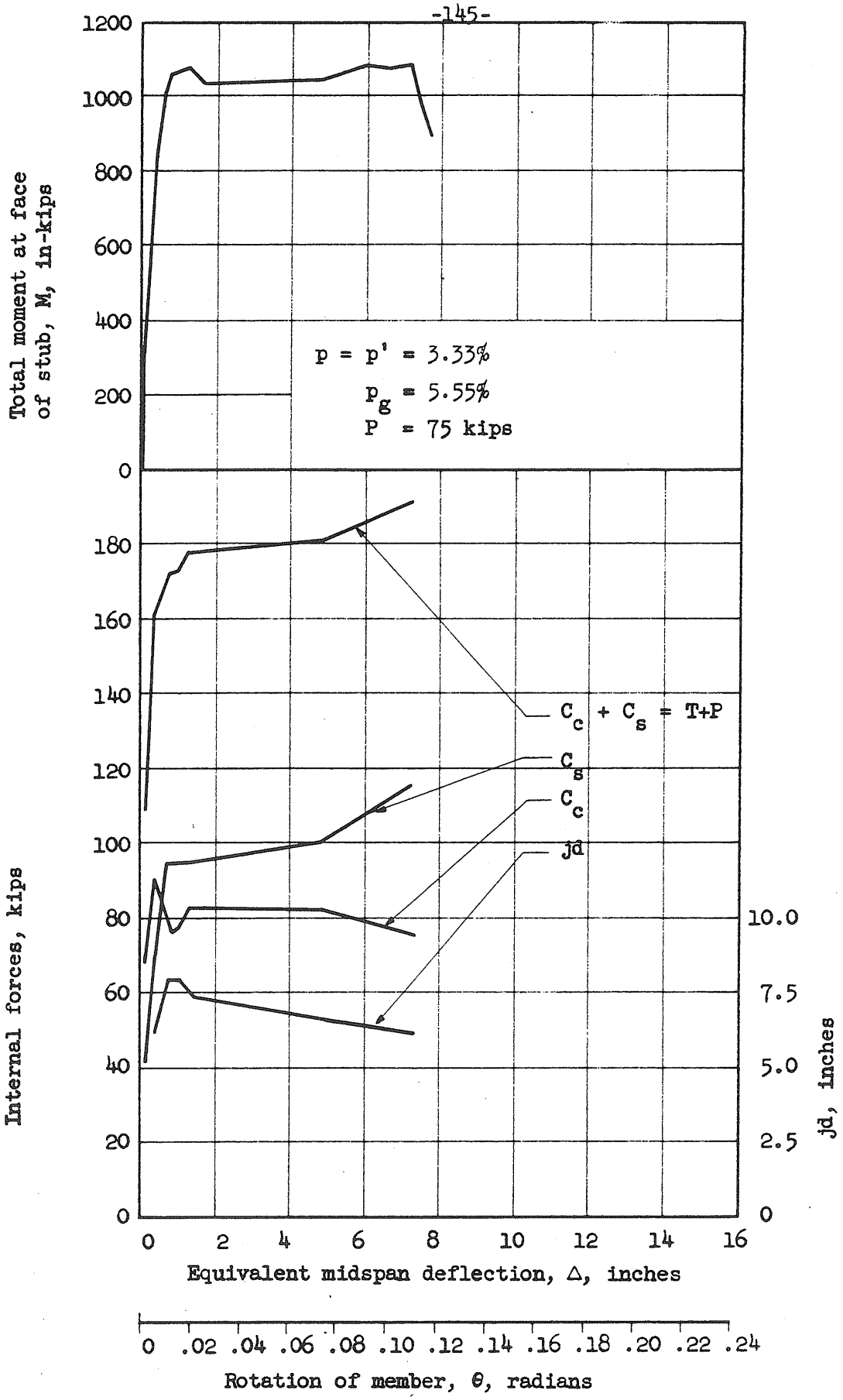

FIG. 3.28 INTERNAL FORCES VERSUS ROTATION FOR SPECIMEN J-31

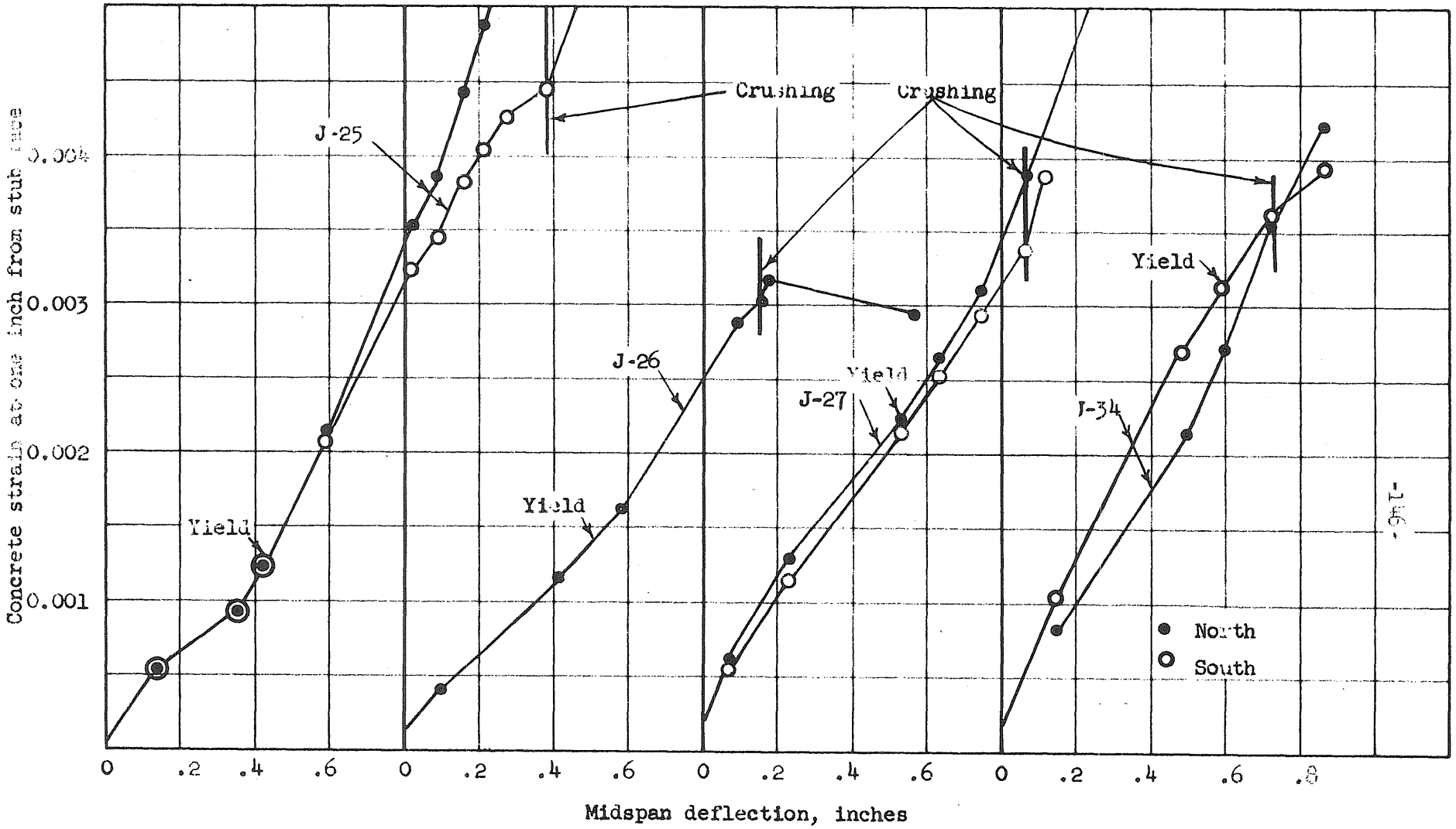

FIG. 3.29 MAXIMUM CONCRETE STRAIN VERSUS MIDSPAN DEFLECTION, $p_g = 1.11\%$

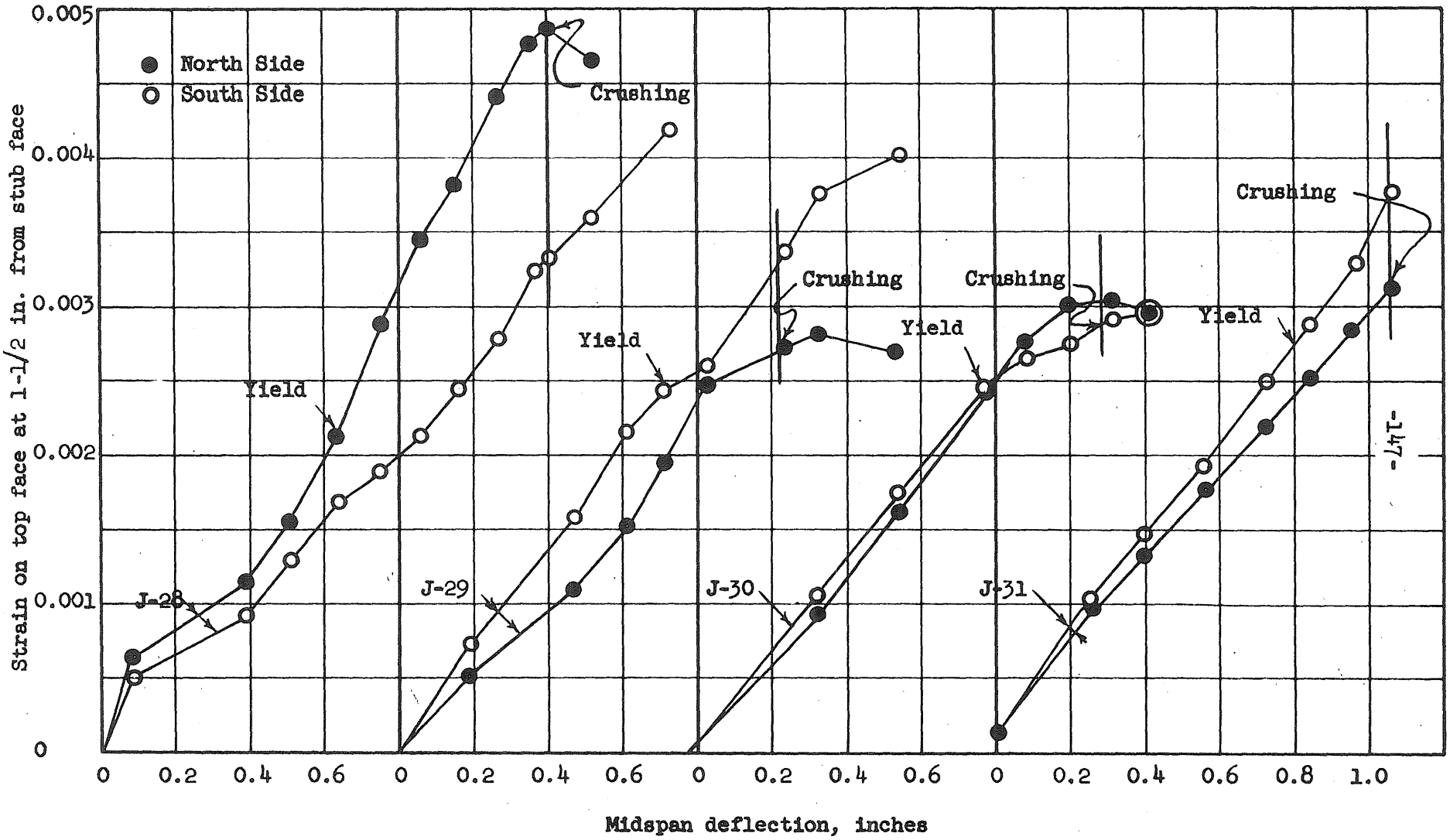

FIG. 3.30 MAXIMUM CONCRETE STRAIN VERSUS MIDSPAN DEFLECTION, p_g = 5.55%

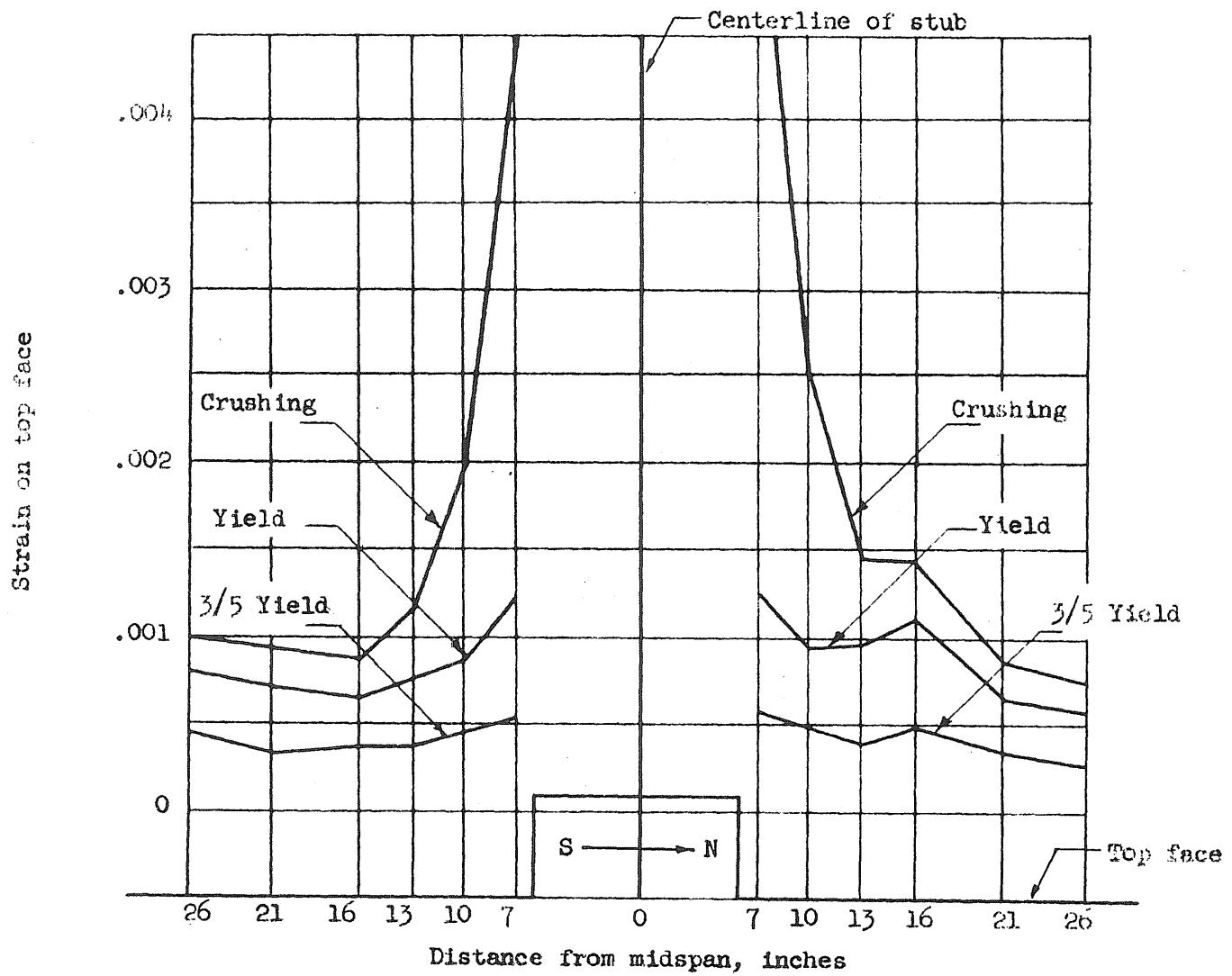

FIG. 3.31 DISTRIBUTION OF STRAIN ON TOP SURFACE OF SPECIMEN J-25

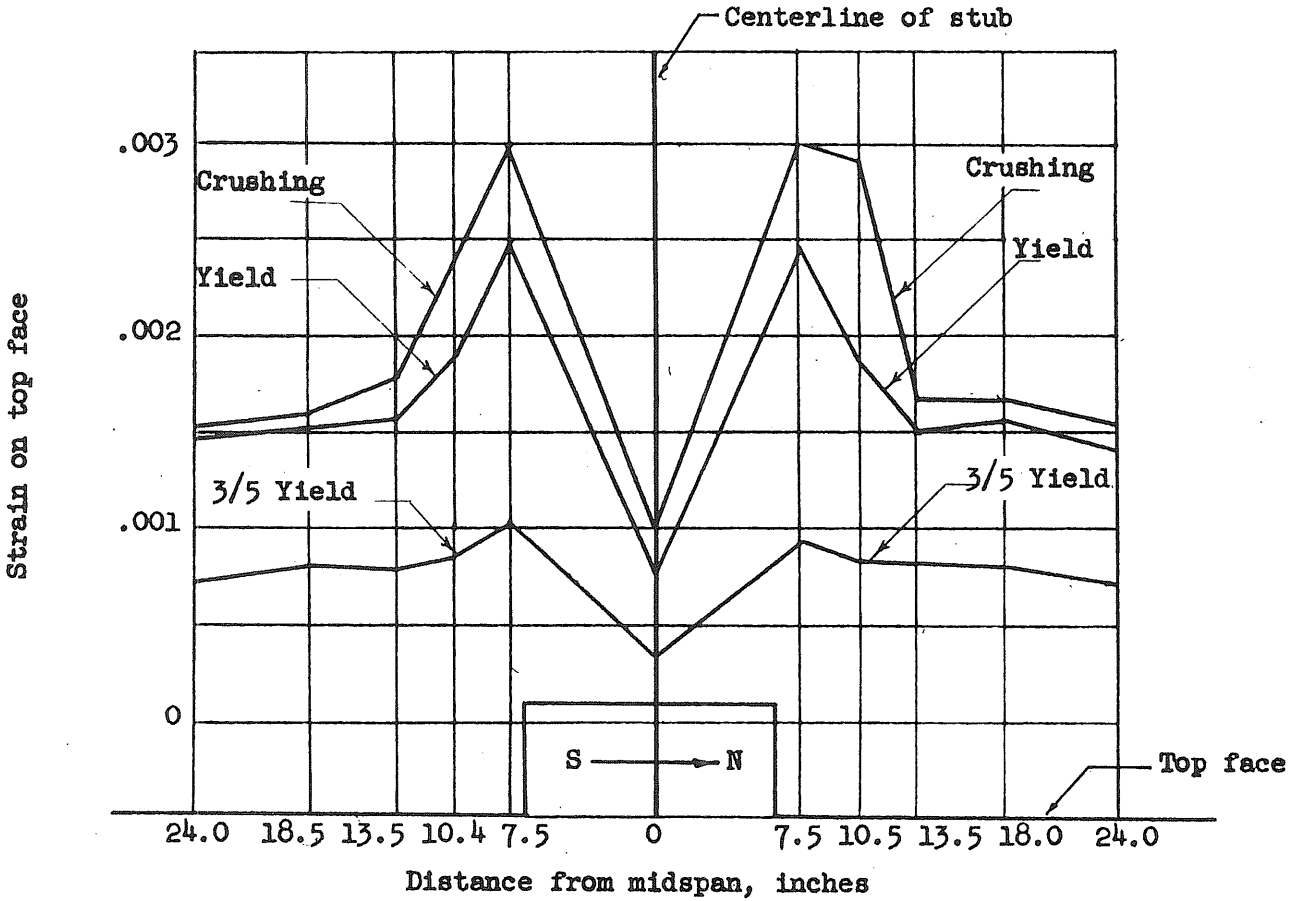

FIG. 3.32 DISTRIBUTION OF STRAIN ON TOP SURFACE OF SPECIMEN J-30

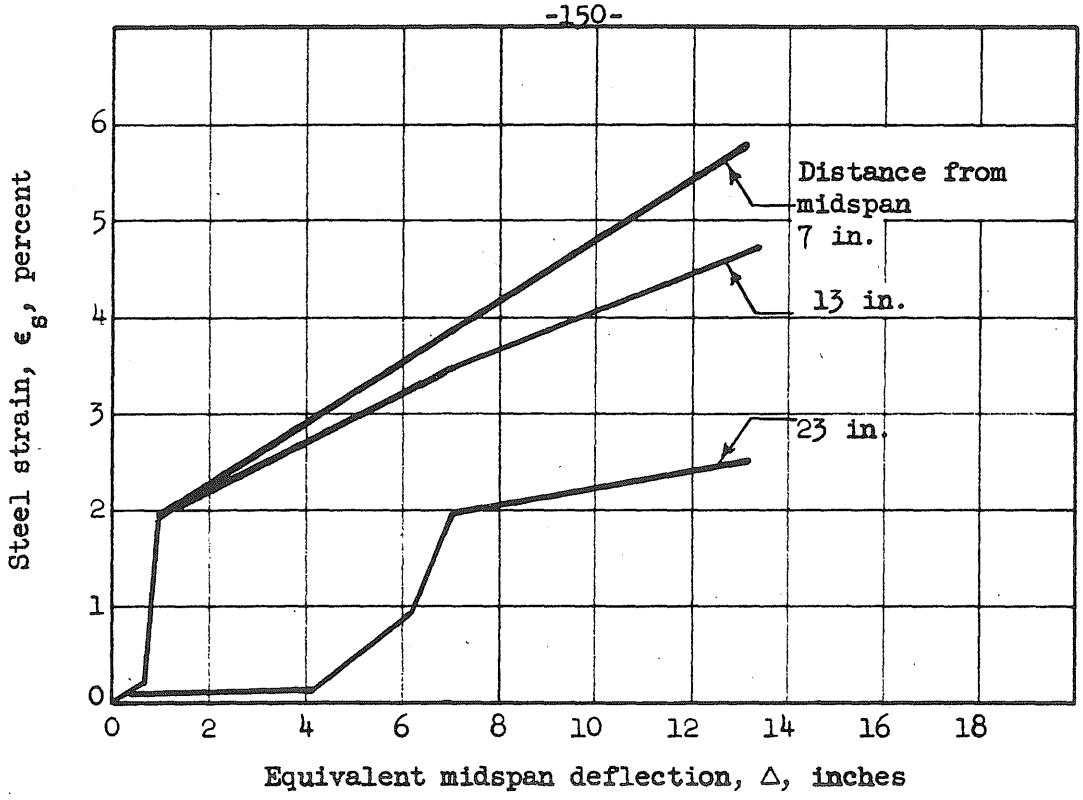

(a) Relationships Between Steel Strains and Deflections

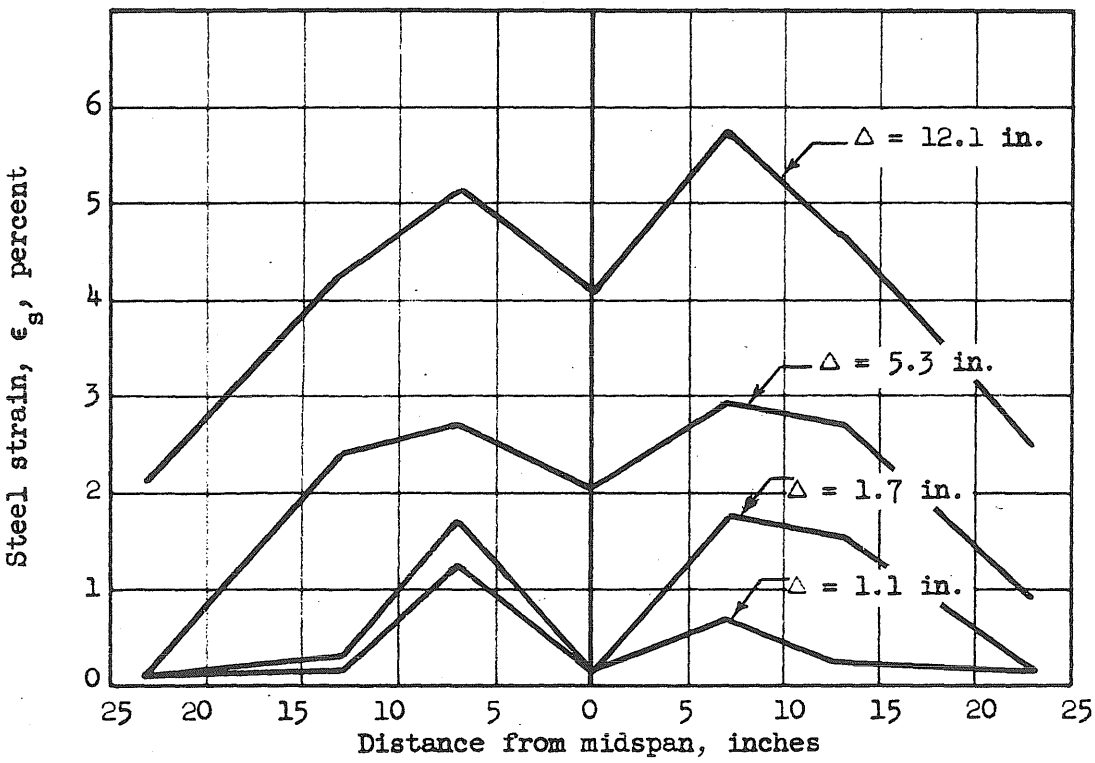

(b) Strain Distribution in Tension Steel

FIG. 3.33 STRAIN IN TENSION STEEL VERSUS EQUIVALENT MIDSPAN DEFLECTION AND DISTRIBUTION OF STRAIN IN THE TENSION REINFORCEMENT

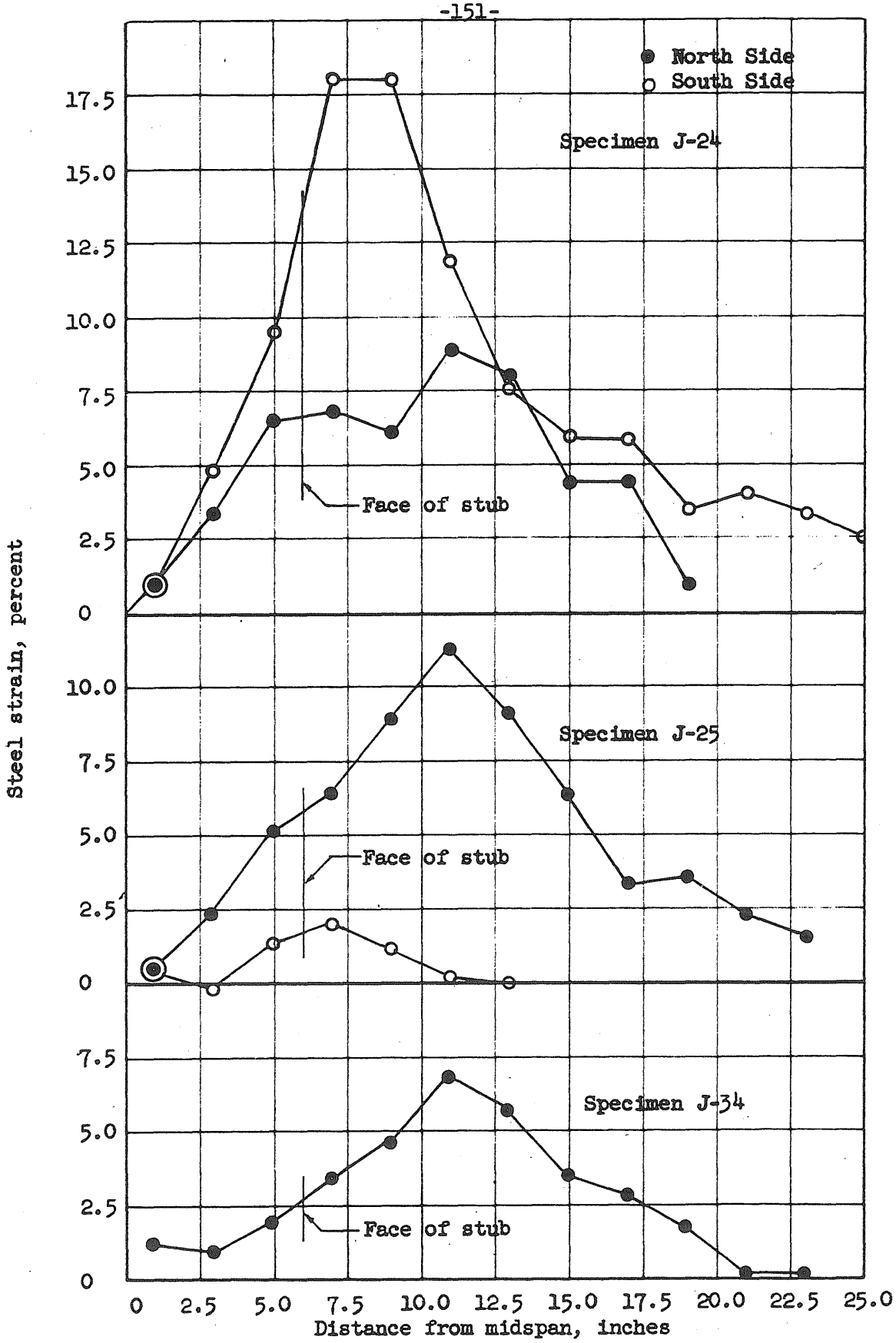

FIG. 3.34 DISTRIBUTION OF STRAIN IN THE TENSION REINFORCEMENT AT ULTIMATE, #4 BARS

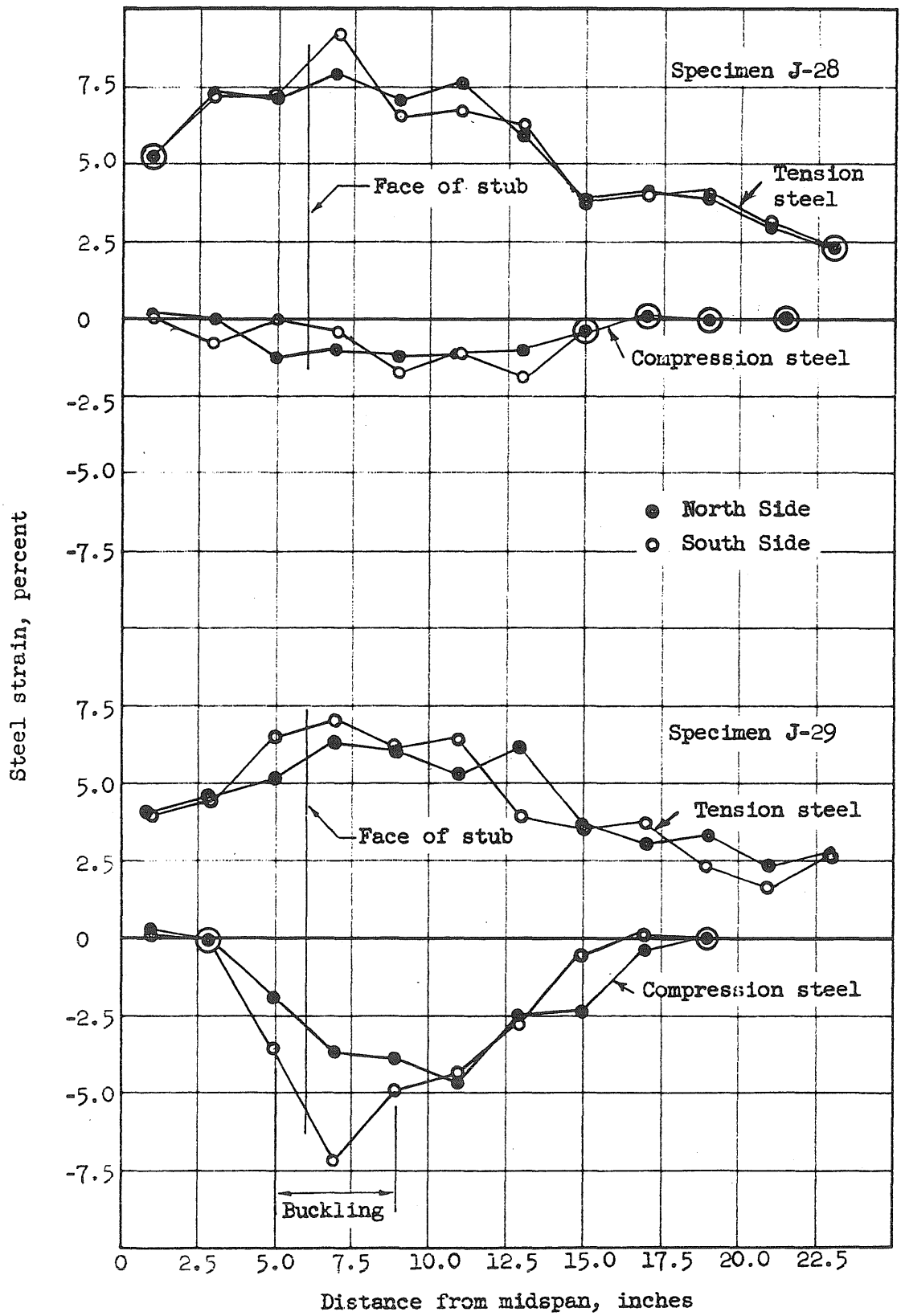

FIG. 3.35 DISTRIBUTION OF STRAIN IN THE TENSION AND COMPRESSION REINFORCEMENT AT ULTIMATE. #9 BARS

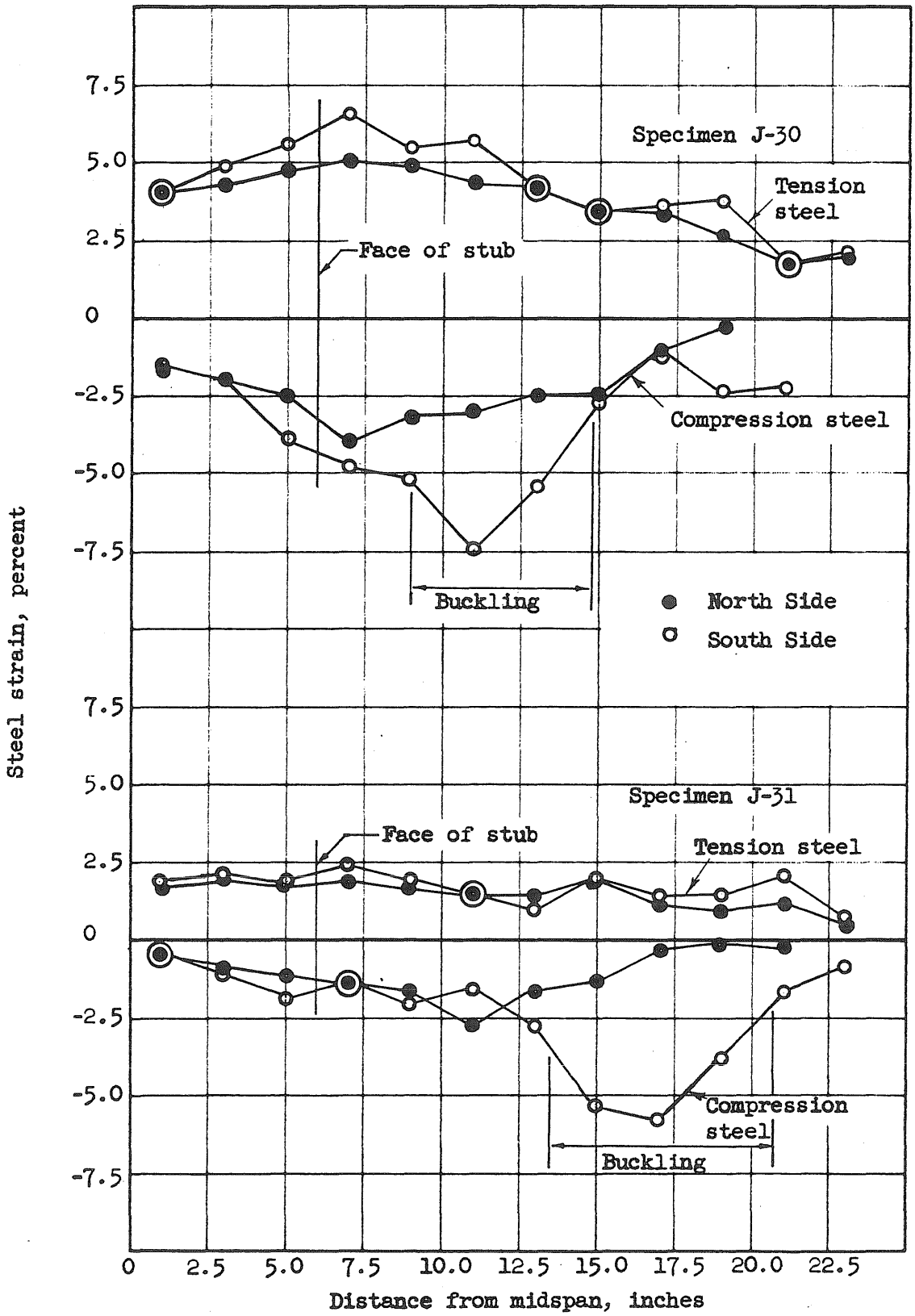

FIG. 3.36 DISTRIBUTION OF STRAIN IN THE TENSION AND COMPRESSION REINFORCEMENTS AT ULTIMATE, #9 BARS

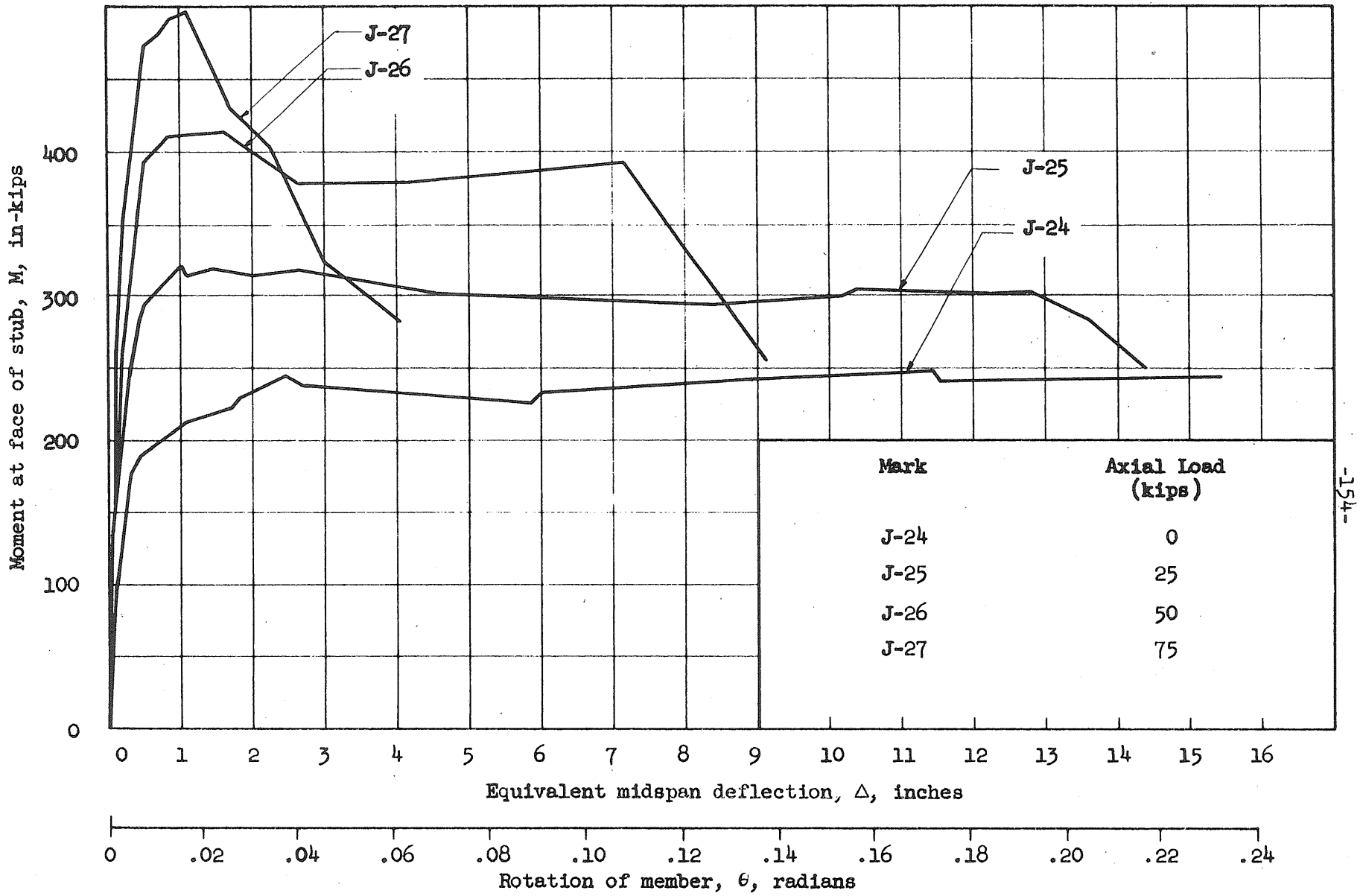

FIG. 3.37 EFFECTS OF AXIAL LOAD ON MOMENT VERSUS ROTATION RELATIONSHIPS, p_g = 1.11%

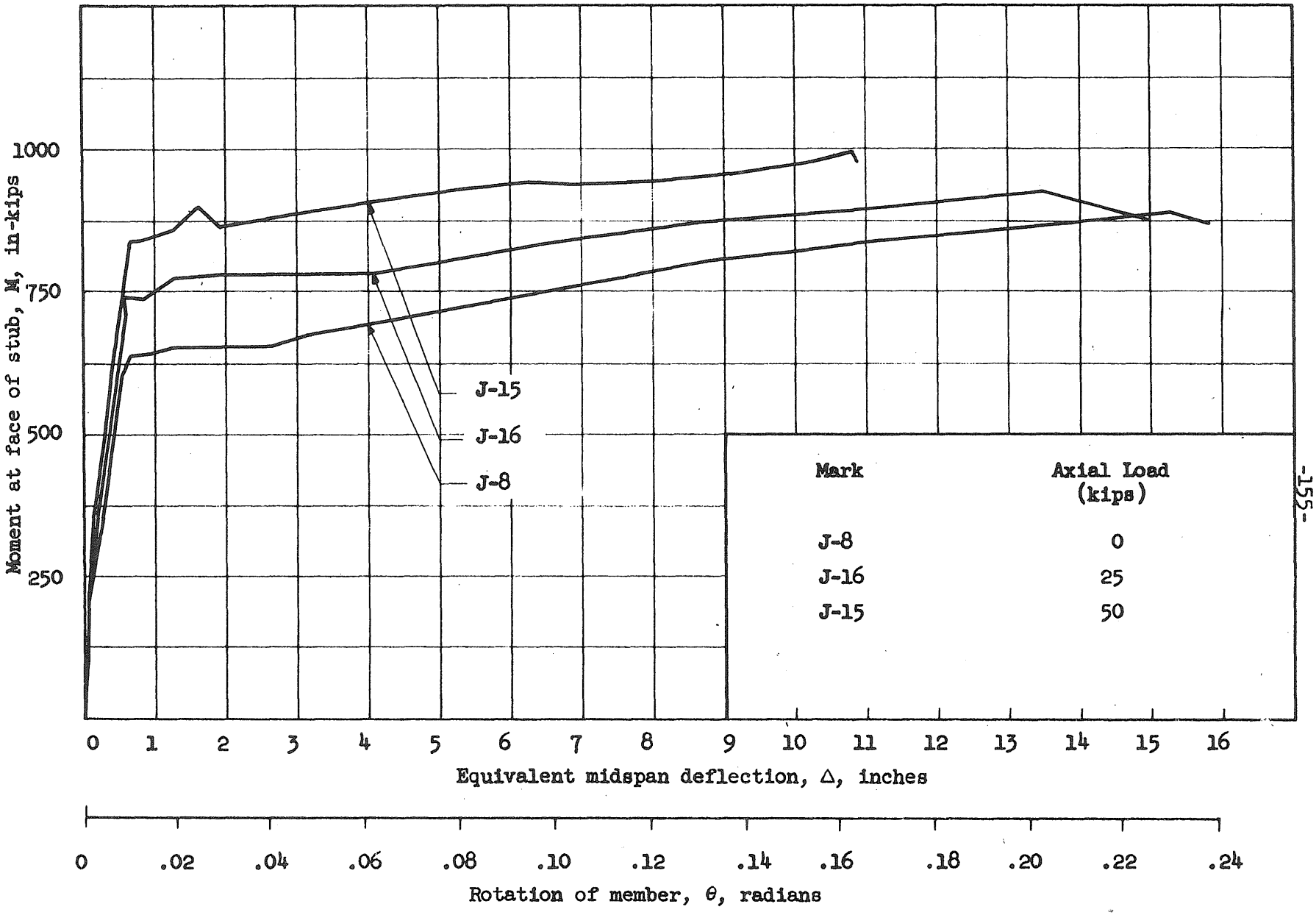

FIG. 3.38 EFFECTS OF AXIAL LOAD ON MOMENT VERSUS ROTATION RELATIONSHIPS, p_g = 3.29%

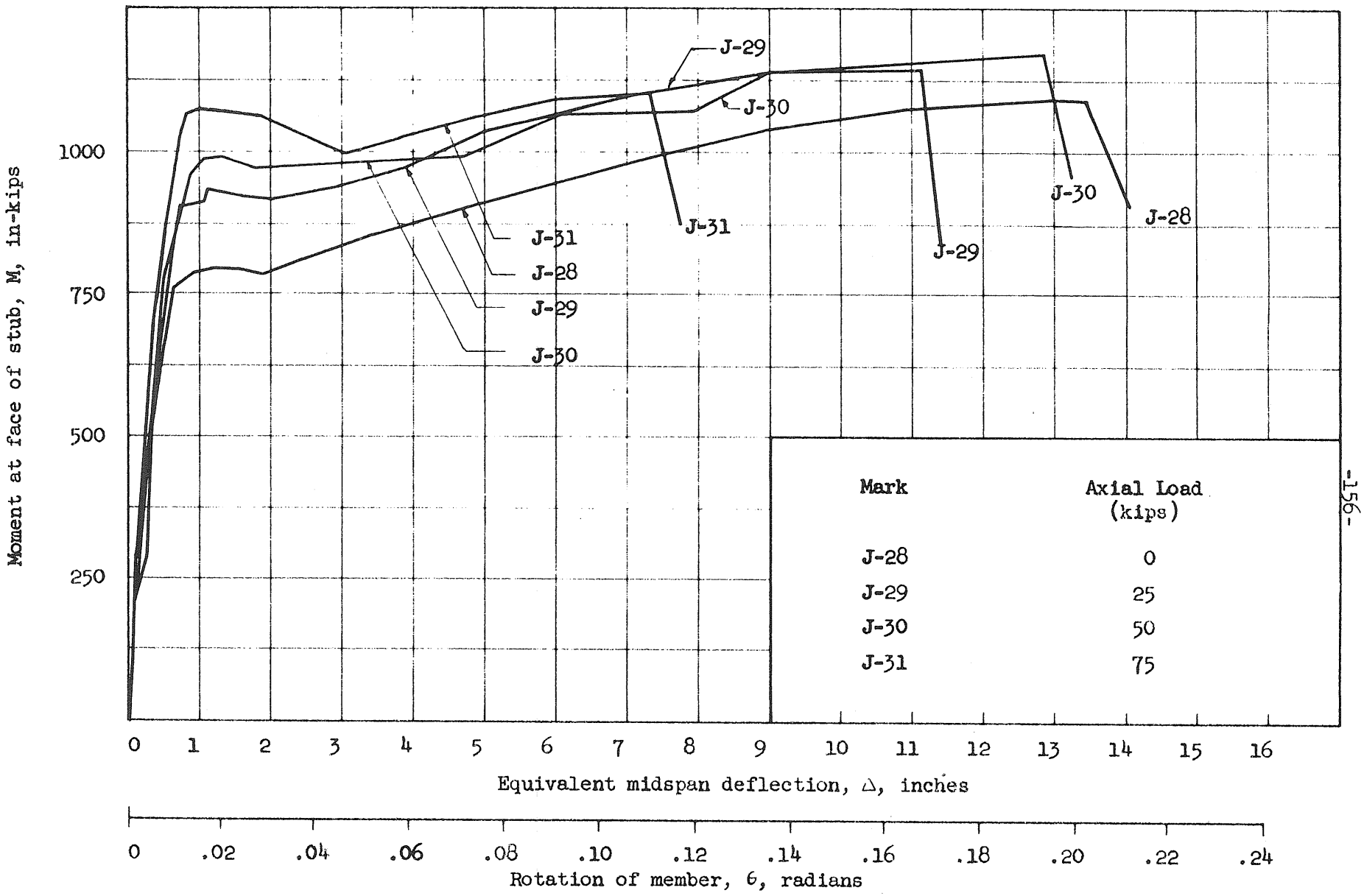

FIG. 3.39 EFFECTS OF AXIAL LOAD ON MOMENT VERSUS ROTATION RELATIONSHIPS, p_g = 5.55%

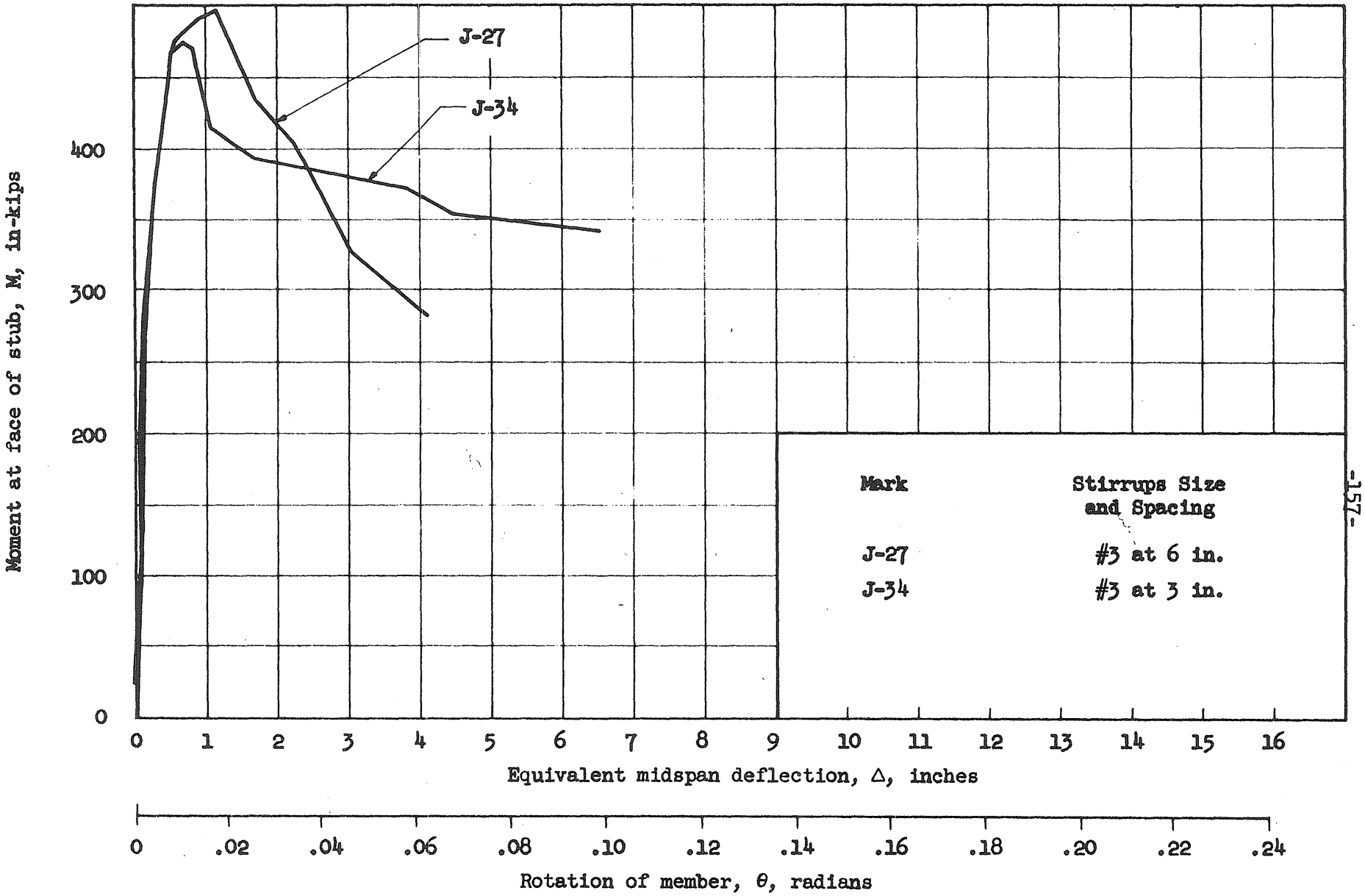

FIG. 3.40 EFFECTS OF TRANSVERSE REINFORCEMENT ON MOMENT VERSUS ROTATION RELATIONSHIPS, p_g = 1.11%

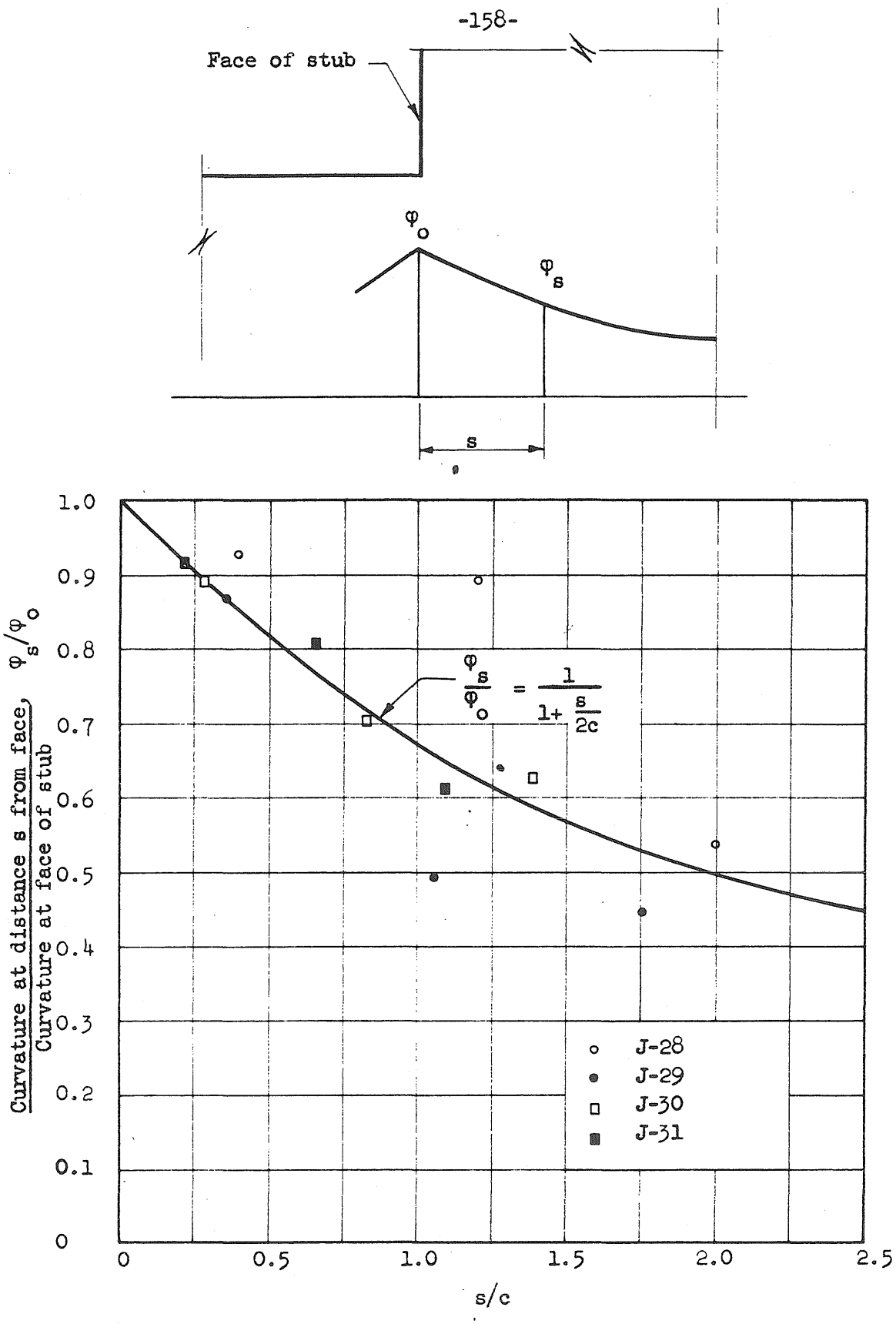

FIG. 4.1 "CURVATURE" DISTRIBUTION IN STUB

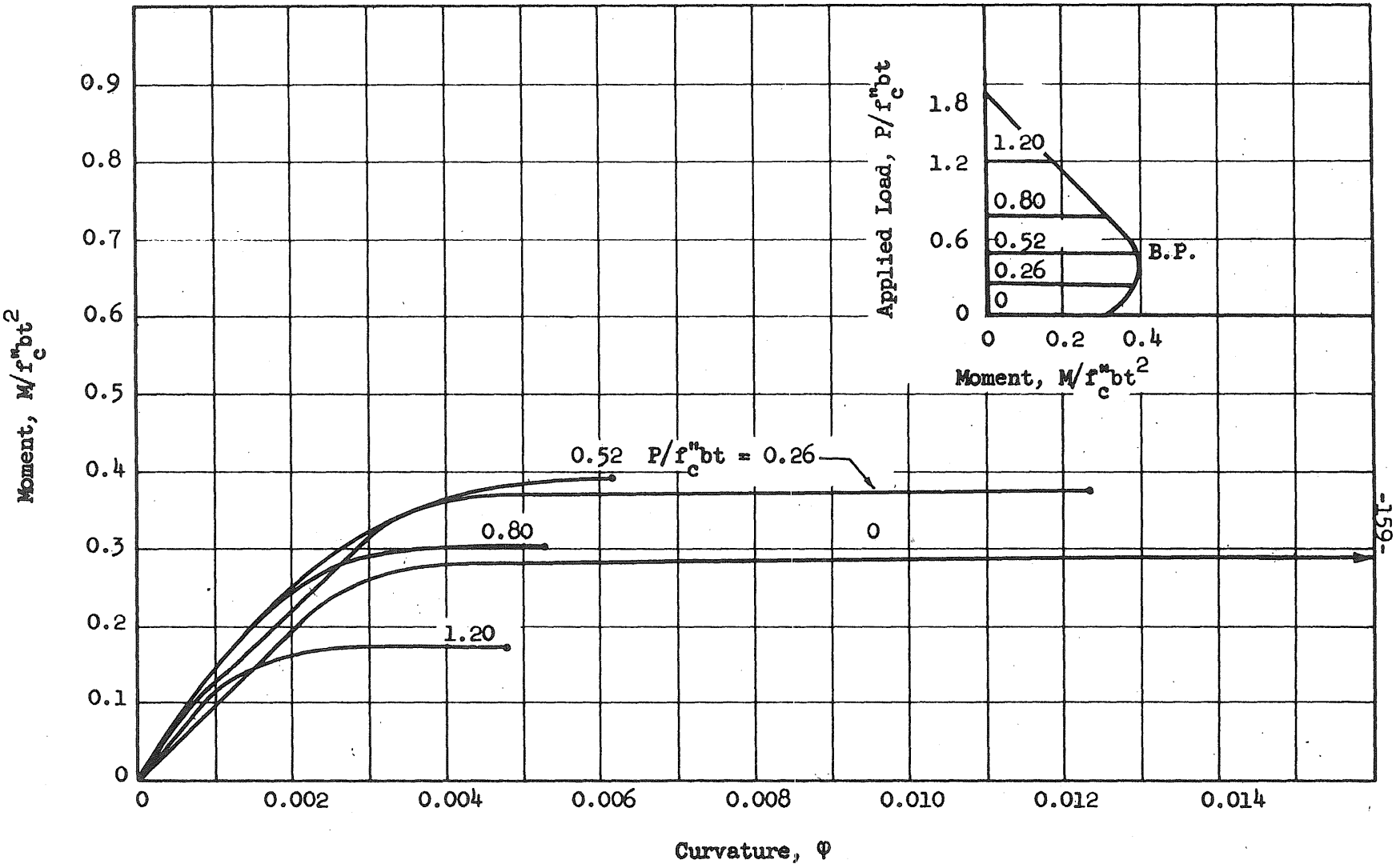

FIG. 4.2 MOMENT VERSUS CURVATURE, p_g = 4% (Adapted from Reference 7)

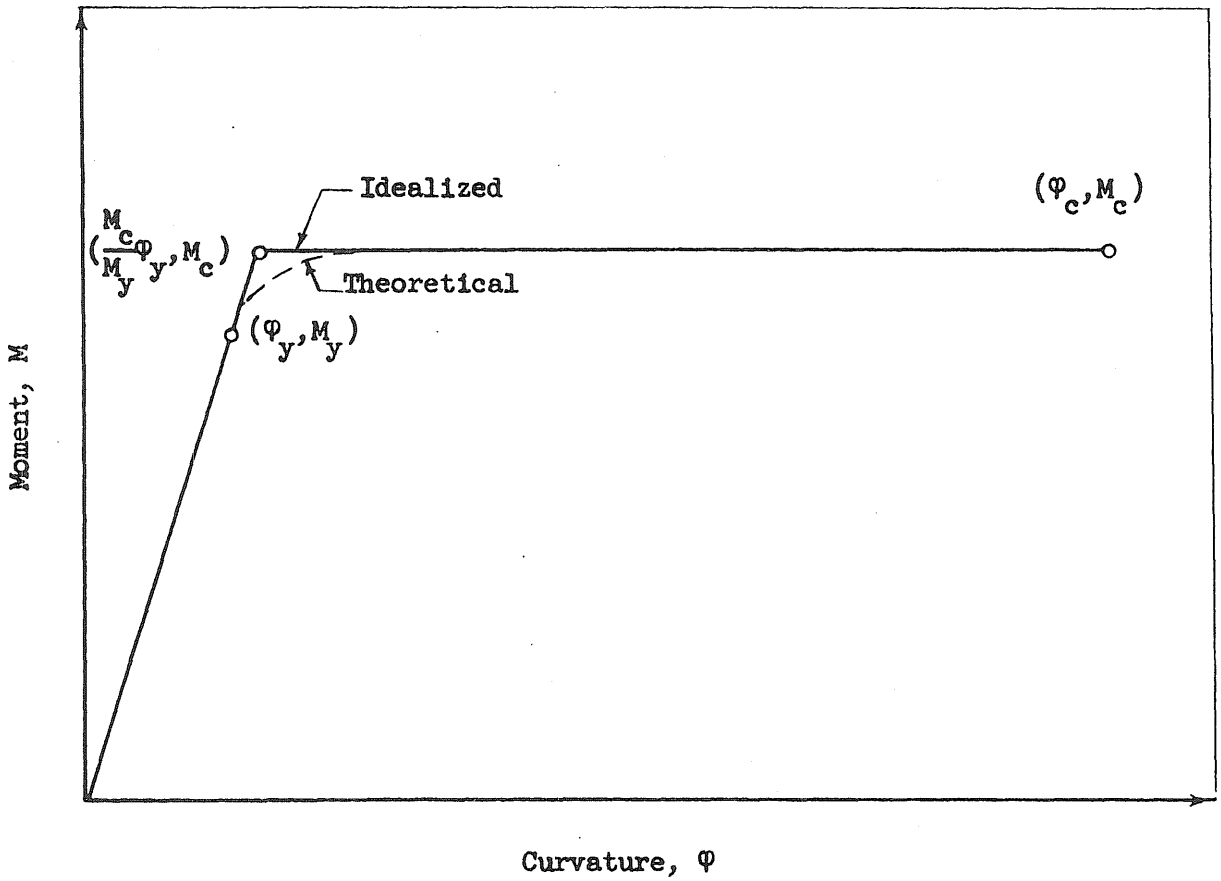

FIG. 4.3 IDEALIZED MOMENT-CURVATURE RELATIONSHIP

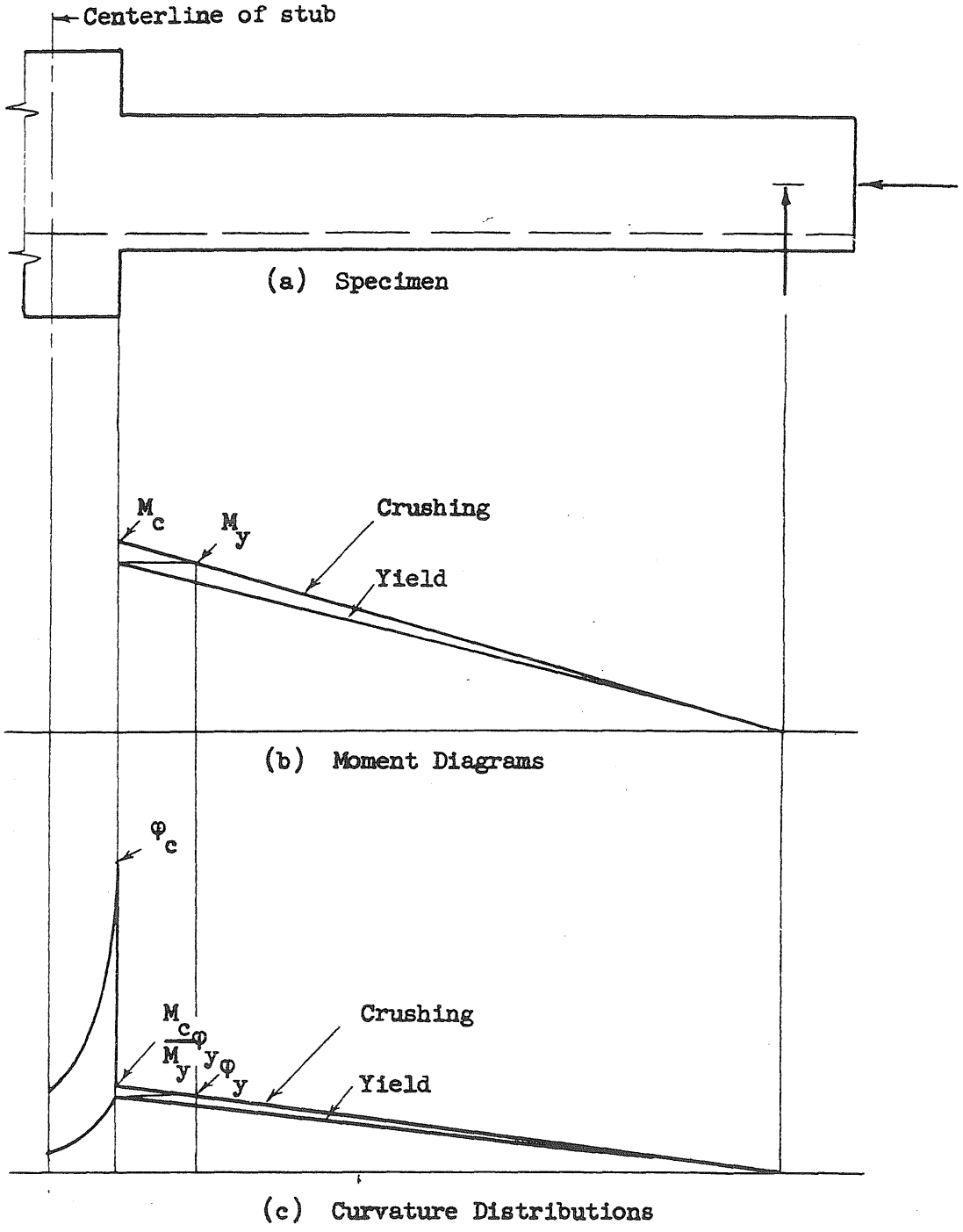

FIG. 4.4 CURVATURE DISTRIBUTION AT YIELD AND CRUSHING ACCORDING TO VERTICAL CRACK THEORIES

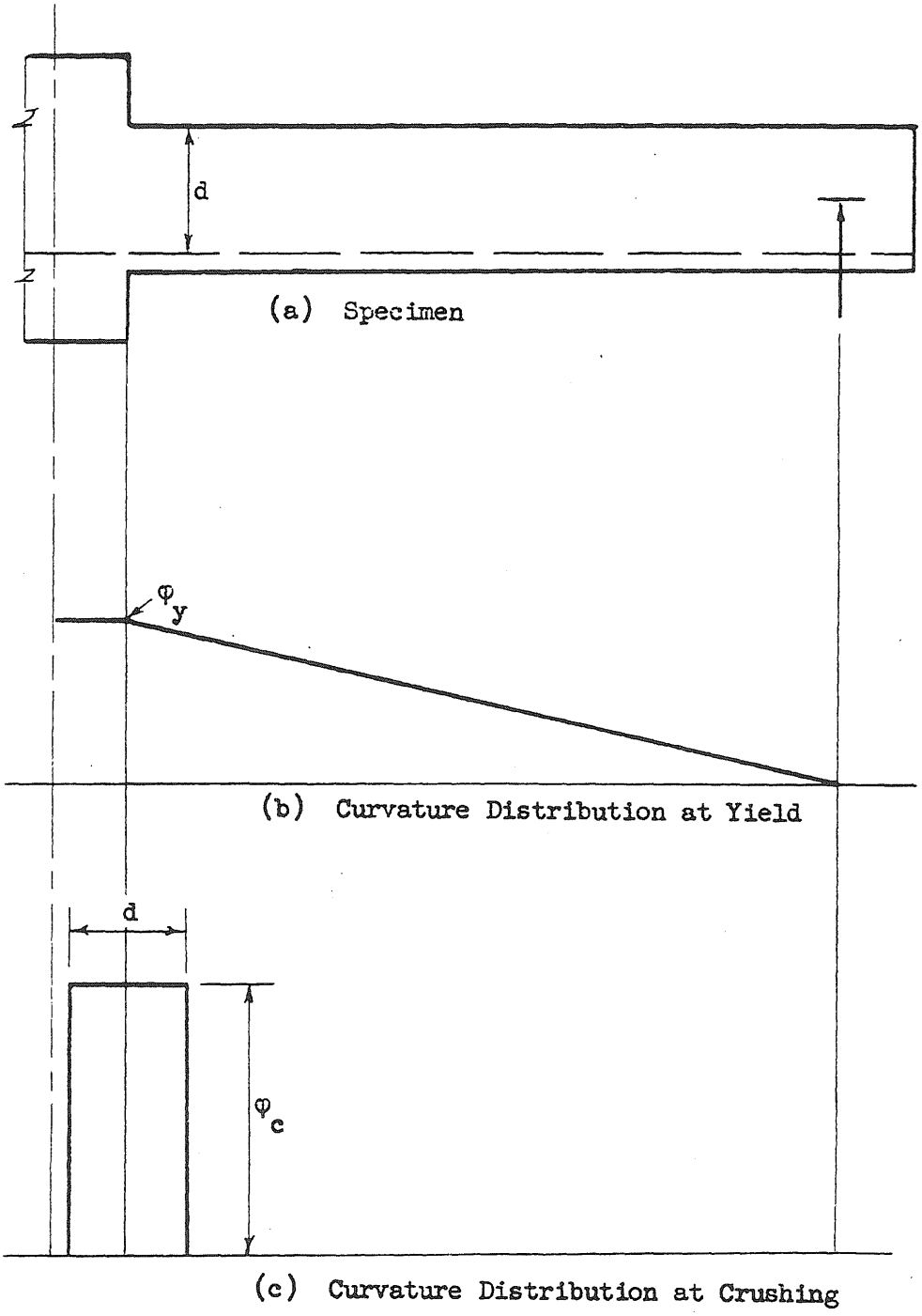

FIG. 4.5 CURVATURE DISTRIBUTION AT YIELD AND CRUSHING ACCORDING TO McCOLLISTER

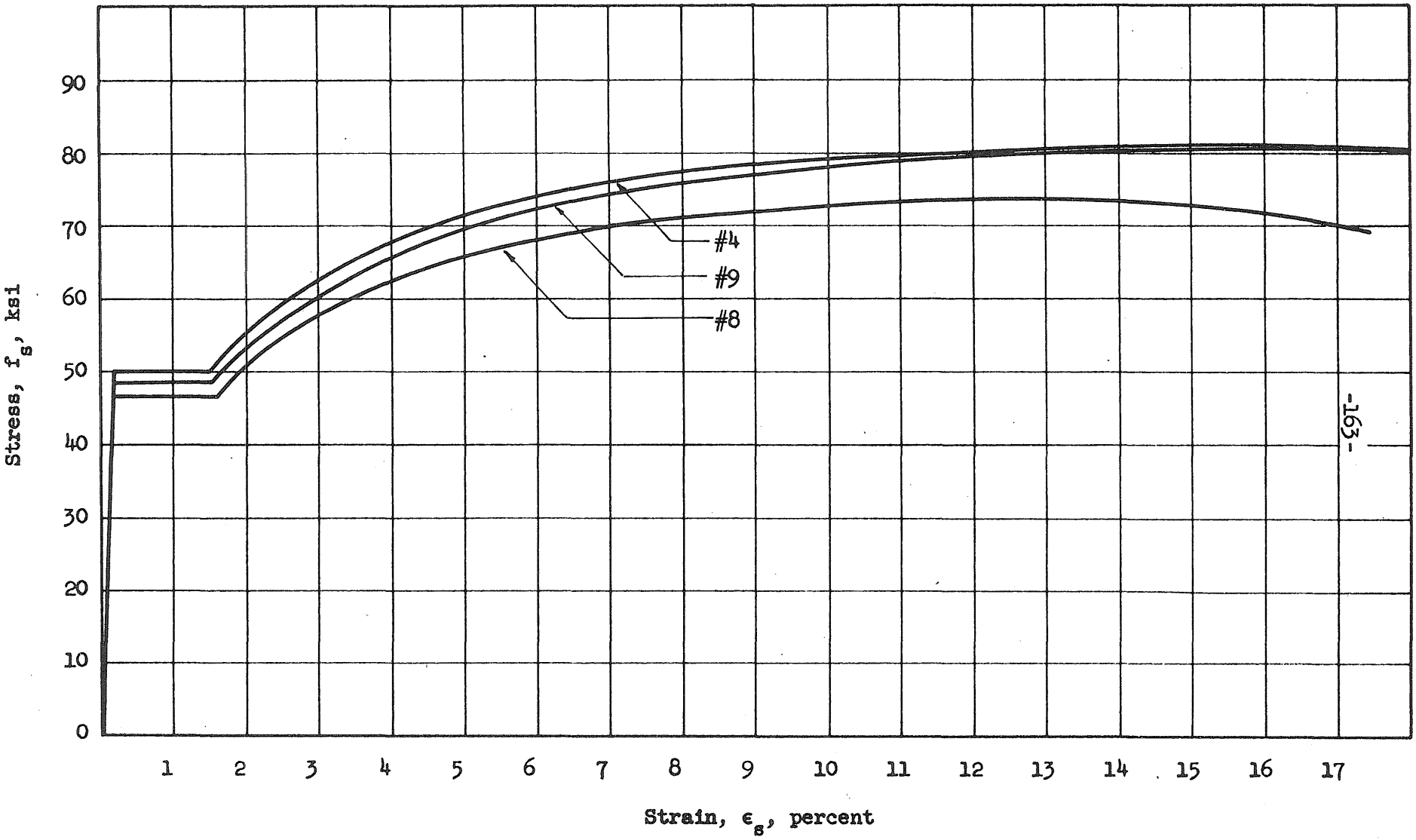

FIG. 4.6 TYPICAL STRESS-STRAIN CURVES FOR REINFORCEMENTS

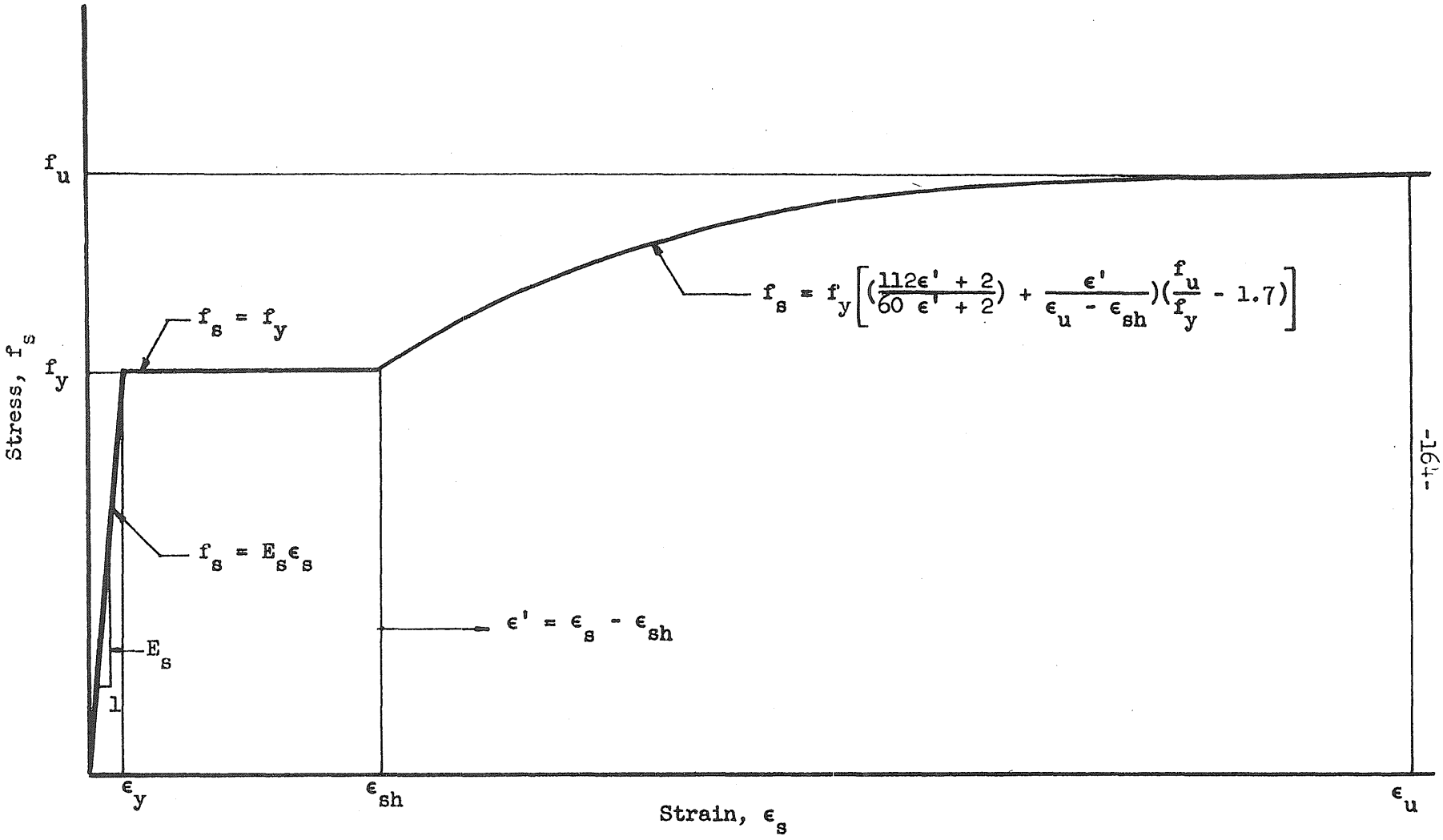

FIG. 4.7 COMPLETE GENERALIZED STRESS-STRAIN CURVE FOR INTERMEDIATE GRADE STEEL (Adapted from Reference 1)

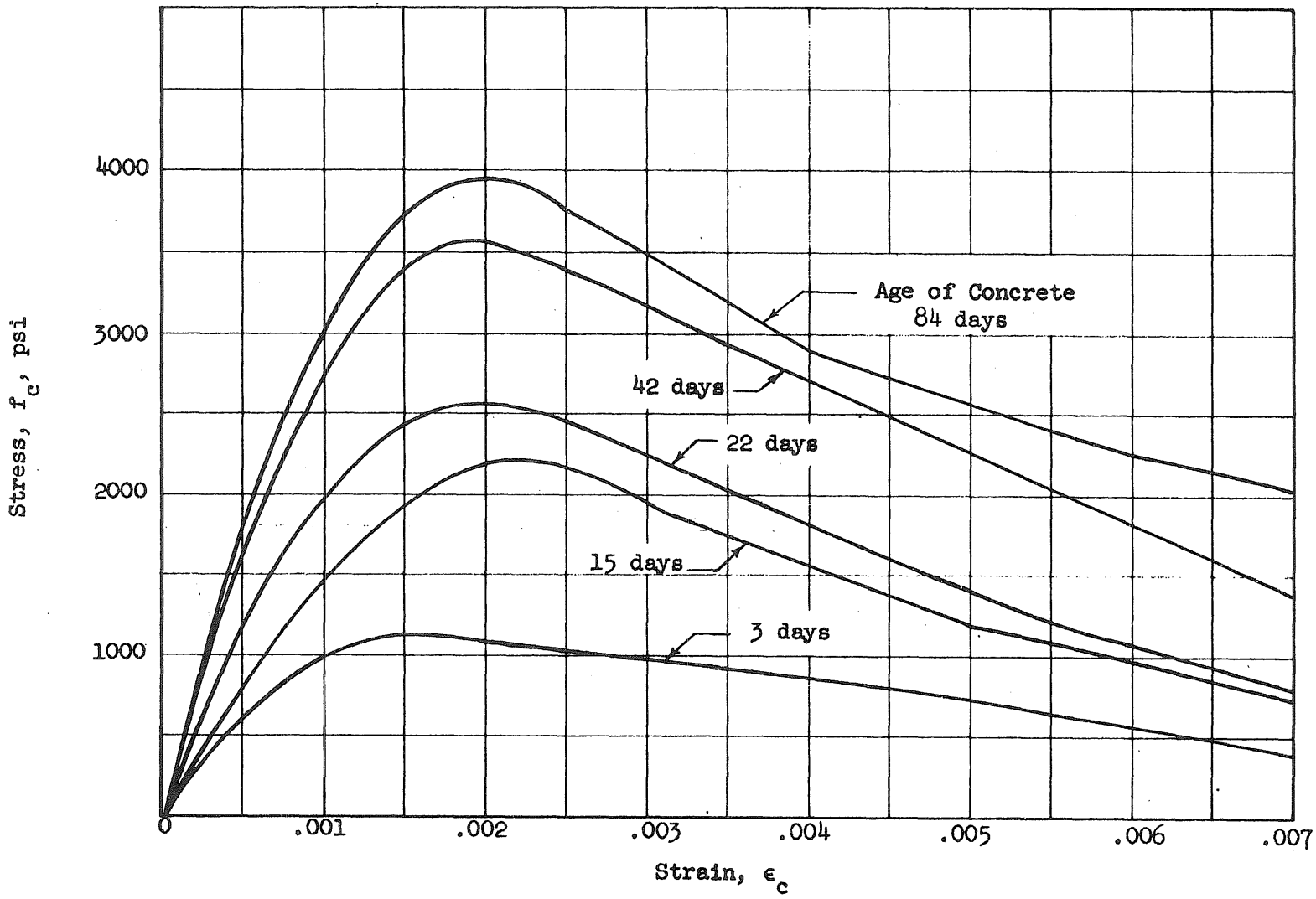

FIG. 4.8 STRESS-STRAIN CURVES FROM COMPRESSION TESTS OF CONCRETE CYLINDERS (Adapted from Reference 11)

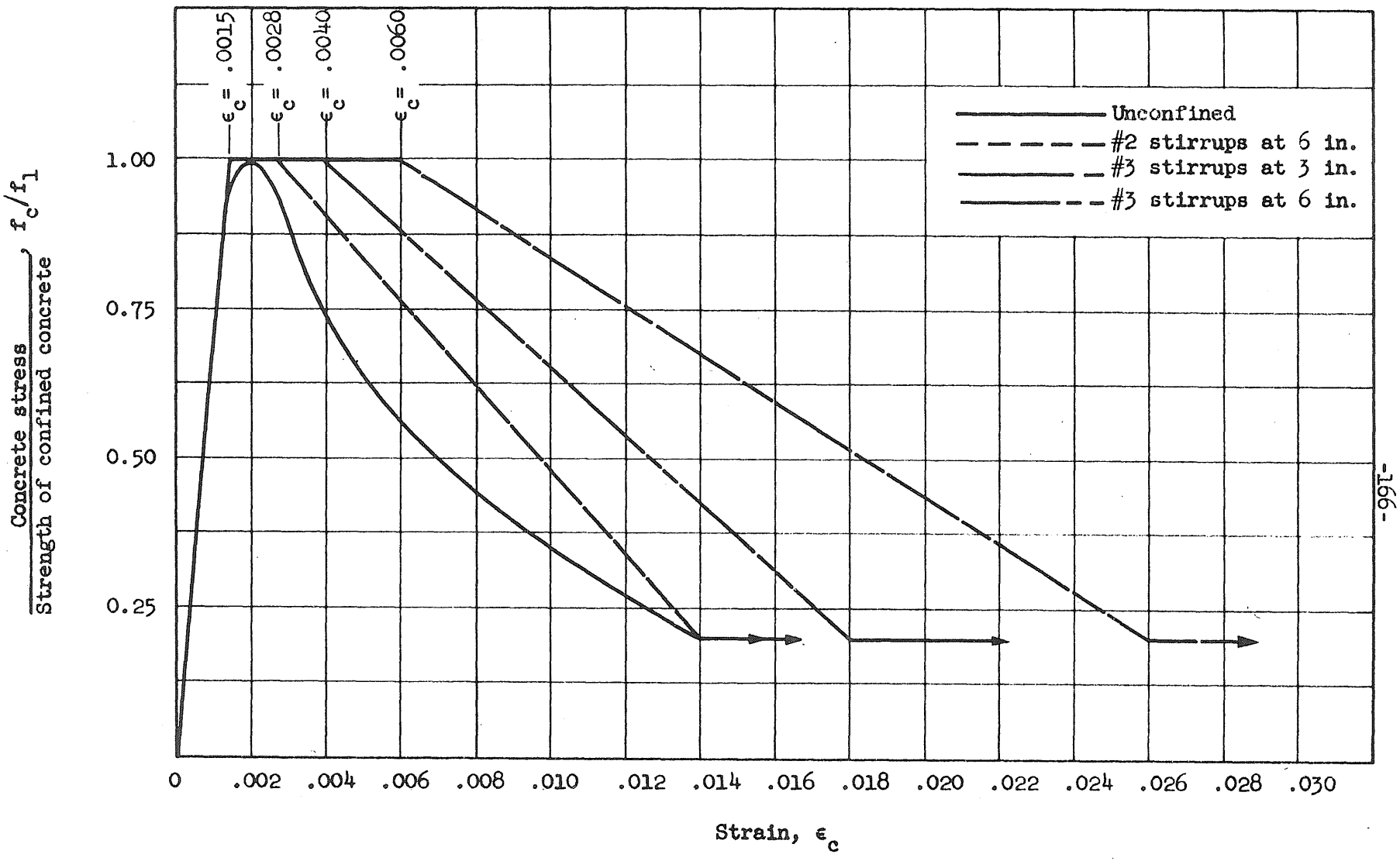

FIG. 4.9 ASSUMED STRESS-STRAIN CURVES FOR CONFINED CONCRETE

Curve No.	Stirrups		f''_y	b"	s
	Size	Area sq. in.	ksi	in.	in.
1*	#2	.05	50.0	5	6
2	#2	.05	50.0	5	6
3	#3	.11	50.0	5	6
4	#3	.11	50.0	4	6
5	#3	.11	50.0	4	3

*U-stirrups; all others closed stirrups.

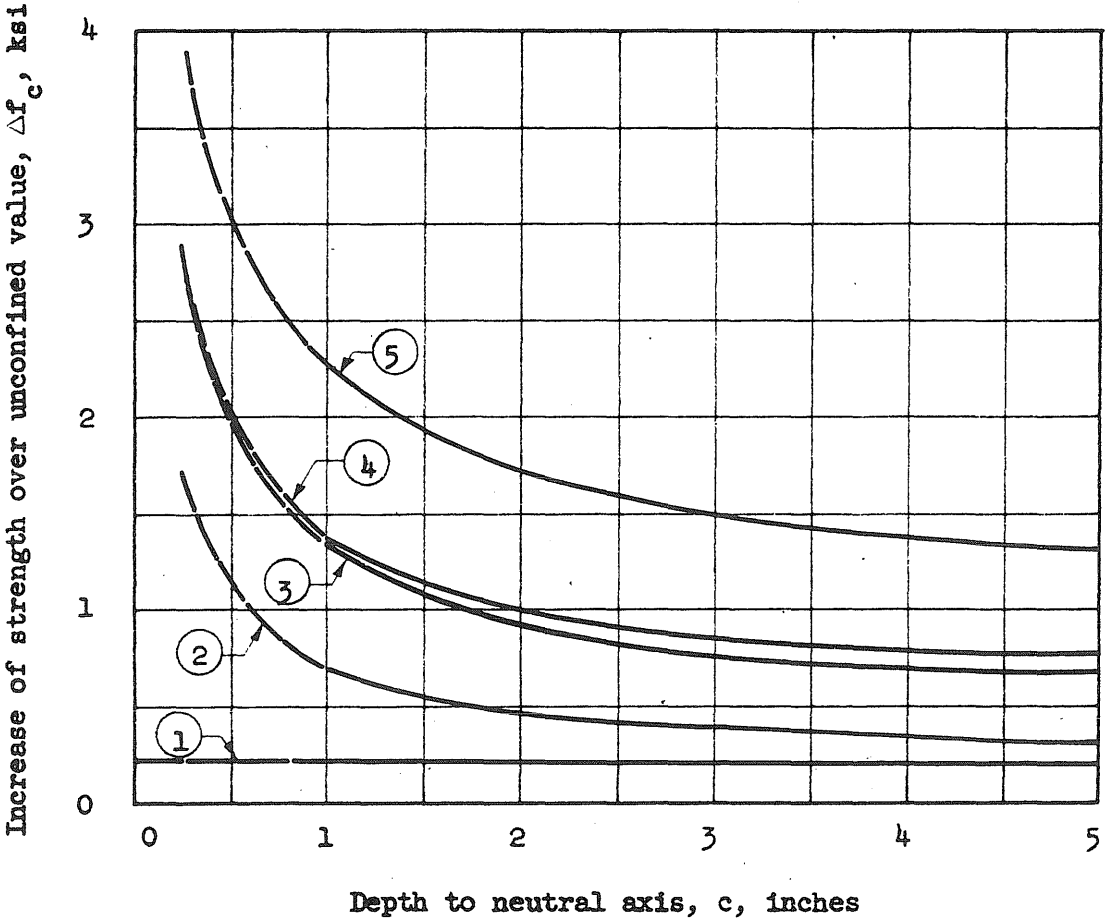

FIG. 4.10 INCREASE OF CONCRETE STRENGTH DUE TO CONFINEMENT

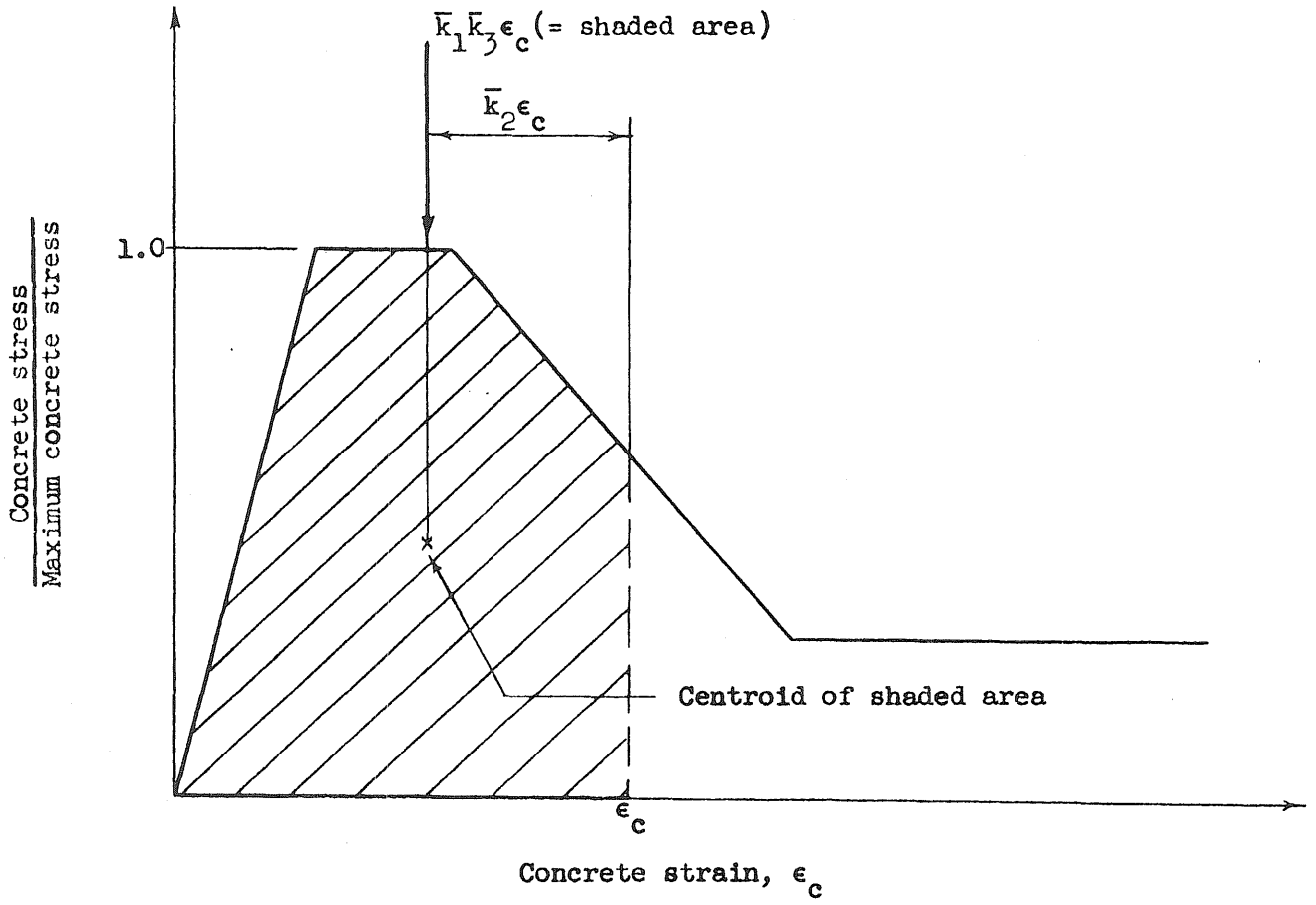

FIG. 4.11 STRESS BLOCK FOR CONFINED CONCRETE

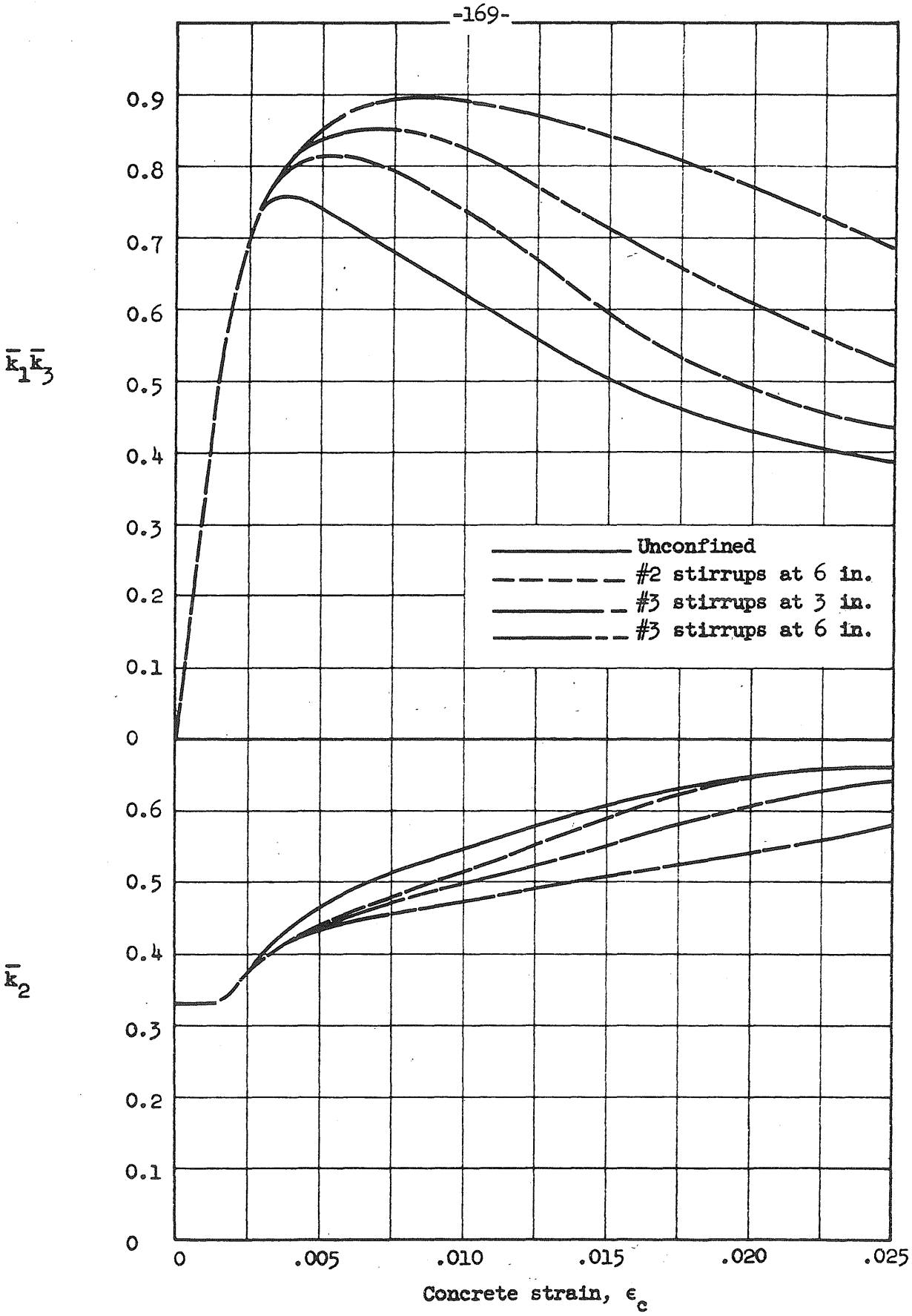

FIG. 4.12 PROPERTIES OF STRESS BLOCK FOR CONFINED CONCRETE

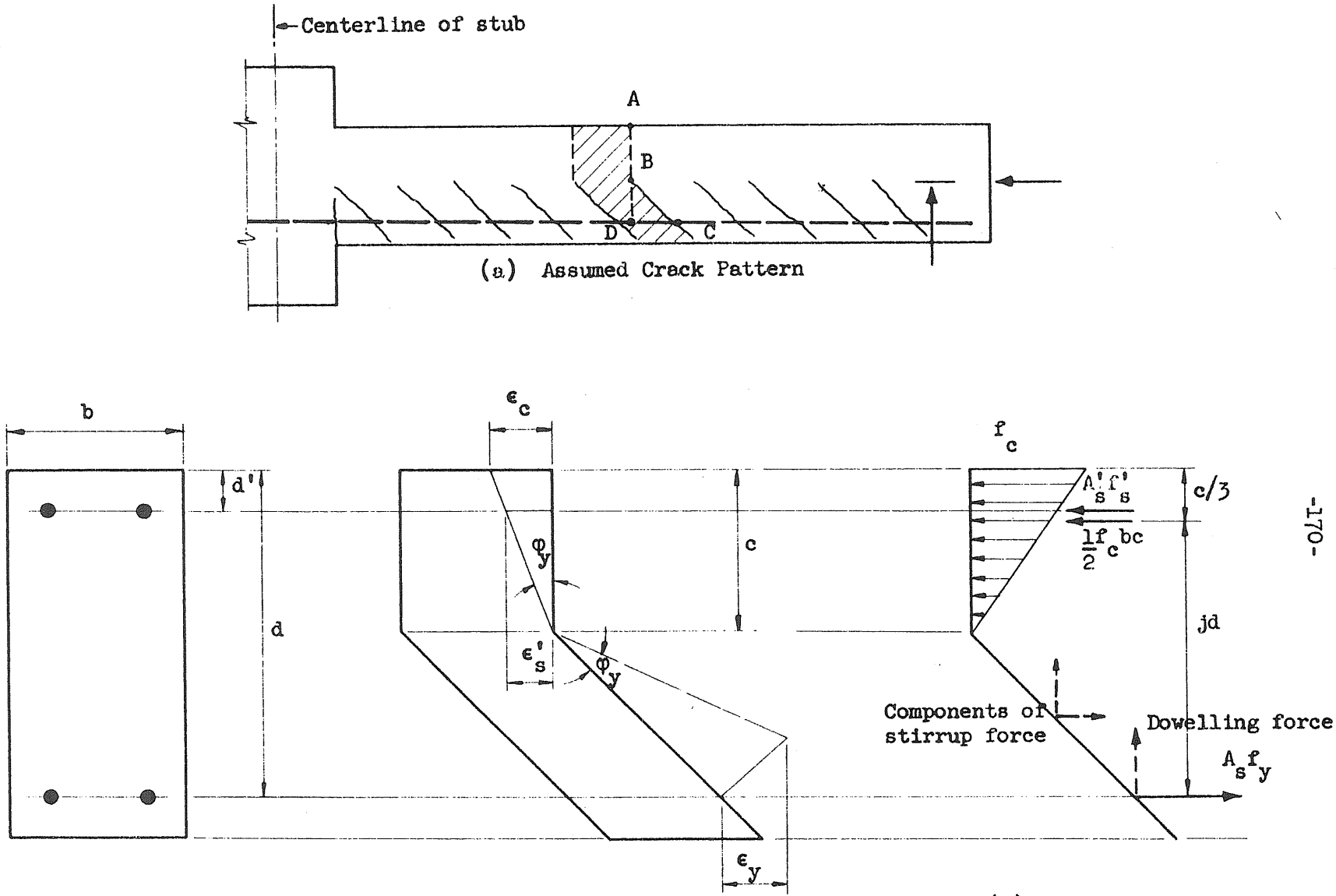

F G. 4.13 STRESS AND STRAIN DISTRIBUTION AT A "CROSS-SECTION" AT YIELD

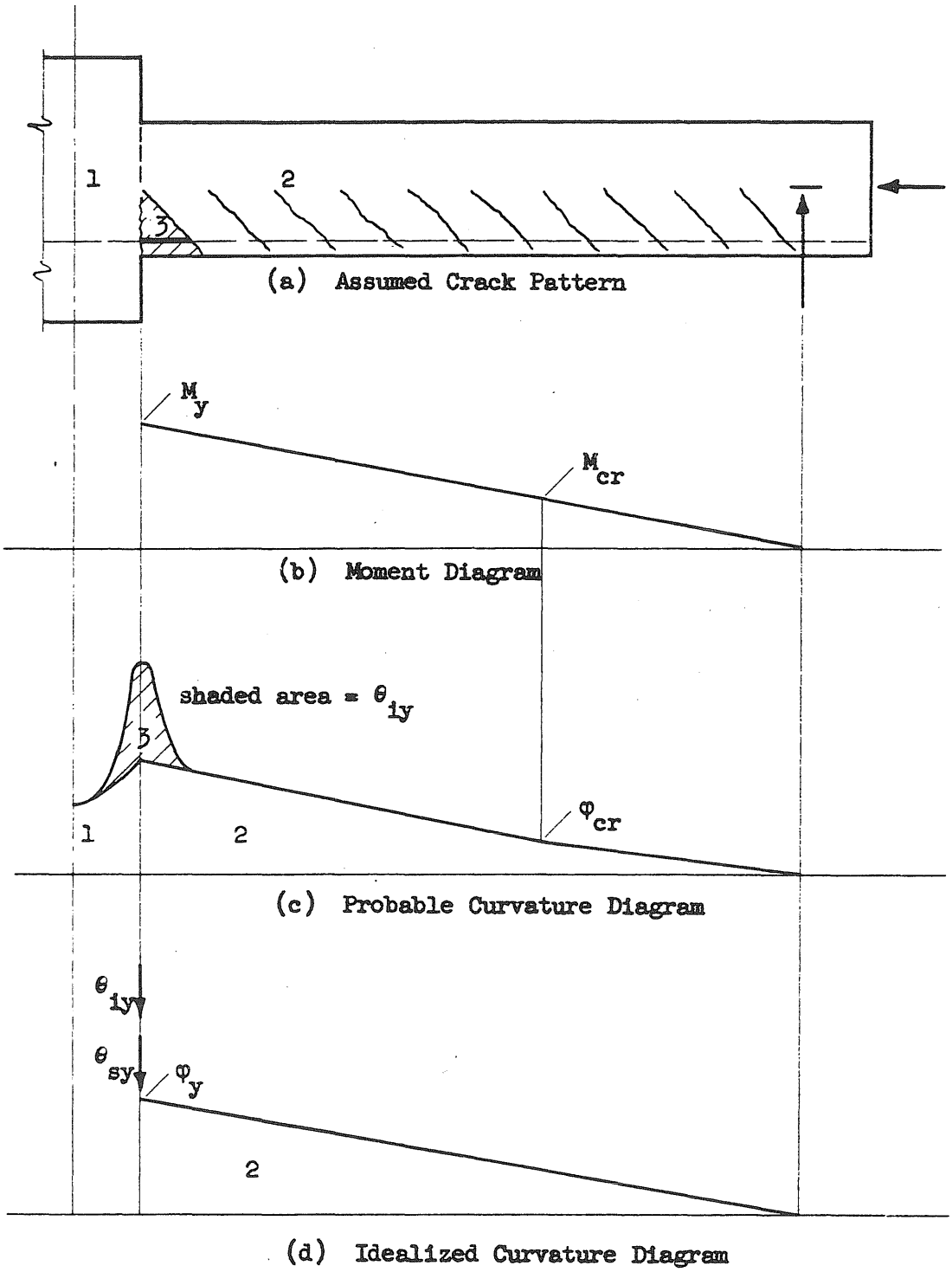

FIG. 4.14 CURVATURE DISTRIBUTION AT YIELD

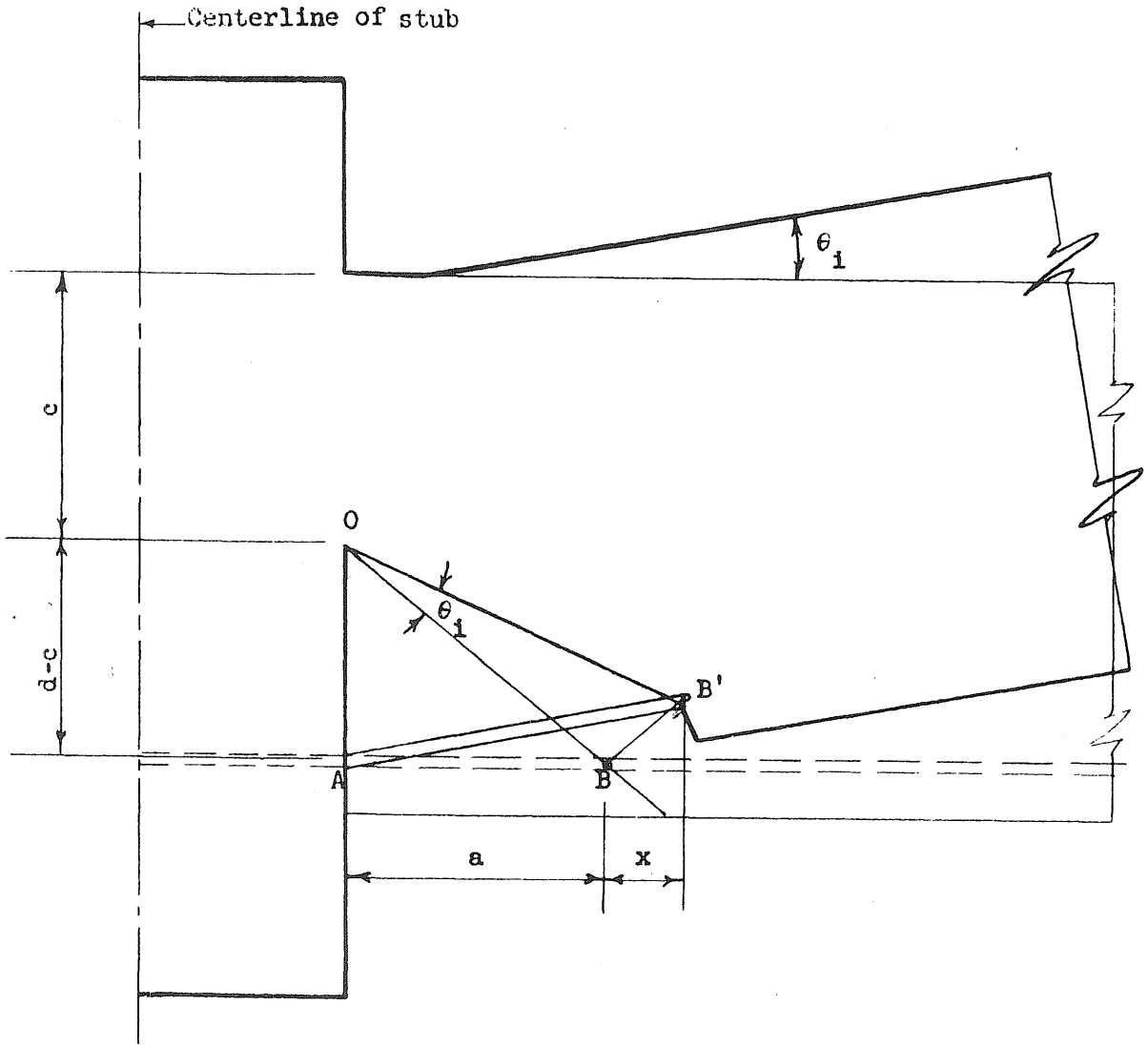

FIG. 4.15 RELATIONSHIP BETWEEN THE ELONGATION OF THE REINFORCEMENT IN THE WEDGE AND THE CORRESPONDING CONCENTRATED RATATION

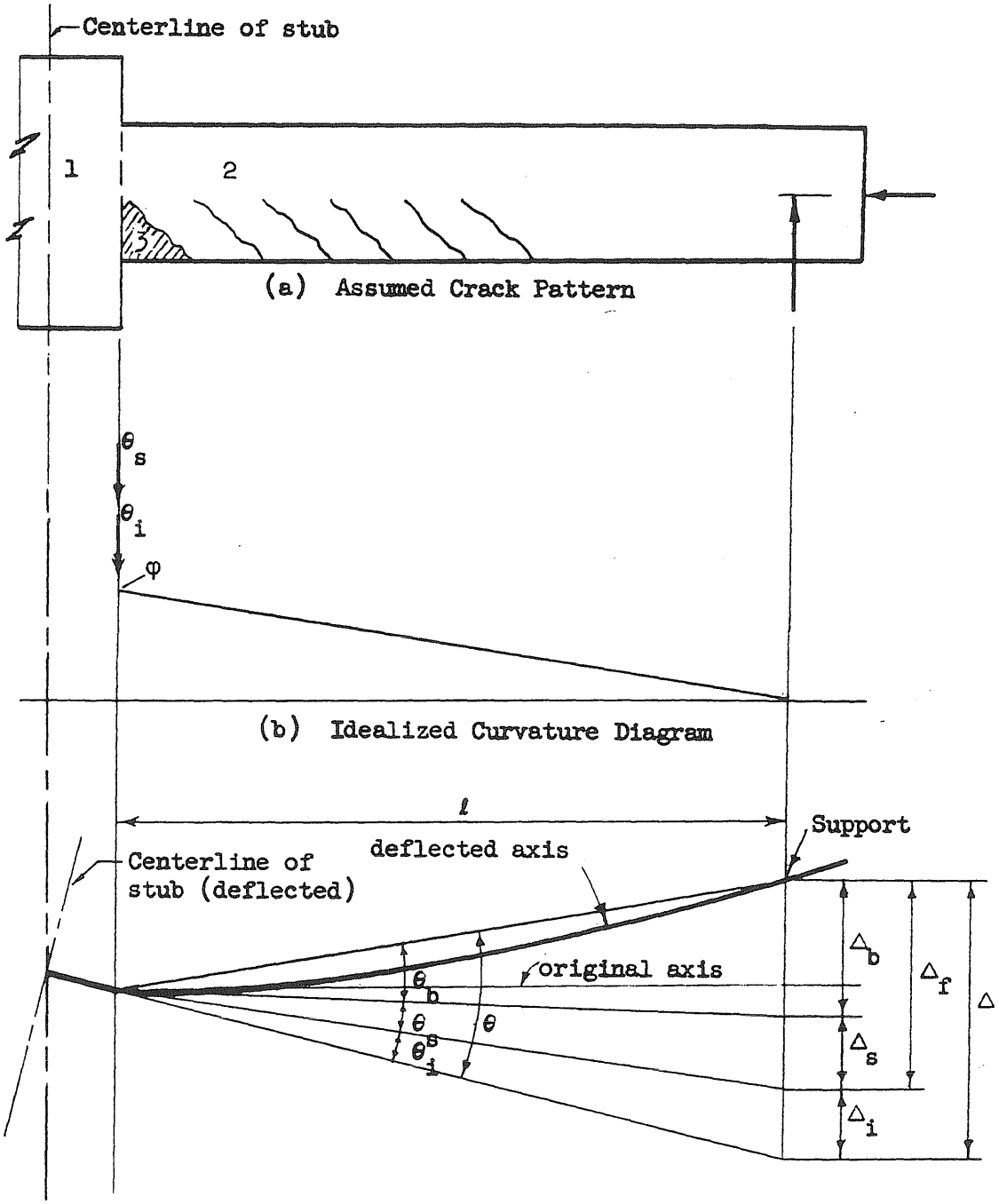

FIG. 4.16 RELATIONSHIP BETWEEN THE CURVATURE DIAGRAM AND THE DEFLECTED CONFIGURATION OF THE SPECIMENS

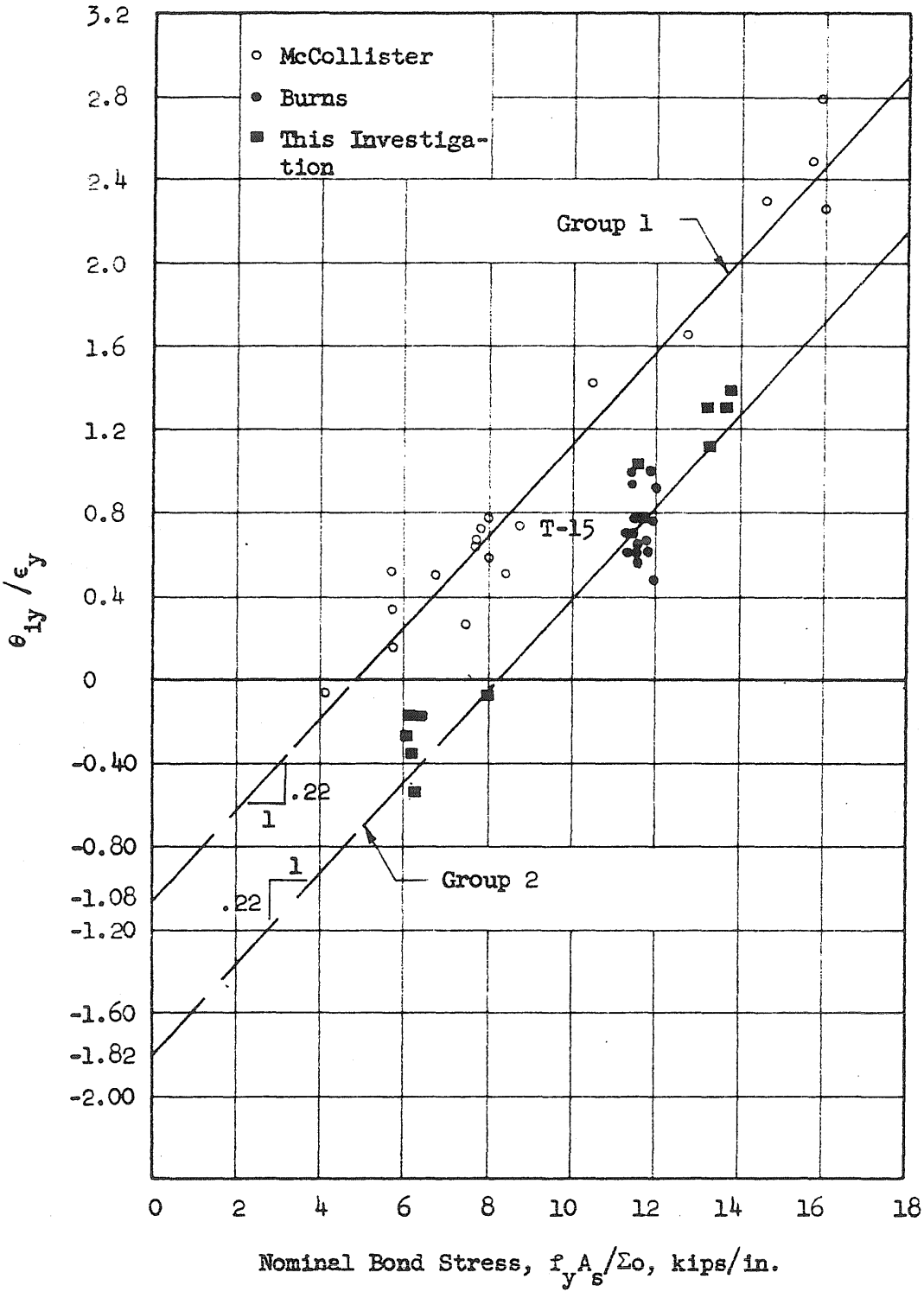

FIG. 4.17 CONCENTRATED ROTATION DUE TO DEFORMATIONS IN WEDGE VERSUS NOMINAL BOND STRESS

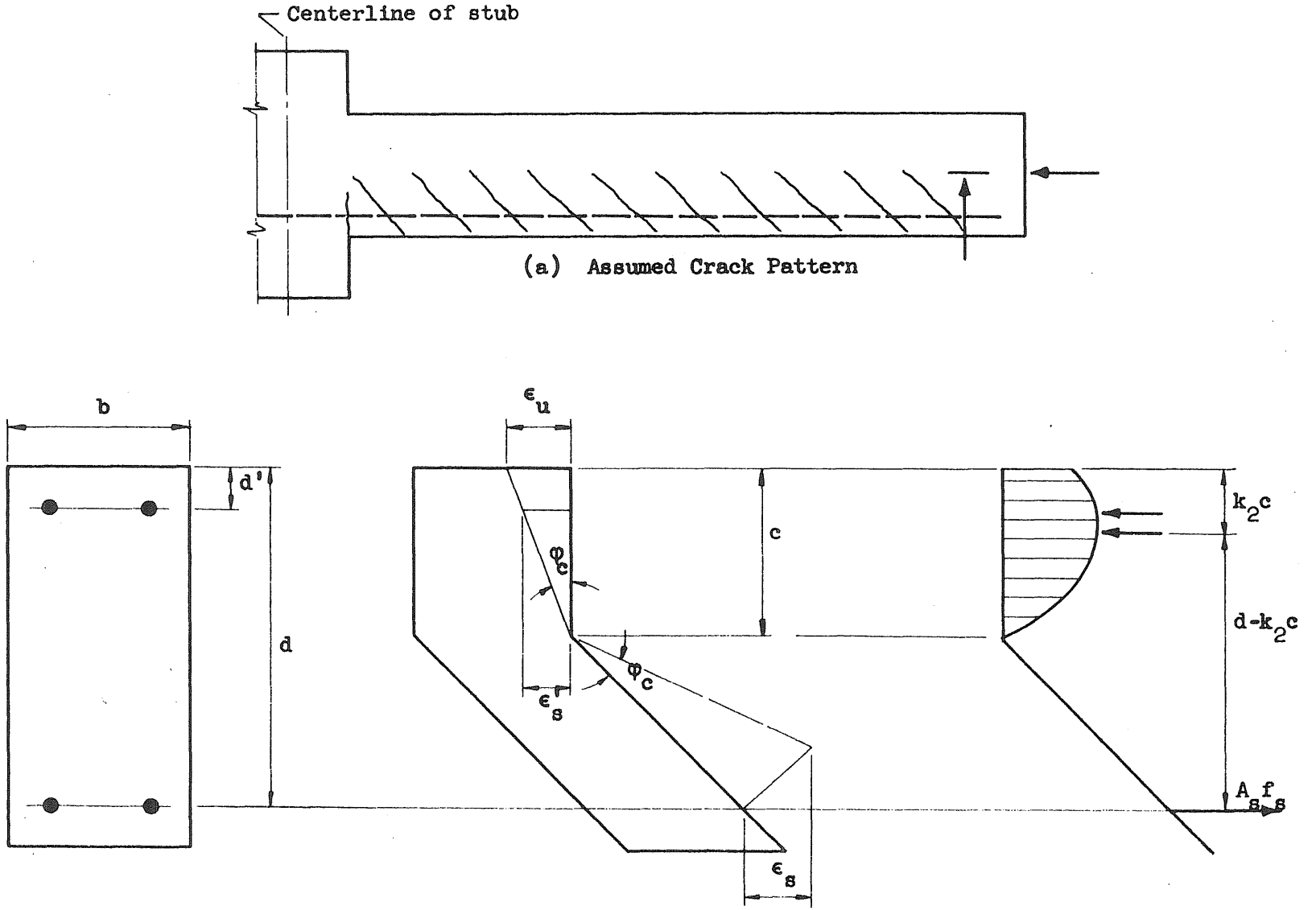

FIG. 4.18 STRESS AND STRAIN DISTRIBUTION AT A "CROSS-SECTION" AT CRUSHING.

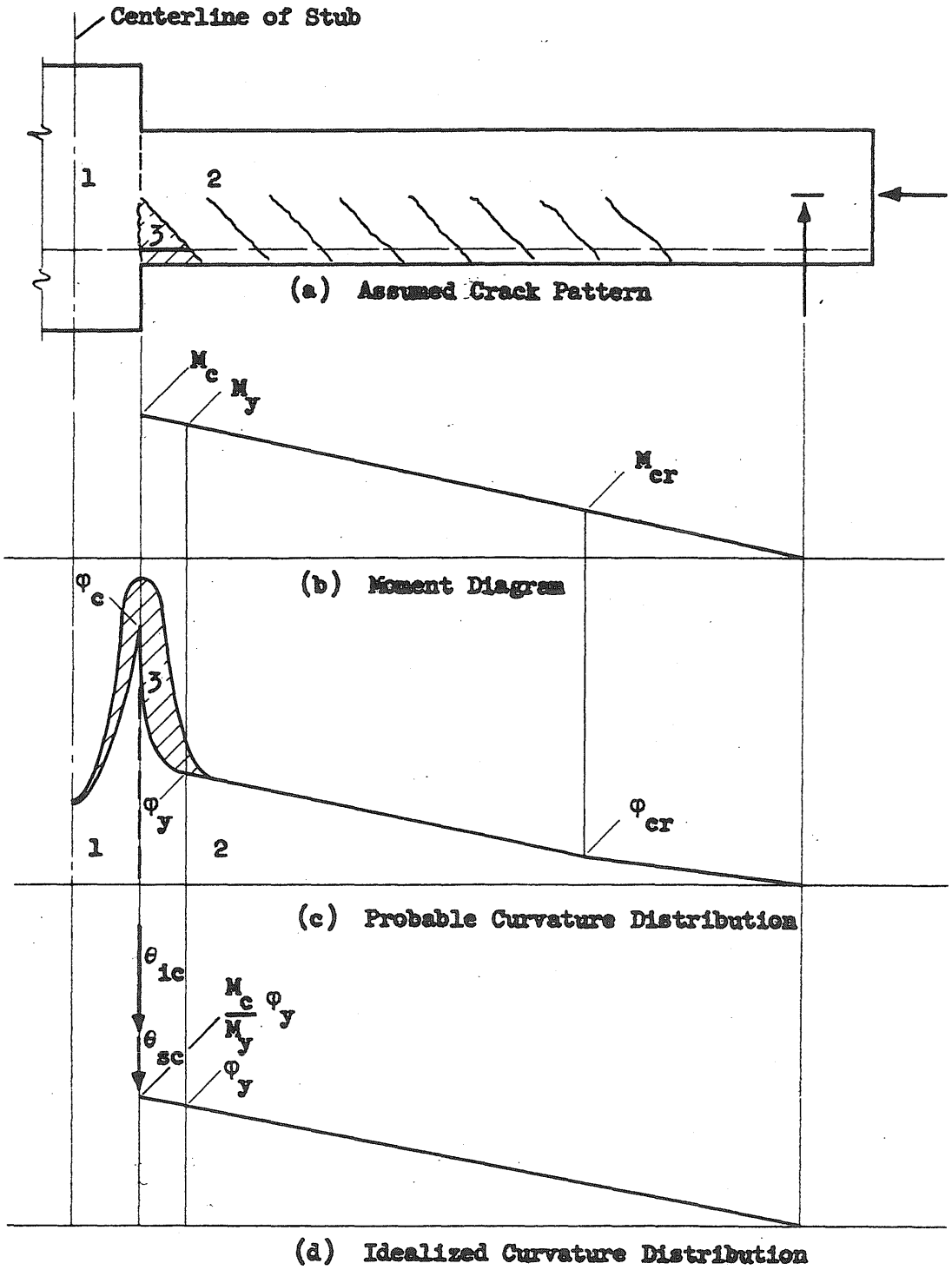

FIG. 4.19 CURVATURE DISTRIBUTION AT CRUSHING

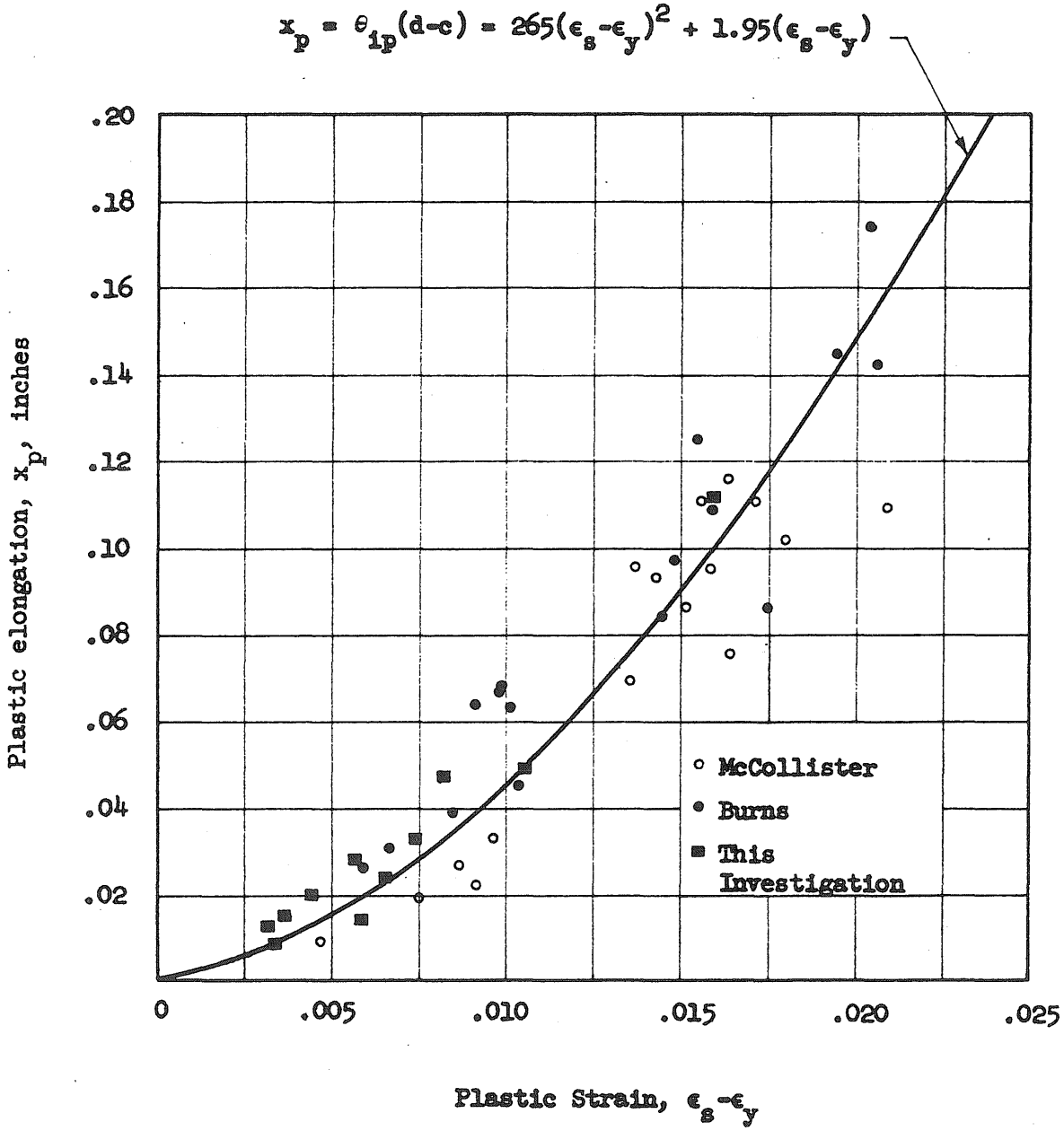

FIG. 4.20 CONCENTRATED ROTATION AT CRUSHING DUE TO PLASTIC DEFORMATIONS IN WEDGE

$$\theta_{ip} = \frac{265(\epsilon_s - \epsilon_y)^2 + 1.95(\epsilon_s - \epsilon_y)}{d-c}$$

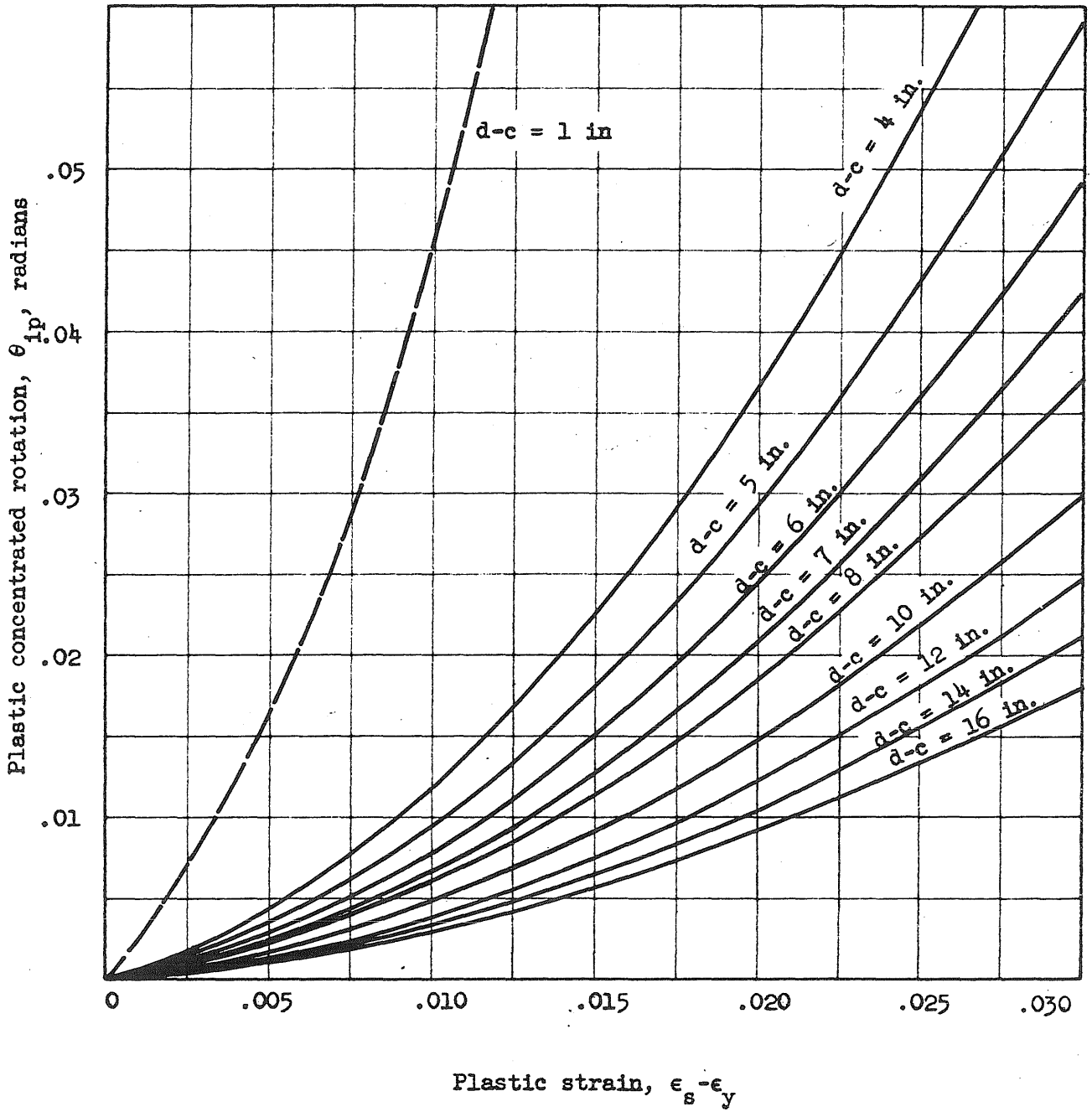

FIG. 4.21 RELATIONSHIPS BETWEEN PLASTIC CONCENTRATED ROTATION AT CRUSHING AND PLASTIC STRAIN FROM EQ. 4.43

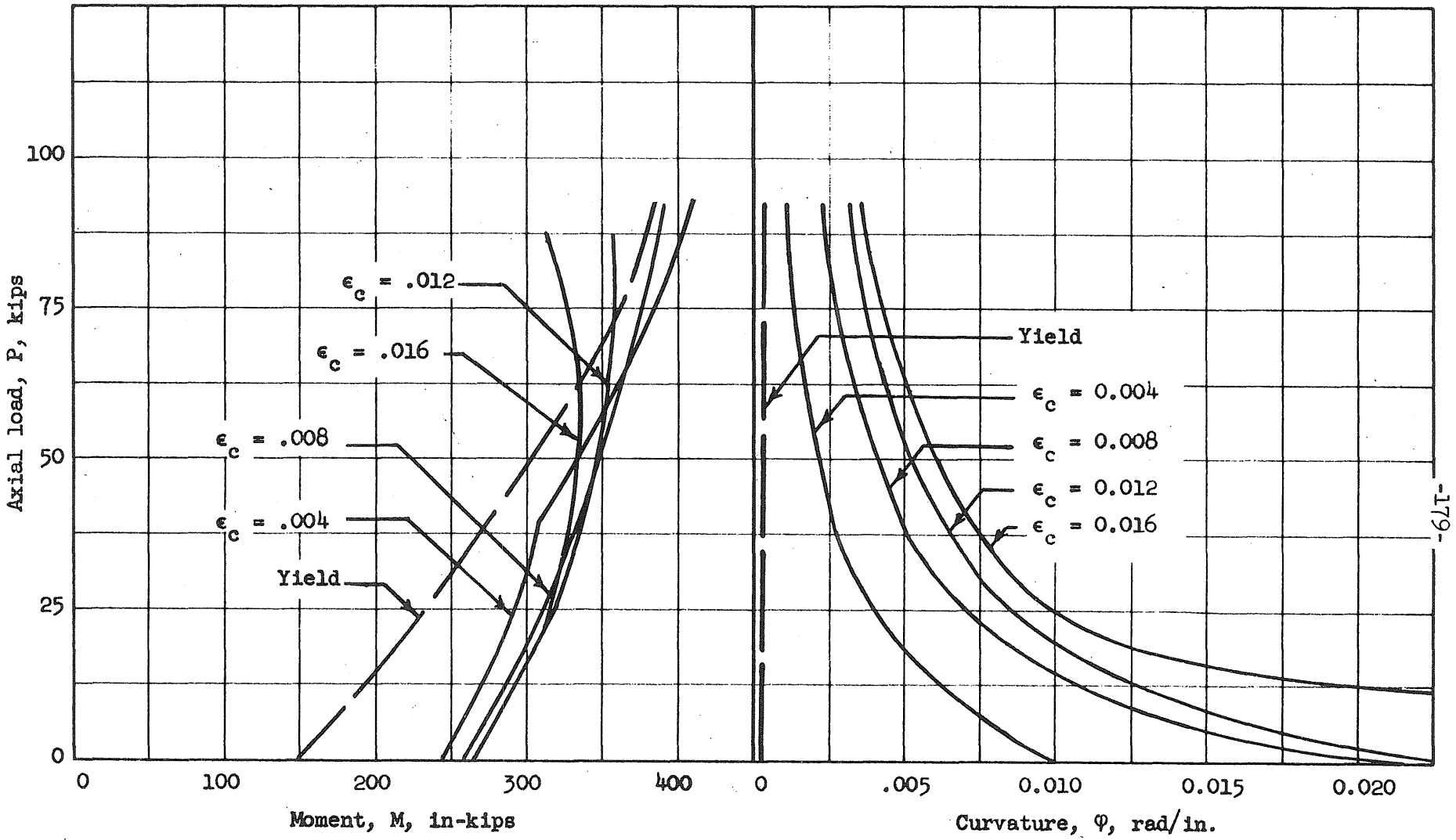

FIG. 4.22 INTERACTION CURVES FOR ADVANCED STAGES OF BEHAVIOR, p_g = 1.11%

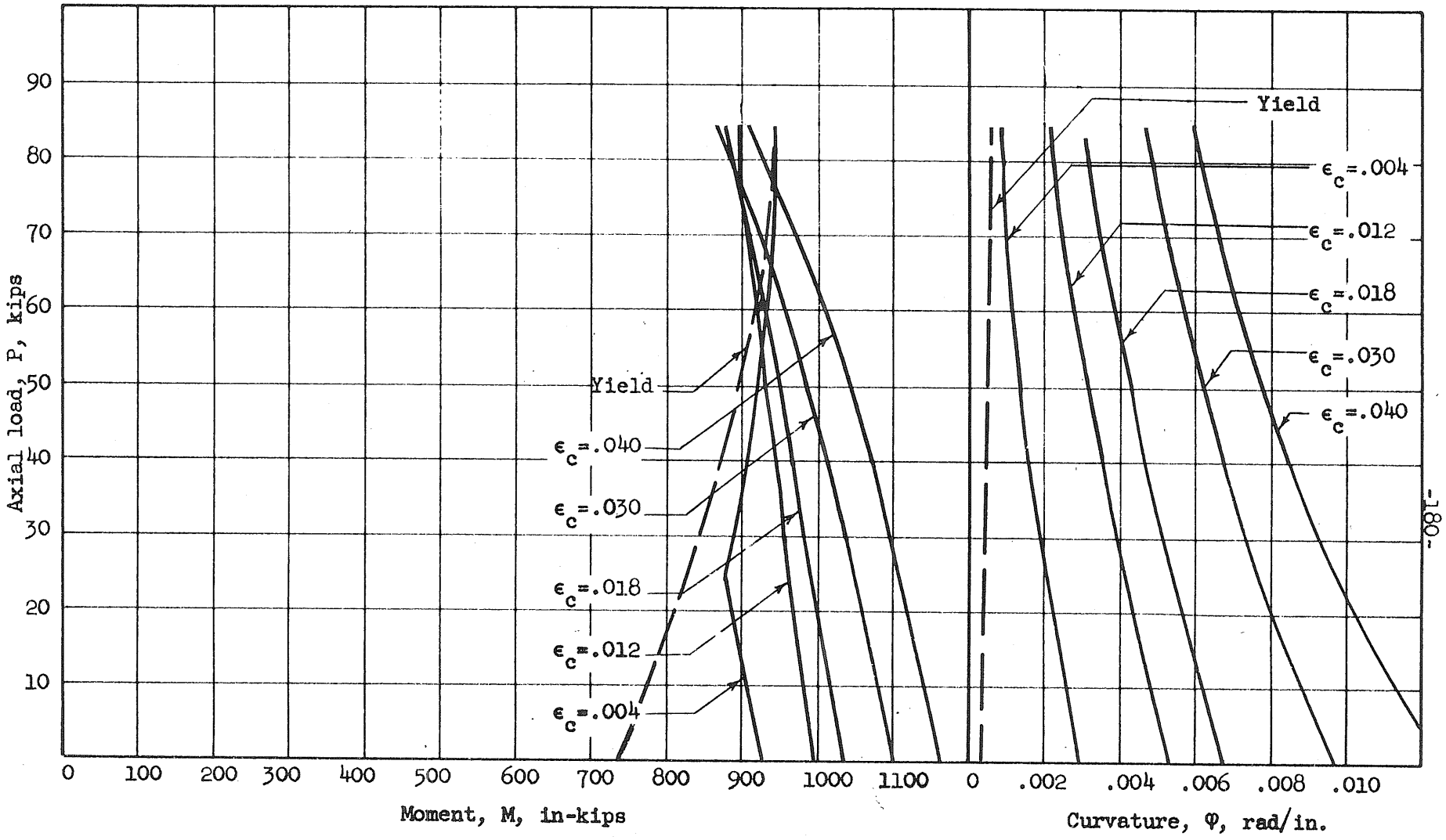

FIG. 4.23 INTERACTION CURVES FOR ADVANCED STAGES OF BEHAVIOR, p_g = 5.55%

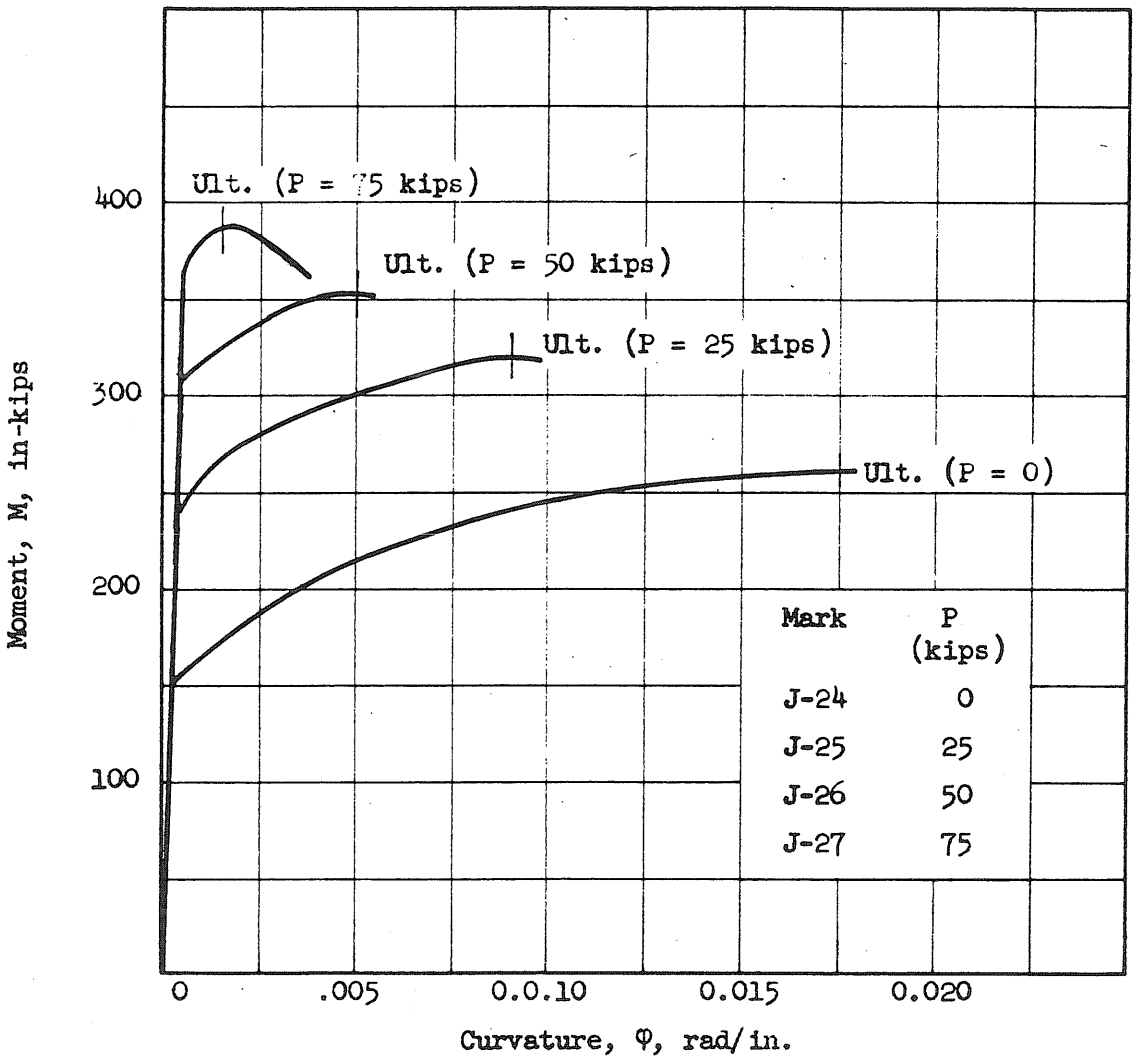

FIG. 4.24 MOMENT-CURVATURE RELATIONSHIPS FOR ADVANCED STAGES OF BEHAVIOR, p_g = 1.11%

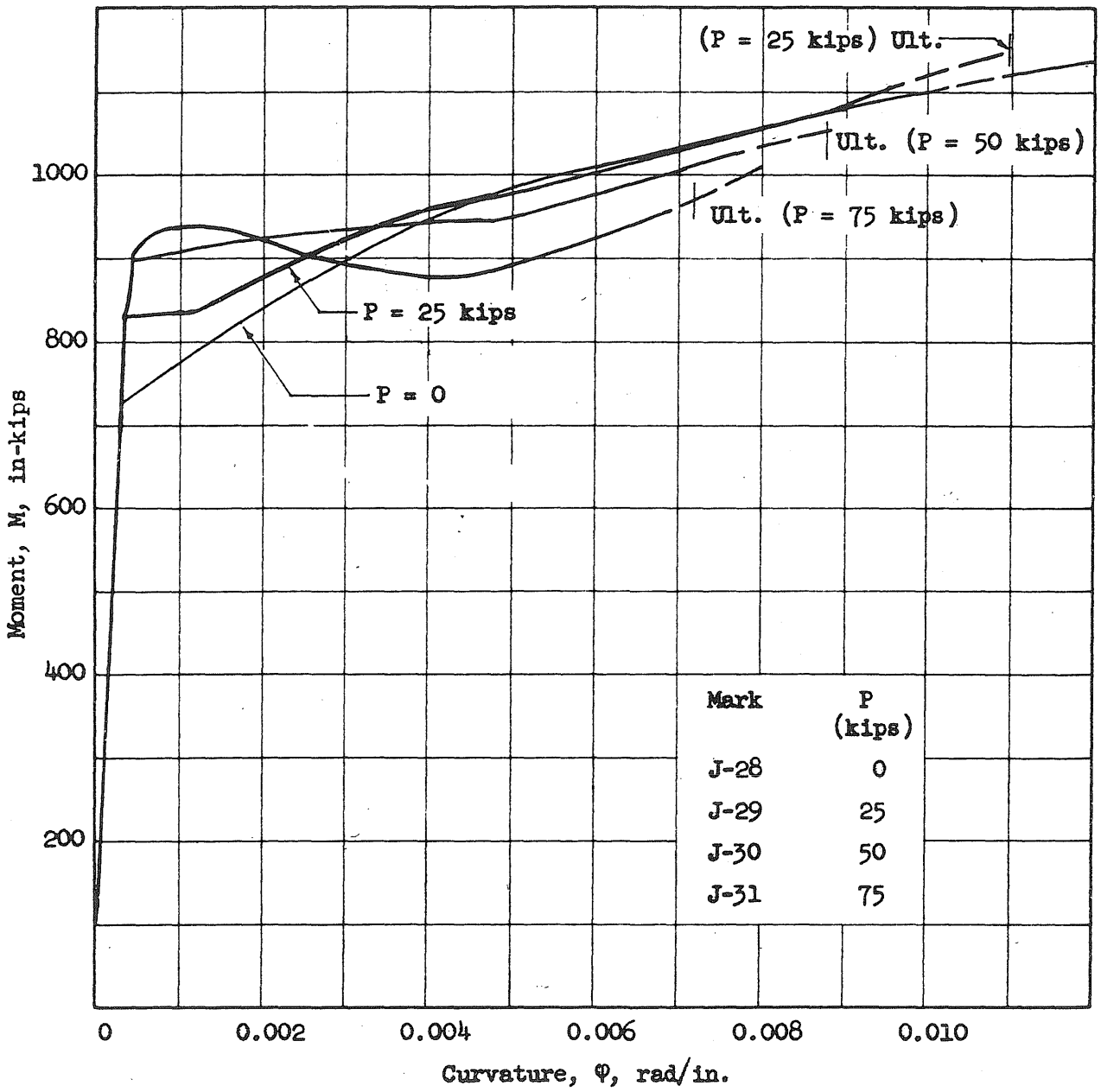

FIG. 4.25 MOMENT-CURVATURE RELATIONSHIPS FOR ADVANCED STAGES OF BEHAVIOR, p_g = 5.55%

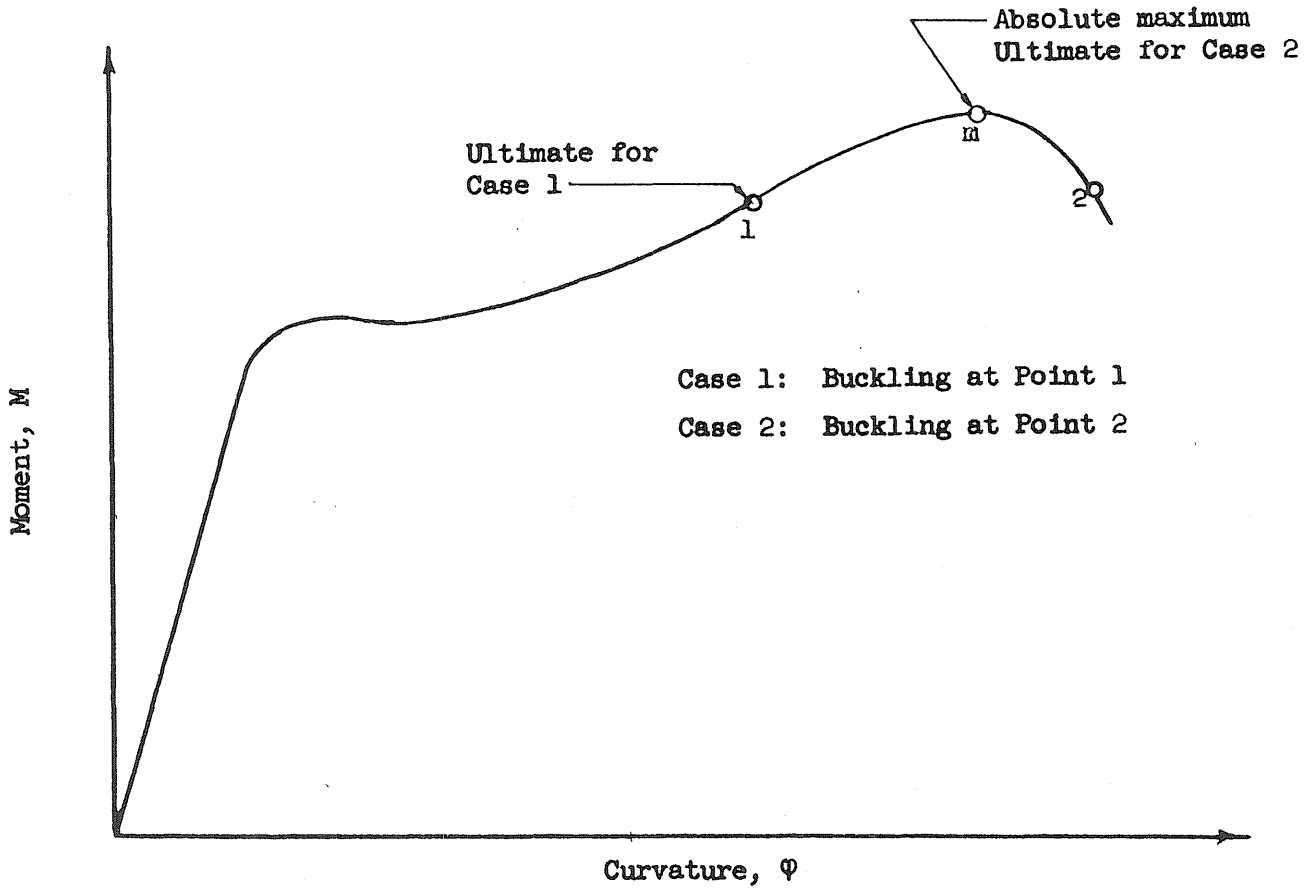

FIG. 4.26 ILLUSTRATION OF CRITERION FOR DETERMINING MOMENTS AND CURVATURES AT ULTIMATE

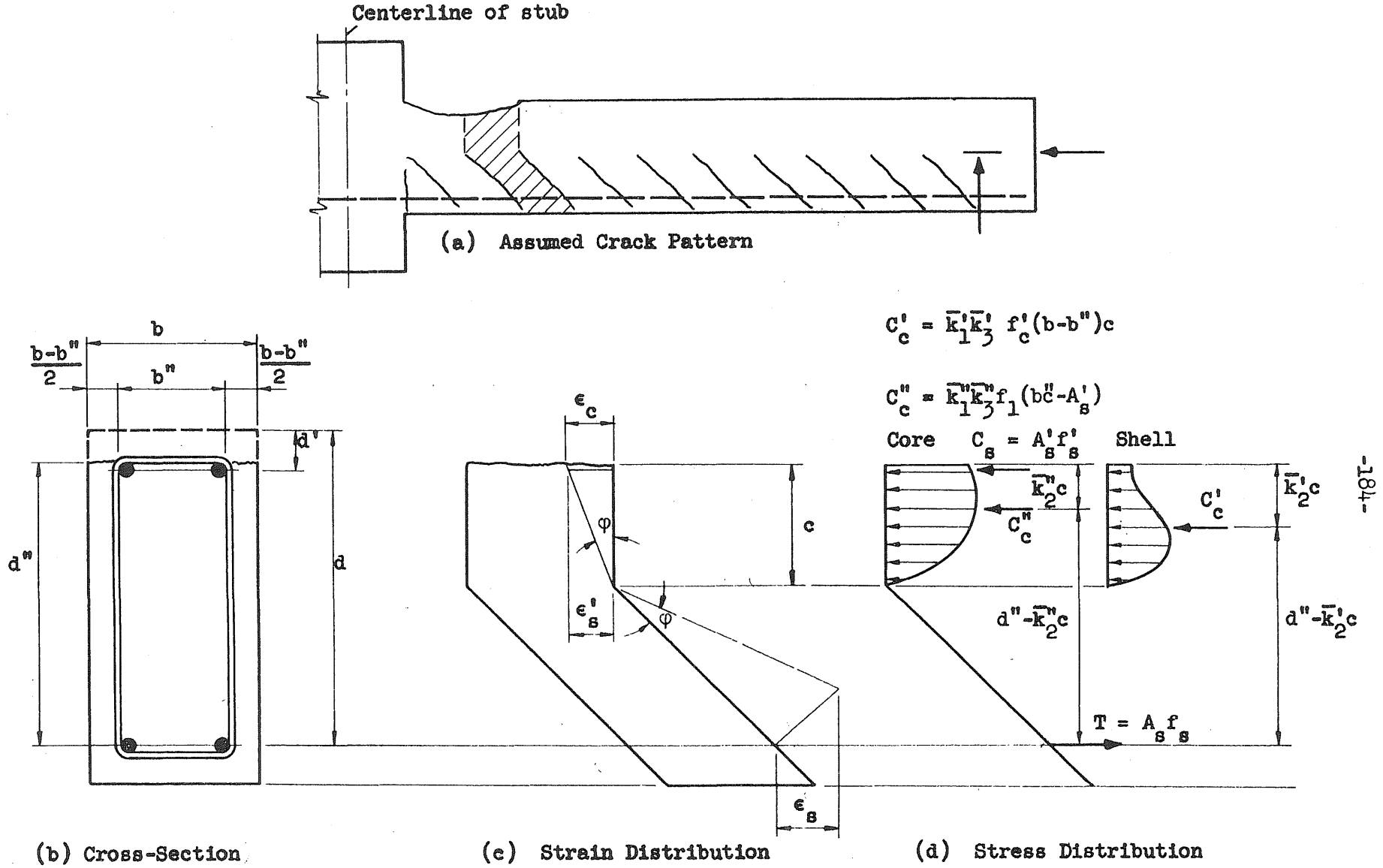

FIG. 4.27 STRESS AND STRAIN DISTRIBUTION AT A "CROSS-SECTION" AT ADVANCED STAGES OF BEHAVIOR

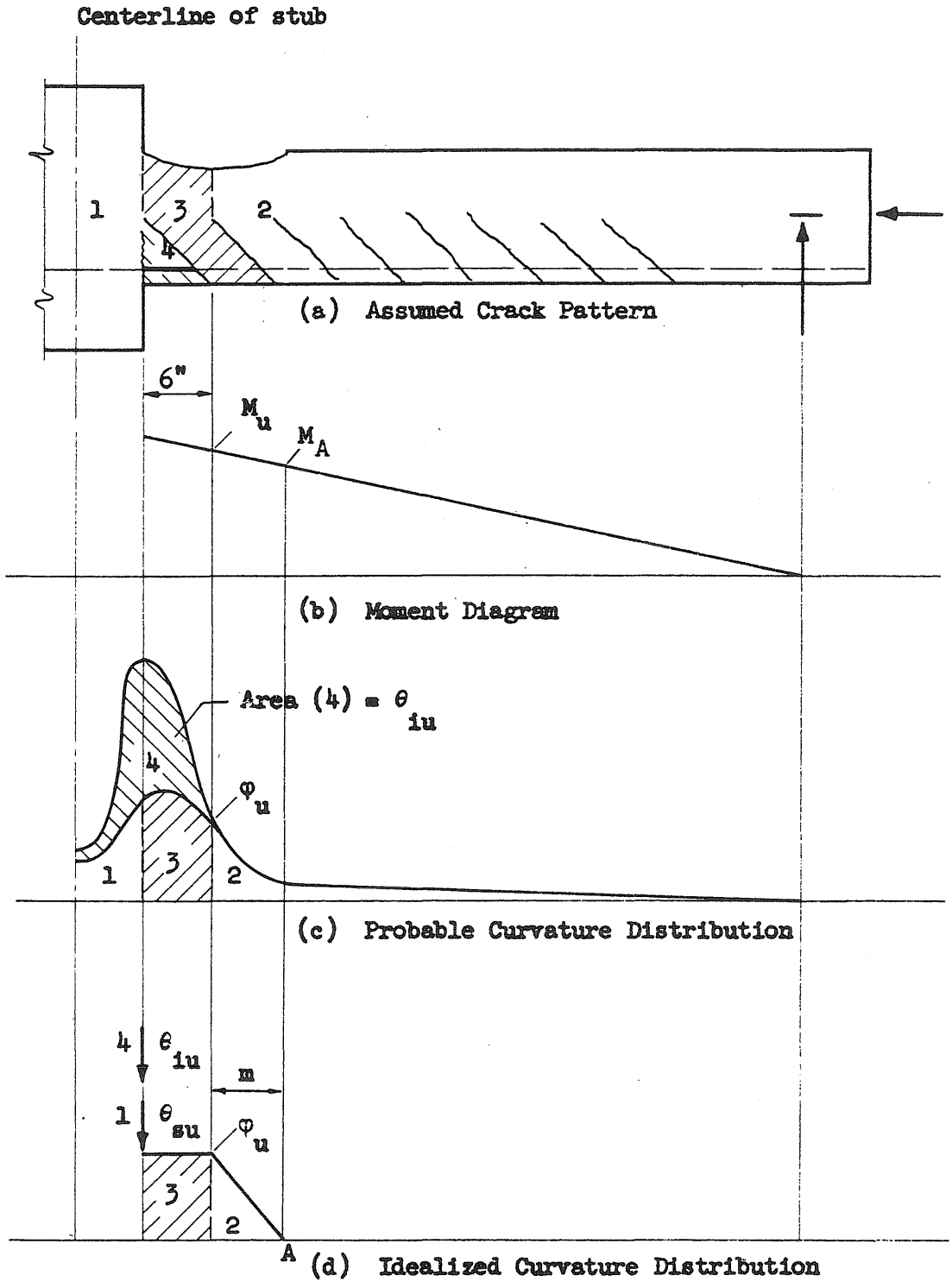

FIG. 4.28 CURVATURE DISTRIBUTION AT ULTIMATE

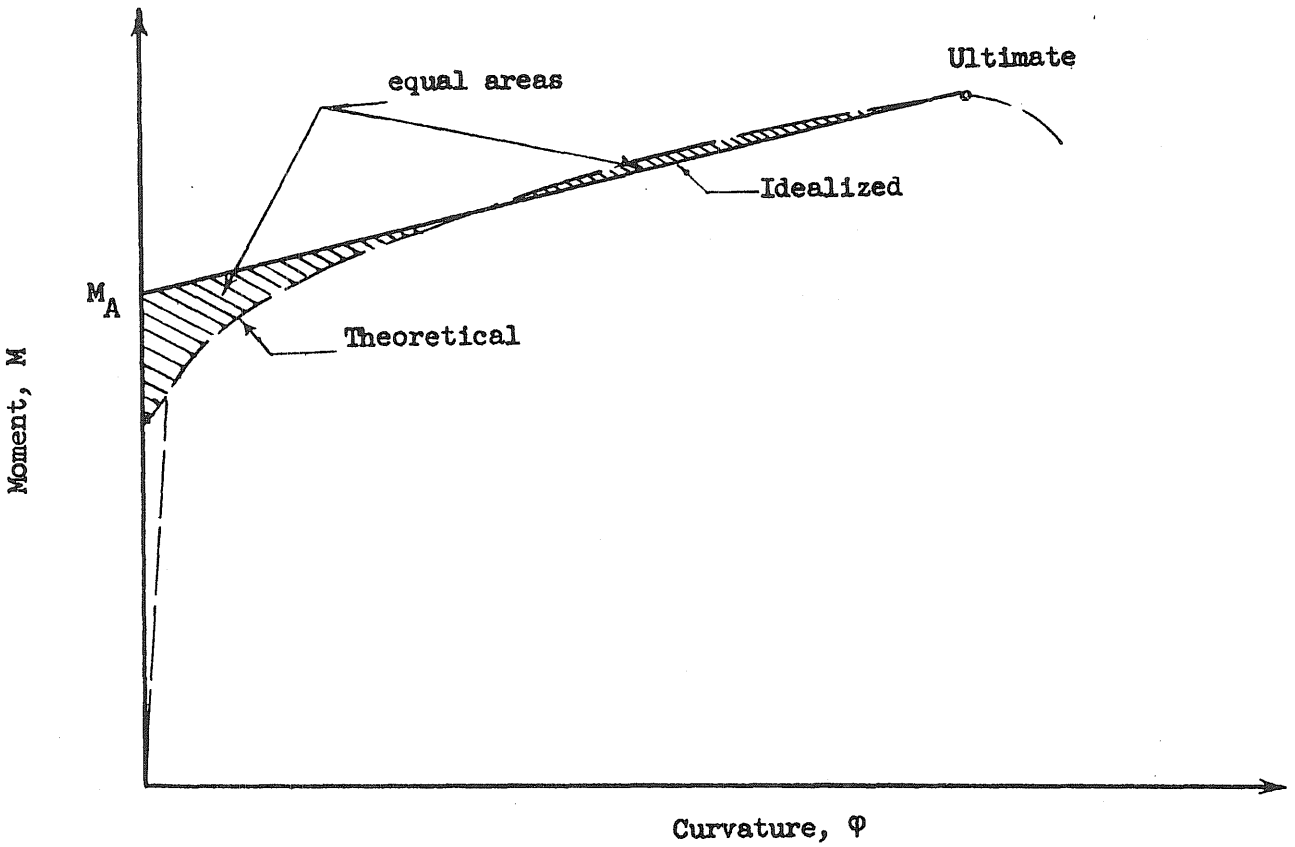

FIG. 4.29 IDEALIZED MOMENT-CURVATURE RELATIONSHIP USED FOR THE DETERMINATION OF THE POINT OF ZERO CURVATURE AT ULTIMATE

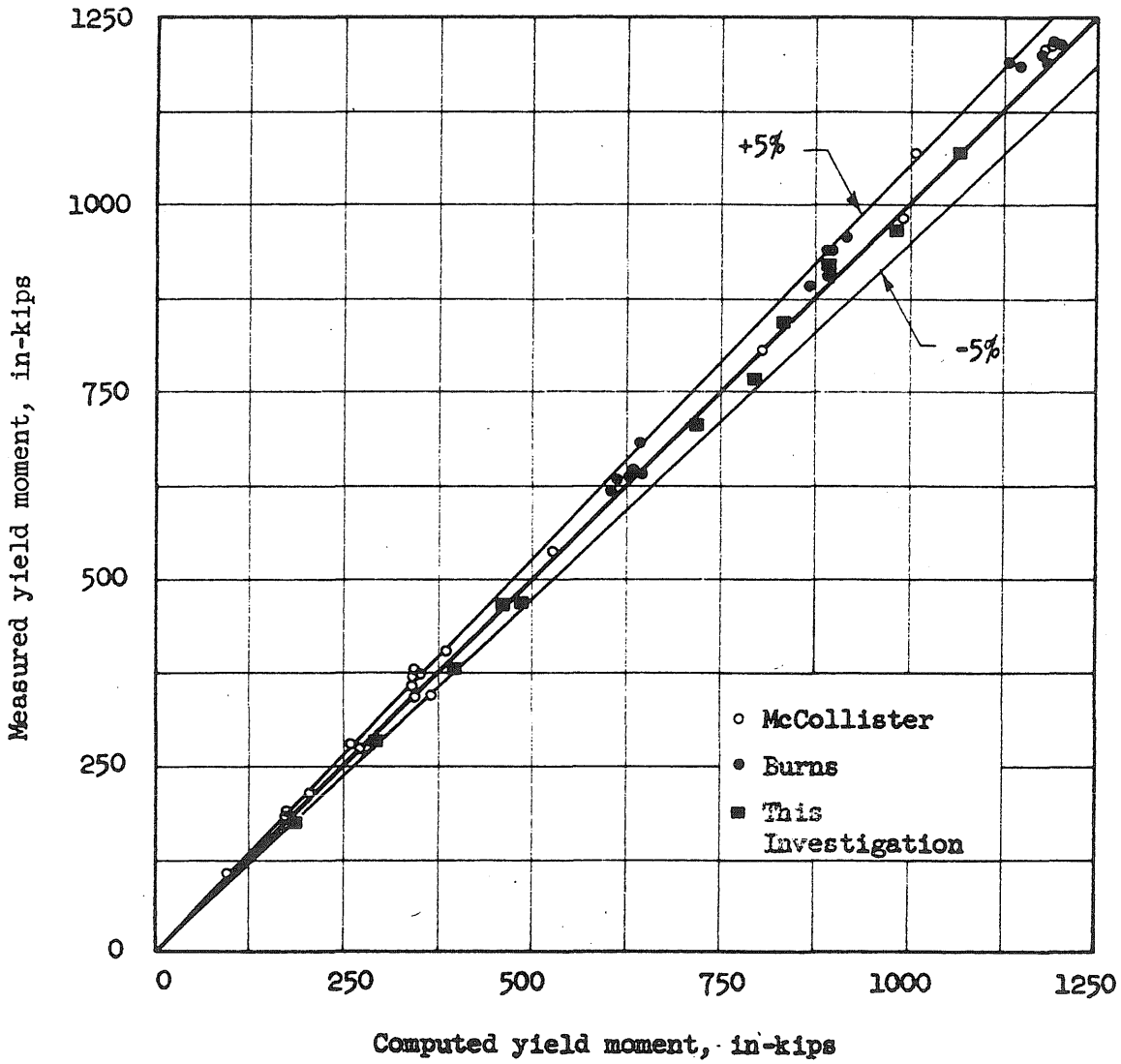

FIG. 5.1 COMPARISON OF MEASURED WITH COMPUTED YIELD MOMENTS

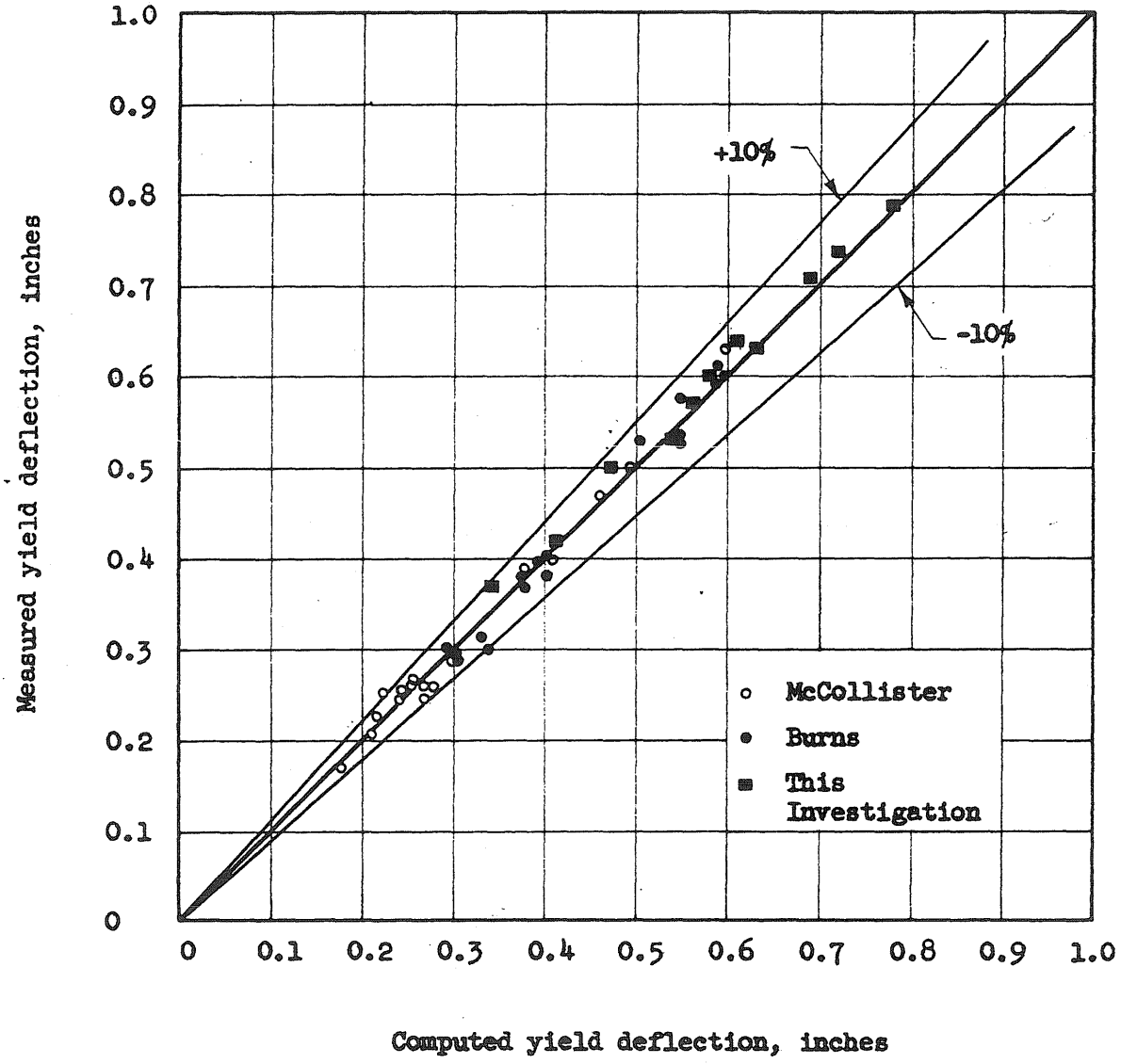

FIG. 5.2 COMPARISON OF MEASURED WITH COMPUTED YIELD DEFLECTIONS

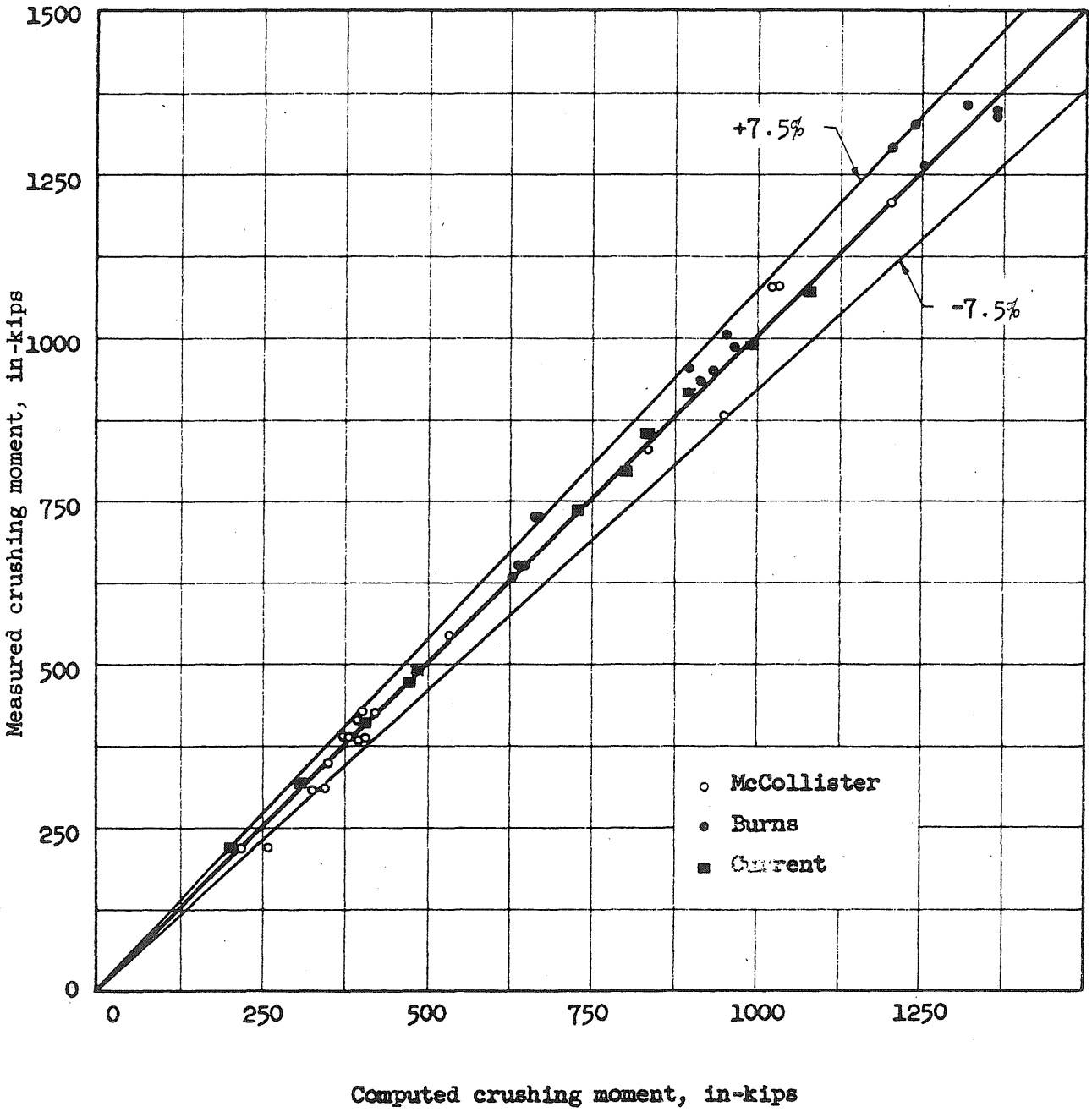

FIG. 5.3 COMPARISON OF MEASURED WITH COMPUTED CRUSHING MOMENTS

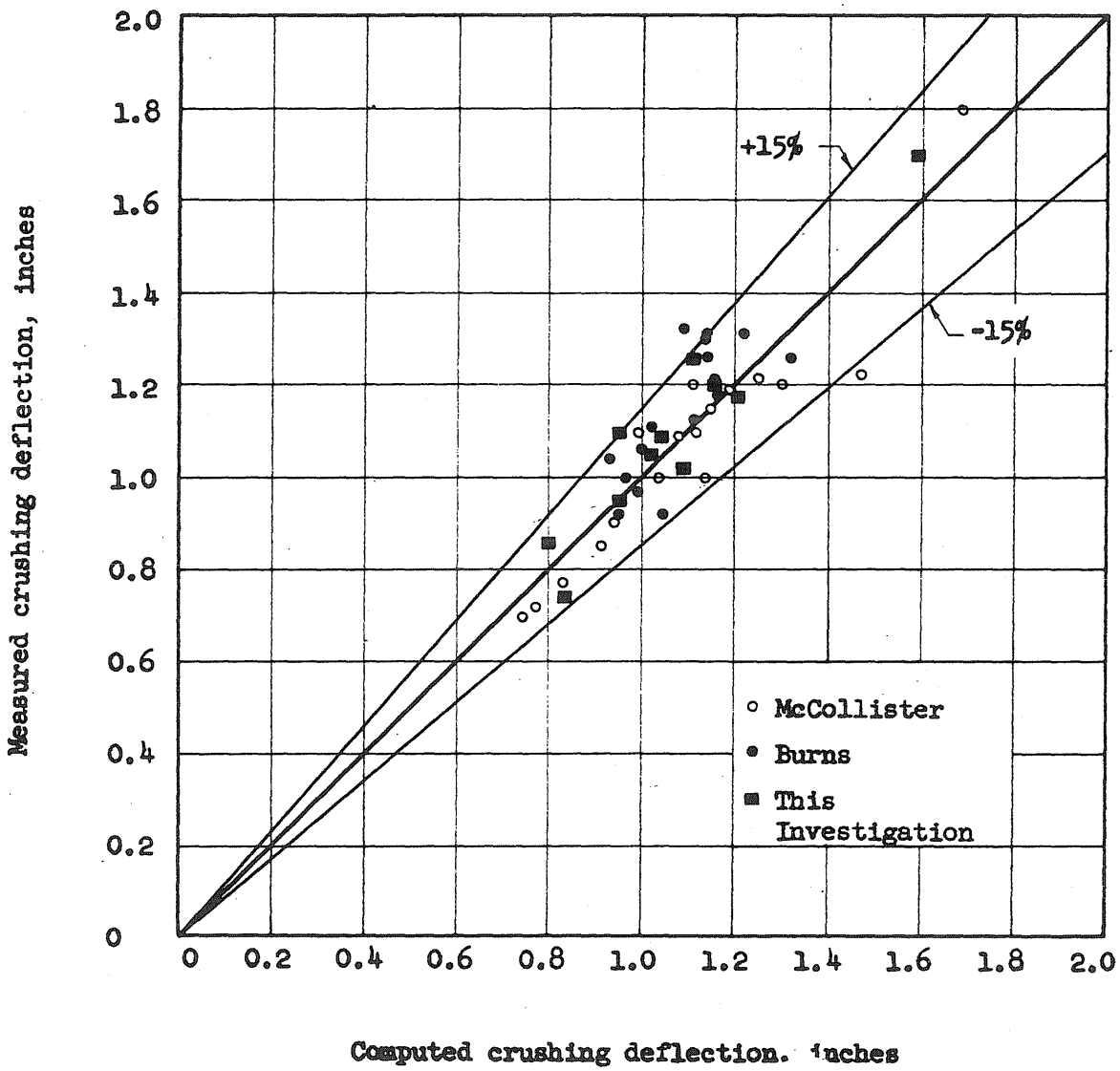

FIG. 5.4 COMPARISON OF MEASURED WITH COMPUTED CRUSHING DEFLECTIONS

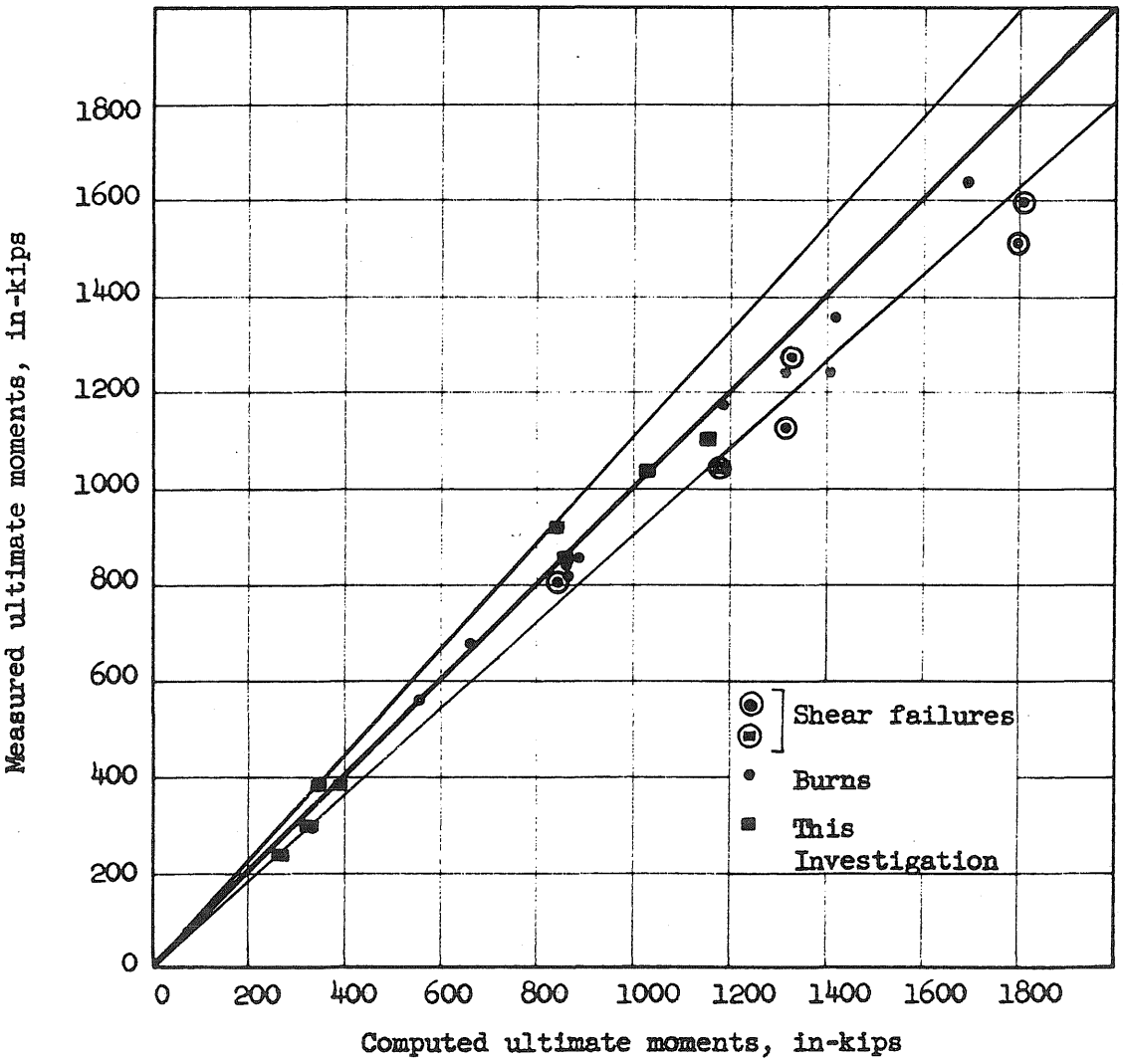

FIG. 5.5 COMPARISON OF MEASURED WITH COMPUTED ULTIMATE MOMENTS

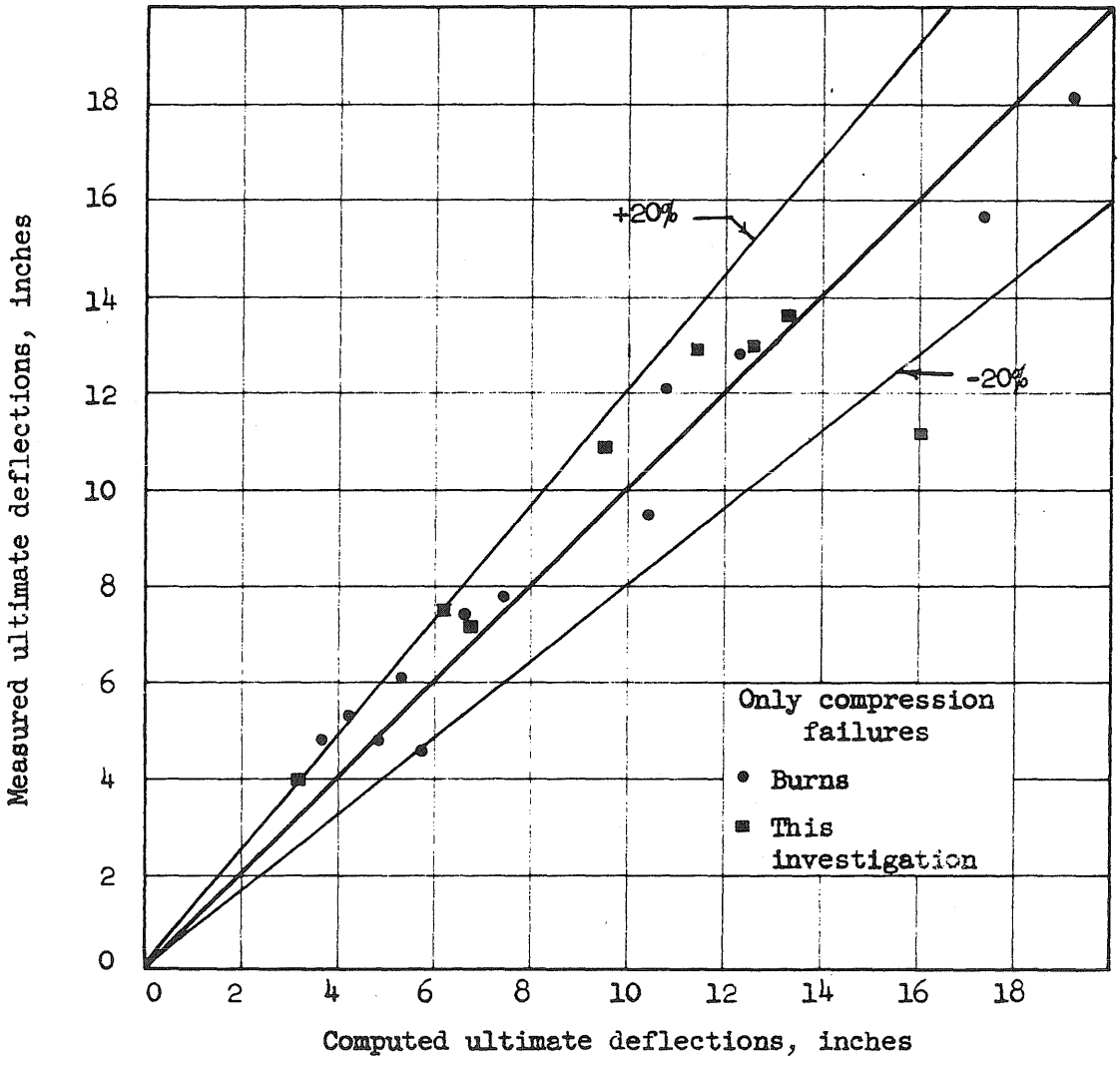

FIG. 5.6 COMPARISON OF MEASURED WITH COMPUTED ULTIMATE DEFLECTIONS

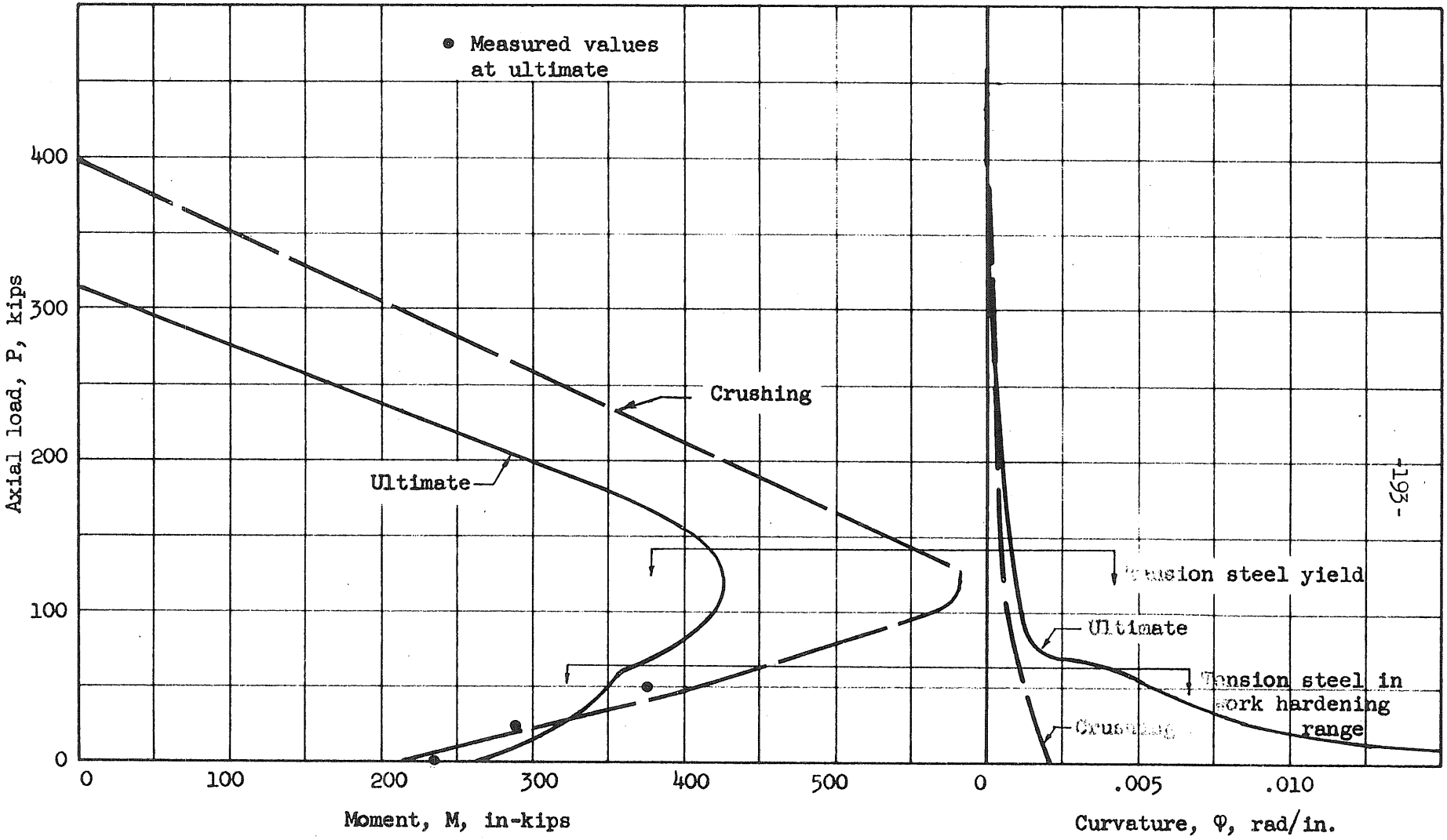

FIG. 5.7 INTERACTION CURVE FOR ULTIMATE STAGE, p_g = 1.11%

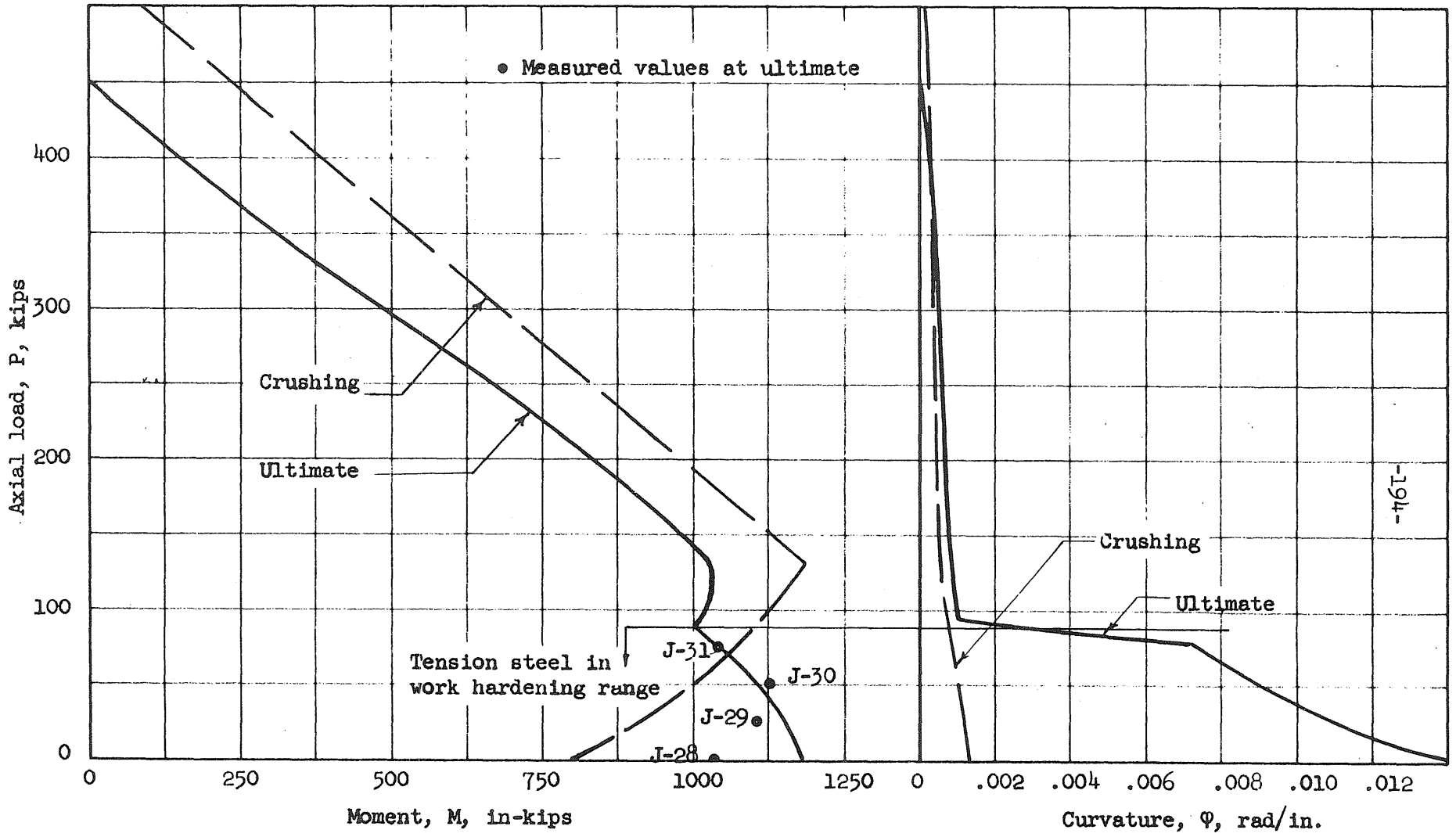

FIG. 5.8 INTERACTION CURVE FOR ULTIMATE STAGE, p_g = 5.55%

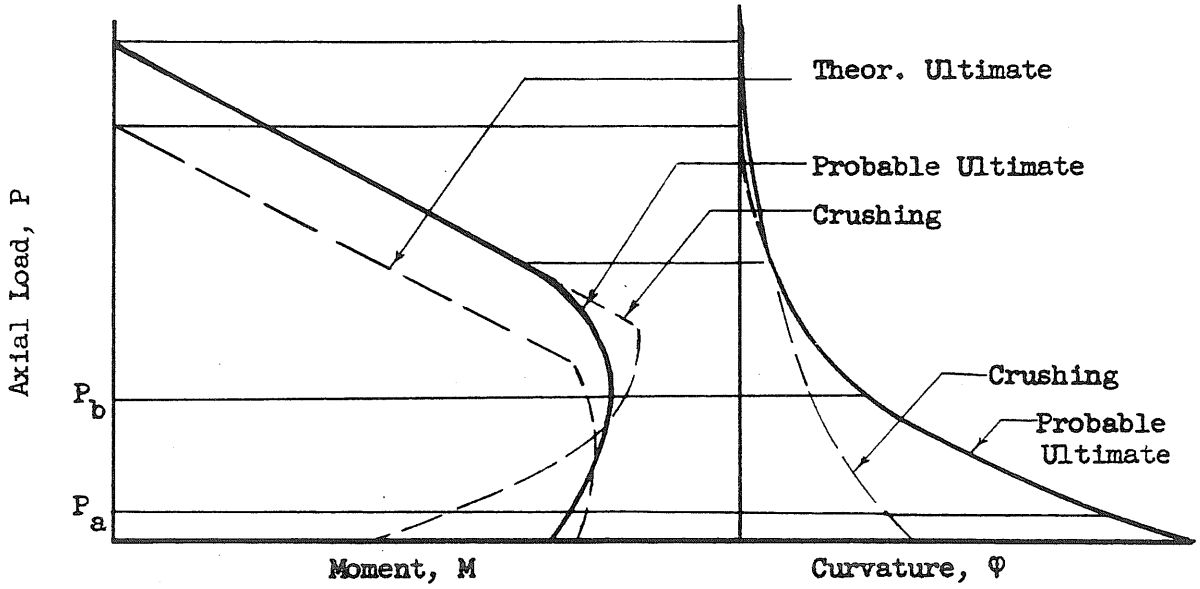

(a) P-M Curves (b) P-φ Curves

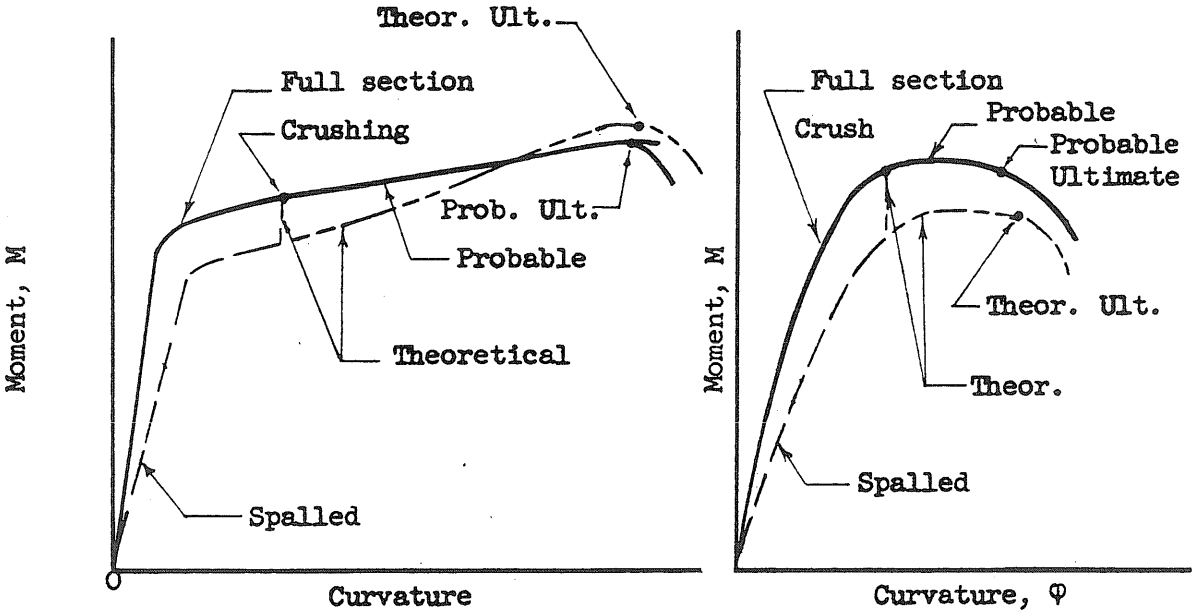

(c) M-φ Curve for $P = P_a$ (d) M-φ Curve for $P = P_b$

FIG. 5.9 COMPARISON OF THEORETICAL INTERACTION CURVES FOR ULTIMATE AND MOMENT-CURVATURE RELATIONSHIPS FOR ADVANCED STAGES OF BEHAVIOR WITH THE CORRESPONDING ACTUAL RELATIONSHIPS

APPENDIX A

MATERIALS AND FABRICATION OF TEST SPECIMENS

A.1 Materials

Cement

Marquette brand Type III portland cement was used for all specimens.

Aggregates

Wabash river sand and gravel were used for all specimens. Both aggregates have been used in this laboratory for many previous investigations and have passed the usual specification tests. The coarse aggregate had a maximum size of one inch. The sand and gravel had specific gravities of 2.65 and 2.70, respectively. The absorption of both fine and coarse aggregates was about one percent by weight of surface-dry aggregate.

The origin of these aggregates is an outwash of the Wisconsin glaciation. The major constituents of the gravel were limestone and dolomite with minor quantities of quartz, granite and gneiss. The sand consisted mainly of quartz.

Concrete Mixes

Concrete strength was not a variable in this investigation. A concrete mix used in previous investigations and which was known to have a strength of about 4500 psi at about 3 weeks was used. In Table A.1 the following properties for each batch are listed: compressive strength, slump, and age at time of test. The values for the compressive strength are the averages of the tests of three 6 by 12-in. cylinders.

Reinforcing Bars

The intermediate grade deformed bars used for reinforcement met the requirements of ASTM Designations A15-39 and A305-50T. All the bars in each size were of the same heat in order that the properties might be maintained as uniform as possible. The bars were purchased in 28-ft lengths; two lengths of 12 ft-11 in. for use as reinforcement and a 26-in. test sample were cut from each bar.

The stress-strain characteristics of the reinforcing bars were determined from tension tests made in a 120,000-lb. capacity Baldwin Southwark Take-Emery hydraulic testing machine. The elongation in an 8-in. gage length up to about two percent strain was measured with an 8-in. extensometer employing a Baldwin "microformer" coil and recorded with an automatic device. Beyond this strain, the elongation in the 8-in. gage length was measured with divider and scale in order to obtain the complete stress-strain curve. Figure 4.6 shows typical stress-strain curves for bars used in this investigation. Table A.2 lists the properties of the bars used in each beam as determined from the tension tests.

A.2 Preparation of Reinforcement

Since the overall length of the specimens was 13 ft, the reinforcing steel was cut to lengths of about 12 ft-11 in. The deformation lugs were ground flush with the bar at the locations where the electrical gages were to be mounted. Medium and fine grade emery cloth were used to smooth the bar surface. After cleaning the bar surface with acetone, the strain gages were mounted using a Baldwin post-yield cement. To insure reliable readings at very high levels of strains, a special waterproofing procedure was used. A piece of polyethylene plastic slightly larger than the gage was placed on top

of the gage to insure complete unbonding between the gage and the waterproofing material. The plastic was kept in place by strips of masking tape. A layer of wax was then brushed on and around the polyethylene plastic to insure waterproofing. On top of the wax a layer of epoxy cement was placed in order to protect the wax from damage during the handling and casting operations. Waterproofing of the gages was checked after the beam was cast by measuring the resistance of the gages and the resistance to ground. Only the strains from gages which past these tests were considered in the analysis of the test data.

The type and locations of the gages are described in Section B.1.

Punch marks at 2-in. centers were made along the ribs of one of the tension bars in each beam. In the specimens reinforced with #9 bars (J-28 through J-31), punch marks were also made along the rib of one of the compression bars. Measurements of the gage length before casting the beam and after the end of the test made it possible to obtain the magnitude and distribution of the residual strains in the longitudinal steel after failure.

The stirrups were made of #3 deformed intermediate grade bars welded into a closed rectangle. In specimens J-28 through J-31, in order to measure residual strains in the transverse reinforcement, punch marks at 2-in. centers were made in one of the vertical legs of each of the first two stirrups outside the column stub on either side. In specimen J-34, both punch marks at 2-in. centers and an SR-4 A-7 electrical gage were placed on the top side of each of the first two stirrups outside the stub on either side.

The reinforcement was assembled into a cage with one longitudinal bar securely tied at each of the corners of the stirrups, which were spaced at 6-in. intervals in all specimens (Fig. 2.2) except J-34. In specimen J-34, Fig. 2.2, a spacing of 3 in. for a length of 12 in. on either side of the

column stub was used; the remainder of the stirrups were spaced at 6-in. intervals as in the other specimens. This cage was then placed in the form and chairs beneath the bottom bars assured the desired position of steel.

A.3 Casting of Test Specimens

A non-tilting drum-type mixer with 6 cu. ft. capacity was used for mixing all concrete. Three batches were required for specimens J-15 and J-16 and two batches for all the others. The mixing time for each batch was about three minutes. Slump was determined immediately after mixing.

Three 6 by 12-in. control cylinders and one 6 by 6 by 24-in. control beam were cast from the first batch. Three control cylinders, and for some specimens, one control beam were cast from the second and third batches.

The first batch was placed in a layer of decreasing height from the ends of the beam up to near the column stub. The second layer was placed on top of the first one and filled part of the column stub for the larger specimens. For the smaller specimens the second layer filled the remainder of the specimen. A third layer was needed for the larger specimens. All of the concrete in the compression zone of the member was from the last batch.

The concrete in the test specimens and in the control beams and cylinders was vibrated with a high frequency internal vibrator.

One day after the specimens were cast, the plywood forms were removed; the specimens were then covered with wet burlap and surrounded by polyethylene plastic to hold in the moisture. This curing continued for one week. After which the specimens were left in the lab uncovered until tested. The control cylinders and beams were cured in the same way; and except in two instances, they were tested on the same day as the beam-column specimen.

APPENDIX B

INSTRUMENTATION AND LOADING APPARATUS

B.1 Instrumentation

Electrical Strain Gages on Reinforcing Bars and Stirrups

Except in specimen J-34, strains in the longitudinal reinforcement were measured with Type PA-3 SR-4 gages, which have a nominal gage length of 13/16 in. In specimen J-34, Budd metal film strain gages C6-141-B, having a shorter gage length, were used because the stirrups were closely spaced. These gages were used in order to obtain strain readings in the post-yield range. They required the use of a special strain indicator with a range of strain readings much wider than that of ordinary indicators. The location of these gages are given in Table B1 and in Fig. B.1.

In order to check the magnitude of the stresses on the top side of stirrups in the critical zone, in specimen J-34, Type A7-4 SR-4 gages were mounted on the first two stirrups outside of the stub on either side. Baldwin portable strain indicators were used to obtain the strain readings.

Electrical Strain Gages on Concrete

As listed in Table B1, electrical gages were used to measure strains on the compressed face and on the sides of the specimens at points above the estimated location of the neutral axis. Type A-3 SR-4 gages (13/16-in. gage length) were used in the first four specimens tested. Since their gage length was relatively short for the 1-in. maximum size of the coarse aggregate, sets of two type A-12-2 SR-4 gages (1-1/2-in. gage length each) in series were used for specimens J-28 through J-31. As shown in Fig. B.1, the two gages of the set were placed wither side by side at 3/4-in. centers at points having a large strain gradient, or were so spliced that an uninterrupted

3-in. gage length was obtained. (The trimmed edges of the paper backing were brought into contact without overlapping.) The location of the gages are shown in Fig. B.1 and indicated in Table B.1.

Mechanical Strain Gages

A 6-in. Berry strain gage was used to measure strains on the compression face and on one side of the specimen at locations where strains were small and their relatively small importance did not justify the use of the expensive electrical gages. Steel plugs with gage holes drilled in their faces were cemented to the surface of the concrete at the locations shown in the photograph of Fig. 3.19b.

Load Cells

Two load cells were inserted between the jack used to apply the transverse load and the specimen. One was connected to a portable strain indicaaor and was used to measure the transverse load; the other was connected to the y-axis system of an x-y automatic plotter, a deflection device being connected to the x-axis system, so that a continuous record of the transverse load could be obtained. The sensitivity of these load cells was about one kip per 100 microinches of indicator reading. A more detailed description of these load cells may be found in Reference 1.

As shown in Fig. B.3a, the tension force in each of the four prestressing strands used to apply the axial load was measured by aluminum dynamometers placed between the strand anchor and the bearing plate at the end of the specimen opposite that at which the tension was applied. The sensitivity of these dynamometers was about one kip per 300 microinches of indicated strain on a portable strain indicator.

Deflection Dials

Deflections were measured at four points along the centerline of the specimen. Two of the readings were taken at points in line with the faces of the stub and the other two midway between the support and the face of the stub on either side. Dial indicators with 4-in. travel and 0.001-in. dial divisions were used. They were carried by a bridge supported at the end bearings, which gave a non-deflecting reference for deflections. These dials bore against short pieces of angle cemented to the face of the specimen at mid-height.

Automatic Load-Deflection Plotter

An Autograph Model 3 x-y Plotter was used to obtain a continuous transverse load-deflection record. The midspan deflection was measured by a slidewire displacement device having 18-in. travel in either direction which was connected to the x-input of the plotter. A transverse load dynamometer was connected to the y-input as described earlier. The displacement measuring device was supported on the cross-beam of the test frame. Since the cross-beam deflected upon loading, the automatic plotter did not record the actual deflection of the member. Although the deflection coordinate could have been easily corrected by using data from the deflection dials, the more accurate dial readings were used in the analysis of the data.

B.2 Loading Apparatus

The specimens were loaded in the specially constructed frame shown in the photographs of Fig. B.2. The transverse load was applied by means of a 50-ton hydraulic ram reacting against the cross-beam of the test frame. A loading block made of an 8 by 12 by 2-in. steel plate was seated in plaster on top of the stub. The load was applied through a 3/4-in. pin, and the stub was therefore free to rotate.

A rather complicated support system, which was originally designed for tests with reversal of loading, was used. It provided a simple support at mid-depth of each end of the specimen. As can be seen in the photographs of Fig. B.3, it consisted of two 6 by 8 by 3/4-in. side plates bolted to chanel-shaped pieces on top and bottom, and leaving in between a rectangular space slightly larger than the cross-section of the specimens. These four pieces were placed around the specimen at each end, with the channel pieces seated on plaster to insure uniform contact with the specimen. Rollers were fitted on shafts welded to the side plates at mid-height. Each of the four rollers reacted on the milled horizontal surfaces at the end reaction supports, which were securely attached to the test frame.

The compressive axial load was applied as shown in the photographs of Fig. B.3. The reactive force was transmitted from one end of the specimen to the other through four lengths of 7-wire prestressing strands of 3/8 or 1/2 in. diameter. At the dynamometer end of the specimen (so called because the dynamometers for measuring the forces in the cables were at this end), Fig. B.3a, the strands were anchored against a thick steel plate which bore against another steel plate cemented to the end of the specimen. At the jack end of the specimen (the jack used to apply the axial load was at this end), Fig. B.3b, the strands were anchored to a 2-in.-thick plate. Between this plate and the end of the specimen was a 50-ton hydraulic jack bearing against a thick plate, which in turn bore against another thick plate cemented to the end of the specimen.

The two plates next to either end of the specimen had a cylindrical contact surface with its axis coinciding with that of the support rollers. This arrangement made it possible to readjust both ends of the axial load device so as to reduce the eccentricity of the axial load with respect to the

axis of the support rollers that originated as the ends of the specimens rotated upon loading.

To prevent the specimens from failing prematurely due to lateral instability, a lateral support was provided at midspan as shown in the photographs of Fig. B.2. This support allowed the specimen to deflect freely vertically, but restricted its lateral deflection to less than 1/4 in.

APPENDIX C

PROPERTIES OF CONFINED CONCRETE

C.1 General Remarks

If concrete is compressed in one direction it tends to expand laterally. If this expansion is restricted, concrete is said to be "confined," and as a result of such restriction compression stresses develop in all directions. On the other hand, if such lateral expansion can occur freely, concrete is said to be "unconfined," and principal compression stresses exist only in one direction. The strength and the ductility of confined concrete may be considerably larger than the corresponding values for unconfined concrete. Because of these properties, confined concrete has a very practical use in the design of members to resist earthquake motions or blast loadings, in which cases the ability of a member to undergo large deformations without a considerable reduction in its strength is at least as important as its ability to carry loads.

In Section C.2, the strength of concrete prisms under axial load, and confined by lateral reinforcement is presented. In flexural members only part of the section is usually in compression, and very little is known about the properties of concrete confined under this condition. An approximate procedure for estimating the confining action of the transverse reinforcement for this case is suggested in Section C.3. In Section C.4, information on deformation characteristics of confined concrete is presented. Since such information was insufficient to carry out the analyses presented in Chapter 4 of this report, the stress-strain curves for confined concrete assumed in this study are also presented.

C.2 Strength of Confined Concrete Under Concentric Axial Load

On the basis of tests on concrete cylinders under concentric axial load and confined laterally by fluid pressure (13) the following simple relationship for the strength of confined concrete has been suggested:

$$f_1 = f''_c + 4.1\, f_2 \qquad (C.1)$$

where f_1 = unit compressive strength of confined concrete

f''_c = unit compressive strength of unconfined concrete

f_2 = average lateral unit pressure

In reinforced concrete members, the confining force is furnished by the transverse reinforcement. This reinforcement is provided in the form of a continuous helical reinforcement or circular hoops in the case of members with circular sections. If the member has a rectangular section it is provided in the form of closed rectilinear ties.

Beyond a stress of approximately 85 percent of the unconfined strength, lateral deformations in the concrete increase appreciably. The transverse reinforcement reacts against this tendency of the concrete to expand laterally and transverse compressive stresses are induced in the concrete.

In the case of circular prisms the average confining stress, f_2, may be computed from the equilibrium of the free body diagram shown in Fig. C.1a as follows:

$$f_2 = \frac{2A''_s\, f''_s}{s\, D_s} \qquad (C.2)$$

where A''_s = cross-sectional area of transverse reinforcement

f''_s = unit stress in transverse reinforcement, which may be assumed to be equal to the yield stress for mild steels

s = longitudinal spacing of the transverse reinforcement

D_s = diameter of concrete core enclosed by the transverse reinforcement

If Eq. C.1 is used, the strength of circular prisms confined by lateral reinforcement is

$$f_1 = f''_c + \frac{8.2\ A''_s\ f''_s}{s\ D_s} \qquad (C.3)$$

This relationship was found to hold for short circular columns (14). The unconfined strength f''_c for the short circular columns is (15):

$$f''_c = 0.85\ f'_c \qquad (C.4)$$

Equation C.3 can also be written as follows:

$$f_1 = f''_c + 4.1\ \frac{p''\ f''_s}{2} \qquad (C.5)$$

where $p'' = \dfrac{\text{volume of lateral reinforcement}}{\text{volume of confined concrete}}$

The evaluation of the confining action of the transverse reinforcement in rectangular prisms is more difficult than for the case of circular prisms. For rectangular prisms, the equilibrium of the various sections resulting from longitudinal cuts made in several directions indicates different average stresses acting in different directions. On the basis of tests on specimens with various amounts of longitudinal and transverse reinforcement, and loaded longitudinally with a small eccentricity, Chan (16) suggested the following expression for the increase of strength due to confinement:

$$K_u - K_o = \sqrt{\frac{p''}{0.189}} \qquad (C.6)$$

where $K_u - K_o$ = contribution of the transverse reinforcement to the unit compressive strength of the concrete expressed as a ratio of the cube strength

This expression ignores the effect of the strength of the transverse reinforcement. Therefore, it may not be applicable for cases in which the strength of the transverse reinforcement differs significantly from that of the reinforcement used in Chan's tests.

Tests on rectangular prisms with transverse reinforcement only, and tested under concentric axial load are reported in Reference 12. It is suggested in that report that the average normal stress across a line joining the midpoint of two adjacent sides be taken as the measure of the effect of the transverse reinforcement. The confining stress, f_2, computed in this way is

$$f_2 = \frac{p'' f''_y}{(\frac{b}{h} + \frac{h}{b})} \qquad (C.7)$$

where f''_y = yield stress of transverse reinforcement

b = width of enclosed section

h = height of enclosed section

This expression takes into account the effect of shape. However, a plot of the measured increase of strength over the unconfined value (Δf_c) versus the confining stress (f_2) computed using Eq. C.7 shows a very wide scatter of the points representing the test results. In this study, a different definition for the stress f_2 was tried. It was taken as the average of the normal stresses in two perpendicular directions, which is a constant. If the directions parallel to the sides of the section are considered, as shown in Fig. C.1b, a simple expression for f_2 can be derived as follows:

$$f_2 = \frac{1}{2} (\frac{2A''_s f''_s}{bs} + \frac{2A''_s f''_s}{hs}) = A''_s f''_s (\frac{b + h}{bhs})$$

or

$$f_2 = \frac{p'' f''_s}{2} \qquad (C.8)$$

It is interesting to note that this expression is exactly the same as that for a circular prism. Figure C.2 shows a plot of the measured increase of unit compressive strength for the tests reported in Reference 12 versus the

confining stress computed using Eq. C.8. It can be seen that the points representing the test results follow a consistent trend. In a recent statistical study (17) of results from various investigations the following expression relating the increase of compressive strength due to confinement and the confining stress (according to the notation used herein) is suggested:

$$\Delta f_2 = 2f_2 \tag{C.9}$$

where Δf_c = increase of unit compressive strength

However, if this equation is used for the tests reported in Reference 12, the values for Δf_c are on the unsafe side for f_2 larger than about 1000 psi, as shown in Fig. C.2. In this study, the following more complicated expression is proposed:

$$\Delta f_c = \frac{6000}{1 + \frac{2300}{f_2}} \tag{C.10}$$

It describes well the trend of the points representing the test results shown in Fig. C.2.

C.3 Strength of Confined Concrete in Bending

In flexural members, the strains vary over the depth of the cross-section. The whole section or only part of it may be in compression. Since the latter was true in all specimens analyzed here, it will be the only case considered in this discussion. The confining effect of the transverse reinforcement for this case is much more difficult to determine than for the concentric axial load, for several reasons. For example, lateral deformations tend to be larger at the extreme compression fiber, and practically nonexistent at the neutral axis; nor do all points of the ties offer the same restraint against lateral expansion of the core concrete. Consequently, the confining

stresses in this case are more unevenly distributed than with a concentric axial load.

No basis for computing the strength of concrete confined under these conditions could be found in the technical literature. For the purpose of analyzing the results of the tests considered in this study, it was assumed that Δf_c for this case is given by Eq. C.10, and f_2 was taken equal to the average of the confining stresses in the directions parallel to the sides of the section computed according to the assumptions shown in Fig. C.3. The expression for f_2 thus computed is

$$f_2 = \frac{1}{2}(f_{21} + f_{22}) = \frac{A''_s f''_y}{s}\left(\frac{1}{2c} + \frac{1}{b''}\right) \qquad (C.11)$$

where $f_{21} = \dfrac{A''_s f''_y}{sc}$ = average normal stress on a plane perpendicular to the neutral axis

$f_{22} = \dfrac{2A''_s f''_y}{b''s}$ = average normal stress in a plane parallel to the neutral plane

c = depth of the neutral axis from the inside face of the transverse reinforcement

and all other terms are as defined before.

It was assumed that the yield stress was reached at all points of the transverse reinforcement surrounding the compression stress block. This was verified by strain measurements at several locations in the ties taken during the course of this investigation. It was also assumed that the concrete on the tension side did not contribute to the confining phenomena.

Equation C.11 neglects the effects of the spacing of the lateral reinforcement and of the presence of longitudinal reinforcement on the effectiveness of the confinement offered by the ties. A quantitative estimate of such effects could not be made because of lack of experimental data.

Other properties of the stress block needed for the flexural computations are presented in the following section.

C.4 Deformation Characteristics of Confined Concrete

Experimental investigations (12) (13) (14) (16) have shown that the shape of the stress-strain curve for concrete varies with the confining stress, which in turn is a function of the amount and properties of the transverse reinforcement.

On the basis of his tests, Chan (16) derived the following expressions relating the ultimate strains observed in the tests to the amount of lateral reinforcement:

$$\epsilon_u - \epsilon_o = \sqrt[3]{\frac{p''}{17}} \qquad \text{for circular hoops or helical reinforcement} \qquad (C.12)$$

and

$$\epsilon_u - \epsilon_o = \sqrt[3]{\frac{p''}{24.5}} \qquad \text{for rectangular ties} \qquad (C.13)$$

where $\epsilon_u - \epsilon_o$ = increase of strain over the unconfined value

Again, as in the case of his equations for strength of confined concrete, the above expressions do not consider the physical properties of the transverse reinforcement. They do, however, give an indication of the relative efficiency of circular and rectangular ties. Means for obtaining the complete stress-strain curve for confined concrete were not suggested by Chan.

In Reference 18, a stress-strain relationship for confined concrete in terms of the properties of both the transverse reinforcement and the bound concrete is suggested. However, the authors recognize that the suggested stress-strain curve is well on the conservative side.

In view of the limited information in this area, no attempt has been made in this study to derive a general expression for the stress-strain curve

of confined concrete. However, since such curves are needed in order to evaluate the results of the tests considered in this study, the stress-strain curves shown in Fig. 4.9 were assumed on the basis of curves reported in Reference 12 for concentrically-loaded rectangular prisms with amounts of transverse reinforcement comparable to those of the specimens being analyzed.

To summarize, the stress-strain relationships for confined concrete used in Chapter 4 of this report are based primarily on the tests reported in Reference 12. The shape of the curves was assumed on the basis of the curves reported there, and the maximum of the stress-strain curve was computed using Eqs. C.10 and C.11 which are also based on the results of those tests.

TABLE A.1

CONCRETE PROPERTIES

Mark	Cylinder Strength, f'_c (ksi)			Slump (inches)			Age in Days
	Batch 1	Batch 2	Batch 3	Batch 1	Batch 2	Batch 3	
J-24	4.88	5.06	----	2.0	1.5	---	90
J-25	4.54	5.05	----	2.0	2.0	---	88
J-26	4.64	4.60	----	2.0	2.0	---	100
J-27	4.80	4.92	----	2.5	1.5	---	35
J-34	4.56	4.52	----	2.0	2.0	---	27
J-15	5.15	5.18	4.40	0.5	1.0	2.0	57
J-16	4.26	4.32	4.55	1.5	2.0	2.0	16
J-28	5.35	5.02	----	2.0	3.5	---	40
J-29	4.48	4.41	----	1.0	2.0	---	42
J-30	4.97	4.50	----	1.5	2.5	---	22
J-31	4.64	4.28	----	1.5	2.5	---	24

TABLE A.2

PROPERTIES OF REINFORCING BARS

Mark	Size	Yield Stress f_y ksi	Yield Strain ϵ_y %	Work Hard. Strain ϵ_{sh} %	Ult. Stress f_{su} ksi	Ult. Strain ϵ_{su} %	Rupt. Stress ksi	Rupt. Strain %	Young's Modulus $E_s \times 10^{-3}$ ksi
				Tension Reinforcement					
J-24	#4	48.5	0.180	1.61	77.8	16.0	68.1	24.1	27.0
J-25	#4	49.2	0.175	1.80	78.8	17.0	73.5	19.5	28.1
J-26	#4	49.9	0.175	1.44	81.9	16.0	71.9	17.4	28.5
J-27	#4	50.0	0.175	1.50	80.1	15.5	68.5	19.9	28.6
J-34	#4	48.8	0.175	1.40	81.2	14.0	73.5	17.0	27.9
J-15	#8	46.9	0.170	1.57	75.3	14.5	71.8	17.5	27.6
J-16	#8	45.9	0.150	1.68	72.8	15.0	67.9	18.8	30.6
J-28	#9	46.9	0.160	1.53	77.6	17.0	76.0	19.9	29.3
J-29	#9	48.8	0.180	1.36	80.2	16.0	75.8	24.3	27.1
J-30	#9	47.0	0.150	1.62	77.5	16.0	75.0	17.9	31.3
J-31	#9	48.3	0.145	1.39	78.3	18.0	74.5	24.3	33.3
				Compression Reinforcement					
J-24	#4	47.8	0.175	1.55	76.9	17.5	65.2	22.8	27.4
J-25	#4	49.2	0.175	1.77	78.0	15.5	68.0	22.3	28.1
J-26	#4	49.0	0.170	1.42	80.3	16.0	69.0	20.6	28.8
J-27	#4	50.1	0.175	1.48	81.3	18.0	69.7	21.4	28.6
J-34	#4	50.3	0.175	1.40	81.9	16.0	74.0	20.4	28.7
J-15	#8	47.3	0.160	1.57	75.3	15.0	71.8	18.1	29.6
J-16	#8	44.7	0.150	1.69	71.4	15.0	67.9	18.8	29.8
J-28	#9	46.7	0.170	1.62	77.6	17.5	75.0	23.4	27.5
J-29	#9	48.6	0.160	1.50	80.4	15.6	76.2	25.0	30.4
J-30	#9	47.2	0.145	1.00	80.2	15.8	75.0	24.1	32.5
J-31	#9	47.9	0.160	1.44	80.2	18.7	75.5	24.5	29.9
								Mean	29.1

TABLE B.1

SUMMARY OF STRAIN MEASUREMENTS TAKEN

(see also Fig. B.1)

Mark	Tension Steel*	Comp. Steel*	Top Surface		Miscellaneous++
			Type	Location**	
J-24	7,16,26	7,16,26	A-1	1,4,7,10,15,20	MS
J-25	7,16,26	7,16,26	A-3	1,4,7,10,15,20	MS
J-26	7,16,26	7,16,26	A-3	1,4,7,10,15	A-3 S
J-27	0,7,13,23	7,13,19	A-3	1,4,7,10,15	A-3 S
J-34	7,13	7,10	A-12-2+	1.5	ST
J-16	7,16,26	7,16,26	A-3	1,4,7,10,15,20	MS
J-15	7,16,26	7,16,26	A-3	1,4,7,10,15,20	MS
J-28	0,7,13,23	7,13,19	A-12-2+	1.5,4.5,7.5	A-12-2 S, ST
J-29	0,7,13,23	7,13,19	A-12-2+	1.5,4.5,7.5	A-12-2 S, ST
J-30	0,7,13,23	7,13,19	A-12-2+	1.5,4.5,7.5	A-12-2 S, ST
J-31	0,7,13,23	7,13,19	A-12-2+	1.5,4.5,7.5	A-12-2 S, ST

* Type PA-3 SR-4 gages on all specimens except J-34 (Budd metal film C6-141-B gages). Distance from midspan, in inches.

** Distance from the face of the stub, in inches.

+ Sets of two gages in series.

++ MS = mechanical gages on side of specimen; S = on side of specimen; ST = strains in transverse reinforcement.

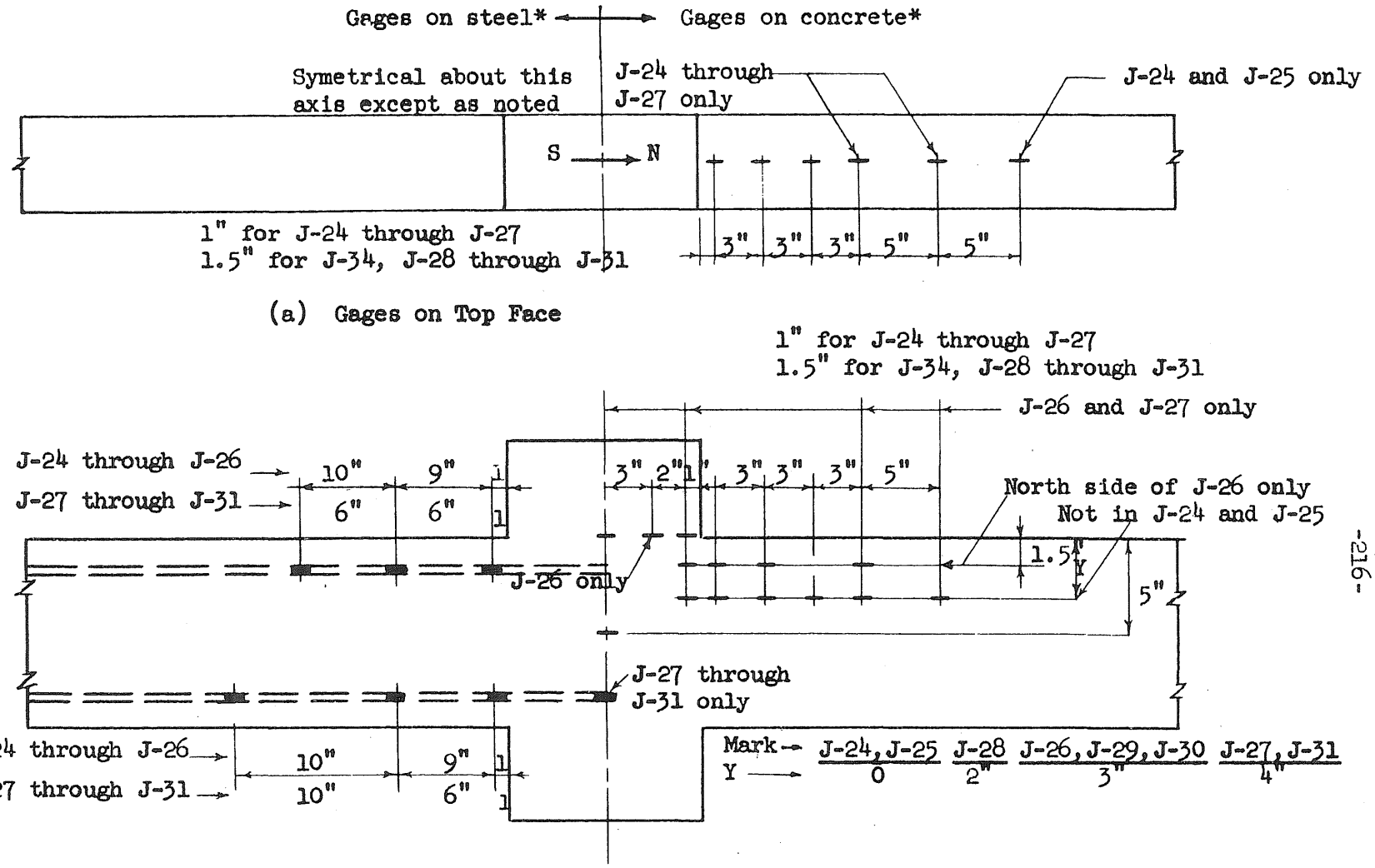

FIG. B.1 LOCATION OF ELECTRICAL STRAIN GAGES ON CONCRETE AND REINFORCEMENT

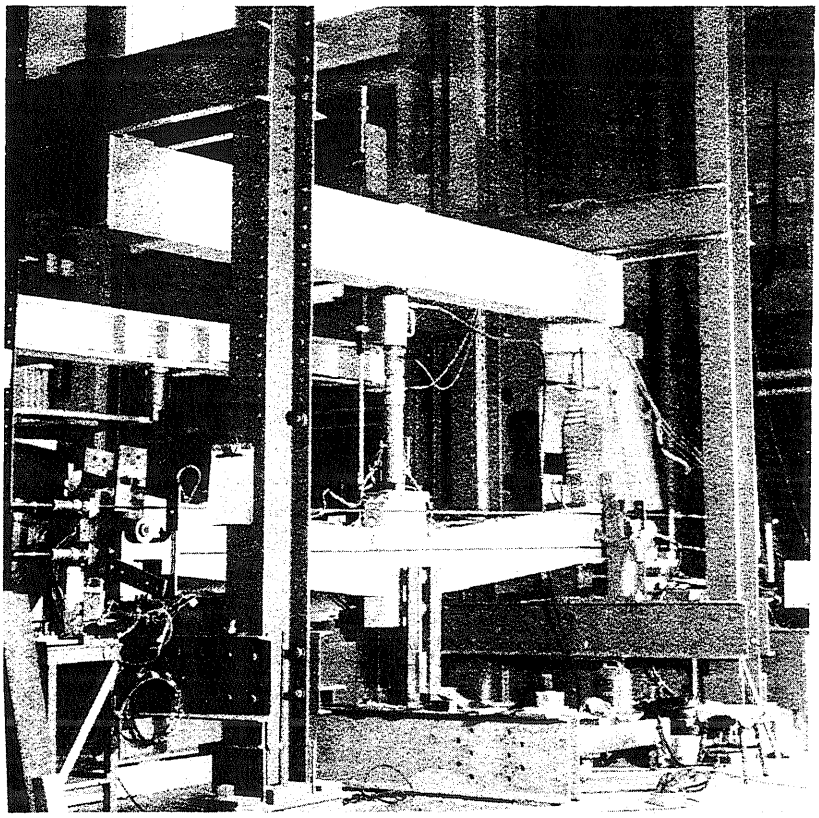

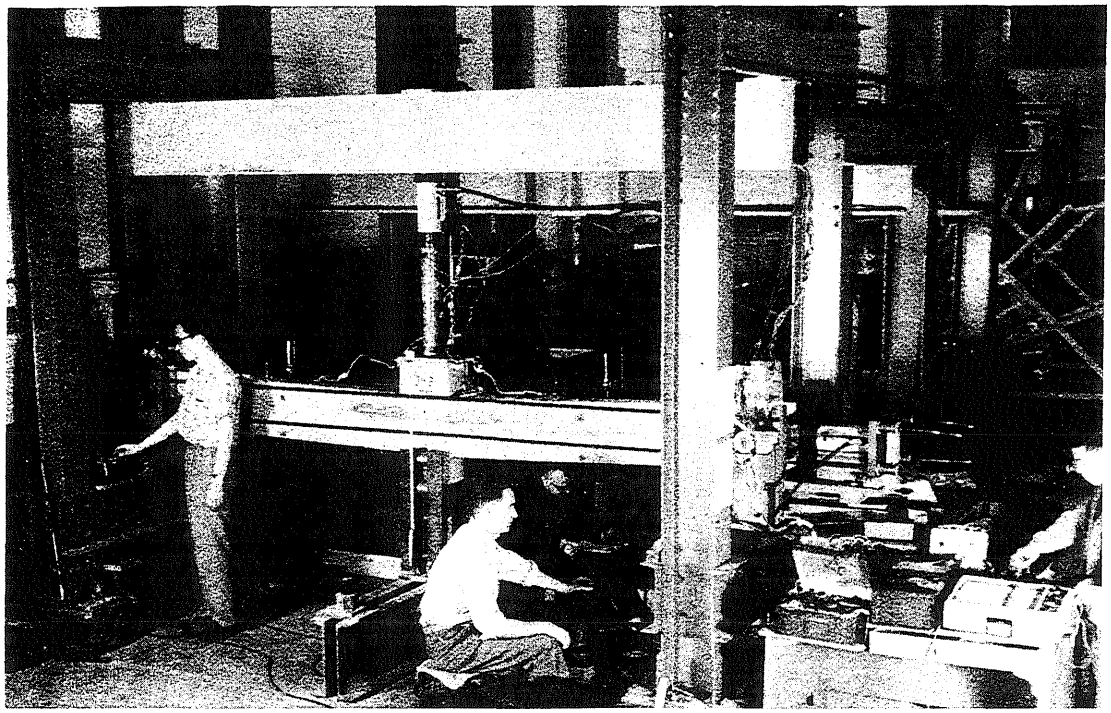

FIG. B.2 PHOTOGRAPHS SHOWING TEST SET-UP

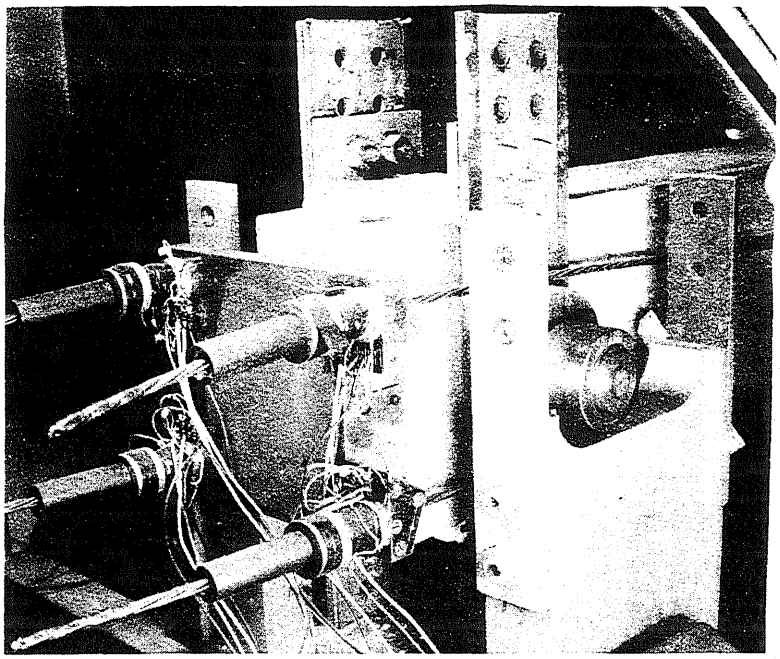

(a) Dynamometer End

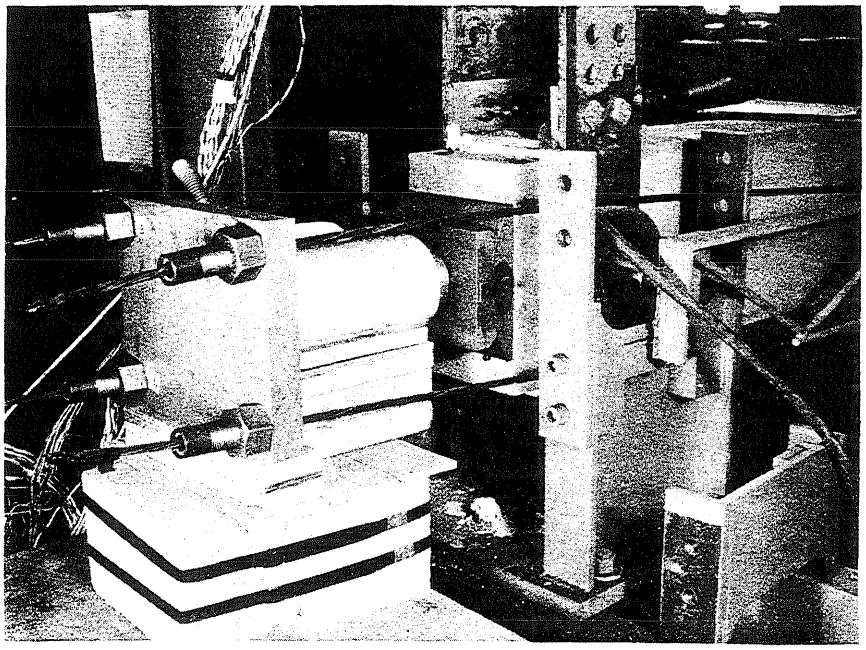

(b) Jack End

FIG. B.3 PHOTOGRAPHS SHOWING AXIAL-LOAD EQUIPMENT

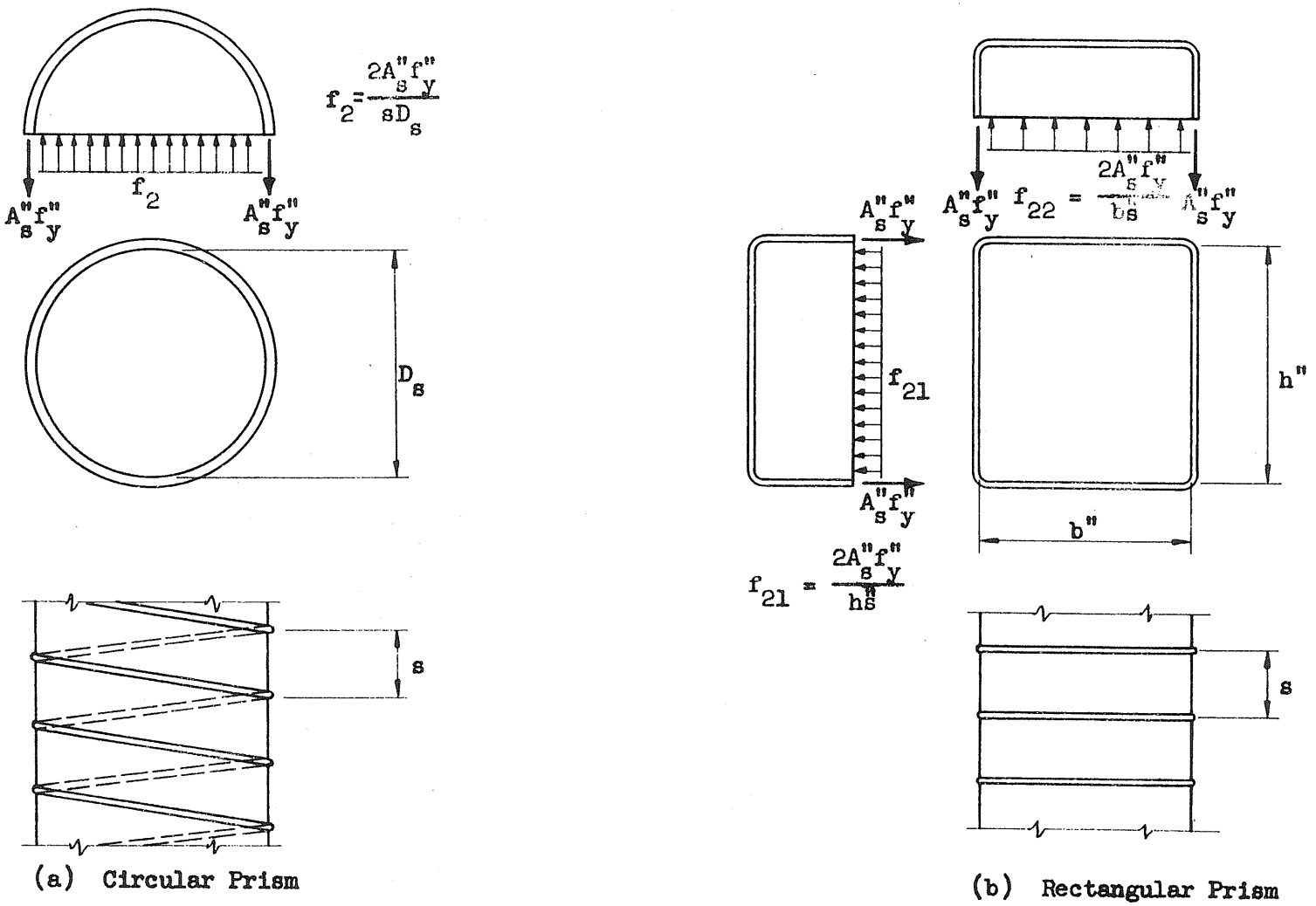

FIG. C.1 DETERMINATION OF AVERAGE TRANSVERSE STRESS FOR CIRCULAR AND RECTANGULAR PRISMS SUBJECTED TO A CONCENTRIC AXIAL LOAD

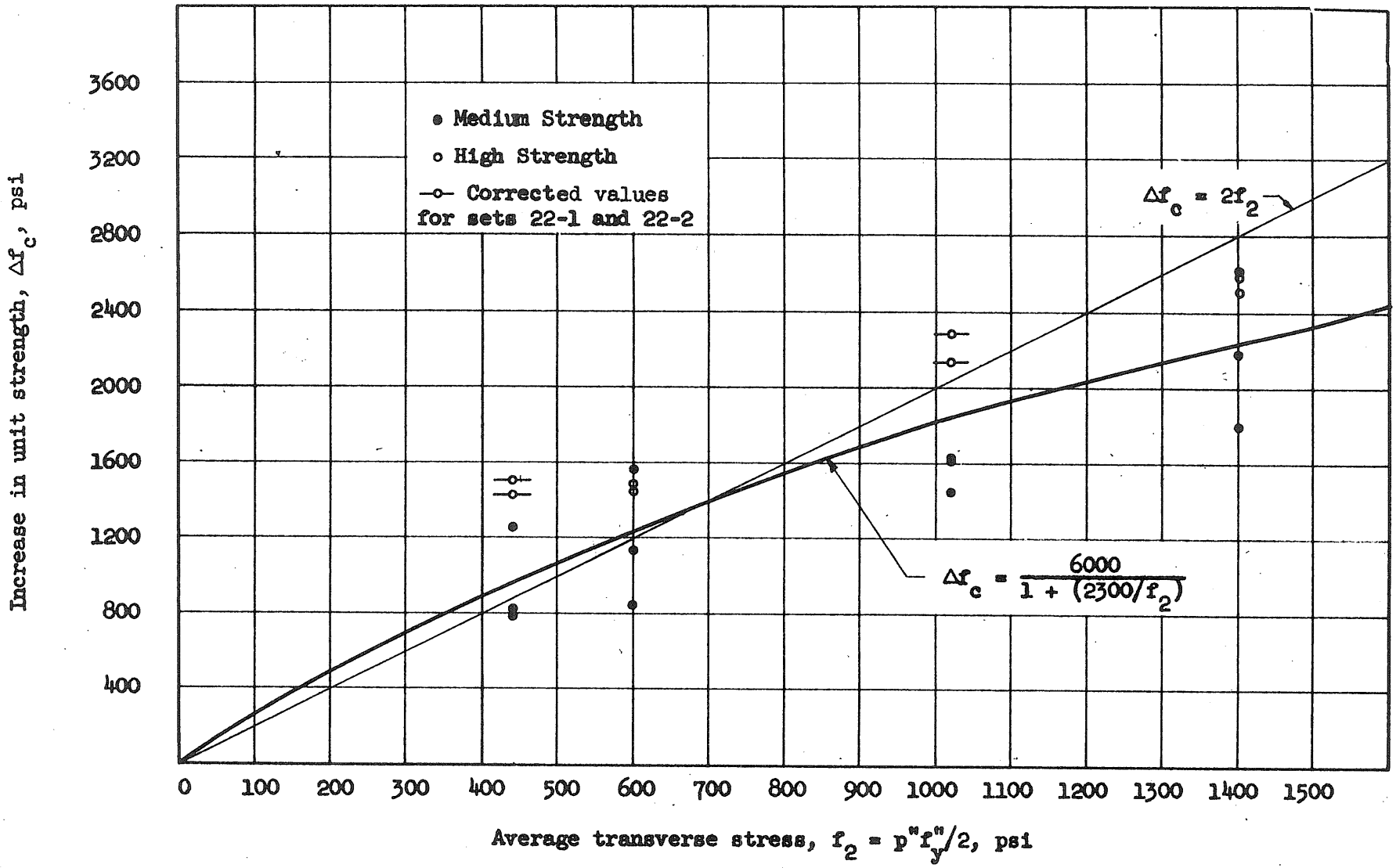

FIG. C.2 COMPARISON OF INCREASE IN UNIT STRENGTH WITH AVERAGE TRANSVERSE STRESS

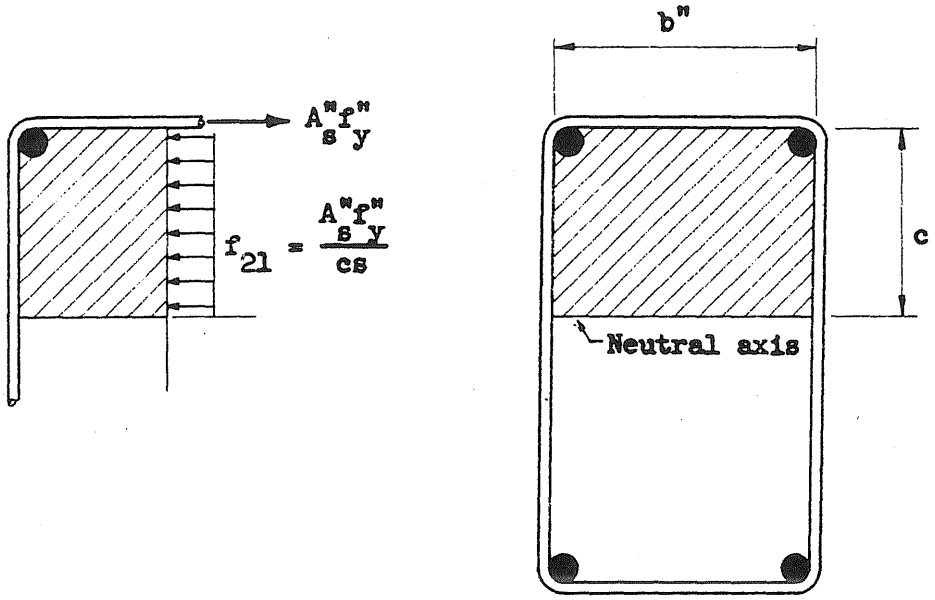

$$f_2 = \frac{1}{2}(f_{21} + f_{22})$$

$$= \frac{A_s''f_y''}{s}\left(\frac{1}{2c} + \frac{1}{b''}\right)$$

s = spacing of ties

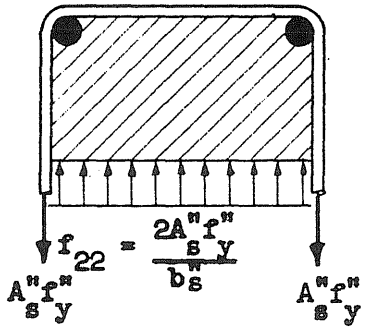

FIG. C.3 DETERMINATION OF AVERAGE TRANSVERSE STRESS FOR A SECTION IN BENDING